Rewilding a rainforest in the heart of Rio *p. 113*

Cerebrospinal fluid dynamics in the brain *p. 176*

Using CAR-T cells to treat autoimmunity *p. 179*

Science

$15
8 JULY 2016
sciencemag.org

AAAS

RAY OF LIGHT

Photoresponsive heart cells drive a robot swimmer *pp. 111 & 158*

CONTENTS

8 JULY 2016 • VOLUME 353 • ISSUE 6295

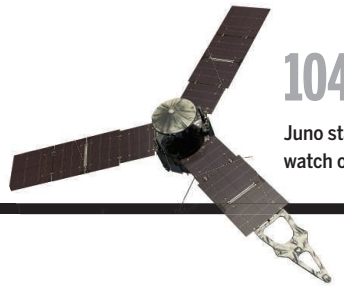

104 Juno starts its watch over Jupiter

Not far from downtown Rio de Janeiro, ecologists plot a forest comeback.

NEWS

IN BRIEF

IN DEPTH

FEATURES

INSIGHTS

PERSPECTIVES

POLICY FORUM

BOOKS *ET AL.*

PHOTOS: (TOP RIGHT) NASA; (TOP LEFT) LUCIANO CANDISANI

Published by AAAS

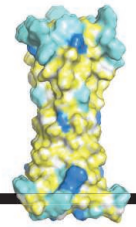

172

The transmembrane domain of the HIV-1 Env protein

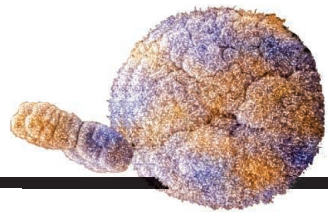

126

Building human chromosomes

ON THE COVER

A robotic stingray made up of rat heart cells, gold, and a polymer commonly used in breast implants. The robot ray mimics the form and function of a swimming stingray, but with a twist: Genetically altered rat cells allow the "creature" to sense and swim toward light. See pages 110 and 158. For more on the process behind the cover image, see http://scim.ag/29lfI5O.
Photo: Ken Richardson

SCIENCE (ISSN 0036-8075) is published weekly on Friday, except the last week in December, by the American Association for the Advancement of Science, 1200 New York Avenue, NW, Washington, DC 20005. Periodicals mail postage (publication No. 484460) paid at Washington, DC, and additional mailing offices. The title SCIENCE is a registered trademark of the AAAS. Domestic individual membership and subscription (51 issues): $165 ($74 allocated to subscription). Domestic institutional subscription (51 issues): $1522; Foreign postage extra: Mexico, Caribbean (surface mail) $55; other countries (air assist delivery) $89. First class, airmail, student, and emeritus rates on request. Canadian rates with GST available upon request, GST #1254 88122. Publications Mail Agreement Number 1069624. **Printed in the U.S.A.**
Change of address: Allow 4 weeks, giving old and new addresses and 8-digit account number. **Postmaster:** Send change of address to AAAS, P.O. Box 96178, Washington, DC 20090–6178. **Single-copy sales:** $15.00 current issue, $20.00 back issue prepaid includes surface postage; bulk rates on request. *Science* is indexed in the *Reader's Guide to Periodical Literature* and in several specialized indexes.

Science
AAAS
1200 New York Avenue, NW, Washington, DC 20005
Clarendon House, Clarendon Road, Cambridge, UK CB2 8FH

SUBSCRIPTION SERVICES For change of address, missing issues, new orders and renewals, and payment questions: 866-434-AAAS (2227) or 202-326-6417, FAX 202-842-1065. Mailing addresses: AAAS, P.O. Box 96178, Washington, DC 20090-6178 or AAAS Member Services, 1200 New York Avenue, NW, Washington, DC 20005

INSTITUTIONAL SITE LICENSES 202-326-6730 **REPRINTS:** Author Inquiries 800-635-7181 **COMMERCIAL INQUIRIES** 803-359-4578 **PERMISSIONS** 202-326-6765, permissions@aaas.org **AAAS Member Services** 202-326-6417 or http://membercentral.aaas.org/discounts

INFORMATION FOR AUTHORS See pages 624 and 625 of the 5 February 2016 issue or access www.sciencemag.org/authors/science-information-authors

EDITORIAL

The communities of Science

Jeremy Berg
Editor-in-Chief
Science *Journals*
Email: jberg@aaas.org

My father was a mathematician. When I was a teenager, I talked to him about careers. I love math, even fairly esoteric stuff. He surprised me by saying, "Math is something to pursue only if you cannot imagine doing anything else. You can follow other careers and still do math, but pure math can be very isolating; only a few people in the world are likely to really understand what you are working on." I was surprised that he was discouraging me from his career path. But wait, what? He was also implying that science was a social activity in an essential way.

I took his advice and pursued chemistry, driven in part by my interest in geometry and three-dimensional structures. Over my career, I have moved from chemistry to structural biology and crystallography, to synthetic inorganic chemistry, back to structural biology, to biophysics, to biochemistry, to informatics, to computational biology, and to personalized medicine. Along the way, I also have had great opportunities to lead scientific organizations. I helped build a department of biophysics and directed the most fundamental science-focused institute at the U.S. National Institutes of Health (NIH), with programs spanning the basic biomedical and related sciences, key clinical areas such as anesthesiology, and research training. With regard to the clinical areas, my expertise has been greatly bolstered by "home schooling" in clinical research by my wife, Wendie Berg, an accomplished breast imaging researcher and clinician who has run several major clinical trials.

While at NIH, I had many intense discussions with a colleague about the social science research relevant to developing inclusive training programs. He would frequently challenge me with results that did not fit my intuition. He had the habit of adding aphorisms to his email signature block, and one of my favorites was, "Don't believe everything you think." This directive nicely captures the power of the scientific method. If you have an idea, you can collect data and analyze them to determine whether your observations are consistent with your hypothesis or refute it. I, like most practicing scientists, have had my eyes opened when an attractive hypothesis was demolished by an incisive experiment.

Returning to my father's comment, science is, indeed, a profoundly social activity. Many hypotheses come not from single individuals but from groups with individuals at different career stages and with diverse interests, discussing previous results and ideas. Small or large teams of researchers perform many experiments. Other scientists then review the results, critically examining the experiments, analyses, and interpretation. All of this is conducted in a highly competitive environment where personal satisfaction, funding, recognition, and career stability often depend on being the "first" to make an advance, creating tension with collaborative efforts.

"...science is, indeed, a profoundly social activity."

It is daunting to be added to the list of incredibly impressive individuals who have previously served as editor-in-chief. Most recently, Marcia McNutt has led the *Science* journals admirably over her relatively short tenure. She is leaving only because her accomplishments led to another amazing opportunity, and the scientific community is fortunate to have her as president of the U.S. National Academy of Sciences.

The position of the editor-in-chief of *Science* and the other journals of the *Science* family presents both a tremendous opportunity and an intimidating responsibility. Science is a key tool in addressing the pressing problems facing humankind and our planet. To make progress, scientists must engage with the public, policy-makers, and many other groups. Scientists must communicate their results fairly and listen to the perspectives of others. *Science* serves as a premier journal for presenting the most exciting scientific results from a wide range of disciplines and is a key forum for relevant news and discussions of policy. I look forward to working with the communities of *Science*.

– Jeremy Berg

10.1126/science.aah4023

IMAGES: (INSET) ANTIKWAR/ISTOCKPHOTO ADAPTED BY G. GRULLÓN/*SCIENCE*; TERRY CLARK

NEWS

> “Under the law, it says you must report. If you don’t report, the law says you shouldn’t get funding.”
>
> **Vice President Joe Biden**, at a 29 June summit officially launching the White House’s “moonshot” to fast-track cancer research, promising to crack down on research institutions that don’t report their clinical trial data.

IN BRIEF

Juno (here in an artist’s rendition) signaled its safe arrival at Jupiter with three simple tones.

Jupiter has a new orbiter

After a 5-year journey, NASA’s latest planetary probe, Juno, safely completed a tricky maneuver on 4 July to enter into orbit around the solar system’s biggest planet. By the end of August, the craft will settle into a 14-day elliptical orbit that will bring it within 4000 kilometers of Jupiter’s outer veil of clouds, closer than any spacecraft has gone before. Juno will peer through the clouds to study the planet’s structure; scientists hope it will answer questions such as how far down the surface stripes and swirling storms go, what is the source of Jupiter’s intense magnetic field, and whether the planet has a rocky core. Theorists believe that, as the solar system’s largest resident, Jupiter holds the key to understanding how the whole body of planets formed around the protostar that became our sun. The probe will circle the planet pole to pole 33 times over the next year and a half before plunging into the clouds at the end of its mission to prevent an accidental collision with one of Jupiter’s moons, which could contaminate it with earthly microbes.

AROUND THE WORLD

NEON’s price tag goes up

WASHINGTON, D.C. | The National Science Foundation (NSF) has agreed to spend $35.5 million more to complete its National Ecological Observatory Network (NEON), raising its total price to $469 million. The money is expected to allow the troubled project, already reduced in scope and delayed by a year, to begin full operations at all 81 sites by the end of 2017. The additional construction money comes from a pot earmarked for maintenance and operations for NEON; that money had not yet been spent because the project is behind schedule. But the project could still siphon away money from NSF’s existing biology research program, because NEON’s new contractor, Battelle Memorial Institute, hasn’t yet worked up a detailed proposal for how much the continent-wide observatory will cost to operate. NSF’s current estimate of $60 million to $80 million is not reliable, says Maria Zuber, chair of the National Science Board in Arlington, Virginia, which oversees NSF and approved the additional spending last week. “If operating costs become an issue, then we may be talking about another descoping”—altering the project’s objectives, Zuber says. “But let’s get it built, and then we can look closely at managing the impact of NEON on the rest of the bio budget.” **http://scim.ag/NEONfunding**

A research tower at NEON’s Front Royal, Virginia, site.

Call for research integrity office

PARIS | Like many countries, France started giving attention to the issue of scientific misconduct in the 1990s, culminating in a 2015 charter for scientific integrity signed by several major national research organizations and the country’s Conference of University Presidents. But compared with other European and North American countries, the country’s research organizations and universities have “been lagging behind in putting in place appropriate measures,” suggests a 29 June report commissioned by Thierry Mandon, France’s state secretary for higher education and research.

CREDITS: (ILLUSTRATION) NASA/JPL-CALTECH; (PHOTO) C. STEELE/SCIENCE

Research organizations in the survey, and in particular the French National Institute of Health and Medical Research, generally had stronger procedures in place than universities, and most institutions had a policy for paper authorship, the report found. But there were "partial, and sometimes even nonexistent" procedures reporting and investigating alleged misconduct at many institutions. The report calls for a national strategy and the creation of a French Office for Research Integrity to monitor questionable research practices and support institutions in their handling of misconduct. It also suggests handing out research grants only to institutions that have a scientific integrity policy.

Charity's open access push

LONDON | The Wellcome Trust, the U.K.-based charity that has become one of the biggest nongovernmental funders of biomedical research, will launch its own open-access online journal this autumn. Publication will be limited to the thousands of scientists working on research funded by a Wellcome grant, and it will be free for authors as well as for readers—the $24 billion charity is covering the costs of the journal's software and online platform. Peer review will occur postpublication, the charity said in a statement. The move has excited many critics of traditional scientific publishing. "This really is a potential game changer for a major funder to be taking control of the research output," says Paul Ginsparg, the Cornell University physicist who founded arXiv, the massive online scientific preprint server. Wellcome previously launched the open access journal *eLife* in 2012, in collaboration with the Howard Hughes Medical Institute and the Max Planck Society.

Dawn, New Horizons updates

WASHINGTON, D.C. | NASA announced 1 July that it is denying a third act to its Dawn spacecraft, which has so far explored the two largest bodies in the asteroid belt, Vesta and Ceres. Rather than visiting a 150-kilometer-wide asteroid known as 145 Adeona in 2019, as proposed by its mission leaders, the spacecraft will remain in orbit around Ceres, the administration announced, following the recommendations of a senior review panel. Chris Russell, the mission principal investigator at the University of California, Los Angeles, says he was surprised and disappointed to hear of the decision. "We thought that everyone we had talked to about this plan was enthusiastic about it," he says. "I had no negative vibes until this particular moment." Meanwhile, NASA said it will support a mission extension for New Horizons, the spacecraft that flew past Pluto in July 2015. The spacecraft will now pursue 2014 MU69, an icy Kuiper belt object about 30 kilometers across, for a rendezvous on 1 January 2019.
http://scim.ag/NASAupdates

Mexico's wind farms, like this one on the Isthmus of Tehuantepec, face community opposition.

PHOTO: AP PHOTO/LUIS CRUZ HERNANDEZ

Mexico's clean energy challenge

Last week, Mexico, Canada, and the United States signed an agreement to commit to generating 50% of their electricity from clean energy sources by 2025. That may present a particular challenge for Mexico, which relies on fossil fuels for 78% of its electricity (compared with 25% in Canada and 67% in the United States). "I think it's doable. It's good to have such an ambitious goal," says Juan Bezaury-Creel of the Nature Conservancy, who is based in Mexico City. A controversial energy reform enacted in Mexico between 2013 and 2015 opened the market to decentralized renewable energy providers and will require businesses to pay if they exceed their allotment of energy from fossil fuels. Still, many energy policy experts wonder whether enforcement will be up to snuff in a country where corruption and impunity thrive. Mexico has also committed to tripling its wind power capacity by 2018. The Isthmus of Tehuantepec in the state of Oaxaca in Mexico—the thin strip of land between the Atlantic and Pacific Oceans—is one of the windiest places in the world and already hosts about 1600 turbines. But several ambitious wind projects have been delayed or canceled by conflicts with indigenous communities over land rights.

Nobelists: Drop anti-GMO stance

WASHINGTON, D.C. | More than 100 Nobel laureates have signed a letter, publicized last week in *The Washington Post*, that strongly chastises the Washington, D.C.–based environmental group Greenpeace for its opposition to genetically modified organisms, stating that the group has "misrepresented their risks, benefits, and impacts" and suggesting that such opposition is based on "emotion and dogma" rather than scientific data. In particular, the letter calls on Greenpeace to "cease and desist" its campaign against so-called golden rice, a genetically engineered variety of rice intended to protect against vitamin A deficiency in children; it is enriched with β-carotene, a precursor of vitamin A. Greenpeace posted a response to the letter on its website, denying that its opposition is responsible for the failure of golden rice to come to market.

AWARDS

On 27 June, *Science* won four 2016 EXCEL Awards, which recognize excellence in art and design for nonprofit media. The awarded work included cover designs for the 6 November and 4 December 2015 issues and the design for the 5 June 2015 Feature on isolated tribes. *Science* was also recognized for design excellence for three consecutive issues: 4 December, 11 December, and 18 December 2015.

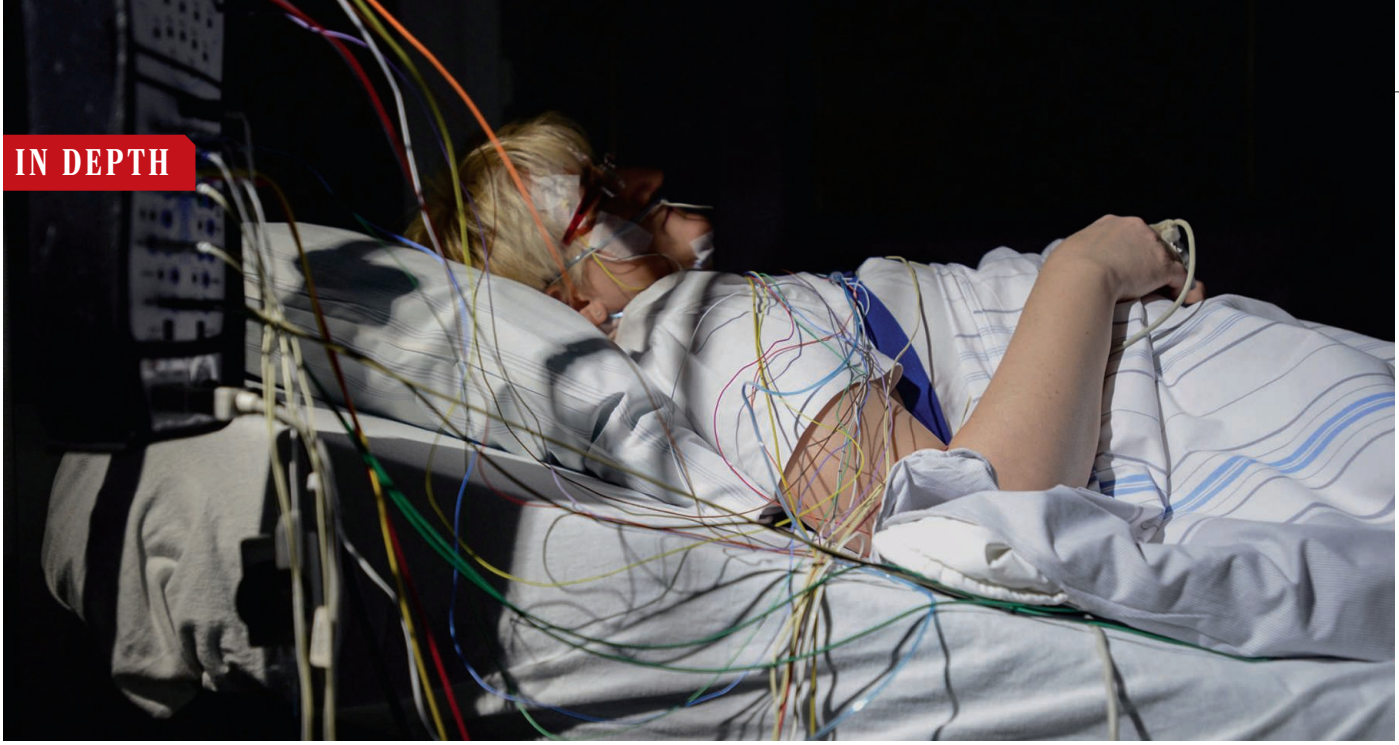

PHOTO: BSIP/UIG VIA GETTY IMAGES

RESEARCH REGULATION

Panel slams plan for human research rules

National Academies report urges creation of new national commission on ethical studies

By **David Malakoff**

In a surprise development certain to fuel a long-running controversy, a prominent science advisory panel is calling on the U.S. government to abandon a nearly finished update to rules on protecting human research participants. It should wait for a new high-level commission, created by Congress and the president, to recommend improvements and then start over, the panel says.

Policy insiders say the recommendation, made 29 June by a committee of the National Academies of Sciences, Engineering, and Medicine that is examining ways to reduce the regulatory burden on academic scientists, is the political equivalent of a comic book hero trying to step in front of a speeding train in a bid to prevent a wreck. It's not clear, however, whether the panel will succeed in stopping the regulatory express—or just get run over. Both the Obama administration, which has been pushing to complete the new rules this year, and lawmakers in Congress would need to back the halt—and so far they've been silent.

Still, many researchers and university groups are thrilled with the panel's recommendation, noting that they have repeatedly objected to some of the proposed rule changes as unworkable, but with little apparent impact. "We've been saying for some time that there is no rush to issue this rule by the end of this administration," says Lisa Nichols, director of research and regulatory reform at the Council on Governmental Relations in Washington, D.C., which represents universities and other research institutions. "The panel offers more support for the idea that we need further discussion among experts and stakeholders before we move ahead."

At the center of the debate is the so-called Common Rule, which sets ethical standards for federally funded researchers who work with human subjects. The rule spells out consent rules and governs how researchers can use data and tissue specimens from humans, alive or dead. Officials formulated the rule in 1981, with help from an influential 1978 study known as the *Belmont Report*, which was produced by a presidential commission. Since then, the rule has undergone periodic tweaks, but in 2009 more than a dozen federal agencies launched a major effort to modernize it, concluding that shifting ethical concerns and new biomedical and digital technologies had rendered it outdated. Late last year, the agencies asked for public comment on a draft rule that proposed scores of changes.

> ***The Common Rule proposal "is marred by omissions ..."***
>
> Committee on Federal Research Regulations and Reporting Requirements

Although academic researchers generally support the intent of the changes, they have blasted many of the proposals as overly burdensome and counterproductive. One lightning rod has been a proposal to allow researchers to use anonymized tissue samples only if they come from people who have given explicit written consent—a plan critics say would create a paperwork nightmare and place many useful samples off limits (*Science*, 20 May, p. 878). Researchers also have argued that it isn't clear how key components might work, including what kinds of social science research—such as analyses of tweets—might be exempt from consent rules.

The National Academies panel, which was created to examine a range of federal regulations that affect academics, echoes those concerns. The Common Rule proposal "is marred by omissions, the absence of essential elements, and a lack of clarity," the report states, and should be withdrawn. The "inadequacies," it says, "signal a pressing need for a comprehensive review of the nation's ethical, legal, regulatory and institutional frameworks for protecting research subjects." To conduct that review, the panel calls for a national expert panel modeled on the one that produced the *Belmont Report*.

Debate surrounds rules to protect human research subjects, such as this person in a sleep study.

The idea for the new commission—and the Common Rule halt—largely arose from the committee's "realization that the past consensus over how we should regulate human research is broken," says panelist Arturo Casadevall, a microbiologist at Johns Hopkins University in Baltimore, Maryland. Now, said Larry Faulkner, chair of the committee and president emeritus at the University of Texas, Austin, in a statement, "Congress and the administration have an opportunity for a course correction."

Neither administration officials nor lawmakers, however, were immediately willing to buy in. A spokesperson for the Department of Health and Human Services, which is helping lead the reform effort, wrote in an email that officials planned to read the report, but suggested that the reform effort may continue. "If a final rule is issued this fall, it will be the first time in 25 years that the regulations governing research using human participants has been updated," the spokesperson said.

Senator Lamar Alexander (R–TN), who requested the panel's report and chairs the Senate's health committee, is still reviewing the recommendation, his press secretary Louie Brogdon told *Science*. But he says that Alexander believes the Common Rule "must strike a balance between allowing researchers access to biospecimens, such as blood or tissue, and ensuring the privacy of patients." Alexander's committee could be a potential launching pad for legislation creating the proposed commission.

Many critics of the Common Rule draft had essentially given up hope that the administration would back away from its push to issue a final rule this year. But the panel's unexpected move has raised "a glimmer of hope," says Emma Meagher, an associate vice provost for human research at the University of Pennsylvania. The "recommendation can't be ignored given the profile of this group and [its] thoughtfulness," predicts Elisa Hurley, executive director of Public Responsibility in Medicine and Research in Boston.

That doesn't mean the administration will agree with the proposal, Hurley adds. One possibility, observers say, is that the administration will withdraw particularly controversial elements and push ahead with the rest. Such a move could still leave room for a new commission to "really think logically about research regulations in general," Meagher says. And Casadevall says, "we are really in need of a comprehensive, fresh look at the problem." ■

With reporting by Dianne Lugo.

PHOTO: TILL MIDDELHAUVE/FAIR

PHYSICS

Long-delayed nuclear center looks set for construction

FAIR moves ahead despite remaining budget shortfalls

By **Edwin Cartlidge**

What was supposed to be a global beehive of nuclear physics is, for now, still a large, muddy field outside the German city of Darmstadt. The Facility for Antiproton and Ion Research (FAIR), an extension of the GSI Helmholtz Centre for Heavy Ion Research planned by a collaboration of eight European Union countries plus Russia and India, was first expected to open in 2009, and then in 2015. But a series of planning errors and other problems pushed the price tag up to some €1.7 billion—an overall rise of about 75%—and stalled construction.

The site reserved for the Facility for Antiproton and Ion Research near Darmstadt, Germany, pictured in 2014.

Now, however, FAIR may finally get built. At a council meeting on 27 and 28 June, the partner countries concluded that they have enough money to cover a €320 million budget gap that came to light in 2014, and they will now seek building permits from the German government. If all goes well, FAIR could be completed in 2025. "It is absolutely great news," says Carsten Welsch, a physicist at the University of Liverpool in the United Kingdom, which became an associate partner of FAIR in 2013. "The scientific community has been waiting for years for this project to go ahead."

Yet not all of the financial problems have been solved. Some countries still have to commit their share of the missing cash, including Russia, which had agreed to bear about 18% of FAIR's total construction cost, the second largest contribution after Germany's 70%. A statement issued by the FAIR council is short on details about the exact financial situation.

At FAIR, an 1100-meter-circumference synchrotron housed in a circular tunnel will propel extremely intense ion beams to very high energies and direct them to storage rings and detectors located above ground, allowing scientists to study everything from the origin of chemical elements to the cosmic imbalance between matter and antimatter (*Science*, 2 November 2007, p. 738).

In the first proposal, in 2001, FAIR was predicted to cost €675 million and to start operations in 2009. That was too optimistic. First, design additions, an increase in the cost of raw materials, and inflation upped the price to some €1.2 billion. Then, an additional roughly €100 million was needed to stabilize the unexpectedly sandy ground at the location. In 2009, the nine full-partner countries decided to commit just over €1 billion in 2005 prices for a scaled-back design with fewer instruments, to open by 2015.

Then the new €320 million hole emerged, mostly due to the introduction of tighter fire regulations in Germany that had major design consequences, says Ulrich Wiedner,

a nuclear physicist at Ruhr University Bochum in Germany and former spokesperson of Antiproton Annihilation at Darmstadt (PANDA), an experiment that is one of FAIR's four scientific "pillars."

One potential solution was to scrap PANDA, which an expert group had judged to be the least internationally competitive pillar. But in September 2015, the FAIR council decided to stump up the missing cash rather than sacrifice the experiment, designed to study the structure of protons and neutrons. The partner countries agreed to find €158 million of the missing funds (in 2005 prices) by the end of this June and then settle the balance in 2019; that way, experiments could start in 2022 and FAIR could be fully operational in 2025.

After further negotiations, the FAIR partners last week concluded that "the necessary provision of funds is assured," says FAIR Scientific Managing Director Boris Sharkov in Darmstadt, Germany. He declined to say how much has actually been guaranteed, and by whom, but admits that neither Russia nor the third largest partner, India—due to foot about 3.5% of the bill—has yet signed on the dotted line. Negotiations with both countries are "progressing very positively," Sharkov says.

But one of India's two representatives on the FAIR council, Bikash Sinha of the Variable Energy Cyclotron Centre in Kolkata, says discussions have been "acrimonious" and that India and other countries "are not prepared to bear the costs" of strict German laws. FAIR may lose out to other nuclear labs worldwide as a result, he says, adding: "Time is of the essence." FAIR council member Vladimir Fortov of the Russian Academy of Sciences did not respond to calls from *Science*.

Physicist Angela Bracco of the University of Milan in Italy, a former member of FAIR's joint scientific committee, is confident that digging of the synchrotron tunnel will start next year. If the shortfall isn't made up, one option under discussion is to use part of FAIR's operational budget, she says. Bracco also expects that some instruments will be built or installed late to ensure others are completed on time.

Wiedner says he doesn't know whether "technicalities or real problems" are holding Russia back, but believes other FAIR members would not have given the green light "without being rather confident that the whole financing is available." He now hopes that FAIR's membership can be expanded. "Other countries have to have confidence that FAIR will really fly," he says. ■

Edwin Cartlidge is a writer based in Rome.

ASTROPHYSICS

Titanic balloon sets record and tantalizes scientists

Curtailed flight highlights remaining challenges of "superpressure" balloon technology

By **Patrick Monahan**

The latest and largest pressurized balloon to be launched by NASA has set a record for endurance: the longest midlatitude flight by a large scientific balloon. Packing 532,000 cubic meters of helium and measuring 114 meters in diameter, the balloon circled the Southern Hemisphere for 46 days, lofting a gamma ray telescope to the edges of space. Nightly dips in altitude forced a premature end to the voyage on 2 July, but the flight still marks a milestone in NASA's efforts to develop so-called superpressure balloons as a low-cost alternative to satellites.

For decades, conventional "zero-pressure" balloons have given researchers a high-altitude platform for studying atmospheric chemistry, the cosmic microwave background, and many other phenomena. But at temperate latitudes, the endurance of conventional balloons is limited. During the daytime, sunlight heats the helium, causing the gas to expand and leak. At night, the balloon cools and must drop ballast to avoid drifting too low. Zero-pressure balloons can only achieve long flights during summertime near the poles, when constant daylight allows them to stay afloat for weeks at a time.

Superpressure balloons promise to bring that endurance to temperate latitudes, opening new phenomena to observation. Their helium is pressurized; because their volume doesn't change as they are heated or cooled over the course of the day, they can remain at a constant altitude and don't need to shed gas or ballast. Over the past decade, NASA has launched ever larger and more ambitious superpressure balloons, clocking midlatitude flights of up to 32 days.

On 17 May, the agency launched its latest model from Wanaka, New Zealand. But after

Going the distance

NASA's longest heavy-lift flight spanned 55 days in 2012–13, but the Super-TIGER zero-pressure balloon traced a tight path (in blue) around the South Pole. The latest balloon set a midlatitude duration record.

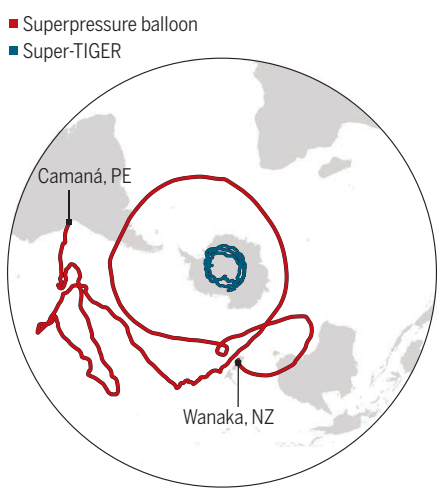

CREDITS: (PHOTO) NASA; (GRAPHIC) ADAPTED FROM NASA BY V. ALTOUNIAN/*SCIENCE*

NASA's latest superpressure balloon and its gamma ray telescope prepare to take off from New Zealand.

a few weeks of smooth sailing, the balloon's flight path during the long austral nights and short days became as erratic as a zero-pressure balloon's: It dipped as much as 10 kilometers nightly from its cruising altitude of about 33 kilometers, possibly because of a transient helium leak. And rather than circling the Southern Ocean for 100 days as intended, the balloon veered off over the South Pacific after just one circumnavigation, having slipped out of the winter cyclone winds that circle Antarctica. "Mother Nature is in charge of our business," says NASA Balloon Program Office Chief Debora Fairbrother in Wallops Island, Virginia. "She truly has been exercising her rights." NASA brought the balloon down in mountainous western Peru and will seek to draw lessons for future flights after retrieving it.

Still, the wayward balloon hauled in some novel astrophysical data. It carried the Compton Spectrometer and Imager (COSI), a gamma ray telescope that aims primarily to probe how elements are forged in supernovae. COSI observes gamma rays emitted by radioactive nuclei in supernova debris, and may be able to measure their polarization. Such observations are hard to make from the poles because of background gamma radiation from cosmic rays channeled toward the poles by Earth's magnetic field.

COSI, a lightweight instrument designed for superballoon flight, was capable of sending data back in real time in case it couldn't be recovered. Besides studying supernovae and other gamma sources, the telescope's long flight allowed it to detect a bright gamma ray burst, says lead COSI investigator Steven Boggs, an astrophysicist at the University of California, Berkeley. "You have to be in the right place at the right time to catch [gamma ray bursts]."

Stratospheric balloon observations have limitations. For research that produces very high volumes of data, such as studies of the cosmic microwave background, "we have to store all the data onboard," says Shaul Hanany, an astrophysicist at the University of Minnesota, Twin Cities. Such research will have to wait for superpressure balloons to prove their reliability—that they and their payloads won't be lost in the ocean.

Still, NASA has a full slate of superpressure balloon missions lined up in the coming years, studying phenomena ranging from dark matter to cosmic rays. As more superpressure balloon projects produce useful data, says Eliot Young, a planetary scientist at the Southwest Research Institute in San Antonio, Texas, "everyone is going to realize it's a great opportunity." ■

CREDIT: USGS, ADAPTED BY K. SUTLIFF/*SCIENCE*

ECONOMIC GEOLOGY

Massive helium fields found in rift zone of Tanzania

Commercial development could struggle in a stabilizing market for the world's best coolant

By **Eric Hand**

In 2013, Tom Abraham-James and Josh Bluett, geologists and mates from Australia, were on a holiday road trip to Serengeti National Park in Tanzania. Like any good mineral explorers, they kept a copy of *Industrial Minerals in Tanzania: An Investor's Guide* in their Land Cruiser. Several of its pages described hot springs in the East African Rift that seeped a seemingly boring, inert gas. It was mostly nitrogen, the guide said, with between 4.4% and 18.2% helium by volume. That's 10 to 100 times more helium than is typically found in natural gas, the usual source. "We thought there was a discrepancy with the decimal places in the article," Abraham-James says.

But after the researchers traced the data to their source—geological surveys from the 1950s—they began snatching up mineral leases. By 2015, they had founded Helium One, based in Bergen, Norway. And last week, they disclosed details about their claims to three massive fields of helium—a nonrenewable resource and precious commodity not just for purveyors of party balloons, but for scientists and medical technicians who need to keep things really cold. (Liquid helium, with a boiling point of 4 K, is the world's best coolant.)

The firm's best-characterized reservoir contains 1.5 billion cubic meters of helium, enough to satisfy world demand for 7 years. Two other nearby fields could contain much more. But the announcement is not just about size; unusually, Helium One plans to find and extract helium as a standalone product, rather than by sieving it from natural gas. "This is the first time that anyone has prospected for helium in a deliberate way," says Chris Ballentine, a geochemist at the University of Oxford in the United Kingdom who presented his analysis of Helium One's fields last week at the Goldschmidt Conference in Yokohama, Japan.

But prospectors have looked at Tanzania before, and experts question whether Helium One's fields are really worth developing in a relatively calm helium market that has recently moved from shortage to surplus. "Now that there's a surplus, we're skeptical as to how well it's going to work economically," says John Campbell, a consultant at Intelligas in Dedham, Massachusetts. That could change when the rest of a strategic U.S. helium reserve is auctioned off a few years from now. But Campbell adds that although large for a single field, the discovery is small in the grand scheme of things. The most recent assessment of worldwide helium resources, prepared by the U.S. Bureau of Land Management (BLM) in 2006, estimated that the world has 52 billion cubic meters of proven, probable, or possible reserves.

Pumped up

Rich fields in Tanzania could add to worldwide supplies of helium, which is usually harvested as a byproduct of natural gas production. But production from other countries could crowd the newcomers out of the market for the near future.

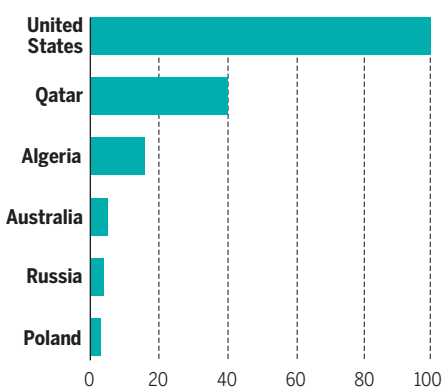

Fresh helium comes from the decay of radioactive uranium and thorium in Earth's crust. Over time, those elements emit α particles—helium nuclei—which pick up electrons and end up lodged in mineral defects as solitary helium atoms. Old rocks have more time to accumulate atoms. So the ideal source rocks are granites like those in the 3-billion-year-old Tanzania craton, an island of ancient crust in Africa. The Tanzanian helium fields have a second key ingredient: a source of

heat—in this case the volcanic systems of the East African Rift—that can cook the rocks and release the helium into "traps" consisting of porous rock capped by an impervious layer.

Ballentine reported helium concentrations of between 2.5% and 4.2% at the Ruksa field, where the gas seems to be trapped in sandstone reservoirs 0.5 to 2.5 kilometers down. Two other fields, Balangida and Eyasi, contain much higher helium concentrations, up to 10.5%, although their volumes have not been explored as fully. If Helium One can raise $40 million, it plans to begin drilling in the second quarter of 2017, Abraham-James says. He says the Tanzanian fields can provide a standalone helium supply that is independent of the price of natural gas. "You can turn up and turn down helium production according to market demand," he says.

Maura Garvey, a consultant for Intelligas, is skeptical. She consulted on a 1998 assessment of a nearby helium field in Tanzania by a different company. "We killed it," she says. "We couldn't justify the price of their helium." There was no local market, roads were poor, and prices at the time couldn't justify the capital cost of liquefying helium for export, she says.

Those conditions have improved since the late 1990s, she acknowledges. Prices for crude helium nearly doubled between 2005 and 2015, reaching $3.75 per cubic meter, driven by growing demand from medical imaging facilities. And cheap sales from the U.S. helium reserve, which for many years kept crude helium prices low, are about to dry up. In 2013, Congress altered the law so that the reserve would be auctioned off closer to market prices. The reserve could be exhausted by 2019, says Robert Jolley, the BLM field office manager in Amarillo, Texas.

Still, Garvey says, prices have plateaued in the past year because of new helium production coming online in places like Qatar just as demand has slackened. Welders have shifted to using argon rather than helium, and MRI facilities and scientists have invested in machines that recycle helium. "The problem is, we have plenty of helium right now," she says.

And other suppliers are eyeing the imminent end of the U.S. reserve. Russia's Gazprom, which owns vast stores in the Far East, plans to boost helium production in 2023, Campbell says. For projects like the ones in Tanzania to have long-term viability, Campbell says, new demand pressure must arrive. One long shot: fusion power, which would need helium to cool its superconducting magnets. "If fusion energy ever were to be developed and become a significant power provider, that would use all the helium we could muster." ■

At Lake Balangida in Tanzania's rift zone, volcanoes are near enough for their heat to liberate helium from underground rocks but far enough away not to dilute it with their own gases—perfect conditions for a high-yield helium field, researchers say.

PHOTO: HELIUM ONE/DR PETER BARRY

ROBOTICS

Heartmaker's next step: a ray 'biohybrid'

Light-controlled cardiac muscle cells guide swimming of raybot

By **Elizabeth Pennisi**

Kevin Kit Parker wants to build a human heart. His young daughter loves the New England Aquarium in Boston. On p. 158, father's and daughter's obsessions have combined in an unlikely creation: a nickel-sized artificial stingray whose swimming is guided by light and powered by rat heart muscle cells.

Incorporating advances in engineering, cell culture, genetics, and biomechanics, the "living" robot is "clearly a technical tour de force," says Adam Summers, an integrative biologist at the University of Washington, Seattle. And some think that by melding cells and artificial materials into a pulsating structure, the device brings Parker's dream of engineering a human heart a step closer. "One can imagine that one day we can use this technology to rebuild parts of the human body," says Kedi Xu, a neural engineer at Zhejiang University in Hangzhou, China.

Parker, an applied physicist at Harvard University, made his first foray into robotics 5 years ago after he was captivated by the jellyfish during a visit to the aquarium. The creature's rhythmic pumping reminded him of the beating heart. His team had already gotten heart muscle cells to grow into thin films on silicone, and he wondered whether he could put the cells to work by incorporating them into a jellyfishlike "pump."

The result was a "medusoid"—a simple artificial creature composed of heart muscle cells overlaid on a sheet of silicone molded into a shallow cup rimmed with flaps. A bath of salt-sugar solution sustained the cells, and tiny jolts of electricity made the cells contract, changing the shape of the silicone cup so that the "jellyfish" expelled liquid, propelling it through its bath. "For me this was just a training exercise," Parker recalls. "I'm trying to get better and better at building muscular pumps."

His new effort was also inspired by a visit to the aquarium. When his daughter touched a stingray in the petting tank, it flicked one

Part machine and part living cells, this artificial stingray can be maneuvered through obstacle courses.

side of its body and veered away. "Maybe there is something similar with how the stingray changes direction and heart flow," Parker thought. So he decided to move up the tree of life, from jellyfish to rays, and increase the complexity of his team's "biohybrids."

Again thanks to his daughter, he envisioned a simple way to control the new robot: light. When she was a toddler, Parker would guide her down the sidewalk by shining his laser pointer on the ground and having her stomp on the light. Perhaps his team could do something similar in an artificial ray by making the muscle cells contract in response to light. They turned to optogenetics, in which cells are genetically endowed with light-responsive molecules that trigger signaling cascades. Parker's team had no experience with the method, but with a bravado befitting a lieutenant colonel who fought in Afghanistan before and after joining Harvard's faculty, he decided to go ahead—cobbling together funding from the Army, the National Institutes of Health, and others. Parker asked a new postdoc, Sung-Jin Park, to oversee the work, confidently predicting the project would produce a paper featured on the cover of *Science*. "I thought it was crazy … impossible," Park recalls.

It took 4 years to fulfill Parker's prediction. Park and others began by taking apart stingrays to learn how the muscles were arranged; later, colleagues in another lab analyzed how the muscles drive the fins in the synchronized undulations that propel the ray. To mimic the animal's basic anatomy, Park experimented with many soft-robot configurations, eventually settling on a multipronged gold skeleton sandwiched between two silicone layers.

Animating each ray are about 200,000 heart cells harvested from 2-day-old rat embryos and placed on top of the silicone. The silicone bears a template consisting of an extracellular protein, fibronectin, which guides the growth of the cells into a radiating pattern similar to the muscles in the real ray. Getting this architecture right was critical to making cardiac cells do the work of skeletal muscles, says Andrew McCulloch, a bioengineer at the University of California, San Diego, who was not involved with the work.

But Parker's group didn't follow the ray's muscle structure exactly. "They took a shortcut," says Frank Fish, a biomechanist at West Chester University in Pennsylvania. Real rays have two sets of muscles within each pectoral fin, pulling in opposite directions to move a fin down, then up. The ray robot has just one set of muscles, which bend the fins downward; the spring action of the gold skeleton pulls the fins back up.

Kevin Kit Parker and his daughter compare a ray robot on a slide with a skate.

Infected with a virus that delivers the gene encoding the optogenetic molecular switch, the modified cardiac cells twitch when blue light shines on them. But translating that effect into coherent motion took months of tweaking; simply getting a robot ray to move forward when light stimulated the front of its fin took Park 200 tries. Ultimately, he built 100 more robots and showed they could navigate underwater obstacle courses. To negotiate turns, Park guides a ray with two light sources, one pointed at each fin. Changing the frequency of the light slows or speeds up the contraction rate; by making one side beat faster than the other, he steers the robot left or right.

The rays move only about 9 meters per hour and turn slowly—quite pathetic by real stingray standards. Even so, "putting it all together is remarkable," says Alexander Smits, a mechanical engineer at Princeton University. Fish, who helped design larger "manta bots" with silicone fins flapped by electronic-controlled rods and cables, calls the rays "a major leap forward in terms of robotics." He adds, "we're getting to the point where there really is a fusion between biology and engineering."

There's a long way to go, however. Live-muscle robots work only in nutrient-filled solutions warmed to a rat's body temperature; keeping them going in a more natural environment will be a challenge, Fish says.

And it's unclear whether the approach will lead to practical robots or to Park and Parker's true interest: a bioartificial heart. Simply putting down a second layer of muscle cells is daunting, nevermind recapturing the full complexity of the heart or a complete animal. The ray robot "is not really particularly related to anything in the heart," especially because the heart muscle cells are "being used in a fairly unnatural way," says Denis Buxton, a program officer at the National Heart, Lung, and Blood Institute in Bethesda, Maryland.

But to Parker and others that "unnatural way" is very informative. "The heart is a hollow muscle," explains Simon Hoerstrup, a cardiovascular surgeon at the University of Zurich Institute for Regenerative Medicine in Switzerland. "Many of the features you see in this ray, you find in the heart."

Parker regards his team's miniature ray robot as a piece of art as well as technology: "Everyone is going to see something different" in it, he says. "I'm looking at it and I'm trying to understand the heart—and impress my 7-year-old daughter." ■

PHOTOS: (TOP TO BOTTOM) KARAGHEN HUDSON AND MICHAEL ROSNACH; KARAGHEN HUDSON

FUNDING

In Canada, peer-review changes stir outrage

Reforms by nation's lead biomedical funder result in shoddy reviews, critics say

By **Wayne Kondro**

One day, historians might call it the Peer Uprising.

Nearly 1000 Canadian researchers are demanding that the government immediately reverse "radical" changes that the nation's main biomedical research funder has made to its system for awarding research grants. In particular, the researchers want the Canadian Institutes of Health Research (CIHR) to scrap its new online system for evaluating grant proposals.

The new system "shows deep flaws and erroneous assumptions" and has led to shoddy review practices, the critics charge in a 27 June open letter to Jane Philpott, Canada's minister of health. "There is little hope that the best ideas and projects will be funded. We posit this represents a fundamental failure of CIHR's primary mandate."

The letter represents the latest salvo against a controversial reform effort launched roughly 4 years ago by Alain Beaudet, president of CIHR, which spends about $790 million annually on health research. In a move designed to create more stable funding for the nation's elite researchers and reduce time spent chasing grants, the agency essentially obliterated its existing grant programs, replacing them with just two flavors: "Foundation scheme" grants that provide $38,800 to $1.16 million annually to "established researchers" for open-ended research and "Project scheme" grants of $38,800 to $581,000 annually for up to 5 years for more focused projects.

CIHR also remade its grantsmaking process. Under the old system, applications were distributed among 53 discipline-based expert panels, which met face-to-face to rank applications. Now, researchers submit applications to a central pool; each application is assigned to four reviewers, who are supposed to participate in a virtual, "asynchronous" electronic discussion through an internet chat room. Proponents argued the changes would boost efficiency, reduce reviewer fatigue, and promote multidisciplinary projects. Critics, however, worried that the funding changes would favor established scientists and were skeptical of online reviews. After the first Foundation grant competition in 2015, success rates and award levels for both female and younger researchers were lower than for male, more elderly counterparts, says geneticist Janet Rossant of The Hospital for Sick Children and the University of Toronto in Canada, and a former member of CIHR's governing council. "The criteria, I think, became very much skewed not toward outstanding science, but outstanding leadership," says Rossant, a winner in the competition.

Shifts in CIHR's spending resulting from the program restructuring added to the disadvantage for early career researchers, says Michael Hendricks, co-founder of the Association of Canadian Early Career Health Researchers and assistant professor of biology at McGill University in Montreal, Canada. The shifts "took almost half of the open, operating grants funds off the table for new investigators," he says. "We're looking at probably over a 30% loss, in dollars, in funding support."

As a result of such concerns, earlier this year the U15 group of research-intensive Canadian universities asked CIHR to put a "temporary moratorium on further changes to research funding programs" and to convene a national summit to discuss the changes. But Beaudet, who in 2013 was appointed to a second 5-year term as CIHR president by former Conservative Prime Minister Stephen Harper in 2013, rebuffed the request.

Worries about the new peer-review system crystallized earlier this year, after CIHR conducted its first Project grant competition. Tight funding had caused CIHR to cancel two previous competitions, so "the majority of this country's health researchers applied to the latest competition," notes the 27 June letter, which was drafted by Jim Woodgett, director of research at the Lunenfeld-Tanenbaum Research Institute at Toronto's Mount Sinai Hospital. "Despite warnings, CIHR scrambled to find sufficient reviewers, at least some of whom were inexperienced or unqualified."

The shortage of reviewers forced the agency to rely on a matching algorithm that assigned applications to reviewers based on keywords. Some were asked to assess applications in disciplines that they knew nothing about, Woodgett says. Reviewers, who often had just days to respond, sometimes didn't bother to provide written reviews or participate in the online discussions, and applicants were given no chance to submit revisions in response to feedback. The new system may be more cost-efficient, Woodgett says, but it represents "the abandonment of scientists evaluating other scientists in front of other scientists."

Critics say CIHR needs to beat a hasty retreat from its reforms. They want Philpott to immediately meet with a representative group of scientists to iron out concerns, and for CIHR to revert to traditional peer review until the new methodology has been assessed by international experts. The government should also convene a national summit on health research.

Beaudet declined *Science*'s request for comment. But he has posited that the criticism of CIHR is linked to funding struggles, and will dissipate if Prime Minister Justin Trudeau's new Liberal government boosts spending for the health agency. It's unlikely, however, that money alone would quell the uprising over the perceived threat to the time-honored tradition of face-to-face peer review. ■

Jim Woodgett of Toronto, Canada's Mount Sinai Hospital drafted a protest letter signed by nearly 1000 researchers.

PHOTO: COURTESY OF SALLY SZUSTER/MOUNT SINAI HOSPITAL

Wayne Kondro is a writer based in Ottawa.

Kala gave birth to the first brown howler monkey born in Tijuca Forest in more than a century.

PHOTO: LUCIANO CANDISANI

REWILDING RIO

A team of ecologists is recreating a living rainforest in the heart of the Olympic city

By **Herton Escobar**, *in Rio de Janeiro, Brazil*

Seen from the Corcovado, the 710-meter-high gneiss mountain topped by the iconic Christ the Redeemer statue, Tijuca National Park rolls out below like a lush green carpet, edged with Rio de Janeiro's urban sprawl. As the city scrambles to finish preparations for the Summer Olympics next month, scientists here are playing a longer game. They are embarked on a decades-long effort to transform Tijuca—one of the biggest urban forests in the world—from a verdant forest park inhabited mainly by hikers and stray dogs into something more akin to a genuine rainforest. "People have this naïve impression that the forest is full of animals," says Fernando Fernandez, an ecologist at the Federal University of Rio de Janeiro (UFRJ). "Our goal is to fill this forest with life again."

Decades ago, an expanding Rio de Janeiro surrounded Tijuca, severing its 4000 hectares from other forest tracts. Jaguars were long gone, but now hunters and loggers extirpated the monkeys, rodents, and other mammals living in the forest island, setting

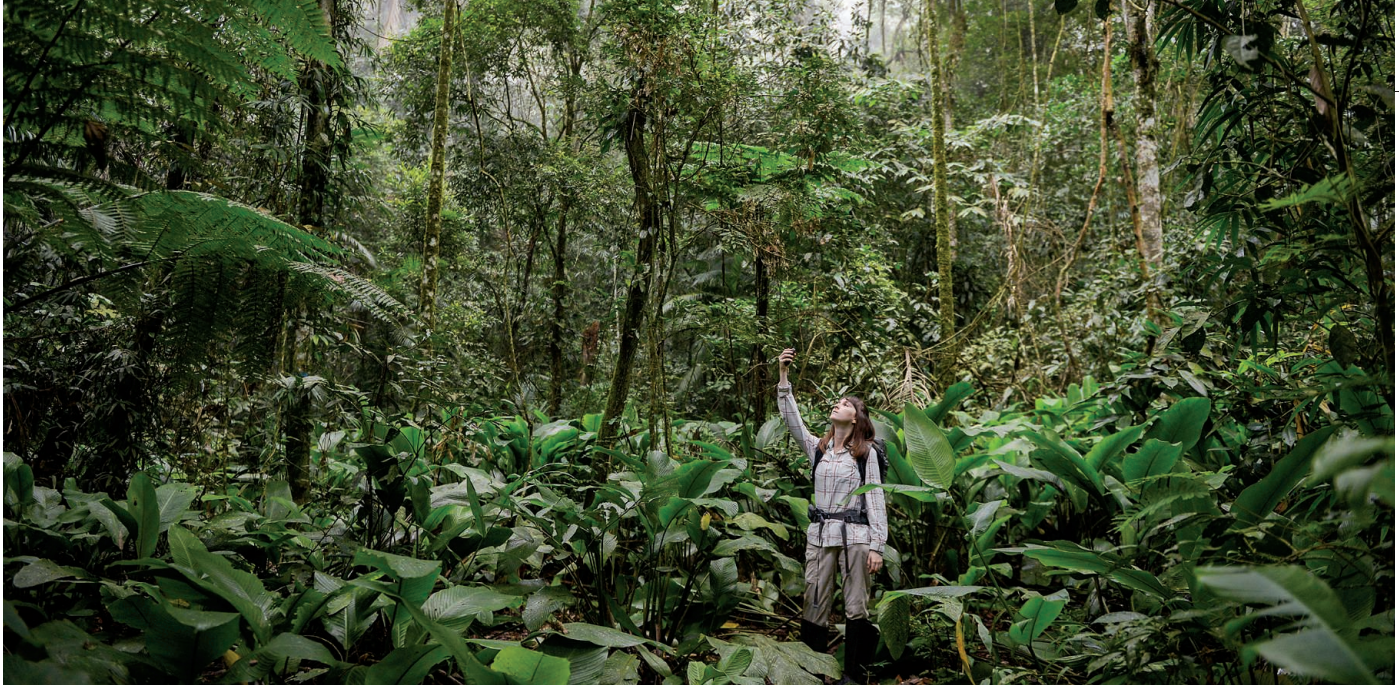

The brown howlers' radio collars are broken or lost, so Luísa Genes spends many hours tracking down the monkeys on weekly expeditions to monitor their behavior.

in motion profound ecological changes. Trees that rely on animals to disperse their large, hard seeds gave way to less dense, faster-growing trees whose seeds are dispersed by wind or water. The forest's carbon storage capacity shrank. "Every aspect of an empty forest is a disaster," Fernandez says.

His team has embarked on a pioneering effort to restore Tijuca's original fauna. Six years ago, they began releasing red-rumped agoutis (*Dasyprocta leporina*), a rodent that is an important seed disperser, fitted with radio collars. The refaunation effort entered a new phase last September, when the team released four brown howler monkeys (*Alouatta guariba*) in Tijuca, and more will follow this year.

The refaunation stands out in restoration ecology for its attempt to heal an entire ecosystem, conservationists say. In contrast to many other reintroduction efforts, Fernandez's team isn't trying to save a particular endangered species. "The coolest thing is that they are working with very common species—[ones] that are not threatened, but are very important for the environment," says Mauro Galetti, a conservation biologist at São Paulo State University, Rio Claro, in Brazil. "Regrowing a forest is relatively easy. Rebuilding an ecosystem is a lot harder."

There is no formula for restoring a tropical forest, Fernandez says, so he and his colleagues are proceeding cautiously, introducing species one by one and monitoring how each one fares and how it affects the forest. "Every time you lose species, you lose ecological interactions. And when you change the ecology, you change the course of evolution," Fernandez says. "So, if we bring those species back, can we put evolution back on track?"

ONE OF THE LAST to record Tijuca as a living forest, resounding with the guttural calls of brown howler monkeys, was Charles Darwin himself. During his epochal voyage on the *Beagle*, Darwin stopped here and explored the nearby forest. As he noted in his diary, on 4 June 1832 a young hunter led him to a spot in the forest where he had shot "two large bearded monkeys" the day before. One of the dead howlers still clung to a tree with its prehensile tail.

Tijuca is a fragment of Brazil's Atlantic Forest, which once covered most of the country's Atlantic seaboard but now is a fragmented 12.5% of its former self. Near Rio, the destruction started early. Around the time Darwin was exploring Tijuca, vast swaths of forest around what was then Brazil's imperial capital were being razed and replaced with coffee plantations. Within a few years, Tijuca itself was mostly leveled. As a result of the deforestation, the city started running low on water and temperatures soared, prompting authorities to launch a major reforestation effort in the 1860s.

Laborers replanted hundreds of thousands of native and exotic trees. But the fauna did not bounce back. "Fruits are the bribe that plants offer to animals to disperse their seeds. So if you see fruits rotting on the forest floor, it's an empty forest," Fernandez says. His team is seeking to complete Tijuca's drawn-out recovery by adding animals. "Essentially, what we are doing is a continuation of that early reforestation process," says biologist Ernesto Castro, park manager at Tijuca. "The forest is so isolated that the only way for these animals to return is to bring them back ourselves."

In 2008, one of Castro's predecessors, Ivandy Castro-Astor, suggested the refaunation project to Fernandez. Fernandez saw a chance not only to rebuild a beloved park, but also to conduct a large-scale ecological experiment. He brought back agoutis first, he says, because they are "the best seed dispersers in the world." More than 20 tree species at the park depend heavily on these rodents to gather their seeds and bury them in caches all over the forest. Those trees were being "held hostage," reproductively, by the absence

Repopulating an 'empty' forest

In the 19th century, vast swaths of Tijuca were razed. Bringing back native mammals is an extension of reforestation efforts.

CREDITS: (PHOTO) LUCIANO CANDISANI; (MAP) GOOGLE EARTH. ADAPTED BY G. GRULLÓN/*SCIENCE*

of the agoutis, Galetti says. "A forest without animals is like a stage without actors."

By now at least 35 red-rumped agoutis roam Tijuca. And this year they have an accomplice: the first howler monkeys, which contribute to seed dispersal and nutrient recycling as they move around the canopy, eating and defecating.

IN LATE MAY, a visitor in Tijuca heard a baby wailing in the forest, and sounded the alarm. Authorities dispatched a ranger to find the lost infant. To everyone's relief, the ranger quickly tracked down the source of the plaintive ululations: a brown howler, maybe 6 months old, bawling as its mother, Kala, munched leaves on a nearby tree. The cries had sounded like a parent's nightmare, but they represented a triumph: the first howler baby born at Tijuca in more than a century.

Of the four adult howlers released last fall, one pair came from a private breeder, and the other from a federal facility for seized animals. They had lived for 8 months in adjacent cages at the Rio de Janeiro Primatology Center getting accustomed to each other and to a leaf-based diet, similar to what they would have in the wild. After that, they spent 20 days in a pen in Tijuca to adjust to the environment.

Fernandez's team was anxious to see what would happen once they opened the pen, as the monkeys "had never climbed a tree before," says Marcelo Rheingantz, a biologist at UFRJ. "But as soon as we opened the door, they all climbed up immediately." Three mostly stay up in the trees. One male, the youngest of the four, settled in public areas of the park and began taking food from visitors and sunbathing on the park road. The scientists brought him back into captivity, for his own safety—and to protect humans who might provoke him. "He wasn't fulfilling any ecological role there," Rheingantz says. The other male also began interacting with people, and was moved to a more remote location. One of the two fathered Kala's baby, named Juca.

Keeping tabs on the monkeys isn't easy. All four were released with GPS tracking collars, but three collars soon malfunctioned and Kala lost hers after 6 months. So the only way to locate and monitor the monkeys now is by naked eye. That takes a lot of patience: The monkeys don't howl often, and spend most of their time quietly chewing leaves high in the canopy.

Luísa Genes and Tomaz Cezimbra, two of Fernandez's graduate students, are responsible for tracking the primates. They note the howlers' behaviors and mark with pink tape the trees they sleep in or feed on for later identification. Genes also scans the forest floor for monkey feces and insects. She is studying how the howlers influence the ecology of the forest's dung beetles, some species of which feed exclusively on large primate excrement and are important for secondary seed dispersal.

Kala is the easiest to monitor, as she tends to stay near the pen area. Still, on a foggy day in early June, it took 7 hours to find her. Cezimbra spotted movement behind a clump of branches 20 meters up in the canopy, and there Kala was—in a place he and Genes had passed several times before—collecting leaves with her hands while gripping a branch with her tail.

Genes and Cezimbra were happy to find Kala, but they worry about Juca, who was not with her. It was the first time they had failed to spot the baby. "It's a bad sign," Fernandez says. "This is not a success story yet," he says. "It could fail at any moment." As *Science* went to press, Juca was still missing. "There's a chance it could be with the other female," Genes says. "But it could be dead."

Agoutis were brought back first because they are supreme seed dispersers. Luísa Genes (bottom) holds a hard rind gnawed by one of the rodents.

PHOTOS: (TOP TO BOTTOM) LABORATÓRIO DE ECOLOGIA E CONSERVAÇÃO DE POPULAÇÕES/UFRJ; LUCIANO CANDISANI

To boost the odds of establishing a viable howler population, Fernandez's team plans to release 10 more by year's end. Provided that goes well, another candidate for reintroduction is the endangered golden lion tamarin (*Leontopithecus rosalia*), a flagship species of Brazilian biodiversity conservation, which is also a seed disperser. For the tamarins to move in, however, another small primate, the common marmoset (*Callithrix jacchus*), must be evicted first. It is one of several exotic species that have prospered in the park after the original inhabitants disappeared. Other candidates for reintroduction are the maned three-toed sloth (*Bradypus torquatus*)—a voracious leaf eater and nutrient recycler—and the kinkajou (*Potos flavus*), a seed disperser and pollinator.

Larger mammals of Brazil's Atlantic Forest, such as the tapir or the jaguar, will never return. Tijuca is too confined for them; prey is too scarce and conflicts would arise with surrounding communities. "Maybe some smaller cats," such as the oncilla (*Leopardus tigrinus*), could eventually be reintroduced after prey return to sustainable levels, Fernandez says. The oncilla would be good competition for the feral dogs, now the top predators in Tijuca and a threat to the agoutis and other smaller critters.

But the cats wouldn't arrive for years: a late thread in the slow, patient process of repairing Tijuca's frayed fabric. "We will start with the easiest animals," Fernandez says, "and try to reconstruct the ecosystem little by little." ■

Herton Escobar is a writer in São Paulo, Brazil.

Marcia McNutt on the grounds of the National Academy of Sciences building, with Albert Einstein looking on.

HURDLING OBSTACLES

Meet Marcia McNutt, scientist, administrator, editor, and now National Academy of Sciences president

By **Ellen Ruppel Shell**

PHOTO: STEPHEN VOSS

When geophysicist Marcia McNutt took over as director of the U.S. Geological Survey (USGS) in 2009 as part of the new Obama administration's "dream team" of scientist-administrators, her first priority was to reorganize the agency to respond to real-world problems. But USGS scientists, many of whom had been with the agency for decades, were known for their resistance to change, so McNutt devised a remarkable strategy. She could not fire department heads, but she could assign them to a regional office outside their beloved Menlo Park, California, and the post she offered was her home town, Minneapolis, Minnesota. One by one, McNutt recalls, department heads retired or quit, leaving her free to set a new direction.

"We were living in geologic time, so Marcia took some getting used to," says Bill Werkheiser, now deputy director at USGS in Reston, Virginia, who was McNutt's associate director at the time. "She made decisions very quickly … we knew we had to change, and she made it happen. But she was always clear, you knew where you stood, and she was fiercely loyal to us."

That mix of decisiveness, humanity, and negotiating skill served McNutt well both as a researcher and an administrator: In addition to USGS, she was the first female president and CEO of the Monterey Bay Aquarium Research Institute (MBARI) in Moss Landing, California, and, from 2013 until last week, the first female editor-in-chief of *Science*. This month, she became the first female president of the National Academy of Sciences (NAS), the government's premier science advisory organization.

None of this has been easy. Indeed, starting with college, hurdling obstacles has been a constant in her life. In the fall of 1970, William H. Wright, a professor of physics at Colorado College in Colorado Springs, ushered freshman Marcia McNutt into his office with what she recalls as this observation: "You are here because you must have said something silly on your application about being a physics major. I've seen girls come and go in this department, but I've yet to see one graduate." For perhaps the first time in her young life, McNutt was struck speechless. Class valedictorian at the all-girls Northrop Collegiate School in Minneapolis and with perfect SAT scores, she had chosen Colorado over Stanford University in Palo Alto, California, partly for its promise of closer contact with faculty … but not this sort of contact. "No one had ever told me I couldn't do something," she told me. "The one thought in my mind was, 'I'll show him!'"

McNutt went on to ace all four of Wright's required classes and graduate summa cum laude with a degree in—of course—physics. Years later, as a chaired professor of geophysics at the Massachusetts Institute of Technology (MIT) in Cambridge, McNutt declined an invitation to pen a testimonial about Wright in honor of his retirement. "He wouldn't want to read what I had to say," she says firmly.

McNutt is an expert barrel racer, an event where speed and control are key.

Wright wasn't the last person to underestimate Marcia McNutt, or the only one to regret it. "I bow my head to Marcia," says MIT physical oceanographer Paola Malanotte-Rizzoli. "She has a spine of iron."

MCNUTT GREW UP IN MINNEAPOLIS and spent her childhood summers in a lakeside cabin, where reading was the default rainy day activity. She spent many a morning at a nearby farm, mucking out the stables in exchange for a chance to ride. (She later became an expert barrel racer, a rodeo event that entails galloping around a tight cloverleaf of barrels; speed rather than finesse is paramount.) But perhaps her most vivid memory of those summers involves an old Sunfish that an uncle dropped off for the family's use. Too impatient to wait for an adult to teach her the fine points of navigation, she jumped into the boat and set sail. "I knew nothing, just pushed off from shore and in no time was out in the middle of the lake," she recalls. "I could see our cabin, but I had no idea how to get back. Then I remembered reading a Nancy Drew story that mentioned something about 'tacking into the wind.' Eureka! I tried one thing after another, and somehow learned the difference between jibing and coming about. Eventually, I made it back to shore. After that, I was an experimentalist."

That experimental bent led her to physics and mathematics as an undergraduate and then to the geosciences, particularly the then-nascent theory of plate tectonics. It was a field wide open to a young scientist eager to make her mark: Major expeditions were often fully staffed and even led by graduate students, as many senior scientists were hesitant to embrace the new paradigm.

While in graduate school at the Scripps Institution of Oceanography in San Diego, California, McNutt relished the opportunity to follow her research wherever it took her, especially when it led upstream from received wisdom. "I wanted to go places, see things personally, collect data, and revise on the fly," she says. But rather than focus on what other researchers were studying—the boundaries between plates, where most of the action seemed to be taking place (earthquakes, volcanoes, mountain building, ocean trench creation)—she turned her attention to the plate interiors, and to a mystery that had thwarted other scientists: why so much volcanic activity appeared to be happening so far from the plate boundaries.

Sean Solomon, currently director of the Lamont-Doherty Earth Observatory at Columbia University, was instrumental in recruiting McNutt to MIT in 1982, when he was on the faculty there. He recalls being impressed by the young scientist's tenacity and drive, and by her ability to speak convincingly to both scientific and lay audiences. "All of us knew who the great graduate students were, and she was clearly among them. She was audacious, quite willing to go where others wouldn't."

Scientists had long noted that the ocean floor deepens with increasing distance from the ocean ridges, where new crust is created. But an area beneath French Polynesia posed a puzzle: Why was that swath of ocean thousands of miles from a plate boundary so shallow and its floor riddled with volcanoes? McNutt plunged in. Using sonar signals to map the seafloor topography, she discovered what she described as a "superswell," a broad region of unusually shallow ocean floor buoyed by hot rock welling up from the mantle. In a groundbreaking paper in *Science*, McNutt concluded that the rock's excess heat and extremely low viscosity had

PHOTO: COURTESY MARCIA MCNUTT

allowed the volcanism to readily pierce the lithospheric plate, liberating fully 30% of the heat flux from all hot spots on Earth in that patch of Pacific Ocean floor.

This and a number of other discoveries brought McNutt many accolades, among them the prestigious Macelwane Medal from the American Geophysical Union. Karen Fischer, now a geophysicist at Brown University, was one of McNutt's graduate students at the time. She recalls the awards ceremony as a "quintessentially Marcia" experience. "She wore an Oscar[s]-style evening gown and looked incredibly glamorous," Fischer says. "We were incredibly proud of her … she had succeeded in science on her own terms."

McNutt made a practice of setting her own terms. She rode a red Honda 500 motorcycle to the office, always wearing fashionable footwear. She made more than a dozen ocean expeditions, and spent months at a time in Tibet and Tahiti. And she fought fiercely for her graduate students, once telling off another senior scientist for showing disrespect to a female member of her team.

For most of that time she was bringing up three daughters—Meredith, Ashley, and Dana—as a single parent. Their biological father died suddenly when the youngest, identical twins, were only 2 years old, and the oldest not yet in school. (In 1996, McNutt married Ian Young, an MBARI ship captain.) "That Marcia managed to hold everything together under those crushingly difficult circumstances seemed to us amazing," Fischer says. "At a time when not all that many women were succeeding in science, she made it normal for women to succeed."

Geophysicist Carolyn Ruppel, who was one of McNutt's MIT advisees at the time, has a more nuanced take: "She's an amazing person, an amazing scientist, and has made significant contributions in areas that were difficult to navigate. But she was not a role model. None of us thought we could do what Marcia did—she played at a level well beyond [the level to] which the rest of us were headed."

MCNUTT'S AMBITIONS went beyond academia. "As a scientist, working in a lab, publishing papers that only a few specialists in the field really cared about, it felt to me like being trapped in a box canyon," she says. She determined that what she calls her "highest and best use" was not doing science, but enabling other scientists to do theirs. So she did what almost no one else in her situation would do: In 1997 she left a tenured position at MIT, packed up her daughters, their nanny, Ann, and Ann's daughter, and moved to Salinas, California, ("salad bowl of the world") to run MBARI. "Her leaving was a terrible loss for MIT," Malanotte-Rizzoli says. "She wanted a new experience, and she deserved that. But geophysics suffered."

MBARI, funded by the David and Lucile Packard Foundation, was a relatively new venture with a lofty mission: to apply cutting-edge technology to inform and shape the future of the world's oceans. McNutt took the reins shortly after Founding Director David Packard died, and, according to aquarium Executive Director Julie Packard, she quickly bridged the leadership gap. "One of my father's most deeply held principles was to invest in people and give them the space to pursue their ideas," Packard says. "Marcia built and expanded on that vision. She took a big risk leaving MIT where she was at the top of her game to come to what was basically a startup operation. And we were very lucky she did."

McNutt soon faced an unexpected challenge: The market plunge after 11 September 2001 sharply eroded the foundation's assets. With fewer resources at her disposal, she directed staff to dig even deeper into matters of public (and funders') concern, such as protecting the oceans from acidification and algae blooms and understanding the role the oceans play in climate change. Under her leadership, MBARI built a chemical sensor laboratory to detect ocean pollutants in real time, and grew an autonomous underwater vehicle program to make sample collection safer and more efficient. And, somehow, despite the economic downturn, it doubled its staff.

While at MBARI, McNutt also served as president of the American Geophysical Union (2000 to 2002). And yet, once again, she wanted greater influence. So when Sean Solomon met with her in 2008, this time as chair of an NAS committee convened to recommend a new USGS head, McNutt listened. Joining the Obama administration's "dream team" of scientific administrators, she decided, would be her next "highest and best use."

Presenting at the fall 1992 American Geophysical Union meeting, when McNutt was at MIT (left); heading a task force following the *Deepwater Horizon* disaster in 2010, as U.S. Geological Survey director (center); on the Monterey Bay Aquarium Research Institute's flagship vessel in 1999, when she was the institute's CEO (right).

PHOTOS (LEFT TO RIGHT): COURTESY MARCIA MCNUTT; FEARNSTOCK/ALAMY; COURTESY MARCIA MCNUTT

McNutt wasn't alone in recognizing the need to overhaul the structure of USGS. "USGS was full of ivory tower types each in his or her own silo—the seismic folks, geology folks, public health folks," says her then-boss David Hayes, who was deputy secretary of the interior under both President Bill Clinton and President Barack Obama and is now on the faculty of Stanford Law School. "When Marcia arrived the agency was not, to my view, living up to its potential to provide the science needed to help undergird smart decision-making. She reorganized it to align with today's science challenges—climate change, land use—and she did it in a remarkable way, with a sense of openness and respect."

Her strategy of offering department heads reassignment to the Minneapolis regional office could have taken a toll on morale, but USGS Deputy Director Werkheiser recalls that "Marcia was a great boss, and

I can't think of anyone who had serious issues with her."

She needed that support to handle a series of jolting disasters in her first 6 months at USGS: major earthquakes in Haiti and Chile, a water crisis in California, an invasion of Asian carp in the Great Lakes, and a volcano in Iceland that disrupted trans-Atlantic air travel for nearly 10 days. And then, on 20 April 2010, came what McNutt calls her "Omaha Beach"—the explosion of BP's *Deepwater Horizon* oil rig, which killed 11 workers, injured 17, and over a period of 87 days released 4.9 million barrels of crude oil into the Gulf of Mexico. McNutt says she and her colleagues were caught totally unawares, thanks in part to deceptive assurances from the oil industry that "you don't have to worry about" oil escaping from deep-sea wells.

Anyone who has spent more than 5 minutes with Marcia McNutt knows this: She will patiently suffer fools but has zero tolerance for deceit. She rushed to Houston, Texas, with an overnight bag, expecting a short trip. She ended up spending 4 months in a windowless 2-by-3-meter office at BP headquarters, huddling late nights and early mornings with scientists and engineers, calling every expert she knew who might offer insight.

Soon after her arrival she was tapped to lead the Flow Rate Technical Group charged with gauging the volume of oil erupting from BP's well, a highly contentious issue. BP put the number first at 1000 and then at 5000 barrels a day. The group's estimate, based on bits of high-definition video footage Congress had forced BP to share, was far higher: as much as 60,000 barrels a day. "Others—in government, academia, the press—were shooting from the hip," McNutt says. "But we had the data." Pushing through the bluster of what she called BP's "cowboy, get it done and go home" attitude, McNutt announced the technical team's findings to the world. "Marcia was pragmatic, she understood what needed to be done to bring the stakeholders together," Hayes says. "And she showed a surprising willingness to let it rip—she wrote some emails she shouldn't have, believe me."

MCNUTT LEFT USGS IN 2013, many assumed to take over as head of the Scripps Institution of Oceanography. But she chose to remain in Washington, D.C., to take the helm at *Science*, where, among other things, she presided over the founding of *Science Advances*, an open-access, peer-reviewed journal that reflects her concern with maintaining scientific integrity in an increasingly cutthroat publishing environment.

"At *Science*, the paradigm is changing," she says. "We're talking about asking authors, 'Is this hypothesis testing or exploratory?' An exploratory study explores new questions rather than tests an existing hypothesis. But scientists have felt that they had to disguise an exploratory study as hypothesis testing, and that is totally dishonest. I have no problem with true exploratory science. That is what I did most of my career. But it is important that scientists call it as such and not try to pass it off as something else. If the result is important and exciting, we want to publish exploratory studies, but at the same time make clear that they are generally statistically underpowered, and need to be reproduced."

McNutt and family. Marcel Hoffman, her first husband, died suddenly in 1988, when their three daughters were not yet school-age. She married Ian Young (right), a research ship captain, in 1996.

PHOTO: ANN BARRIE

McNutt put her stamp on the editorial page of *Science* with some 60 editorials in 3 years as editor-in-chief. But she admits that she took a wrong turn on the Keystone Pipeline, a proposed route for oil produced from Canada's oil sands—a project she regrets having publicly endorsed. "I would do things differently now," she says. "I should have said that I would support Keystone 'if this happens,' 'if' being changing the process for extraction to make it cleaner, taxing the pipeline so that there is no decrease in the cost of oil, and imposing environmental scrutiny."

McNutt also regrets the sexism scandal that rocked *Science* beginning in July 2014, when the journal published a cover photo featuring a pair of transgender women in platform shoes and skin-tight dresses with their heads cropped out of the shot. Though McNutt publicly vowed to "strive to do much better," that faux pas was followed by another: a *Science* columnist who advised a female scientist to "put up with" a male superior sneaking glimpses down her shirt. "Had I known, I would not have run that column," she says, adding that the editor involved no longer works for *Science*. "Women have to decide for themselves what path to take in a situation like that, find a resolution that allows her to go on with her career and allows her to feel okay."

Now, McNutt will have an even higher profile as head of NAS. "My hope is that she will be an outspoken public face for science, with a focus and emphasis on evidence-based decision-making," says Diane Griffin, professor of molecular microbiology and immunology at Johns Hopkins Bloomberg School of Public Health in Baltimore, Maryland, and vice president of NAS.

McNutt is more than ready to embrace the challenge. She sees her job at NAS as improving reproducibility and ethics in science, promoting women in science, and guiding the public conversation toward an understanding of science not as a bloodless series of facts, but as a structured approach to elucidating the laws of nature. "The academy has the job of providing scientific advice to government, and that's a role that has never been more vital," she says. "It's not the role of the academy to say what the policies should be, but it is the role of science to project the consequences. Advice from the academy could be transformational to help the nation—and the world—do the right thing."

Once again, and perhaps not for the last time, it seems that McNutt has found her "highest and best" use. ■

Ellen Ruppel Shell, professor and co-director in the graduate program in science journalism at Boston University, is author of Cheap: The High Cost of Discount Culture. *Colin Norman, who was* Science*'s news editor until 2013, edited this article.*

Energy-efficient chemical separations p. 121 ▸

Powering the expanding Internet p. 124

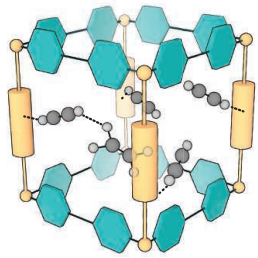

PERSPECTIVES

PALEONTOLOGY

Learning to move on land

Interdisciplinary research suggests that early four-limbed vertebrates relied on their tails

By **John A. Nyakatura**

How did early four-limbed vertebrates, or stem tetrapods, move on land? On page 154 of this issue, McInroe and co-workers bring together expertise from several fields—including biomechanical analysis of a modern analog, mathematical modeling, controlled drag measurements in granular media, and bio-inspired robotics—to address this question (*1*). They find that properly coordinated tail movements make locomotion efficient when limb motion is suboptimal and substrates are challenging. Thus, the tail may have helped stem tetrapods to move on land. The work exemplifies a move in paleontology toward increasingly interdisciplinary research (*2*).

In the Late Devonian and Early Carboniferous (about 360 million years ago), an important yet only partly understood evolutionary transition took place. Before this time, stem tetrapods may have almost never left the water. During the transition, the first truly land-living forms appeared, some of which eventually gave rise to all modern tetrapods.

Salamanders with alternating limb movements and hindlimb-generated propulsion are regarded as suitable modern analogs for these earliest fully terrestrial tetrapods. However, Pierce *et al.* recently assessed limb joint mobility in the stem tetrapod *Ichthyostega*—a well-known species from the Late Devonian with fully evolved limbs—and concluded that its hindlimbs in particular were likely unsuited to effectively generate propulsion on land (*3*). Hence, the salamander model appears not to be adequate for the more aquatic Devonian stem tetrapods in the rare cases when they ventured out of the water.

Pierce *et al.* proposed a crutching locomotion powered by simultaneous forelimb movements for Late Devonian stem tetrapods (*3*). A similar mode of locomotion is used by modern mudskippers, bony fishes that spend a considerable amount of time on land (see the photos). Further adding to our understanding of mudskipper locomotion, McInroe *et al.* now show how these fishes use their tail to improve locomotor robustness.

However, locomotion in *Ichthyostega* may have been different from that of other Devonian stem tetrapods. Furthermore, the reconstruction of locomotor characteristics from studying limb joint range of motion is generally challenging (*4*), and the earli-

Bild Wissen Gestaltung: Ein Interdisziplinäres Labor, Exzellenzcluster der Humboldt-Universität zu Berlin, 10099 Berlin, Germany, and Institut für Biologie, Humboldt-Universität zu Berlin, 10115 Berlin, Germany. Email: john.nyakatura@hu-berlin.de

est potential tetrapod trackways suggest a mode of locomotion more similar to that of salamanders (*5*). If the locomotion seen in mudskippers is a more adequate model, it needs to be shown how alternating, hindlimb-driven (salamander-like) locomotion evolved later on (*6*, *7*). More intermediate fossils are needed (*8*), but alternative modern analogs should also be considered (*9*). Moreover, the mostly aquatic Late Devonian stem tetrapods with highly limited terrestrial capabilities probably encountered challenging inclined sandy or muddy banks when moving onto land. This is the issue that McInroe *et al.* address in their interdisciplinary study. Drawing from diverse lines of argumentation and using the crutching model as their starting point, the authors propose that stem tetrapod tails may have improved the robustness of locomotion on challenging substrates, in a similar fashion as seen in mudskippers.

Coordinated tail use. Mudskippers use their fins and tail to navigate difficult terrain while out of the water. McInroe *et al.* use biomechanical analysis of mudskipper motion, mathematical modeling, drag measurements in granular media, and bioinspired robots to investigate whether early land vertebrates also relied on their tails to move on land.

Both in robots and mathematical models, parameter combinations can systematically be varied to access the sensitivity of the result to variation in individual parameters (*2*, *10*)—something that is not possible when only living organisms are used as analogs. Bioinspired robots are increasingly used as heuristic tools to investigate animal adaptive behavior (*11*). Similarly, computer animation has great power for generating hypotheses on motion using digital models (*10*). However, both approaches face the same problem: how to decide which of the many possible modes of locomotion is the most realistic (*10*). To validate a model, it needs to be shown that its predictions closely match experimental data of the biomechanics measured in modern analogs. Only if this is achieved should the model be used to infer characteristics of a fossil (*12*).

Using bioinspired robotics as well as animations or even sophisticated musculoskeletal modeling (*13*) to elucidate function in extinct organisms has further advantages. Optimization criteria can be used to find plausible parameter combinations without user interference (*10*, *11*). The results become less dependent on subjective opinion, and future insights can more readily be incorporated into existing models. It is this integrative methodology, exemplified by McInroe *et al.*'s study, that fosters increasingly interdisciplinary analyses of function in fossils.

Whether or not mudskippers' tail use is an adequate modern analog for stem tetrapods remains debatable. It can only be confirmed by identifying morphological correlates that are present both in modern analogs and in fossils. McInroe *et al.* do not resolve this issue, but rather contribute to a more general understanding of the mechanism of coordinated tail use during crutching locomotion on soft substrates. The authors were interested in the overarching principle of tail use, and their models serve as templates. In contrast, attempts to reconstruct the function of a structure of a specific fossil should use its anatomical details as anchors for the model (*3*, *14*).

McInroe *et al.*'s study shows that recruiting expertise from different fields facilitates integrated modeling approaches to problems of form and function in extinct organisms. This enables new hypotheses to be generated and existing ones to be tested in a transparent and reproducible manner. ■

REFERENCES AND NOTES

1. B. McInroe *et al.*, *Science* **353**, 154 (2016).
2. D. Jablonski, *Science* **284**, 2114 (1999).
3. S. Pierce *et al.*, *Nature* **486**, 523 (2012).
4. P. Arnold *et al.*, *J. Anat.* **225**, 31 (2014).
5. G. Niedzwiedzki *et al.*, *Nature* **463**, 43 (2010).
6. S. M. Kawano, R. W. Blob, *Integr. Comp. Biol.* **53**, 283 (2013).
7. H. M. King *et al.*, *Proc. Natl. Acad. Sci. U.S.A.* **108**, 21146 (2011).
8. J. S. Anderson *et al.*, *PLOS ONE* **10**, e0125446 (2015).
9. J. A. Nyakatura *et al.*, *Evol. Biol.* **41**, 175 (2014).
10. J. R. Hutchinson, S. M. Gatesy, *Nature* **440**, 292 (2006).
11. A. J. Ijspeert, *Science* **346**, 196 (2014).
12. P. S. L. Anderson *et al.*, *Biol. Lett.* **8**, 119 (2011).
13. S. L. Delp *et al.*, *IEEE Trans. Biomed. Eng.* **54**, 1940 (2007).
14. R. J. Full, D. E. Koditschek, *J. Exp. Biol.* **202**, 3325 (1999).

ACKNOWLEDGMENTS

I thank E. Amson, J. Wölfer, and B. Kilbourne for their insightful critique of this manuscript. Bild Wissen Gestaltung: Ein Interdisziplinäres Labor is supported by DFG grant EXC 1027.

10.1126/science.aag1092

CHEMISTRY

Molecular sieves for gas separation

Metal-organic framework materials enable efficient separation of similar gases

By **Jerry Y. S. Lin**

Separation and purification are critical industrial processes for separating components of chemical mixtures, and these processes account for about half of industrial energy usage (*1*). Gas mixtures of compounds with very similar physical properties are particularly difficult to separate. On pages 137 and 141 of this issue, Cadiau *et al.* (*2*) and Cui *et al.* (*3*), respectively, show that microporous materials can be designed to have high adsorption capacity and selectivity for particular hydrocarbons, enabling energy-efficient separation.

Traditional gas separation technologies use distillation, requiring repeated evaporation and condensation of the mixture, or absorption with a liquid medium that requires cooling and heating a large amount of nonactive solvent to complete a separation cycle. Both technologies are energy intensive. Newer technologies use solid separation media and are generally more energy efficient. For example, membrane-based separation can require 90% less energy than distillation to separate propylene–propane mixtures (*1*, *4*). The cornerstone of these newer separation processes is a solid adsorbent or membrane, often made of a microporous material with a pore size smaller than 0.5 nm and a large internal pore surface area (>300 m^2/g).

In many microporous solid media used as adsorbents or membranes (*5*), there is a trade-off between adsorption capacity (or permeability) and selectivity for separating challenging gas mixtures, making it difficult for the adsorption or membrane process to achieve high separation efficiency. To improve adsorption capacity while also maintaining selectivity, scientists have modified the internal surface properties of porous media to enhance interaction of the adsorbent surface with a specific component and thus increase the adsorption capacity for that component. For example, the crystalline microporous zeolite LiX provides good adsorption capacity for nitrogen over oxygen due to Li cation–

nitrogen interactions (*6*). Selectivity can also be achieved by varying the pore size of the solid media to provide molecular sieving, as in carbon molecular sieve (CMS) materials (*6*). However, zeolites have a limited number of crystal structures and CMS materials have amorphous pore structures, making it hard to generalize these approaches.

Metal-organic frameworks (MOFs) are microporous crystalline materials constructed from transition-metal ions and bridging organic ligands (*7*). These materials can form a vast variety of ordered structures, pore sizes, porosity, and functional groups. MOFs can be made into effective adsorbents or membranes for gas separation by introducing surface functionalities, such as exposed metal centers (*8*) or amines (*9*), in MOF-74 families to enhance CO_2 adsorption capacity and selectivity over N_2. Alternatively, their molecular sieving characteristics can be exploited, as has been shown for the MOF material ZIF-8 for propylene–propane separation (*10*).

These MOF materials have improved separation characteristics compared to classical materials, but they still suffer from the adsorption capacity versus selectivity trade-off for gas separations. For example, for acetylene–ethylene separation, the MOF-74 family with a high density of open metal sites shows high acetylene adsorption capacity but low separation selectivity (*8*). For the same separation, the ultramicroporous mixed metal–organic framework (M'MOF) family has high selectivity but low acetylene adsorption capacity (*11*). The two studies in this issue overcome this trade-off problem through crystal engineering that controls both surface chemistry and pore size of the MOF materials. The resulting MOF materials have high adsorption capacity and selectivity for separation of acetylene–ethylene mixtures, as reported by Cui *et al.*, and propylene–propane mixtures, as shown by Cadiau *et al.*

The materials are based on a group of MOF materials with a pillared square-grid structure (see the figure) (*12*). The unit cell consists of eight metal nodes, joined by an organic linker containing one or two pyridines or pyrazines, that form the upper and bottom squares. The squares are pillared apart via $(SiF_6)^{2-}$ anions (called SIFSIX). The pore aperture size on the squares can be controlled by varying the length and/or orientation of the organic linker. The surface chemistry is determined by the pillar ions, metals, and organic linker molecules.

Cui *et al.* synthesized four $(SiF_6)^{2-}$-pillared MOF materials with different pore sizes by changing the length of the organic linker or creating an interpenetrated polymorph structure. They obtained high acetylene adsorption capacity on MOFs of appropriate pore size by optimizing hydrogen-bond interactions between acetylene molecules and strongly basic $(SiF_6)^{2-}$, van der Waals interactions between acetylene molecules and the organic linker, and the guest-guest molecule interaction. These interactions are much weaker for ethylene because it is far less acidic than acetylene. They identify MOFs with very high acetylene adsorption capacity and acetylene–ethylene selectivity (2.1 mmol/g and ~44.8 at 0.025 bar, both higher than for previously reported materials). Variation in the MOF pore size does not influence the kinetics of acetylene and ethylene adsorption. Rather, it influences the host-guest and guest-guest interactions and hence the equilibrium adsorption capacity and selectivity.

Cadiau *et al.* study the same class of MOFs but take a different approach, designing an adsorbent for propylene–propane separation based on the molecular exclusion principle. They focus on the pillar-structured MOF with the smallest cage, using an organic linker containing only one pyrazine (see the figure). Furthermore, they replace the $(SiF_6)^{2-}$ pillars in the cage with somewhat bulkier $(NbOF_5)^{2-}$ pillars (called NbOFFIVE). This causes tilting of the pyrazine molecule on the linker, effectively reducing the aperture opening from 0.50 nm [with $(SiF_6)^{2-}$ pillars] to 0.30 nm. With strong host-guest and guest-guest interactions for propylene, the small aperture permits transport of the smaller propylene molecules into and out of the MOF cage, but excludes the slightly bulkier propane. Thus, this MOF shows high propylene adsorption capacity and unprecedented (essentially infinite) propylene–propane selectivity.

The two studies present a novel direction for the design and synthesis of MOF-based adsorbents for challenging gas separations. The authors report some stability data, but it remains to be shown whether the adsorbents are stable under industrially relevant conditions. The adsorption kinetics should also be studied, especially the kinetic effects of MOF framework flexibility at high adsorbate loading. Industrial application requires pelleting, which might affect the adsorption characteristics. Future studies should also aim to integrate these MOFs into membranes for continuous gas separation processes. ■

Highly selective

In this issue, Cadiau *et al.* report a pillared square-grid–structured MOF with a controlled aperture opening for molecular sieving of propylene over propane (right). Cui *et al.* have designed similar structured MOFs with optimized surface functionalities and cage sizes for preferential adsorption of acetylene over ethylene (left).

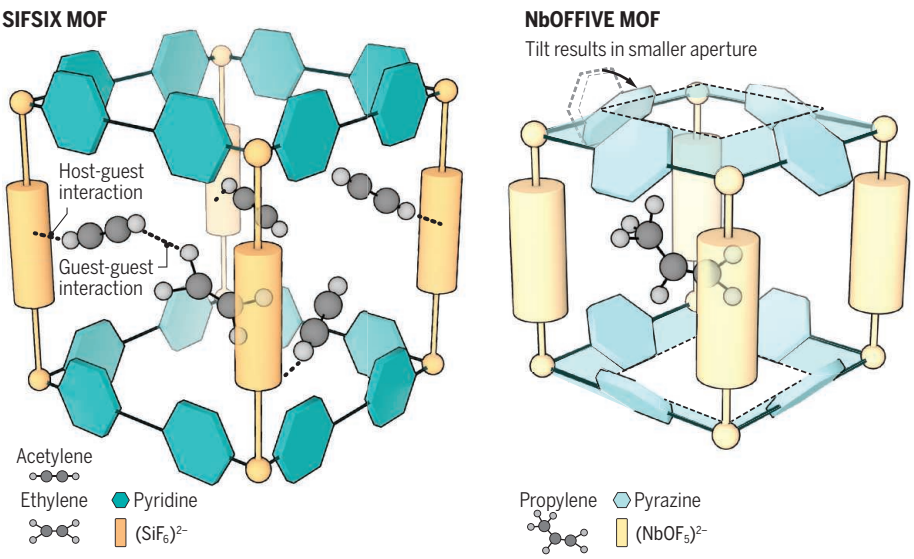

Chemical Engineering, School for Engineering of Matter, Transport and Energy, Arizona State University, Tempe, AZ 85287, USA. Email: jerry.lin@asu.edu

REFERENCES AND NOTES

1. D. S. Sholl, R. P. Lively, *Nature* **532**, 435 (2016).
2. A. Cadiau *et al.*, *Science* **353**, 137 (2016).
3. X. Cui *et al.*, *Science* **353**, 141 (2016).
4. A. Motelica *et al.*, *Ind. Eng. Chem. Res.* **51**, 6977 (2012).
5. Y. S. Lin, M. C. Duke, *Curr. Opin. Chem. Eng.* **2**, 209 (2013).
6. R. T. Yang, *Adsorbents: Fundamentals and Applications* (Wiley, Hoboken, NJ, 2003).
7. M. Eddaoudi *et al.*, *Science* **295**, 469 (2002).
8. E. D. Bloch *et al.*, *Science* **335**, 1606 (2012).
9. T. M. McDonal *et al.*, *Nature* **519**, 303 (2015).
10. C. Zhang *et al.*, *J. Phys. Chem. Lett.* **3**, 2130 (2012).
11. M. C. Das *et al.*, *J. Am. Chem. Soc.* **134**, 8703 (2012).
12. P. Nugent *et al.*, *Nature* **495**, 80 (2013).

ACKNOWLEDGMENTS

I am grateful to the NSF (CBET-1160084 and CBET-1511005) and the Department of Energy (DE-FE0026435) for supporting work on microporous materials and to Y. Liu and J. James for help in preparing this Perspective.

10.1126/science.aag2267

Network analytics in the age of big data

How can we holistically mine big data?

By **Nataša Pržulj** *and* **Noël Malod-Dognin**

We live in a complex world of interconnected entities. In all areas of human endeavor, from biology to medicine, economics, and climate science, we are flooded with large-scale data sets. These data sets describe intricate real-world systems from different and complementary viewpoints, with entities being modeled as nodes and their connections as edges, comprising large networks. These networked data are a new and rich source of domain-specific information, but that information is currently largely hidden within the complicated wiring patterns. Deciphering these patterns is paramount, because computational analyses of large networks are often intractable, so that many questions we ask about the world cannot be answered exactly, even with unlimited computer power and time (*1*). Hence, the only hope is to answer these questions approximately (that is, heuristically) and prove how far the approximate answer is from the exact, unknown one, in the worst case. On page 163 of this issue, Benson *et al.* (*2*) take an important step in that direction by providing a scalable heuristic framework for grouping entities based on their wiring patterns and using the discovered patterns for revealing the higher-order organizational principles of several real-world networked systems.

To mine the wiring patterns of networked data and uncover the functional organization, it is not enough to consider only simple descriptors, such as the number of interactions that each entity (node) has with other entities (called node degree), because two networks can be identical in such simple descriptors, but have a very different connectivity structure (see the figure). Instead, Benson *et al.* use higher-order descriptors called graphlets (e.g., a triangle) that are based on small subnetworks obtained on a subset of nodes in the data that contain all interactions that appear in the data (*3*). They identify network regions rich in instances of a particular graphlet type, with few of the instances of the particular graphlet crossing the boundaries of the regions. If the graphlet type is specified in advance, the method can uncover the nodes interconnected by it, which enabled Benson *et al.* to group together 20 neurons in the nematode worm neuronal network that are known to control a particular type of movement. In this way, the method unifies the local wiring patterning with higher-order structural modularity imposed by it, uncovering higher-order functional regions in networked data.

Network structures

The four networks shown have exactly the same size (the same number of nodes and edges), and each node in each network has the same degree (the number of interactions with other nodes), but each network has a very different structure.

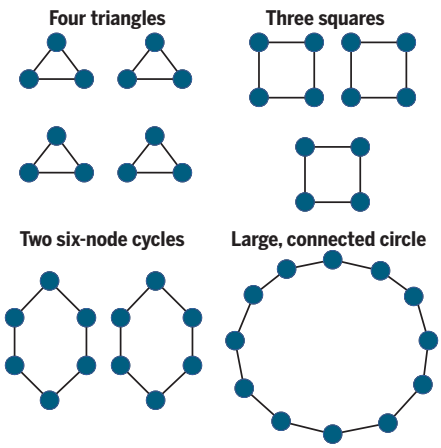

GRAPHIC: N. PRŽULJ AND N. MALOD-DOGNIN/ADAPTED BY V. ALTOUNIAN/*SCIENCE*

The importance of this result lies in its applicability to a broad range of networked data that we must understand to answer fundamental questions facing humanity today, from climate change and impacts of genetically modified organisms, to the environment (*4*), to food security, human migrations, economic and societal crises (*3, 5*), understanding diseases, aging, and personalizing medical treatments (*6–13*). For example, the cell is a complex system of interacting molecules, in which genes are transcribed into RNAs and translated into proteins, which adopt various three-dimensional structures to carry out particular cellular functions. Molecular interactions are captured by different high-throughput biotechnologies and modeled with different types of networks. Individual analyses of molecular networks have revealed that molecules involved in similar functions tend to group together in a network and are similarly wired (*13*), leading to better understanding of gene functions (*6*) and molecular organization of the cell (*7*) and to improved therapeutics (*8–12*).

However, each network type provides limited information about the phenomenon under study. For example, a disease is rarely the consequence of a single mutated gene, or of a single broken molecular interaction. Rather, it is the product of multiple perturbations of complex interactions within and across cells. Network medicine couples network analytics with data integration to mine the wealth of complementary data and reveal common molecular mechanisms between seemingly unrelated diseases (*8–11*). By contrast, patients with seemingly the same disease may have very different molecular mechanisms of disease and reactions to treatment (e.g., cancer heterogeneity) (*8–11*). Therefore, personalized medicine aims at delivering individualized therapies based on genetic and molecular profiles of individual patients that may involve repurposing of known drugs to different patient groups, hence helping to ease the pharmaceutical industry bottlenecks related to the cost and time required to develop new drugs (*11, 12*). Methods for network data analytics and integration will be fundamental to these nascent areas, as full understanding can only come from holistically mining all available genetic, molecular, and clinical data (*11*).

> ***"To mine the wiring patterns of networked data and uncover the functional organization, it is not enough to consider only simple descriptors...."***

Holistic analyses of our interconnected world call for conceptual and methodological paradigm shifts. Rather than analyzing a single data source in isolation, such as aligning genetic sequences (which has already revolutionized our understanding of biology) (*14*), further insights will come from aligning all types of data within a single framework—"the data alignment." For example, all genetic and molecular interaction data about a cell can be integrated into the same computational framework, and methods need to be developed for aligning

Department of Computer Science, University College London, London, UK. Email: natasa@cs.ucl.ac.uk

these "integrated cells" within a new paradigm of "the cell alignment." Similarly, the world's economic system includes networks of trade, financial exchanges, and investments, which thus far have been studied individually (*3, 5*). But a complete understanding of the origins of wealth, crises, and economic recoveries can only come from aligning and collectively analyzing all of these layers of networked economic and geopolitical data. Likewise, climatic measurements are captured by various network types encoding the relationships between climatic elements across geographical regions (e.g., wind speed, atmospheric pressure, and temperature) (*4*), and holistic, data-aligned analyses may help to explain this complex, dynamic system and better predict the effects of human-caused alterations. Mathematical formalisms capable of capturing the intricacies of higher-order organization of the data, along with the algorithms to compute and extract information from those formalisms, should be developed and applied (*15*). Extending the framework of Benson *et al.* to finding higher-order structures within these integrated and aligned data systems may be a way forward. Computational issues remain to be addressed, arising from large sizes, complexity, heterogeneity, noisiness, and different time and space scales of the data. ■

"Holistic analyses of our interconnected world call for conceptual and methodological paradigm shifts."

REFERENCES AND NOTES

1. M. R. Garey, D. S. Johnson, *Computers and Intractability: A Guide to the Theory of NP-Completeness* (Freeman, New York, 1979).
2. A. R. Benson *et al.*, *Science* **353**, 163 (2016).
3. O. N. Yaveroğlu *et al.*, *Sci. Rep.* **4**, 4547 (2014).
4. K. Steinhaeuser, A. A. Tsonis, *Clim. Dyn.* **42**, 1665 (2014).
5. P. Glasserman, H. P. Young, *J. Bank. Financ.* **50**, 383 (2015).
6. R. Sharan *et al.*, *Mol. Syst. Biol.* **3**, 1 (2007).
7. K. Mitra *et al.*, *Nat. Rev. Genet.* **14**, 719 (2013).
8. A.L. Barabási *et al.*, *Nat. Rev. Genet.* **12**, 1 (2011).
9. J. Menche *et al.*, *Science* **347**, 6224 (2015).
10. M. Žitnik *et al.*, *Sci. Rep.* **3**, 3202 (2013).
11. V. Gligorijevic *et al.*, *Proteomics* **16**, 741 (2016).
12. S. M. Strittmatter, *Nat. Med.* **20**, 590 (2014).
13. D. Davis *et al.*, *Bioinformatics* **31**, 1632 (2015).
14. J. Alfoldi, K. Lindblad-Toh, *Genome Res.* **23**, 1063 (2013).
15. S. Boccaletti *et al.*, *Phys. Rep.* **544**, 1 (2014).

ACKNOWLEDGMENTS

This work was supported by the European Research Council Starting Independent Researcher Grant (278212), the National Science Foundation Cyber-Enabled Discovery and Innovation Program (OIA-1028394), the Slovenian Research Agency (ARRS) Project (J1-5454), and the Serbian Ministry of Education and Science Project (III44006).

10.1126/science.aah3449

ENGINEERING

Solar-powering the Internet of Things

Photovoltaics can help to power remote sensors and controllers at the edge of the Internet

By **Richard Haight, Wilfried Haensch, Daniel Friedman**

The Internet connects billions of computational platforms of various sizes, from supercomputers to smart phones. However, the same types of data transmission can connect computational resources to much simpler sensors "at the edge of the net" that collect, analyze, and transmit data, as well as controllers that receive instructions. Devices deployed in the environment, homes and offices, and even our bodies would expand the number of connected devices to the trillions. This "Internet of Things" (IoT) underlies the vision of smart homes and buildings that could sense and transmit their status and respond appropriately (*1*), or track and report on the state of objects (vehicles, goods, or even animals) in the environment. However, the practical implementation of the IoT has been relatively slow, in part because all of these edge devices must draw electrical power from their local environment. We analyze the use of photovoltaics (PV) to power devices and help bring the IoT to fruition.

Wide-scale deployment of devices to remote or inaccessible areas while providing operational power in the absence of wires would require harvesting of available energy to ensure long-term operation. Indeed, one barrier to making an existing building "smart" is the cost of installing wired devices, so devices simply mounted to walls and powered by ambient indoor lighting are attractive for lowering installation costs. Whatever the specific form of energy used (alternatives to PV include kinetic, thermal, or wind energy), it must have sufficient energy density and reliability. The power requirements are dictated by the three components that process, sense, and communicate data. An excellent example of a system at the far edge of the net is the ultralow-power chip developed at the University of Michigan that incorporates much of the required functionality and energy-harvesting infrastructure (*2*).

IBM T. J. Watson Research Center, Yorktown Heights, NY 10598, USA. Email: rahaight@ibm.us.com

An ultralow-power processor that might, for example, be used in a smart phone (*3*) would consume ~85 μW of power when operating at a clock frequency of 1 MHz. Active power consumption in a processor is given by CV^2F, where C is the capacitance, V is the operating voltage of the processor, and F is the clock frequency. Reducing the operating voltage has the biggest benefit, and energy-efficient processors have been demonstrated to run with a supply voltage of <400 mV at 0.83 MHz (*4*). The time constant of the systems monitored is often long (milliseconds to minutes), so the required clock frequency can be well below 1 MHz. Intermittent operation—where the processor can be woken to take a measurement, store data, and later transmit it to a receiving station—would save appreciable power. Hence, ultralow-power operation of an edge device is both required and achievable.

Sensors are another area where low power is critical. As an example, consider an electrochemical sensor (*5*) used to monitor concentrations of toxic gases or other air-dispersed pollutants. A typical sensor might consist of a miniature electrochemical cell that draws 100 to 500 μA of current at 1 to 2 V. The total power consumed depends on whether it operates continuously (as for a carbon monoxide monitor) or periodically (an outdoor ozone monitor for air quality). Typical power requirements for most sensors can range from 100 μW to >1 mW, depending on what is being sensed.

Another critical component of an autonomously deployed edge device is its ability to transmit data to other proximal devices or a central location (hub) where the information can be analyzed. There are several communication modalities that could be used that operate near 1 V but differ in cost and distance range. A simple method would be to transmit the data optically by modulating an infrared light–emitting diode that operates at milliwatt power levels (but limited distance range). Vertical-cavity surface-emitting lasers are highly directional, providing longer range, but operate at several milliwatts. Yet another communication mode involves radio-frequency (RF) transmission being developed for ultralow-power operation in

receive and transmit modes (*6*) with a total power consumption of 6 to 8 mW and data send and receive rates of 150 kilobytes per second (kbps) to 4 Mbps. Devices are larger for RF communication (typically centimeters or larger) because of the antenna size. To reduce edge device power needs, a hub system with a central high-power transmitter would only require low-power backscatter modulation from the edge device. Although the transmit power of the edge device is dramatically reduced, the viable separation distance to its hub is limited.

Smart edge systems can also process data locally and minimize the amount of communication with the central system. The architecture of the network used to enable hub-edge device communication will dictate data rates and distance specifications. At present, ultralow-power devices (*2*) can transmit a few meters, requiring a series of other proximally located devices to relay data over longer distances. Data transmission over hundreds of meters or more is possible but incurs a trade-off between the power cost of processing and that for communication.

Given these power budget estimates, we focus on energy harvesting, voltage regulation, and energy storage. One attractive approach would be to merge thin-film PV devices with an energy storage medium such as a battery or supercapacitor. Batteries have a distinct advantage in that they deliver current at a constant voltage, determined by the particular electrochemistry used, until the stored charge is depleted. The use of batteries as a voltage regulator avoids the need for energy-consuming integrated-circuit voltage regulation. For a small computer-sensor device, we may consider a 1-cm^2 footprint for a battery that is 0.1 cm thick; the maximum energy stored at an energy density of 200 Wh/liter for a lithium-ion battery (*7*) is ~20 mWh. Given our estimates of power consumption for processing and data storage (~100 μW), sensing (~1 mW), data transmission (~5 mW), and intermittent operation totaling 1 hour per day, such an ultrasmall battery would power an edge device for perhaps 3 days. In reality, systems deployed in the field would need to last a year or more.

The foregoing simple analysis reveals the acute need for energy harvesting to dramatically extend the life of the device in the field. Light, as a nearly ubiquitous source of energy, is an optimal choice. For PV cells, the light absorber needs to be cheap, efficient, and, perhaps most important for field applications, environmentally compatible, because once deployed, it likely will not be retrieved at a later date. The multielemental kesterite $Cu_2ZnSn(S_{1-x}Se_x)_4$ (CZTS,Se) is the most efficient Earth-abundant thin-film absorber available today. Although its power conversion efficiency of 12.6% (*8*) is only a little more than half that of CdTe and CdInGaSe (CIGSe), it does not contain metals that are toxic (Cd) or expensive and relatively rare (In and Ga). The entire thin-film PV device stack is only 2 to 3 μm thick, just 1% that of the required 300 μm of Si necessary to fully absorb ambient light.

There are also other important considerations in choosing a thin-film PV device to be merged with a battery. The voltage produced by the PV device at its maximum power point (V_{mpp}) must exceed that necessary to charge the battery. Although the standard voltages, V_{oc} (open-circuit voltage) and V_{mpp}, of a PV device are typically determined under full-Sun illumination, called 1 sun (AM1.5) of ~100 mW cm^{-2}, charging of the battery must occur under a wide range of illumination conditions and is a challenging aspect of PV-based energy harvesting. Typical fluorescent lighting produces about 10^{-3} suns. At such low light levels, the shunt resistance (*9*) of the cell must be at least 500 to 1000 ohm·cm^2 to generate sufficient voltage to charge the battery.

Optimizing the band gap of the PV absorber with the light source is another key consideration. Indoor lighting from fluorescent or LED bulbs has a higher proportion of blue light than the Sun. The band gap of CZTS,Se can be correspondingly increased by increasing its sulfur content. Emerging alloys of CZTS,Se, including (Ag_xCu_{1-x}) ZTS,Se (*10*) with a variable band gap and AgZTSe (*11*) with a 1.3-eV band gap, hold promise for even higher efficiency than traditional CZTS,Se because of suppression of bulk defects. The band gap tunability of CZTS,Se and CIGSe distinguishes them from Si, GaAs, and CdTe. Higher voltages can be achieved by connecting cells in series or fabricating a tandem cell in which a top PV cell with a larger band gap is deposited on a bottom cell of a smaller band gap (*12*).

Truly self-powered, intelligent computers and sensors provide the ability to communicate as a network and to gather information on critically important aspects of even the most remote regions of our planet. They also can help us to better control our nearby environment to make it more efficient and sustainable. ■

Powering edge devices

The Internet of Things can connect sensors deployed remotely, but these sensors must be powered. Photovoltaics could power sensors both inside buildings and in the environment, as shown in this example of a "smart ranch."

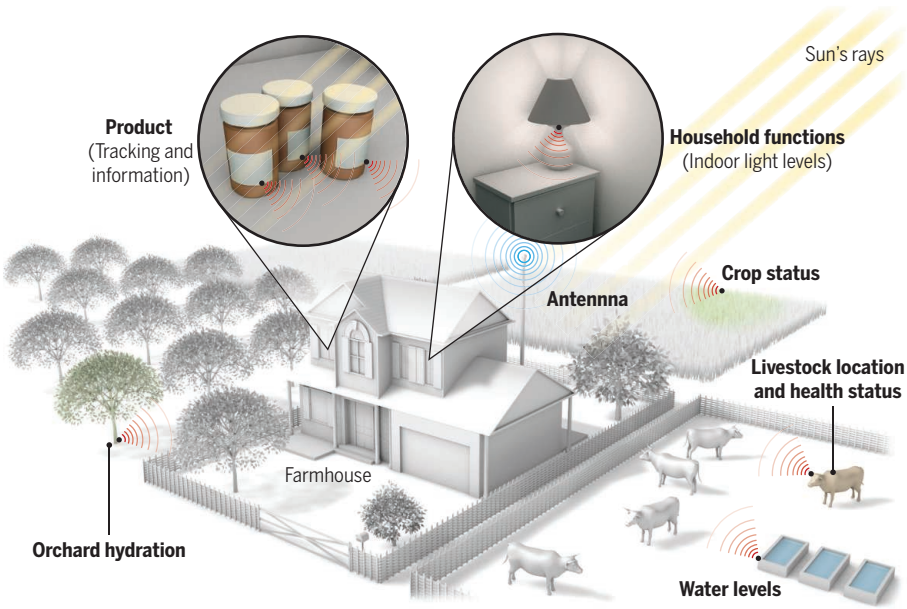

GRAPHIC: C. BICKEL/*SCIENCE*

REFERENCES

1. N. Gershenfeld *et al.*, *Science* **327**, 1086 (2010).
2. P. Pannuto *et al.*, in *Proceedings of the 42nd Annual International Symposium on Computer Architecture* (2015), pp. 629–641.
3. "ARM Launches Its Smallest, Lowest Power, Most Energy Efficient Processor" (press release); www.arm.com/about/newsroom/24418.php.
4. B. Zhai *et al.*, *IEEE Trans. VLSI* **17**, 1127 (2009).
5. U. Guth *et al.*, *Meas. Sci. Technol.* **20**, 042002 (2009).
6. IMEC, "IEEE 802.11AH Wi-Fi HaLow Radio in TSMC 40NM CMOS"; www2.imec.be/content/user/File/Brochures/ip2016/7_ULP%20WIFI%20RADIO_mail.pdf.
7. J. B. Goodenough, K. S. Park, *J. Am. Chem. Soc.* **135**, 1167 (2013).
8. W. Wang *et al.*, *Adv. Energy Mater.* **4**, 130165 (2014).
9. T. J. McMahon *et al.*, in *Proceedings of the 25th IEEE Photovoltaic Specialists Conference* (1996), pp. 1291–1294.
10. T. Gershon *et al.*, *Adv. Energy Mater.* **6**, 1502468 (2016).
11. E. Chagarov *et al.*, *J. Chem. Phys.* **144**, 104704 (2016).
12. J. Kim *et al.*, *Science* **317**, 222 (2007).

10.1126/science.aag0476

Cite as: J. D. Boeke *et al.*, *Science* 10.1126/science.aaf6850 (2016).

The Genome Project–Write

Jef D. Boeke,*† George Church, * Andrew Hessel, * Nancy J. Kelley,* Adam Arkin, Yizhi Cai, Rob Carlson, Aravinda Chakravarti, Virginia W. Cornish, Liam Holt, Farren J. Isaacs, Todd Kuiken, Marc Lajoie, Tracy Lessor, Jeantine Lunshof, Matthew T. Maurano, Leslie A. Mitchell, Jasper Rine, Susan Rosser, Neville E. Sanjana, Pamela A. Silver, David Valle, Harris Wang, Jeffrey C. Way, Luhan Yang

*These authors contributed equally to this work.
†Corresponding author. Email: jef.boeke@nyumc.org
The list of author affiliations is available in the supplementary materials.

We need technology and an ethical framework for genome-scale engineering

The Human Genome Project ("HGP-read") nominally completed in 2004 aimed to sequence the human genome and improve technology, cost, and quality of DNA sequencing (*1*, *2*). It was biology's first genome-scale project, and at the time was considered controversial by some. Now it is recognized as one of the great feats of exploration, one that has revolutionized science and medicine.

Although sequencing, analyzing, and editing DNA continue to advance at breakneck pace, the capability to construct DNA sequences in cells is mostly limited to a small number of short segments, restricting the ability to manipulate and understand biological systems. Further understanding of genetic blueprints could come from construction of large, gigabase (Gb)–sized animal and plant genomes, including the human genome, which would in turn drive development of tools and methods to facilitate large-scale synthesis and editing of genomes. To this end, we propose the Human Genome Project–Write (HGP-write).

Responsible innovation

Genome synthesis is a logical extension of the genetic engineering tools that have been used safely within the biotech industry for ~40 years and have provided important societal benefits. However, recent technological advancements—e.g., standardized gene parts, whole-genome synthesis, and clustered regularly interspaced short palindromic repeats (CRISPR)–Cas9 genome editing technology (*3*, *4*)—are revolutionizing the field (*5*). Some applications are controversial; human germline editing in particular has raised intense moral debate (*6*). As human genome-scale synthesis appears increasingly feasible, a coordinated scientific effort to understand, discuss, and apply large-genome engineering technologies is timely. HGP-write will require public involvement and consideration of ethical, legal, and social implications (ELSI) from the start. Responsible innovation requires more than ELSI, though, and involves identifying common goals important to scientists and the wider public through timely and detailed consultation among diverse stakeholders.

We will enable broad public discourse on HGP-write; having such conversations well in advance of project implementation will guide emerging capabilities in science and contribute to societal decision-making. Through open and ongoing dialogue, common goals can be identified. Informed consent must take local and regional values into account and enable true decision-making on particularly sensitive use of cells and DNA from certain sources. Finally, the highest biosafety standards should guide project work, and safety for lab workers, research participants, and ecosystems should pervade the design process. A priority will be cost reduction of both genome engineering and testing tools to aid in equitable distribution of benefits—e.g., enabling research on crop plants and infectious agents and vectors in developing nations.

To ensure responsible innovation and ongoing consideration of ELSI, a percentage of all research funds could be dedicated to these issues, enabling inclusive decision-making on the topics mentioned above (*7*). In addition, there should be equitable distribution of any early and future benefits in view of diverse and pressing needs in different global regions. The broad scope and novelty of the project calls for consideration of appropriate regulation alongside development of the science and societal debates. National and international laws and regulations differ and, as in stem cell research, a major burden of responsibility of setting standards rests with the scientists and their community. Existing stem cell research guidelines (*8*) may serve as a useful template.

From observation to action

The primary goal of HGP-write is to reduce the costs of engineering and testing large (0.1 to 100 billion base pairs) genomes in cell lines by over 1000-fold within 10 years. This will include whole-genome engineering of human cell lines and other organisms of agricultural and public health significance, or those needed to interpret human biological func-

tions—i.e., gene regulation, genetic diseases, and evolutionary processes.

This goal is necessarily ambitious, since building a human genome at today's prices would cost more than HGP-read (*9*) (see fig. S1). However, an expectation of HGP-write will be to catalyze a sharp price drop as new technology development occurs apace with advancement of the project, as with the cost of DNA sequencing in HGP-read. Small viral (*10*) and bacterial (*11*) genomes synthesized from scratch and organisms with recoded genomes (*12*) derived from large-scale genome editing (*13*) have demonstrated the feasibility and utility of synthetic genomes. By focusing on building the 3 Gb of human DNA, HGP-write would push current conceptual and technical limits by orders of magnitude and deliver important scientific advances.

HGP-write will aim to address a number of human health challenges. Potential applications include growing transplantable human organs; engineering immunity to viruses in cell lines via genome-wide recoding (*12*); engineering cancer resistance into new therapeutic cell lines; and accelerating high-productivity, cost-efficient vaccine and pharmaceutical development using human cells and organoids. The project could encourage broad intellectual property access via patent pooling. Extreme cost-reduction is feasible, as demonstrated by the $1000 genome grant program (*2*) as well as sharing of CRISPR tools from over 80 labs through addgene.org. Furthermore, because DNA synthesis, like sequencing and computation, is foundational technology, HGP-write could also facilitate biological engineering of many organisms, accelerating R&D across a broad spectrum of life sciences and supporting basic R&D of new bio-based therapies, vaccines, materials, energy sources, disease vector control, and nutrition.

Pilot projects

Similar to other Gb-scale genomic projects, including HGP-read, ENCODE (which aims to map genome functional elements), and Sc2.0 (which is synthesizing a heavily edited yeast genome) (*14*, *15*), HGP-write would be conducted in phases with explicit goals and metrics. Each of the earlier large-scale projects began with pilot projects focused on a fraction of the genome, typically ~1%. For HGP-write, the pilots should provide resources of immediate value for advanced biomedical research and/or biotech development. Technology development will likely also occur early in the project to propel large-scale genome design and engineering.

A series of pilot projects making use of very long DNA sequences that are nonetheless short of a full genome are anticipated: (i) synthesizing "full" gene loci with accompanying noncoding DNA to help explain still-enigmatic roles of noncoding DNA variants in regulating gene expression, and leading to more comprehensive models for the role of noncoding genetic variation in common human diseases and traits; (ii) constructing specific chromosomes—e.g., chromosome 21—or complex cancer genotypes to more comprehensively model human disease; (iii) producing specialized chromosomes encoding one or several pathways—e.g., all genes needed to make a prototrophic human cell, or pathways to transform the pig genome to make it more amenable as source for human organ transplantation; (iv) a potential transformation of gene therapy, with freedom to deliver many genes and control circuits to improve safety and efficacy, provided delivery challenges can be met. Indeed, many substantial and useful innovations may be realized in such "stepping stone" projects that are short of whole-genome re-engineering but require substantial improvement in synthesis capacity of Mb- to Gb-sized DNA. Both genome-wide and more modest changes could be tested for their impact on, e.g., organoid development and function in vitro, facilitated by ongoing progress in stem cell differentiation and "organ on chip" technologies. Novel cell culture technologies may, in some cases, be many times more cost-effective and accurate than current whole-organism testing.

Box 1. Some properties of "ultrasafe" cells with a pervasively re-engineered genome.

Virus resistance—can be conferred by systematically recoding certain codons across all genes. Subsequent deletion of tRNA genes would generate a cell line resistant to viruses.

Improved cancer resistance—tumor suppressor genes could be made multicopy; genes like p53 could be recoded to eliminate CpG dinucleotides that give rise to "hotspot" mutations.

Other useful traits—delete potentially deleterious genes such as prion genes.

Improved genome stability—comprehensively eliminate endogenous repetitive "selfish DNA" elements.

Fail-safe security—prevent formation of germ cells, e.g., by removing transcriptional regulators.

Applications— "go to" cell line for stem cell therapies; robust production of biologics.

Additional pilot projects being considered include (v) using induced pluripotent stem cells (*16*) to construct an "ultrasafe" human cell line via comprehensive recoding of protein-coding regions, and deletion of corresponding genome features to increase safety of such a cell line (see Box 1); and (vi) developing a homozygous reference genome

bearing the most common pan-human allele (or allele ancestral to a given human population) at each position to develop cells powered by "baseline" human genomes. Comparison to this baseline will aid in dissecting complex phenotypes such as disease susceptibility. The pervasive nature of the required changes makes whole- or partial-genome synthesis an efficient route to these goals.

Project launch and administration

The goal is to launch HGP-write in 2016 with $100 million in committed support, from public, private, philanthropic, industry, and academic sources from around the world. The costs of the project lie not only in obtaining de novo synthesized DNA but in the assembly, integration, and functional assays required to evaluate and understand the modified genomes. Total project costs are difficult to estimate but would likely be less than the $3 billion cost of HGP-read.

HGP-write could be implemented through one or more centers [similar to Centers of Excellence in Genomic Science (CEGS) and the Brain Research through Advancing Innovative Neurotechnologies (BRAIN) initiative centers] that will coordinate and support formation and work of multi-institutional and interdisciplinary research teams working in a highly integrated fashion responsive to and engaged with a broad public outreach.

We celebrate 2016—the 25th anniversary of HGP-read—as a major step forward for human knowledge and health. In this spirit, we look forward to the launch of HGP-write.

REFERENCES AND NOTES

1. International Human Genome Sequencing Consortium, *Nature* **431**, 931 (2004). Medline doi:10.1038/nature03001
2. C. W. Fuller *et al*., *Nat. Biotechnol.* **27**, 1013 (2009). Medline doi:10.1038/nbt.1585
3. L. Cong *et al*., *Science* **339**, 819 (2013). Medline doi:10.1126/science.1231143
4. P. Mali *et al*., *Science* **339**, 823 (2013). Medline doi:10.1126/science.1232033
5. A. D. Haimovich, P. Muir, F. J. Isaacs, *Nat. Rev. Genet.* **16**, 501 (2015). Medline doi:10.1038/nrg3956
6. D. Baltimore *et al*., *Science* **348**, 36 (2015). Medline doi:10.1126/science.aab1028
7. Presidential Commission for the Study of Bioethical Issues, *New Directions: The Ethics of Synthetic Biology and Emerging Technologies* (Washington, DC, 2010).
8. J. Kimmelman *et al*., *Nature* **533**, 311 (2016). Medline doi:10.1038/533311a
9. P. A. Carr, G. M. Church, *Nat. Biotechnol.* **27**, 1151 (2009). Medline doi:10.1038/nbt.1590
10. K. J. Blight, A. A. Kolykhalov, C. M. Rice, *Science* **290**, 1972 (2000). Medline doi:10.1126/science.290.5498.1972
11. D. G. Gibson *et al*., *Science* **329**, 52 (2010). Medline doi:10.1126/science.1190719
12. M. J. Lajoie *et al*., *Science* **342**, 357 (2013). Medline doi:10.1126/science.1241459
13. F. J. Isaacs *et al*., *Science* **333**, 348 (2011). Medline doi:10.1126/science.1205822
14. N. Annaluru *et al*., *Science* **344**, 55 (2014). Medline doi:10.1126/science.1249252
15. J. S. Dymond *et al*., *Nature* **477**, 471 (2011). Medline doi:10.1038/nature10403
16. K. Takahashi, S. Yamanaka, *Cell* **126**, 663 (2006). Medline doi:10.1016/j.cell.2006.07.024

ACKNOWLEDGMENTS

This paper is the result of meetings held at NYU Langone Medical Center on 31 October 2015 and at Harvard Medical School on 10 May 2016. The authors gratefully acknowledge the financial support of Autodesk, sponsor of the meetings. We thank Debra Mathews (Berman Institute for Bioethics) for helpful discussions. F.J.I. is a cofounder of enEvolv, Inc. G.C. has financial relationships with Gen9, Editas, Enevolv, and Egenesis (companies directly related to this article; for a full list of G.C.'s financial relationships, see arep.med.harvard.edu/gmc/tech.html). J.D.B. is a founder and on the Board of Directors of Neochromosome Inc., owns stock in Sample 6, Inc., and is a member of the Scientific Advisory Board of Recombinetics, Inc. A.H. has investments in Autodesk Inc. G.C. is an inventor on patents and patent applications filed by Harvard Medical School that cover synthesis, assembly and testing of large DNAs..

SUPPLEMENTARY MATERIALS

www.sciencemag.org/cgi/content/full/science.aaf6850/DC1
Author affiliations
Fig. S1

Published online 2 June 2016
10.1126/science.aaf68

]www.sciencemag.org/cgi/content/full/science.aaf6850/DC1

Supplementary Materials for

The Genome Project–Write

Jef D. Boeke,[1]*† George Church,[2]* Andrew Hessel,[3]* Nancy J. Kelley,[4]* Adam Arkin,[5] Yizhi Cai,[6] Rob Carlson,[7] Aravinda Chakravarti,[8] Virginia W. Cornish,[9] Liam Holt,[10] Farren J. Isaacs,[11] Todd Kuiken,[12] Marc Lajoie,[13] Tracy Lessor,[14] Jeantine Lunshof,[15] Matthew T. Maurano,[16] Leslie A. Mitchell,[17] Jasper Rine,[18] Susan Rosser,[19] Neville E. Sanjana,[20] Pamela A. Silver,[21] David Valle,[22] Harris Wang,[23] Jeffrey C. Way,[24] Luhan Yang[25]

*These authors contributed equally to this work.
†Corresponding author. Email: jef.boeke@nyumc.org

Published 2 June 2016 on *Science* First Release
DOI: 10.1126/science.aaf6850

This PDF file includes:

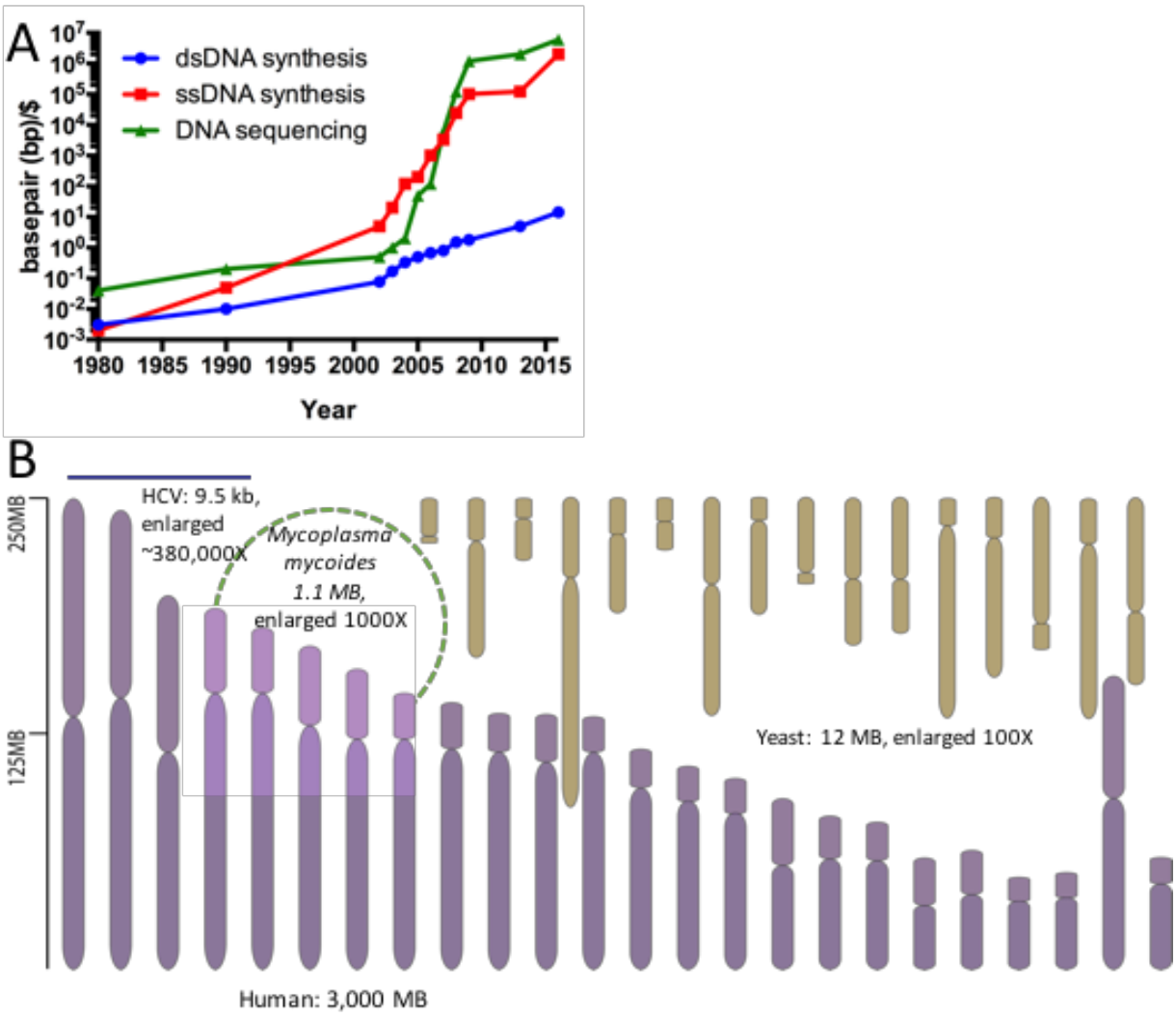

Fig. 1. Synthesizing synthetic or semisynthetic genomes. A. Efficiency trends in DNA sequencing (green) and synthesis of double-stranded DNA (dsDNA, blue) and single-stranded DNA (ssDNA, red) over the past ~35 years. Double-stranded DNA, or gene synthesis, has improved noticeably over the past ~10 years, but still lags behind sequencing and ssDNA synthesis. The disruptive improvement in sequencing and ssDNA (oligonucleotides) synthesis technologies has improved from multiplex and miniaturization technologies in high-throughput DNA sequencing and oligo microarray technologies, respectively. Commercial gene synthesis technologies relies on both oligo synthesis (building blocks) and sequencing (validation of synthesis) technologies. **B.** Graphical representation of four representative genomes benchmarked to the size of the 3,000 MB human chromosomes: 9.5 kb hepatitis C virus (HCV) enlarged ~380,000-fold, 1.1 MB Mycoplasma mycoides enlarged ~1,000-fold, 12 MB yeast enlarged 100-fold.

Bibliography

As further support for the arguments in our paper, this is a (non-comprehensive) sampling of precedents for projects that could take advantage of radical reduction in cost of genome-scale synthesis and high-throughput cellular/organismal testing of consequences. As with HGP-read, this effort need not be restricted to human but could and should include mouse, pig, *Drosophila melanogaster*, *Caenorhabditis elegans*, *Arabidopsis thaliana*, *Saccharomyces cerevisiae*, etc.

The bibliography, along with proposals for pilot projects, maybe found online at the project web site www.hgpwrite.org

Author affiliations

[1]Institute for Systems Genetics at New York University Langone Medical Center, New York, NY, USA. Email: jef.boeke@nyumc.org

[2]Wyss Institute for Biologically Inspired Engineering at Harvard Medical School, Massachusetts Institute of Technology, Boston/Cambridge, MA, USA. Email: gmc@harvard.edu

[3]Autodesk Bio/Nano Research Group, San Rafael, CA, USA. Email: andrew.hessel@autodesk.com

[4]Nancy J Kelley & Associates. New York, NY, USA. Email: nancy@nancyjkelley.com

[5]Department of Bioengineering, University of California, Environmental Genomics and Systems Biology Division, E.O. Lawrence Berkeley National Laboratory, Berkeley, CA, USA. Email: aparkin@lbl.gov

[6]Edinburgh Genome Foundry, School of Biological Sciences at University of Edinburgh, Edinburgh, Scotland. Email: yizhi.cai@ed.ac.uk

[7]Bioeconomy Capital, Seattle, WA, USA. Email: rob@synthesis.cc

[8]McKusick-Nathans Institute of Genetic Medicine at Johns Hopkins University School of Medicine, Batimore, MD, USA. Email: achakra1@jhmi.edu

[9]Departments of Chemistry and Systems Biology at Columbia University, New York, NY, USA. Email: vc114@columbia.edu

[10]Institute for Systems Genetics at New York University Langone Medical Center, New York, NY, USA. Email: liam.holt@nyumc.org

[11]Department of Molecular, Cellular and Developmental Biology, Systems Biology Institute at Yale University, New Haven, CT, USA. Email: farren.isaacs@yale.edu

[12]Science and Technology Innovation Program at Woodrow Wilson International Center for Scholars, Washington, DC, USA. Email: todd.kuiken@wilsoncenter.org

[13]Department of Biochemistry at University of Washington, Seattle, WA, USA. Email: mlajoie@uw.edu

[14]Feinstein Kean Healthcare, Cambridge, MA, USA. Email: tracy.lessor@fkhealth.com

[15]Department of Genetics, Harvard Medical School, Boston, MA, USA; Department of Genetics, University of Groningen, Groningen, The Netherlands. Email: j.e.lunshof@umcg.nl

[16]Institute for Systems Genetics, NYU Langone Medical Center, New York, NY, USA. Email: maurano@nyu.edu

[17]Institute for Systems Genetics, NYU Langone Medical Center, New York, NY, USA. leslie. Email: mitchell@nyumc.org

[18]Department of Molecular and Cell Biology, University of California at Berkeley, Berkeley, CA, USA. Email: jrine@berkeley.edu

[19]Edinburgh Genome Foundry, School of Biological Sciences at University of Edinburgh, Edinburgh, Scotland. Email: yizhi.cai@ed.ac.uk

[20]New York Genome Center; Department of Biology, New York University, New York, NY, USA. Email: nsanjana@nygenome.org

[21]Department of Systems Biology, Wyss Institute of Biologically Inspired Engineering at Harvard Medical School, Boston, MA, USA. Email: pamela_silver@hms.harvard.edu.

[22]McKusick-Nathans Institute of Genetic Medicine at Johns Hopkins University School of Medicine, Baltimore, MD, USA. Email: dvalle@jhmi.edu.

[23]Department of Systems Biology, Department of Pathology and Cell Biology at Columbia University, College of Physicians and Surgeons, New York, NY, USA. Email: hw2429@columbia.edu

24Wyss Institute for Biologically Inspired Engineering at Harvard Medical School, Boston, MA, USA. Email: jeff.way@wyss.harvard.edu

[25]eGenesis, Inc., Boston, MA, USA. Email: luhan.yang@egenesisbio.com

BOOKS *et al.*

PARASITOLOGY

Master manipulators

Emerging research on how parasites affect host behavior fuels speculation about their influence on human history

By **Shelley Adamo**

Adult hairworms are aquatic, but their larvae burrow into the abdomens of terrestrial arthropods, like the cricket, and freeload on nutrients derived from unsuspecting hosts. This represents a potential problem, because crickets are not aquatic animals. By mechanisms still unclear, once the hairworm is ready to transition to the adult life stage, it induces the cricket to jump into water, where the worm is released and the cricket drowns.

In her new book, *This Is Your Brain on Parasites*, Kathleen McAuliffe examines the unusual and often dramatic ways that parasites and microbial manipulators can influence the behavior of their hosts, raising the question of how much control we have over our own behavior. After reading the book, you may come to the conclusion that it is actually far less than you once thought.

The book begins with vivid descriptions of parasites that hijack a range of animal hosts. Like hairworms, many of these master manipulators cannot complete their life cycle unless their host can be compelled to behave atypically. For example, the larva of the parasitic wasp *Hymenoepimecis argyraphaga*, which incubates in the abdomen of the orb-weaving spider *Plesiometa argyra*, induces the spider to build a cocoon for it from the spider's own web before killing and consuming its spider host.

The tales soon take on a more serious note, as McAuliffe reveals how some parasitic manipulators are also implicated in human diseases. For example, some pathogens, such as the *Plasmodium* species that cause malaria, enhance disease transmission by manipulating their insect vectors. They do this by reducing the amount of anticoagulants released by a mosquito during a blood meal. The insect relies on these anticoagulants to keep the blood flowing. In this way, plasmodia reduce the ability of the mosquito to take in a blood meal, resulting in a perpetually hungry mosquito. It then bites multiple people, thereby increasing the chance of parasitic transmission. There is even evidence that suggests that *Plasmodium* can enhance the attractiveness of infected hosts to mosquitoes.

McAuliffe does not limit her discussion to parasitology, referencing recent work on how our gut microbes may influence our behavior and exploring how the presence of parasites may have shaped the evolution of human behavior. Parasites exert a powerful selective force, and behaviors that helped humans avoid infection should still be with us today, she argues. Some evolutionary psychologists suggest that human behaviors such as mate choice, whether a society develops democracy, and the decision to go to war may all be influenced by pathogen pressure.

Mice infected with toxoplasmosis no longer fear cats.

One of the strengths of the book is McAuliffe's exploration of alternative explanations for counterintuitive theories. This presentation style alerts the reader that some of the ideas she recounts are imaginative speculation and not considered consensus. For readers who prefer an authoritarian guide, the caveats and alternative perspectives may be unsatisfying. However, such an approach is preferable to the sensationalism that often surrounds work in this field.

Sometimes McAuliffe simply presents opposing views on a topic without comment, leaving readers to decide how much weight to give each argument. One example can be found in her presentation of *Toxoplasma gondii*, which causes rats and mice to become attracted to cat urine instead of repulsed by it. This strange attraction increases the odds that an infected rodent will be eaten by a cat, the parasite's definitive host.

Humans harbor *T. gondii*, too: About 20% of people in the Western world are infected. Researchers have wondered whether a parasite capable of altering neurotransmitter levels in the brain of a rodent could also affect human brains and behavior. Unfortunately, the only way to know definitively whether a human is infected with *T. gondii* parasites is by autopsy. As a proxy, researchers often use the presence of specific markers in the blood to demonstrate that a person has had contact with *T. gondii*. However, research has shown that only ~50% of rats deliberately infected with *T. gondii* end up with the parasites in their brains. If a similar ratio exists in humans, then there may be as much as a 50% error rate in the assignation of people into infected versus uninfected groups. McAuliffe does not elaborate on how this could represent a serious problem for human work, but her decision to include this information encourages readers to make this inference on their own.

McAuliffe interviewed a wide array of scientists working in the fields of eco-immunology, psychoneuroimmunology, and evolutionary psychology. Their stories demonstrate the importance of perseverance (and serendipity) in science and the critical role mentors can play in a career.

Scientists have much more to learn about the neurological and behavioral effects that parasites and other organisms can have on hosts. Unfortunately, a cursory glance through the web suggests that there are more neurobiologists writing about fictional zombies than there are studying the secrets of real-life zombie-makers. Perhaps this book will inspire more researchers to pursue this intriguing avenue of research.

10.1126/science.aaf9539

This Is Your Brain on Parasites
How Tiny Creatures Manipulate Our Behavior and Shape Society
Kathleen McAuliffe
Houghton Mifflin Harcourt, 2016. 292 pp.

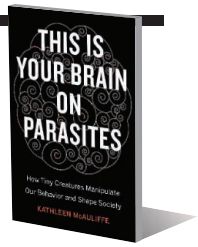

The reviewer is at the Department of Psychology and Neuroscience, Dalhousie University, Halifax, NS B3H 4R2, Canada. Email: sadamo@dal.ca

PHOTO: AFP/STRINGER

A half-century after the largest recorded earthquake struck Chile, a powerful 8.2-magnitude quake hit off the country's Pacific coast in 2014.

SEISMOLOGY

Aftershocks

A far-reaching history explores the cultural, economic, and political effects of earthquakes

By **Sebastiano D'Amico**

Despite advances in monitoring and modern infrastructure, earthquakes continue to represent one of the most serious risks to health, safety, and economic viability in many parts of the world. This is, in part, because science still cannot predict the exact time and place where an earthquake will strike. Yet, despite our insistence on treating such catastrophes as "acts of God," the truth is that we humans seek out areas prone to major seismic activity. Indeed, more than half of today's largest cities lie in areas that are prone to earthquakes.

Traditionally, when scientists discuss earthquakes, we talk about geology and seismology, infrastructure and engineering, as well as management strategies for minimizing human and material losses. Nevertheless, the study of an earthquake's effect on the social and cultural elements of a community can help us understand how different societies have evolved and adapted over time and how cities have built up their relative capacity to withstand future large seismic events.

In fact, as Andrew Robinson describes in his new book, *Earth-Shattering Events*, the effects of an earthquake can reverberate throughout a society's identity. In some cases, they have played a catalyzing role in the evolution of urban and architectural style and have irrevocably altered the communities in question.

Earth-Shattering Events
Earthquakes, Nations, and Civilization
Andrew Robinson
Thames and Hudson, 2016. 256 pp.

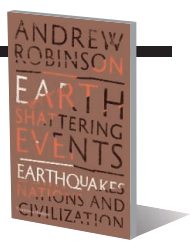

From the first pages, Robinson captures the reader's attention with a whirlwind summary of some of the more memorable earthquakes in recorded history: the devastation of Lisbon in 1755; the 1960 Chilean earthquake—the strongest in recorded history—which caused a destructive tsunami and unleashed more than 20,000 times the energy of the atomic bomb dropped on Hiroshima; the earthquake in Tangshan, China, that killed 750,000 in 1976.

The chronological organization of *Earth-Shattering Events* allows the reader to easily follow the evolution of our understanding of earthquakes. The book opens with descriptions of several memorable incidents that occurred before the advent of seismology, describing, for example, the panic that beset London when an unprecedented five major earthquakes shook Britain in 1750. The Lisbon earthquake in 1755 destroyed the city, caused extensive damage in the nearby areas, and contributed to the birth of modern seismology.

Earthquakes have fostered changes in political environments as well as served to promote industrial and social growth. For instance, Robinson suggests that the Tangshan earthquake, the most lethal earthquake of the 20th century, may have struck the last blow to the flailing Chinese Cultural Revolution. By contrast, he argues that the Gujarat earthquake in 2001 further depressed the economy of an already poor region, thereby reinforcing authoritarianism in India. But in both cases, the respective governments used the earthquake to develop new infrastructures and catalyze industrial growth. Similarly, after the 1906 destruction of San Francisco, the city became an important cultural center with a flourishing high-tech industrial area that lies on the San Andreas Fault—one of the most active systems in North America.

The book concludes with a description of events that recently caught worldwide attention. In 2011, Japan experienced the largest earthquake in its history. Initially estimated at a magnitude of 7.9, the earthquake's true magnitude—9.0—wasn't announced until nearly 24 hours after it occurred. Upgraded warnings about the resulting tsunami heights failed to reach many coastal communities in time, and nearly 19,000 people perished. It was the subsequent failure of the Fukushima nuclear power plant, however, that garnered the most attention, with several media outlets broadcasting uninterrupted coverage of the disaster.

Robinson clearly articulates the difference between earthquake hazard and risk. The first depends on the magnitude and location of likely earthquakes, as well as how often they occur, whereas the second quantifies the potential damage an earthquake could inflict on buildings or urban centers. The latter is strongly linked to the concept of vulnerability and the importance of seismic retrofitting. Robinson places particular emphasis on the fact that the damage caused by past earthquakes is very often neglected when new structures are planned, resulting in modern cities with lax building codes and few or no contingency plans, especially in areas that are perceived as low-seismicity regions. Quoting the engineering seismologist Nicholas Ambraseys, Robinson writes, "Earthquakes don't kill people; buildings do."

In conclusion, this book places earthquakes into proper historical perspective. It will make for an enlightening read, both for scholars and experts in seismology and geosciences and for readers with an interest in history.

The reviewer is at the Department of Geosciences, University of Malta, Tal-Qroqq, Msida, Malta. Email: sebastiano.damico@um.edu.mt

10.1126/science.aaf8465

LETTERS

Edited by **Jennifer Sills**

Science *stands by 2009 fisheries study*

THE EDITORS OF *Science* have become aware of allegations of conflict of interest that Greenpeace has lodged against Ray Hilborn for failing to disclose previous industry funding in connection with his co-authorship of the 2009 *Science* paper "Rebuilding global fisheries" by Worm *et al.* (*1*). In fact, it is not possible to conclude that Dr. Hilborn or other co-authors were personally deficient in their disclosures. At that time, journal policy allowed a single lead author to declare conflicts of interest on behalf of all co-authors, a practice that has since been discontinued. Current journal practice requires each author individually to declare any and all relationships (financial or otherwise) that could constitute a real or perceived conflict of interest. Although the policies in place in 2009 may not have resulted in the transparency we have come to expect in 2016, the editors of *Science* stand by the basic conclusions reached in the Worm *et al.* paper. A group of international fisheries researchers came together from different perspectives to reach consensus on the status of the best-studied marine ecosystems worldwide and agree on solutions and challenges to rebuilding fisheries stocks and achieving sustainable yields.

Marcia McNutt

Editor-in-Chief

REFERENCE

1. B. Worm *et al.*, *Science* **325**, 578 (2009).

10.1126/science.aah3704

Insufficient research on land grabbing

OVER THE PAST decade, an unprecedented boom in land transactions—commonly referred to as land grabbing—has occurred globally. At least 45 million hectares of land have changed hands through concessions, long-term leases, and ownership transfers (*1*, *2*). Driven by volatility in agricultural commodity prices, interest in biofuel production, and eagerness of governments to pursue economic development, transnational and domestic investors have acquired land throughout the global South (*1*). Resulting changes in control over land threaten existing vegetation cover and forests, especially where the new owners successfully implement commercial agricultural production. Changes in control over land can support greater agricultural output, but research on the subject has mostly raised urgent concerns about transactions leading to displacement of local livelihoods and populations (*3*), and compromised ecosystem services (*4*).

The effectiveness of research on land transactions, however, is hobbled by three problems. First, global data sets on land transactions underestimate the total number of transactions. Official statistics for Ethiopia, Peru, and Cambodia show that the numbers of transactions are consistently underestimated in global data (*5*). Second, it is difficult to calculate how much commercial agriculture is taking place because not all of the transacted land is being developed. Many investors, witnessing the rise in large-scale land transactions, have made speculative investments in land that they hope later to sell for a profit. In many other instances, local residents living in and near transacted lands have resisted the implementation of commercial agricultural practices (*6*). Third, findings reported in the literature rest largely on samples that are not statistically representative of the variation in factors such as geography, socioeconomic differences, and contractual arrangements that influence outcomes. Instead, they focus on social dimensions of transaction outcomes such as fairness and inequality (*7*). These are important to consider, but the current dominant focus on social outcomes needs to be supplemented with a greater consideration of ecological outcomes and effects on agricultural output.

A deeper understanding of land transaction outcomes requires studies that are more representative of the range of transactions. More systematic attention to case selection and causal effects of tenure changes is necessary to address research limitations (*8*). Improved representation will also enable more robust estimates of social, economic, and ecological effects of transactions (*9*).

Chuan Liao, Suhyun Jung, Daniel G. Brown, and Arun Agrawal*

School of Natural Resources and Environment, University of Michigan, Ann Arbor, MI 48109, USA.

*Corresponding author. Email: arunagra@umich.edu

REFERENCES

1. B. White, S. M. Borras, R. Hall, I. Scoones, W. Wolford, *J. Peasant Stud.* **39**, 619 (2012).
2. B. Zagema, *Oxfam Policy Pract. Agric. Food Land* **11**, 114 (2011).
3. M. A. Wendimu, A. Henningsen, P. Gibbon, *World Dev.* **83**, 84 (2016).
4. K. F. Davis, K. Yu, M. C. Rulli, L. Pichdara, P. D'Odorico, *Nat. Geosci.* **8**, 772 (2015).
5. Large-Scale Land Transactions as Deivers of Land-Cover Change in Sub-Saharan Africa (www.forestlivelihoods.org/projects/large-scale-land-transactions-as-drivers-of-land-cover-change-in-sub-saharan-africa/).
6. R. Hall *et al. J. Peasant Stud.* **42**, 467 (2015).
7. K. Nolte, L. Voget Kleschin. *World Dev.* **64**, 654 (2014).
8. S. M. Borras, C. Kay, S. Gómez, J. Wilkinson, *Can. J. Dev. Stud. Rev. Can. Détudes Dév.* **33**, 402 (2012).
9. A. Agrawal, *Proc. Natl. Acad. Sci. U.S.A.* **111**, 3909 (2014).

10.1126/science.aaf6565

The company Saudi Star Agricultural Development transports water on the land it has bought in Ethiopia.

PHOTO: © JOERG BOETHLING/ALAMY STOCK PHOTO

Mexico struggles to keep foreign grants

IN HER NEWS In Depth story "Mexico struggles to woo expat genome jocks" (29 April, p. 507), L. Wade discusses the bureaucratic hurdles that are slowing research in Mexico. We would like to highlight a hurdle not mentioned in the story: Researchers at the Mexican National Institutes of Health (INSHAE) encounter obstacles when trying to claim U.S. National Institutes of Health subcontractor grants.

Although not always successful, as Wade points out, the Mexican government has gone to great effort to make funds available for local researchers. More worrisome are

the recent regulations (*1*) that essentially disqualify INSHAE investigators from receiving foreign grants. To claim international grants, researchers must draft extremely complicated legal documents and treaties, which are then rejected by both the Mexican and the U.S. collaborator's legal department. In addition to hindering Mexican research, these requirements place a huge burden on our U.S. collaborators, who have to complete onerous administrative tasks to support scientific research in Mexico.

These funds are required to perform urgent studies aimed at controlling infectious diseases caused for example by the HIV, Chikungunya, and Zika viruses. Scientists at the INSHAE have both experience and geographical opportunity. To allow much-needed funds to reach Mexican scientists, the Mexican government should introduce realistic and compliance-friendly regulations.

Christopher E. Ormsby, Santiago Ávila-Ríos, Gustavo Reyes-Terán*

Instituto Nacional de Enfermedades Respiratorias, Mexico City, DF 14080, Mexico.

*Corresponding author. Email: reyesteran@cieni.org.mx

REFERENCE

1. Legal Notice [Oficio] DGRI/685/2014 to the Head of the INSHAE (2014); www.cieni.org/docs/DGRI_685_2014.pdf [in Spanish].

10.1126/science.aag1021

TECHNICAL COMMENT ABSTRACTS

Comment on "Long-term climate forcing by atmospheric oxygen concentrations"

Colin Goldblatt

Poulsen *et al.* (Reports, 12 June 2015, p. 1238) argued that lower atmospheric oxygen levels during the Phanerozoic would have given a warmer climate. However, radiative and atmospheric structure changes under lower pressure both cause cooling, making their result unusual in that a hierarchy of models gives opposing results. Scrutiny of how radiative and cloud processes were represented, and a mechanistic explanation of the results, are required.

Full text at http://dx.doi.org/10.1126/science.aad6976

Response to Comment on "Long-term climate forcing by atmospheric oxygen concentrations"

Christopher J. Poulsen, Clay Tabor, Joseph White

Goldblatt argues that a decrease in pressure broadening of absorption lines in an atmosphere with low oxygen leads to an increase in outgoing longwave radiation and atmospheric cooling. We demonstrate that cloud and water vapor feedbacks in a global climate model compensate for these decreases and lead to atmospheric warming.

Full text at http://dx.doi.org/10.1126/science.aad8550

ERRATA

Erratum for the Review "Somatic mutation in cancer and normal cells" by I. Martincorena and P. J. Campbell, *Science* **351**, aaf5401 (2016). Published online 4 March 2016; 10.1126/science.aaf5401

Erratum for the Report "Ancient Ethiopian genome reveals extensive Eurasian admixture in eastern Africa" (previously titled "Ancient Ethiopian genome reveals extensive Eurasian admixture throughout the African continent") by M. Gallego Llorente *et al.*, *Science* **351**, aaf3945 (2016). Published online 19 February 2016; 10.1126/science.aaf3945

TECHNICAL COMMENT

CLIMATE CHANGE

Comment on "Long-term climate forcing by atmospheric oxygen concentrations"

Colin Goldblatt

Poulsen *et al*. (Reports, 12 June 2015, p. 1238) argued that lower atmospheric oxygen levels during the Phanerozoic would have given a warmer climate. However, radiative and atmospheric structure changes under lower pressure both cause cooling, making their result unusual in that a hierarchy of models gives opposing results. Scrutiny of how radiative and cloud processes were represented, and a mechanistic explanation of the results, are required.

Poulsen *et al.* (*1*) present results from the Global Environmental and Ecological Simulation of Interactive Systems (GENESIS) global climate model (GCM) that show a warmer climate under lower atmospheric pressure. This contrasts to established radiative-convective model (RCM) results in which lower pressure causes cooling (*2*). Changes to the clear-sky radiation under less pressure have a net cooling effect (in their paper, Poulsen *et al.* described only the warming effects). Likewise, atmospheric structure changes weaken the greenhouse effect, causing cooling. Yet their GCM model output shows a warming via less cloud reflection. This raises fundamental questions: Are the clear-sky processes correctly represented in GENESIS? If they are, what is the physical mechanism by which a negative clear-sky forcing induces a positive cloud forcing strong enough to reverse the sign of the overall change?

Less atmosphere leads to less Rayleigh (molecular) scattering. This can be treated with a simple scaling analysis, given that the amount of scattering is proportional to the number of molecules in the column and that the scattering cross sections for N_2 and O_2 are similar. (The scaling with surface density used by Poulsen *et al.* was erroneous.) To estimate the change in absorbed sunlight, consider a single-layer, scattering only, model atmosphere over a black surface. Let the direct solar beam incident at the top of the atmosphere (TOA) be $I^{\downarrow}_{\mathrm{dir}}(t) = I_0$. Using Beer's law, the direct beam at the surface is found $I^{\downarrow}_{\mathrm{dir}}(s) = I_0 e^{-\tau}$, where optical depth ($\tau$) is directly proportional to the number of molecules in the atmosphere. The Rayleigh scattering phase function is symmetrical, so equal amounts of light are scattered up and down and $I^{\downarrow}_{\mathrm{scat}}(s) = I^{\uparrow}_{\mathrm{scat}}(t) = \frac{1}{2} I_0(1-e^{-\tau})$. $\tau = 0.1$ gives a good fit to Earth's atmosphere [$I^{\uparrow}_{\mathrm{scat}}(t) = 16$ W m^{-2}; observations (*3*) and models (*4*) show that Rayleigh scattering is 15 W m^{-2} today]. Decreasing the number of molecules by 11% would correspond to decreasing τ by 11%, reducing the amount of reflected sunlight at the TOA by 1.7 W m^{-2}. This would tend to warm the planet slightly.

In their scaling analysis, Poulsen *et al.* (*1*) conflate Mie scattering by clouds with Rayleigh scattering by molecules. Quite obviously, there will be less Rayleigh scattering when there are fewer oxygen molecules. However, there is no a priori justification for the number of cloud droplets scaling with the number of air molecules. The decrease of reflected sunlight of 16 W m^{-2} suggested by the Poulsen *et al.* (*1*) scaling cannot be supported.

The other consequence of fewer molecules is less pressure broadening of the absorption lines of radiatively active species like CO_2, so that these absorb less radiation. The natural width of absorption lines is very narrow, but molecular collisions widen them so that more radiation overall is absorbed. Lower palaeopressure would weaken the greenhouse effect and tend to cool the planet. Changes to pressure broadening dominate over Rayleigh scattering, so the net clear-sky radiative effect is negative forcing and cooling (*2*).

Mean atmospheric structure is well approximated by a moist adiabat. Given that saturation vapor pressure depends only on temperature, the amount of water vapor does not change with pressure, but less dry air molecules make the saturation mixing ratio of water larger. Thus, lapse rate is lower (less steep), there is less temperature difference between the surface and the atmosphere, and the greenhouse effect is further weakened (*2*).

A straightforward way to evaluate the combination of the above is to calculate the radiative forcing, with fixed surface temperature and CO_2 inventory but varying O_2 abundance (Fig. 1). The radiative transfer here was performed at line-by-line resolution using the Spectral Mapping Atmospheric Radiative Transfer (SMART) model, with absorption coefficients calculated from HITRAN2012 (High-Resolution Transmission Molecular Absorption Database) (*5*) specifically for these atmospheric profiles, so these results are of reference accuracy. For a decrease in O_2 to 10% of the atmosphere, the radiative forcing at the tropopause is –3.0 W m^{-2}, consisting of thermal and solar contributions of –4.4 and +1.4 W m^{-2} (note the dominance of pressure broadening over Rayleigh scattering). To first approximation, surface temperature change is proportional to radiative forcing. With a typical climate sensitivity of 0.8 K/W m^{-2}), this implies that reducing O_2 to 10% would lead to a planetary cooling of 2.4 K.

Given that a warming is seen in the GCM, one must first ask whether the driving radiative processes are represented correctly. Away from modern conditions, errors in GCM radiative transfer codes are, unfortunately, rather common (*6*, *7*). They have to be heavily parametrized for speed to run a single profile in a fraction of a second (compared to ~20 min for SMART). In palaeoclimate, we take these codes well away from the modern conditions for which they were tuned. Accuracy cannot be presumed, and testing the code in the conditions of interest is a due-diligence step (*8*). Poulsen *et al.* (*1*) did not do this verification for the legacy radiation code, National Center for Atmospheric Research Community Climate Model 3 (CCM3), used in GENESIS.

The standard method for testing GCM radiation codes is off-line comparison to a line-by-line code, comparing radiative fluxes calculated over fixed atmospheric profiles, so that the accuracy of the radiation code may be separated from other model components [see Collins *et al.* (*6*) for a thorough discussion of this methodology]. In correspondence with Poulsen *et al.*, before this comment, I compared results of SMART (Fig. 1) and CCM3 (kindly run by the authors), but the authors did not want their results included here.

Next, one asks whether the model cloud response accurately represents the real world. Generally, the problem of modeling change to marine stratus is fraught (*9*, *10*). Circumstantial evidence of a potential problem comes from an intercomparison project that addressed clouds for a different palaeoclimate topic: GENESIS gave cloud radiative forcing 15 to 20 W m^{-2} higher than any other model, which was linked to how cloud radiative properties were represented (*11*). These should be independent of climate state, so evidence of anomalous warming from clouds raises substantial concerns.

Climate modeling has developed through a hierarchy of models: For the canonical problem of temperature response to CO_2 doubling, all model classes from the original RCMs (*12*) to modern GCMs give an answer of the same sign and similar magnitude. Departure from this precedent is an exceptional result, which requires exceptional evidence. GCMs have the great utility of resolving the interaction of radiative transfer, dynamics, and the hydrological cycle. However, the results are only meaningful if all individual components are accurate for the conditions in which the model is used. For Poulsen *et al.*'s response to this Comment, I would lay down two challenges. First, to demonstrate that clear-sky and cloud radiative processes are verified as accurate for the conditions

School of Earth and Ocean Sciences, University of Victoria, Victoria, British Columbia, Canada. **Email: czg@uvic.ca**

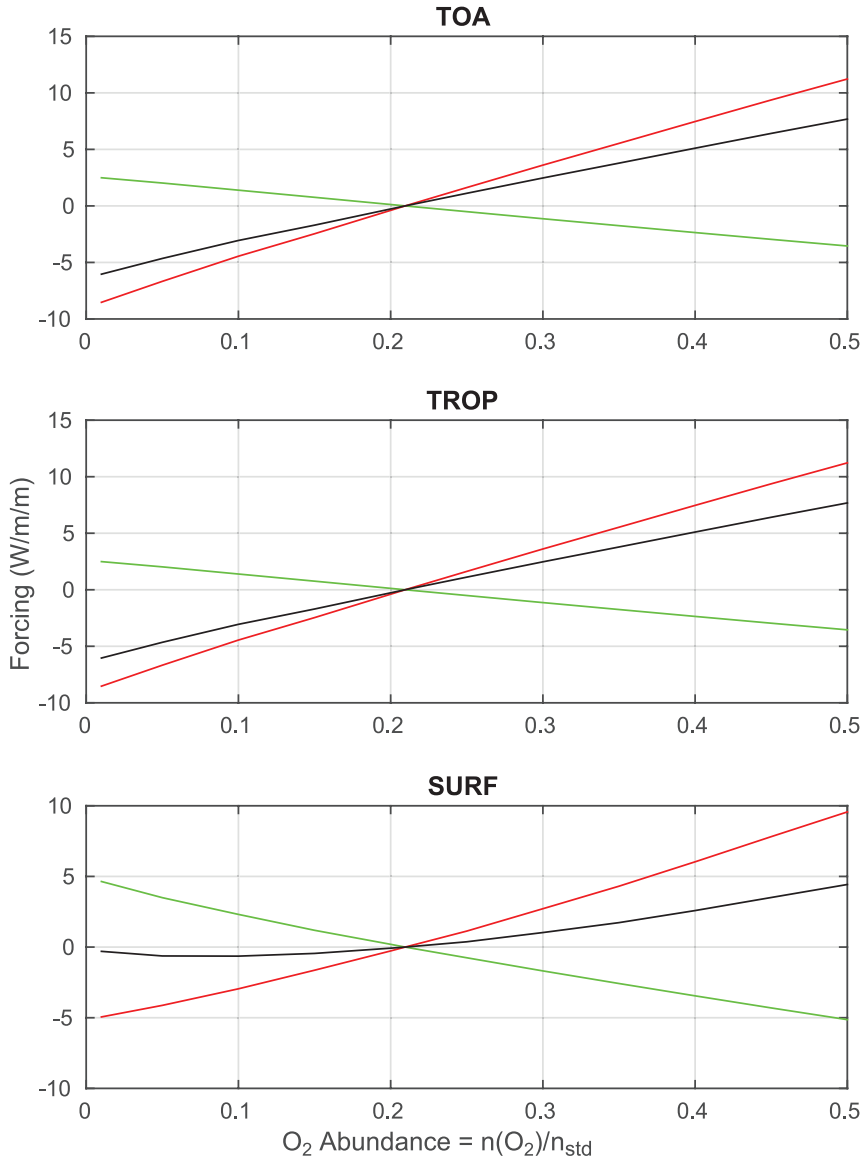

Fig. 1. Forcing from a change in number of moles of oxygen in the atmosphere relative to standard conditions (n_{std}). Colors are red for thermal, green for solar, and black for net. Forcings are positive downward, so a positive forcing warms everything below that level. Atmospheric profiles are constructed as follows. Troposphere (surface to pressure, $p = 10^4$ Pa): a moist adiabat is followed from a 289 K surface to 240 K, and from p (240 K), temperature varies linearly with pressure to 206 K at $p = 10^4$ Pa, resulting in a profile that approximates a global annual mean (GAM) profile well when surface pressure is 10^5 Pa. Stratosphere (above $p = 10^4$ Pa): GAM profile. The CO_2 mixing ratio is adjusted to conserve moles of CO_2 between profiles. Water vapor varies linearly with pressure from the surface to the tropopause [similar to Manabe and Wetherald (*12*)].

at hand. Second, in the context of other climate forcings indicating cooling, to provide a direct, physically based, mechanistic explanation for why lower pressure should lead to less low cloud.

REFERENCES AND NOTES

1. C. J. Poulsen, C. Tabor, J. D. White, *Science* **348**, 1238–1241 (2015).
2. C. Goldblatt *et al.*, *Nat. Geosci.* **2**, 891–896 (2009).
3. Y. C. Zhang, W. B. Rossow, A. A. Lacis, V. Oinas, M. I. Mishchenko, *J. Geophys. Res.* **109**, D19105 (2004).
4. C. Goldblatt, K. J. Zahnle, *Clim. Past* **7**, 203–220 (2011).
5. L. S. Rothman *et al.*, *J. Quant. Spectrosc. Radiat. Transfer* **130**, 4–50 (2013).
6. W. D. Collins *et al.*, *J. Geophys. Res.* **111**, D14317 (2006).
7. C. Goldblatt, T. M. Lenton, A. J. Watson, *Quart. J. R. Met. Soc.* **135**, 619–633 (2009).
8. To reduce the need for ad hoc testing, a Palaeoclimate Radiative Transfer Intercomparison Project has been established; www.palaeotrip.org.
9. B. Stevens, G. Feingold, *Nature* **461**, 607–613 (2009).
10. S. Bony, J.-L. Dufresne, *Geophys. Res. Lett.* **32**, L20806 (2005).
11. D. S. Abbot *et al.*, *Geophys. Res. Lett.* **39**, L20711 (2012).
12. S. Manabe, R. D. Wetherald, *J. Atmos. Sci.* **24**, 241–259 (1967).

ACKNOWLEDGMENTS

This work was supported by a Natural Sciences and Engineering Research Council of Canada Discovery grant to C.G.

21 October 2015; accepted 26 May 2016
10.1126/science.aad6976

TECHNICAL RESPONSE

CLIMATE CHANGE

Response to Comment on "Long-term climate forcing by atmospheric oxygen concentrations"

Christopher J. Poulsen,[1]* Clay Tabor,[2] Joseph White[3]

Goldblatt argues that a decrease in pressure broadening of absorption lines in an atmosphere with low oxygen leads to an increase in outgoing longwave radiation and atmospheric cooling. We demonstrate that cloud and water vapor feedbacks in a global climate model compensate for these decreases and lead to atmospheric warming.

Poulsen *et al.* (*1*) report the results of a global climate model (GCM) used to investigate the climate response to changing atmospheric oxygen (O_2) levels and find that a reduction in O_2 leads to surface warming and enhanced precipitation as a result of radiative changes and cloud, lapse rate, and water vapor feedbacks. The results of Poulsen *et al.* (*1*) differ from previous estimates using a one-dimensional radiative-convective model (RCM) that only crudely represents climate feedbacks (*2*), raising questions from Goldblatt (*3*) about the representation of clear-sky radiation processes in the Global Environmental and Ecological Simulation of Interactive Systems (GENESIS) GCM and the mechanisms that lead to atmospheric warming in the model. We address these two points below.

The GENESIS 3 radiation code is based on the NCAR Community Climate Model (CCM3) radiation scheme (*4*). As noted in Goldblatt, a standard method for testing radiation codes in GCMs is to calculate radiation fluxes using a stand-alone offline version of the radiation code with fixed atmospheric profiles. We have completed this analysis for clear-sky conditions using the same atmospheric profiles of temperature and water vapor for 10 and 21% O_2 scenarios as Goldblatt to facilitate comparisons between GENESIS 3 and Spectral Mapping Atmospheric Radiative Transfer (SMART) models. Clear-sky top of the atmosphere (tropopause) longwave and shortwave responses are approximately –2.5 and 0.3 W m^{-2}, smaller but in line with the results from the SMART model (Fig. 1). Differences in the magnitude of responses obviously result from differences in the radiation code but also stem from choice in insolation, zenith angle, and interpolation of the atmospheric profiles to the radiation model. In sum, as expected, the GENESIS 3 radiation code captures reductions in longwave absorption through Mie scattering and shortwave absorption through Rayleigh scattering.

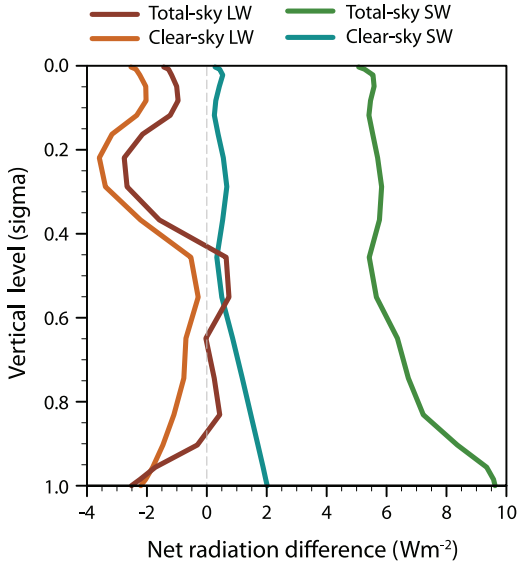

Fig. 1. Clear-sky and total-sky profiles of net shortwave (SW) and longwave (LW) radiation differences between cases with 10 and 21% O_2, estimated using the GENESIS 3 radiation model, which is based on the CCM3 radiation scheme. Clear-sky profiles are consistent with responses simulated by Goldblatt using the SMART model and indicate a decrease in the net TOA radiation as a result of increased LW loss associated with a reduction in pressure broadening of absorption lines of radiatively active gases. In contrast, total-sky profiles that include clouds show an increase in the net TOA radiation. The radiation profiles are estimated using the stand-alone GENESIS 3 radiation scheme using atmospheric profiles of water vapor and temperature provided to us by Goldblatt. For total-sky estimates, cloud profiles come from climatologies of the 21 and 10% O_2 GENESIS simulations. Both sets of profiles assume a TOA solar input of 338 W m^{-2} and a zenith angle of 60°.

It is well known that clouds have a large influence on Earth's radiation budget and that cloud feedbacks can determine the climate response to a forcing (*5*). As a crude illustration of the influence of clouds due to a reduction in O_2, we include results for total-sky conditions using global-average cloud profiles from climatologies of GENESIS 10 and 21% O_2 simulations. The total (cloudy and clear sky) top-of-atmosphere (TOA) response to a reduction in O_2, –1.4 and 5.1 W m^{-2} in longwave and shortwave, respectively, is much different and the net (longwave + shortwave) response is opposite in sign (positive) than the clear-sky response (Fig. 1), confirming the importance and warming effect of cloud feedbacks. We note that the response described here differs, mainly in the surface total-sky longwave response, from the GCM response because the temperature and water vapor profiles are from Goldblatt and do not account for GCM-simulated water vapor and lapse rate feedbacks.

As illustrated by our radiation scheme calculations, feedbacks are responsible for the warming response in GENESIS. The initial response to lower O_2 is an increase in surface shortwave forcing, a warming of the surface and boundary layer, and a reduction in atmospheric stability. Low-level warming has two direct effects: a decrease in low-level, mainly stratus, clouds and an increase in convective activity. Low-level stratus cloud fraction is determined in the model by a relative humidity threshold and the presence of either vertical ascent (for frontal clouds) or low-level stratification (for marine stratocumulus clouds) (*6*, *7*). With greater surface shortwave radiative heating under low O_2, the low-level relative humidity rises slightly (<2%), whereas both vertical velocities in regions of mean ascent and low-level inversions decrease [see, e.g., figs. S3 and S5 in (*1*)]. The net result is a decrease in low-cloud fraction, which acts as a positive feedback on surface shortwave forcing. Between equilibrium runs of 10 and 21% O_2, this positive cloud feedback leads to a net surface shortwave forcing difference of 4.8 W m^{-2}.

Enhanced surface shortwave forcing under low O_2 also drives both deeper and more frequent convection. (The overall increase in convection and reduction in mean vertical velocities are confirmed by corresponding increases and decreases in simulated global-average convective and large-scale precipitation.) Convective moistening of the lower and mid-troposphere is seen in higher relative humidity (by up to 10%) and increases the downward longwave flux at the surface by 9.2 W m^{-2}, acting as an additional positive feedback on surface radiative forcing.

In addition to positive feedbacks, there are two weaker negative feedbacks: (i) the moistening of the atmosphere scatters incoming shortwave radiation, reducing the surface net clear-sky

[1]Department of Earth and Environmental Sciences, University of Michigan, Ann Arbor, MI 48109, USA. [2]National Center for Atmospheric Research (NCAR), Boulder, CO 80305, USA. [3]Department of Biology, Baylor University, Waco, TX 76798, USA.
*Corresponding author. Email: poulsen@umich.edu

shortwave forcing by –0.9 W m^{-2}, and (ii) the reduction in low-level clouds allows greater longwave escape from the surface by 5.6 W m^{-2}.

The explanations above address the two concerns raised by Goldblatt. The feedback mechanisms above were detailed in Poulsen *et al.* With that said, we agree that the description of scattering in Poulsen *et al.* was not as clear as it could have been and should have been referred to as total scattering (Rayleigh and Mie). We do not agree with a series of generalizations made by Goldblatt that are not relevant to Poulsen *et al.* Briefly, the reference to (*8*) is inappropriate. That study examines the differences in radiation code response to atmospheric CO_2, which is not at issue here. Likewise, characterizing the GENESIS GCM cloud forcing in a study of the ice-free mid-Cretaceous based on snowball earth simulations with globally prescribed surface ice is irrelevant. There is no way to assess that the GENESIS cloud response in the snowball Earth comparison study is less correct than the other GCMs considered in that study; the authors of the study do not make such a claim (*9*). Incidentally, Poulsen *et al.* is not the first to have found that clouds may be important in explaining past warm climates [e.g., (*10*–*13*)].

Poulsen *et al.* considers the climate system response to changes in atmospheric mass and, in this way, is a step forward. The study identifies a new forcing and provides mechanisms that potentially mitigate climate model mismatches with past climates. Nonetheless, we caution that the results, as in all modeling studies, have some element of model dependence and must be confirmed through additional climate modeling efforts that incorporate feedbacks. Our hope is that the study motivates a closer look at the effects of changes in atmospheric mass as a potential climate forcing throughout Earth history.

REFERENCES AND NOTES

1. C. J. Poulsen, C. Tabor, J. D. White, *Science* **348**, 1238–1241 (2015).
2. C. Goldblatt *et al.*, *Nat. Geosci.* **2**, 891–896 (2009).
3. C. Goldblatt, *Science* **353**, 132 (2016).
4. J. T. Kiehl *et al.*, *J. Clim.* **11**, 1131–1149 (1998).
5. V. Ramanathan *et al.*, *Science* **243**, 57–63 (1989).
6. P. J. Rasch, J. E. Kristjansson, *J. Clim.* **11**, 1587–1614 (1998).
7. J. M. Slingo, *Q. J. R. Meteorol. Soc.* **113**, 899–927 (1987).
8. W. D. Collins *et al.*, *J. Geophys. Res.* **111**, D14317 (2006).
9. D. S. Abbot *et al.*, *Geophys. Res. Lett.* **39**, L20711 (2012).
10. L. C. Sloan, D. Pollard, *Geophys. Res. Lett.* **25**, 3517–3520 (1998).
11. D. S. Abbot, E. Tziperman, *Q. J. R. Meteorol. Soc.* **134**, 165–185 (2008).
12. L. R. Kump, D. Pollard, *Science* **320**, 195 (2008).
13. C. J. Poulsen, J. Zhou, *J. Clim.* **26**, 7003–7022 (2013).

ACKNOWLEDGMENTS

Preparation of this response was supported by NSF Sedimentary Geology and Paleobiology Program grant F035175 and NSF Marine Geology and Geophysics grant F033663.

21 December 2015; accepted 26 May 2016
10.1126/science.aad8550

RESEARCH ARTICLE SUMMARY

REGENERATION

Asymmetric division of clonal muscle stem cells coordinates muscle regeneration in vivo

David B. Gurevich, Phong Dang Nguyen, Ashley L. Siegel, Ophelia V. Ehrlich, Carmen Sonntag, Jennifer M. N. Phan, Silke Berger, Dhanushika Ratnayake, Lucy Hersey, Joachim Berger, Heather Verkade, Thomas E. Hall, Peter D. Currie*

INTRODUCTION: Mammalian skeletal muscle harbors tissue-specific stem cells that are triggered to replace damaged fibers after injury. Genetic ablation of satellite cells in the mouse results in a failure to regenerate muscle, which indicates that these cells are the major (and possibly only) mediators for repair of skeletal muscle. Further evidence for the central role of satellite cells in muscle regeneration comes from transplantation experiments with genetically marked cells, which demonstrate that satellite cells are highly proliferative myogenic precursors capable of self-renewal and the resumption of quiescence, properties deemed important in a cell population responsible for muscle repair. Considerable in vitro evidence, derived from cultured fibers and myoblasts, is suggestive of a role for asymmetric division in generating both a self-renewing "immortal" stem cell and a differentiation-competent progenitor cell that proliferates and ultimately replaces damaged muscle. However, asymmetric division of satellite cells has not been documented in vivo. Furthermore, considerable doubt remains over how accurately in vitro studies can model satellite cell behavior, given that the isolation and culture of individual muscle fibers and cells stimulates satellite cell proliferation. Finally, it is not clear whether the environment an activated satellite cell encounters in a single fiber explant, or in culture, mimics the molecular and biophysical architecture of a regenerating muscle injury in vivo. Consequently, what role, if any, the wound environment itself plays in regeneration and self-renewal is difficult to address in these systems.

RATIONALE: Using the optical clarity and genetic tractability of the zebrafish system, we developed tools to track and image the regeneration of living muscle tissue after injury. Marking muscle stem and progenitor cells with transgenes and using long-term imaging and lineage-tracing modalities enabled us to visualize cell movements and behaviors during regeneration in vivo.

RESULTS: In vivo cell tracking permitted high-resolution imaging of the entire process of muscle regeneration, from injury to fiber replacement. Using this approach, we were able to determine the morphological, cellular, and genetic basis for zebrafish muscle regeneration. Our analysis identified a stem cell niche in the zebrafish myotome that is equivalent to the mammalian satellite cell system, revealing that this evolutionarily ancient stem cell is probably present throughout the vertebrate phylogeny. Complex interactions were observed between satellite cells and both injured and uninjured fibers within the wound environment. Among the most notable of these was the identification of filopodia-like projections, emanating from uninjured fibers, which adhere to and "lasso" the activated satellite cell to guide it to the wound edge. Furthermore, we documented the in vivo occurrence of asymmetric satellite cell division, a process that drives both self-renewal and regeneration via a clonally restricted progenitor pool.

ON OUR WEBSITE

Read the full article at http://dx.doi.org/10.1126/science.aad9969

CONCLUSION: Asymmetric divisions occur during in vivo muscle regeneration to generate clonally related progenitors required for muscle repair. This finding resolves a long-term debate surrounding the existence of this mechanism of stem cell self-renewal and muscle repair in vivo. Our results also reveal the highly dynamic nature of the wound environment, where uninjured fibers at the wound edge play a crucial role in directing differentiating progenitors to regions of the wound that are most in need of new fiber addition. ■

The list of author affiliations is available in the full article online.
*Corresponding author. Email: peter.currie@monash.edu
Cite this article as D. B. Gurevich *et al.*, *Science* 353, aad9969 (2016). DOI: 10.1126/science.aad9969

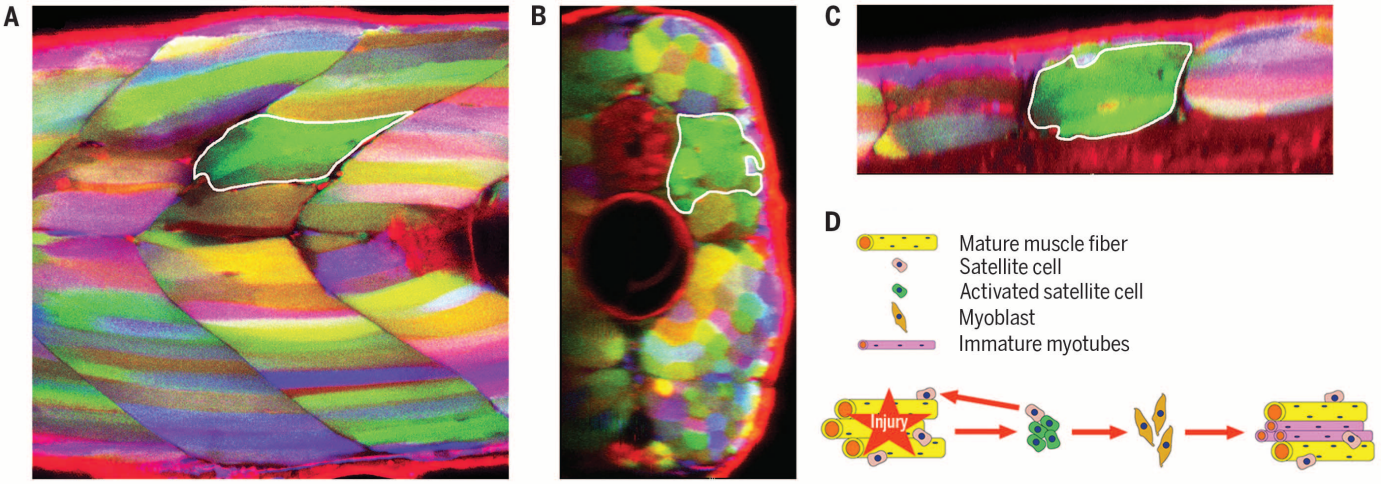

Mechanism of in vivo muscle repair. (**A** to **C**) Muscle regeneration is clonal. Regenerating fibers (outlined in white) express the same color after fluorescent lineage tracing, indicating clonal derivation from a single stem cell. Sagittal, transverse, and coronal sections are shown in (A) to (C), respectively. (**D**) Regeneration dynamics in vivo. Quiescent satellite cells, activated upon injury, undergo asymmetric division, which results in self-renewing or proliferating cells. Proliferative cells undergo myogenesis to generate de novo immature fibers.

RESEARCH ARTICLE

REGENERATION

Asymmetric division of clonal muscle stem cells coordinates muscle regeneration in vivo

David B. Gurevich,[1] Phong Dang Nguyen,[1] Ashley L. Siegel,[1] Ophelia V. Ehrlich,[1] Carmen Sonntag,[1] Jennifer M. N. Phan,[1] Silke Berger,[1] Dhanushika Ratnayake,[1] Lucy Hersey,[1] Joachim Berger,[1] Heather Verkade,[2] Thomas E. Hall,[1] Peter D. Currie[1,3]*

Skeletal muscle is an example of a tissue that deploys a self-renewing stem cell, the satellite cell, to effect regeneration. Recent in vitro studies have highlighted a role for asymmetric divisions in renewing rare "immortal" stem cells and generating a clonal population of differentiation-competent myoblasts. However, this model currently lacks in vivo validation. We define a zebrafish muscle stem cell population analogous to the mammalian satellite cell and image the entire process of muscle regeneration from injury to fiber replacement in vivo. This analysis reveals complex interactions between satellite cells and both injured and uninjured fibers and provides in vivo evidence for the asymmetric division of satellite cells driving both self-renewal and regeneration via a clonally restricted progenitor pool.

Adult muscle stem cells or satellite cells play a critical role in amniote skeletal muscle repair. Normally quiescent and located between the mature muscle fiber and the overlying basal lamina, satellite cells are characterized by the expression of a number of specific markers, including the paired homeobox genes *Pax3* and *Pax7*, the myogenic regulatory factor (MRF) gene *Myf5*, and the hepatocyte growth factor membrane receptor *cMet* (*1*, *2*). Genetic ablation of Pax7-expressing satellite cells from adult muscle results in a failure to regenerate, demonstrating that satellite cells are the major and possibly only mediators of murine skeletal muscle repair (*3*). The ability of satellite cells to self-renew has been demonstrated in transplantation experiments using genetically marked cells (*4*). Transplantation of a single intact myofiber with its complement of less than 10 satellite cells has been shown to produce more than 100 new myofibers containing 25,000 nuclei, as well as a contribution to the host pool of satellite cells from the donor tissue (*4*). Such experiments demonstrate that satellite cells are proliferative myogenic cells capable of self-renewal and reassumption of quiescence, all of which are important requirements for a stem cell population responsible for muscle repair. However, exactly how self-renewal is regulated remains an intense area of investigation. The majority of studies have focused on a possible role for asymmetric divisions of satellite cells in generating a self-renewing "immortal" stem cell and a progenitor cell required for the generation of a differentiation-competent population that proliferates and ultimately replaces damaged muscle (*5*–*9*). Although considerable in vitro evidence derived from cultured fibers and myoblasts is suggestive of a role for asymmetric division during satellite cell self-renewal, asymmetric division of satellite cells has not been documented to date in any in vivo environment. Furthermore, considerable doubt remains over how accurately current in vitro–based paradigms can model satellite cell behavior. This is because the in vitro culture of muscle fibers and the isolation of individual cells is inherently an activating process for satellite cells. Finally, it is not clear whether the environment an activated satellite cell encounters in a single fiber explant or in culture mimics the molecular and biophysical architecture of a regenerating muscle injury in vivo. Consequently, what role, if any, the wound environment itself plays in regeneration and self-renewal is difficult to address. Recent studies using intravital imaging within injured and uninjured mouse muscle have begun to examine these questions in vivo, but technical constraints have prevented the examination of asymmetric cell division and self-renewal (*10*).

[1]Australian Regenerative Medicine Institute, Level 1, 15 Innovation Walk, Monash University, Wellington Road, Clayton, Victoria 3800, Australia. [2]School of Biological Sciences, Building 18, Monash University, Clayton, Victoria 3800, Australia. [3]European Molecular Biology Laboratory Australia Melbourne Node, Level 1, Building 75, Monash University, Wellington Road, Clayton, Victoria 3800, Australia.
*Corresponding author. Email: peter.currie@monash.edu

De novo muscle repair mechanisms in zebrafish

In this study, we subjected transgenic zebrafish to distinct muscle injuries and followed regeneration by simple optical inspection of muscle tissue. Of the injury models tested (*11*–*13*), the one that proved to be the most rapid, reproducible, and amenable to gene expression analyses was the needle-stick larval injury. In this model, an epaxial myotome at the end of the yolk extension of larvae at 4 days postfertilization (dpf) is injured with a single puncture, using a 30-gauge needle held at an angle of 75° relative to the body axis (Fig. 1, B to D, and fig. S1, A to E). This form of injury resulted in the loss of about half of all fibers in the epaxial myotome at all medial lateral levels at the point of injury. The repair process can be directly monitored in the living larvae via the use of transgenes that mark muscle fibers and by using the light-refracting properties of intact muscle sarcomeres (termed birefringence) to quantitate muscle integrity. Our analyses revealed that needle-stick muscle injury in zebrafish larvae results in the rapid activation of endogenous muscle repair, a process that plateaus and concludes by 7 days postinjury (dpi) (fig. S1, A, B, and G, n = 20 fish; fig. S1, C to E, n = 7 fish; and movie S1). Fiber loss occurs immediately after injury and continues for several days. There is little evidence of wound contraction contributing to repair because the wound site remains stable during the regenerative process until it is repaired by new fiber addition (fig. S2, n = 8 fish; and movie S2).

To study the cell biological basis of this repair, we performed needle-stick injuries in fish that were transgenic for both Tg(*actc1b*:mcherry) and Tg(*myf5*:GFP) (GFP, green fluorescent protein), which mark differentiated muscle fibers in red and *myf5* expression in green (Fig. 1, A to D, n = 12 fish; figs. S2 and S3, A to D, n = 38 fish; and movies S1 and S2). *Myf5* in amniotes is expressed in both quiescent and activated satellite cells and transit-amplifying progenitors during muscle regeneration and, consequently, marks an extended phase of the regenerative process (*2*, *14*). We theorized, therefore, that the Tg(*actc1b*:mcherry) and Tg(*myf5*:GFP) transgene combination may allow us to image stem cell activation to muscle differentiation in continuous time-lapse analyses. In uninjured larvae, *myf5*-positive cells are located throughout the myotome, interstitial to differentiated muscles fibers, and first appear at 4 dpf (Fig. 1A). Injury induces a series of dynamic cell shape changes within a proportion of *myf5*-positive cells; these changes include the extension of long filopodial processes into the wound, reminiscent of the behavior deployed by muscle progenitors within injured adult mouse muscle (*10*). Consequently, migrating *myf5*-positive cells exhibit an elongated shape, entering the wound site from multiple levels and positions within the injury (movie S3), following their membrane extensions into the wound site (Fig. 1, B to D, and movie S1). This activated subset of *myf5*-positive cells is chiefly characterized by their polarized, migratory phenotype, with activated cells often elongating and migrating over nonextended *myf5*-GFP cells that are initially closer to the wound (Fig. 1, B to D). By 2 dpi, *myf5*-positive cells within the wound site have begun to elongate as myocytes, with evidence by 3 dpi of fully differentiated muscle fibers replacing those that have been lost (fig. S1, C to E, n = 7 fish; and fig. S3, A to D). *myf5* expression peaks at 3 dpi and declines steadily, returning to

preinjury levels by 7 dpi, when regeneration is complete (fig. S3, A to D).

To examine the nature of the de novo myogenic event induced by muscle injury, we investigated the expression of endogenous genes involved in muscle repair in amniotes. Specifically, we examined the expression of *pax7*, which marks both quiescent and activated muscle stem cells and is the most universally accepted marker of satellite cells in postnatal murine muscle (*5*). We also investigated the expression of the MRF genes *myf5*, *myoD*, and *myogenin*, which are sequentially activated during regeneration in mammals (*2*). For all myogenic regulators, expression is specifically induced at the injury site, in a temporal fashion consistent with their roles in controlling a local de novo myogenic event after injury (*12*) (fig. S3, E to H, n = 10 fish per group).

Furthermore, regenerating fibers initially express an embryonic slow myosin heavy-chain (MyHC) isoform during differentiation. This observation reinforces the notion that different processes, distinct to those that occur during muscle growth, coordinate muscle regeneration. Regenerating fibers express the slow MyHC1 gene (*15*) and protein (*16*), and quantitation of this expression (fig. S1, H to R, n = 6 fish) as well as analysis of the expression of the slow MyHC1:GFP transgene [Tg(*smyhc1*:GFP)] during injury (Fig. 1, E to G, n = 14 fish), revealed that this is a transient expression exhibited specifically by newly regenerating fibers. Embryonic slow MyHC1 expression occurs despite the fact that the injury encompasses a region of the myotome that is mainly composed of fast MyHC-expressing fibers (Fig. 1, E to G, and fig. S1, H to R). Transient embryonic slow MyHC expression, independent of the predominant fiber type of the injured muscle, is also a feature of regenerating fibers in amniote injury models (*17*–*20*). We therefore concluded that muscle injury in zebrafish results in activation of a specific de novo myogenic program.

Stereotypical phases of muscle repair in vivo

Next we induced muscle injuries via laser ablation of muscle fibers in the Tg(*actc1b*:mcherry) and Tg(*myf5*:GFP) double-transgenic line. Laser

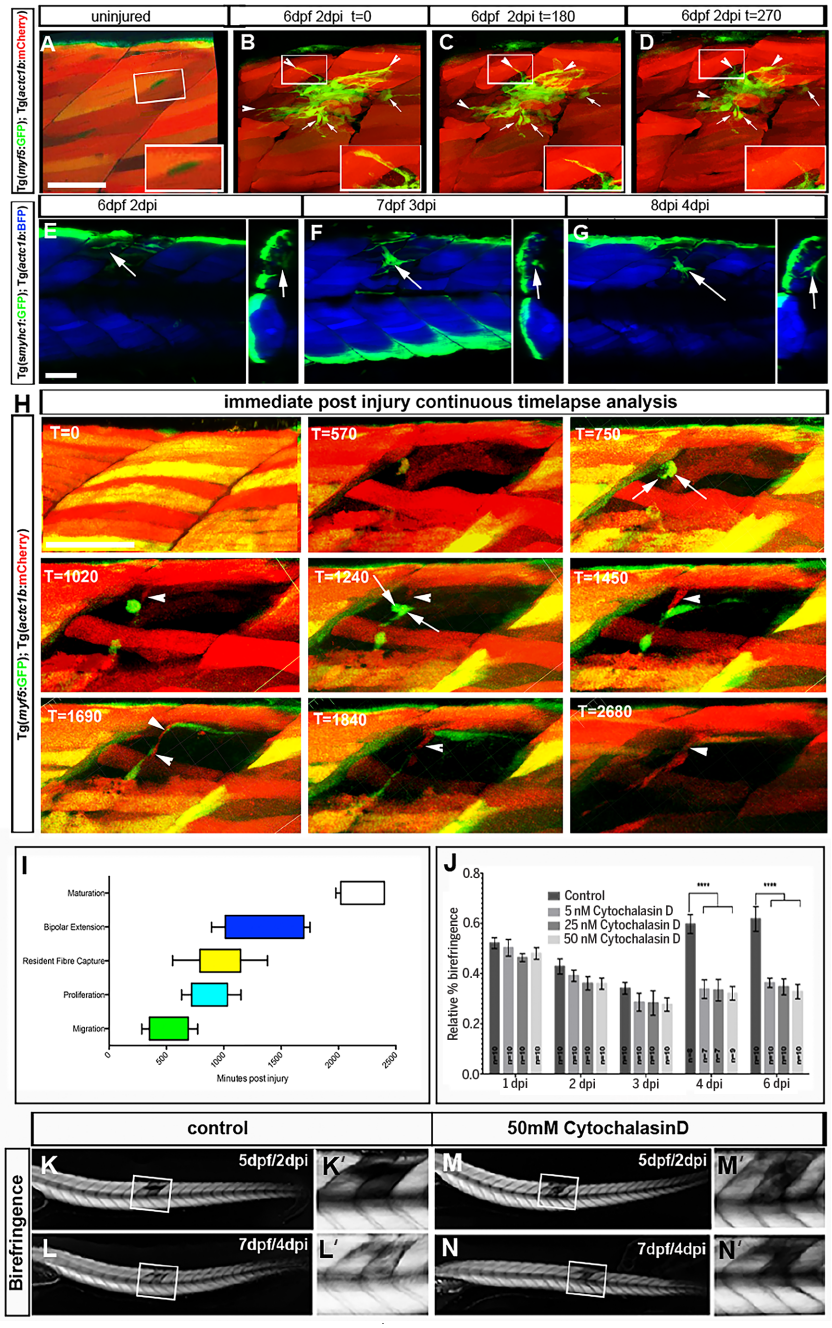

Fig. 1. In toto imaging of muscle regeneration in vivo. (**A** to **D**) Uninjured muscle [Tg(*actc1b*:mCherry), red] contains *myf5*-positive cells [Tg(*myf5*:GFP), green], a subset of which are activated postinjury and exhibit a highly bipolar extended shape [arrowheads in (B) to (D)]. The remainder of the *myf5*-positive cells fail to be activated and do not migrate to the injury (arrows). Representative images taken from n = 12 independent fish. Scale bar, 50 μm. (**E** to **G**) Newly regenerated muscle initially expresses slow MyHC, shown by Tg(*smyhc1*:GFP) (green), despite the injury predominately affecting deeper fast MyHC–expressing muscle [Tg(*actc1b*:BFP), blue]. Representative images taken from n = 14 independent fish. Arrows indicate slow MyHC-expressing fibers in the fast muscle domain. Scale bar, 50 μm. (**H**) Stereotypical phases of muscle regeneration. Maximum intensity projection through Tg(*myf5*:GFP) and Tg(*actcb1*:mCherry) double-transgenic larvae, post–laser wound injury, time-lapsed over 48 hours after injury. Arrows mark cell divisions and arrowheads marks the filopodial extension from the adjacent uninjured muscle. T = time in minutes. Representative images taken from n = 8 independent fish. Scale bar, 50 μm. (**I**) Quantitation of the length of the phases described in (H). (**J** to **N'**) Inhibition of filopodia prevents regeneration. (J) Quantitation of birefringence after needle-stab injury in 3-dpf larvae soaked in a low-concentration range of cytochalasin D, shown to specifically inhibit filopodial extensions in vivo and in vitro. All concentrations inhibit regeneration by 4 dpi; the first time point that a recovery in birefringence is detected in untreated siblings. Error bars indicate mean + SEM. Statistics: t test, two-tailed numbers (n) are indicated at each time point and concentration. ****P < 0.0001. (K to N′) Individual larvae followed over the entire period of regeneration were imaged for birefringence each day. (K to L′) Control untreated siblings recover rapidly form needle-stick injury. (M to N′) Larvae treated with 50 mM cytochalasin D fail to regenerate and reestablish birefringence by 4 dpi. (K′ to N′) High-magnification views of the regions boxed in (K) to (N), respectively.

ablation results in single muscle fibers or small groups of fibers being ablated in a more defined area of injury when compared with the needle-stick injury used above. Regeneration of this laser injury is more rapid and occurs over a 3 days (fig. S1F, $n = 20$ fish). This allows the entire wound to be captured at resolutions that can distinguish individual cells. We were able to capture the entirety of the regenerative process, from the initial injury to the differentiation of replacement muscle cells. This analysis, coupled with those described above, allowed the definition and quantification of specific phases in the regenerative processes (Fig. 1, H and I, and movie S4, $n = 8$ fish).

The initial phase (migration and contact) is characterized by migration of the myf5-positive cell populations into the wound area. Migration of myf5-positive cells is limited to within the injured myotome itself and the neighboring myotomes on either side. Migration to the wound site can occur from any position within these myotomes. However, we never see dorsal-ventral traverse of the horizontal myosepta for discrete wounds within either the epaxial or hypaxial myotomes where the septum remains intact after injury (movies S1 to S7). Once in the wound, cells associate as rounded cells with severed and dying fibers (Fig. 1, H and I, and movie S4, green arrows). In the second phase (proliferation and activation), myf5-positive cells undergo division to generate muscle progenitors (Fig. 1, H and I, and movie S4, cyan arrows), similar to events and behaviors exhibited by myogenic progenitors in early muscle repair in mice (*10*). Quantitation of the total number of proliferative cells confirmed that muscle regeneration was associated with a rapid proliferative burst during the 2 days immediately after injury (fig. S6, A, C, and I, $n = 6$ fish). EdU pulse labeling after needle-stick injury confirmed the proliferative nature of the *myf5*-positive cells detectable within the wound site, in line with our time-lapse observations of laser ablation injuries (fig. S6, F and I, $n = 6$ fish). In the third phase (bipolar-extension and interaction), myf5-positive cells extend to a bipolar shape, increase myf5:GFP expression, and lose contact with the dying cells around them. Bipolar myf5-positive cells in the wound then actively migrate toward each other, extend filopodia to make contact, and then recoil and move rapidly apart (Fig. 1, H and I, and movie S4, blue arrows). Next, resident uninjured differentiated muscle fibers extend filopodial-like membrane protrusions, which adhere and "lasso" around the activated progenitor cells (Fig. 1, H and I, movie S4, yellow arrows, and fig. S4). Filopodia can be observed in every time-lapse analysis of sufficient length that we performed for both types of injury: needle stick and laser ablation ($n = 8$ fish, Fig. 1H, fig. S4). Filopodia are invariably associated with the arrival of the *myf5*-positive cells into the wound site and extend to contact them. The size and nature of the filopodia are dependent on the location and distance between the uninjured muscle at the wound and the position of the *myf5*-positive cells relative to the muscle cell at the wound edge (Fig. 1H, movie S4, and fig. S4). The timing and directionality of the extending filopodia suggest that signals from the migrating and dividing stem and progenitor cells may elicit and guide the filopodia. Consequent filopodial retraction appears to guide the lassoed elongating myocytes to align next to the differentiated muscle fiber from which the contacting filopodia extends (Fig. 1, H and I, and movie S4).

To define the functional role of filopodia in the regenerative process, we inhibited their formation after injury. Low-dose cytochalasin D selectively suppresses filopodia formation by capping actin filament barbed ends while sparing the formation of lamellipodia, another F-actin–dependent membrane extension process (*21*, *22*). Furthermore, cytochalasin D has recently been applied in vivo to specifically inhibit filopodia in developing mouse and zebrafish embryos (*23*, *24*). Using a similar approach, we applied low-dose cytochalasin D to animals injured by needle-stab and assayed regeneration under these conditions. Addition of low-dose cytochalasin D had no overall effect on larval morphology and muscle integrity in uninjured animals (Fig. 1, M to N′, $n = 59$). However, injured animals showed a marked defect in regeneration upon cytochalasin D treatment ($n = 17$, 5 nM; $n = 17$, 25 nM; $n = 19$, 50 nM), which suggests that impeding filopodia formation leads to inhibited regeneration (Fig. 1, J to N′).

After alignment against resident uninjured fibers, myocytes elongate and initiate expression of Tg(*actc1b*:mcherry), signaling the differentiation of the *myf5*-positive progenitor pool into muscle fibers that heralds the end of the final phase (resident fiber capture and differentiation) (Fig. 1, H and I, movie S4, white arrows). Thus, our analyses have determined that muscle regeneration is associated with a series of stereotypical morphogenetic interactions between cells at the wound site and the activated stem cells.

Muscle regeneration is impaired in myogenin *mutants*

Next we examined whether muscle regeneration deployed a genetic program distinct from that required during embryonic myogenesis. In mice, the MRF genes *Myf5* and *MyoD* are individually required to direct regeneration of skeletal muscle (*25*, *26*). Mutations in each of the zebrafish MRF genes (*myf5*, *myoD*, *mrf4*, and *myog*) have been previously generated (*27*, *28*). Using birefringence (fig. S5, B and F, $n = 10$ fish per condition), gene expression, and muscle differentiation markers (fig. S5, C to E, $n = 6$ fish per probe per condition) to systematically monitor regeneration in homozygous mutants, we determined that only homozygous *myogenin* (*myog*^{fh265}) mutants possessed a muscle-repair deficit (fig. S5). Myogenin is required for the differentiation of muscle cells during embryonic amniote myogenesis and is consequently a prenatal lethal mutation in mice (*29*). By contrast, zebrafish *myog* mutants possess no apparent defect in embryonic myogenesis, as *myod* and *myog* act redundantly to coordinate embryonic fast muscle myogenesis (*27*, *28*). Similar numbers of stem cells are present at the wound site initially, with the deficit in repair being accompanied by a subsequent defect in proliferation at the injury (fig. S6, D, E, and H, $n = 6$ fish). To determine more precisely the phase of regeneration that was deficient in *myog* mutants, homozygous *myog*^{fh265} larvae transgenic for both Tg(*myf5*:GFP) and *Tg*(*actc1b*:mCherry) were subjected to laser ablation muscle injury and continuous time-lapse imaging, as described above (Fig. 2A and movie S5, $n = 7$ fish). *myf5*-expressing cells in *myog*^{fh265}-mutant fish migrate effectively to the injury site. However, these cells failed to fully extend and mature to a bipolar shape and were eliminated from the wound site (Fig. 2, A and B, and movie S5), consistent with the marker analyses described above. Specifically, *myog*^{fh265}-mutant fish possessed dying *myf5*-expressing cells only within the injury site (Fig. 2, C to H, $n = 6$ fish), which indicates that *myog* acts as a survival checkpoint for myoblasts involved in muscle repair. This analysis therefore defines a genetically distinct set of *myogenin*-dependent cells that are specifically required for muscle regeneration in zebrafish.

Specific stem cell populations control muscle repair

Although these initial studies reveal that a genetically distinct population of cells contribute to the regenerative process, they do not formally eliminate the possibility that these cells arise through dedifferentiation at the wound site and consequently contribute to muscle regeneration via the de novo myogenesis process described above. To determine whether injured skeletal muscles can undergo dedifferentiation and contribute to repair, we injected the construct *actc1b*:nlsGFP into the Tg(*actc1b*:mCherryCAAX) transgenic fish, which results in mosaic genetically marked myonuclei (green) in a fish with all muscle fiber membranes marked (red) (fig. S7 A′). We performed laser ablation of muscle cells containing these green nuclei and showed that the nuclei of injured muscle fibers are cleared from the site of the wound and subsequently do not play a role in repair via dedifferentiation (fig. S7, A to D′, $n = 6$ fish). To determine whether surrounding uninjured myofibers were capable of dedifferentiating and playing a role in injury repair, we performed needle-stick injuries to fish double-transgenic for Tg(*actc1b*:Cre) and Tg(*ef1a1*:LOXP-eGFP-LOXP-mCherry) (eGFP, enhanced GFP), marking all tissue in the fish as green, except for mature myofibers that expressed *actc1b* (marked as red). Examination of these injured fish reveals that the regenerate consists of green cells early in the repair process, indicating that these cells are not derived from dedifferentiated mature myofibers (fig. S7, E to G, $n = 6$ fish). Together, these results show that skeletal muscle regeneration in zebrafish does not largely occur by dedifferentiation of injured or uninjured muscle cells at the injury site. Skeletal muscle regeneration is therefore fundamentally different from the regeneration of the other striated muscle type, cardiac muscle, which in zebrafish is controlled by the reentry of cardiomyocytes into the cell cycle in response to injury (*30*).

We next looked for a source of potential stem cells within the myotome. Although *myf5* expression

encompasses the broadest temporal phase of an activated stem cell in amniote muscle repair, it occurs extensively throughout all phases of myogenesis and is not a marker specific for the stem cell compartment. We therefore sought to define markers that were specific for muscle stem cells deployed during regeneration. Our analysis revealed that *pax7a*- and *pax3*a-positive cells are evident deep within the myotome, beginning at 4 dpf in a similar location to the *myf5* cells described above (Fig. 3, A to F‴, n = 6 fish). However, these genes are also expressed by cells of the external cell layer (ECL), a progenitor pool for muscle growth located on the superficial surface of the myotome, evident during embryonic and larval periods. Therefore, the expression of these genes is not specific to a muscle stem cell niche (*11*, *12*, *31*, *32*) (Fig. 3, A and D). *cMet* is a marker of quiescent satellite cells in postnatal rodent muscle and is thought to be specifically required for the activation of satellite cells in response to injury (*2*, *33*). In line with its proposed function, *cmet* expression initiates at 4 dpf, later than either *pax3* or *pax7*; is expressed in only a small subset of the deeper cells of the myotome; and is not expressed in the progenitor layer of the ECL (*34*) (Fig. 3, A to F‴, and fig. S8, n = 5 fish). *cmet* is also prominently expressed in nonmuscle progenitor populations, including primary motor neurons and the lateral line nerve (*35*) (Fig. 3, A and D, and fig. S8, H to J). Furthermore, the expression of *cmet* persists into adulthood in a fiber-associated niche (fig. S8, A to G′), similar to that described for the mammalian satellite cell. This observation is consistent with the regenerative capacity of adult zebrafish muscle, as well as data from previous studies of adult fiber isolation in zebrafish (*13*, *31*, *36*). To better characterize these cells in vivo, we generated a bacterial artificial chromosome (BAC) transgenic line that expressed both KALTA4 and mCherry from the *cmet* promoter. This Tg(*cmet*:mCherry-T2A-KALTA4)-modified BAC faithfully recapitulated the expression of the *cmet* gene upon germline transmission (Fig. 3, A to F‴, and fig. S8, A to G′). Furthermore, an antibody against cMet (*36*) colocalizes with mCherry expression in the myotome evident within the *cmet* BAC transgenic line, validating that this line reports endogenous *cmet* expression (Fig. 3 and fig. S8, H to J′). This transgenic line demonstrated a marked increase in *cmet*-positive cell number per myotome section throughout the early development of the fish, leading up to metamorphosis (up to 15 mm in total length), after which this population maintained a stable number throughout postmetamorphic development (15 to 30 mm total length), suggesting a consistent requirement of this cell type within the myotome throughout the life span of the fish (fig. S8, K and L). Using this transgenic line, we established that cmet and pax3a double-positive and cmet and pax7a double-positive cells constituted a minor subset of the interstitial myotomal cells (~15% of non-ECL, myotomal, pax3- or pax7-positive cells) (Fig. 3, A to J, n = 3 per transgenic combination). These cells express a cyclin-dependent kinase inhibitor and therefore probably represent a quiescent population (Fig. 3, K to N‴, n = 8 fish).

Next, we performed in vivo ablation of the aforementioned *cmet* cells to determine whether these cells are required for regeneration in zebrafish. We crossed the Tg(*cmet*:mCherry-T2A-KALTA4) line to Tg(*uas*:E1b:Eco.NfsB-mCherry), which results in the expression of the nitroreductase enzyme specifically within *cmet*-positive cells. Addition of metronidazole (Met) to these embryos ablated *cmet*-positive cells (Fig. 4, A to D, n = 30 fish) and resulted in a failure to initiate regeneration and de novo myogenesis at the wound site (Fig. 4, E to N, n > 20 per treatment and probe). As *cmet* is also expressed within motor neurons, it remained possible that the coablation of neurons with *cmet*-positive muscle stem cells could also directly or indirectly affect the regeneration of muscle cells that they innervate. To control for this possibility, we made use of a previously generated transgenic line, Tg(*cmetMN*:GFP-T2A-KALTA4), which contains only a subset of the *cmet* regulatory regions evident in the full-length BAC clone and expresses KALTA4 and GFP only within the motor neuron expression domain (*35*). Crossing this line to Tg(*uas*:E1b:Eco.NfsB-mCherry)

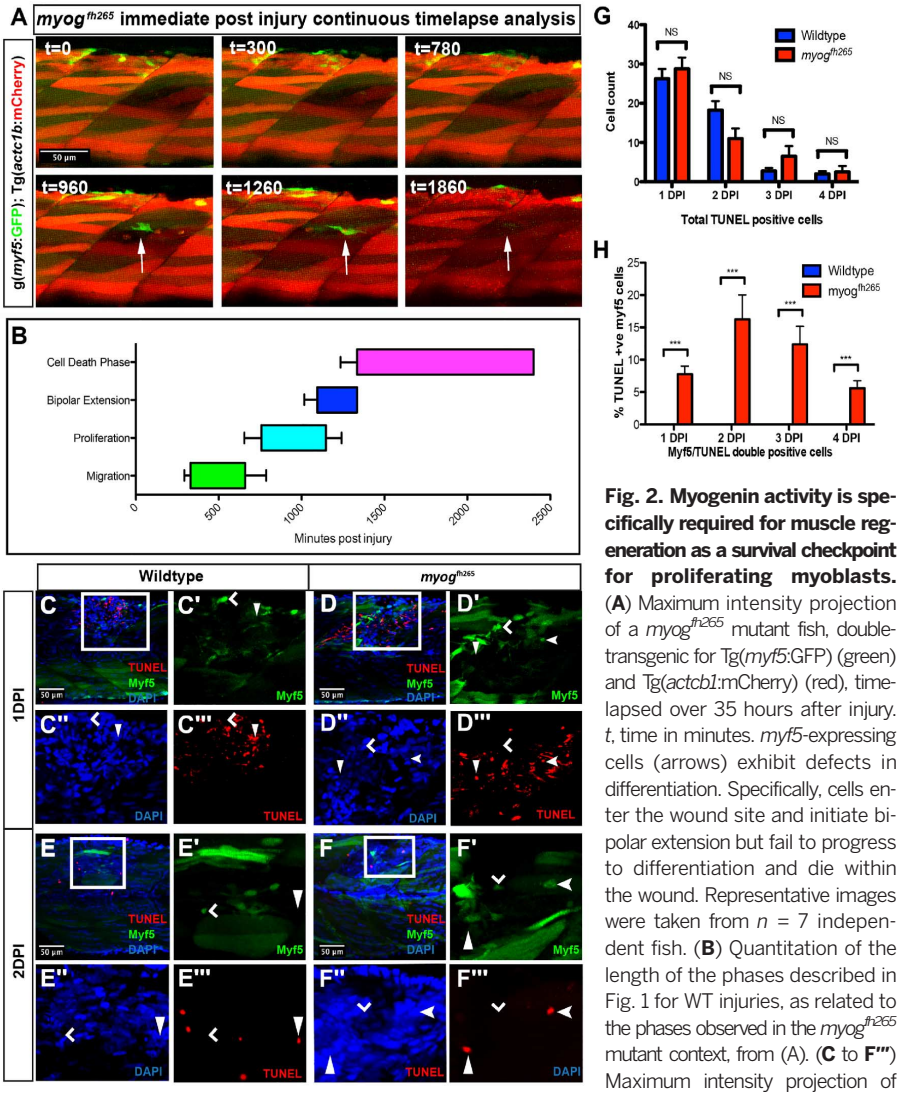

Fig. 2. Myogenin activity is specifically required for muscle regeneration as a survival checkpoint for proliferating myoblasts. (**A**) Maximum intensity projection of a *myog*^{fh265} mutant fish, double-transgenic for Tg(*myf5*:GFP) (green) and Tg(*actcb1*:mCherry) (red), time-lapsed over 35 hours after injury. *t*, time in minutes. *myf5*-expressing cells (arrows) exhibit defects in differentiation. Specifically, cells enter the wound site and initiate bipolar extension but fail to progress to differentiation and die within the wound. Representative images were taken from n = 7 independent fish. (**B**) Quantitation of the length of the phases described in Fig. 1 for WT injuries, as related to the phases observed in the *myog*^{fh265} mutant context, from (A). (**C** to **F‴**) Maximum intensity projection of needle-stick–injured WT and *myog*^{fh265} mutant fish, transgenic for Tg(*myf5*:GFP) (green) and stained with TUNEL (red). *myog*^{fh265} mutant fish possess *myf5*-positive cells that are also positive for TUNEL staining (arrowheads). Examples of non–*myf5*-positive TUNEL-positive cells (triangles) and *myf5*-positive non–TUNEL-positive (open arrowheads) cells are also evident. White boxes denote the specific area of the wound viewed in the subsequent three single-channel images. Representative images taken were from n = 6 independent fish. DAPI, 4′,6-diamidino-2-phenylindole. (**G**) Quantification of the total amount of TUNEL-positive cells. Both WT and mutant fish have comparable levels of TUNEL-positive cells throughout muscle regeneration. Scores shown are means for each measured day post–needle-stick injury (DPI) from n = 6 independent fish per condition (mutant or WT). Error bars indicate mean + SEM. Statistics: *t* test, two-tailed. NS, not significant. (**H**) Quantification of the number of *myf5*-expressing cells costained with TUNEL, expressed as a percentage the total number of *myf5*-positive cells in the wound site. Scores shown are means for each measured day post injury from n = 6 independent fish per condition (mutant or WT). Error bars indicate mean + SEM. Statistics: *t* test, two-tailed. ***P < 0.001.

results in the expression of the nitroreductase enzyme specifically within *cmet*-positive motor neurons. Addition of Met to these embryos resulted in complete ablation of primary motor neurons (Fig. 4, O to P′). In parallel, we also performed ablations in the *cmet* BAC line, which ablates both *cmet*-positive motor neurons and muscle stem cells. To assay the effect of these two different ablation strategies on muscle regeneration, we performed needle-stab injuries on ablated animals and assayed the regenerative capacity of injured larvae. Although the chemical ablations carried out in the BAC transgenic line resulted in defects in muscle regeneration, ablation of cmet-positive motor neurons had no effect on the ability of larvae to regenerate (Fig. 4, Q to U). These studies collectively define *cmet*-positive cells as the functional equivalent of mammalian satellite cells, specifically required for muscle regeneration within the zebrafish myotome.

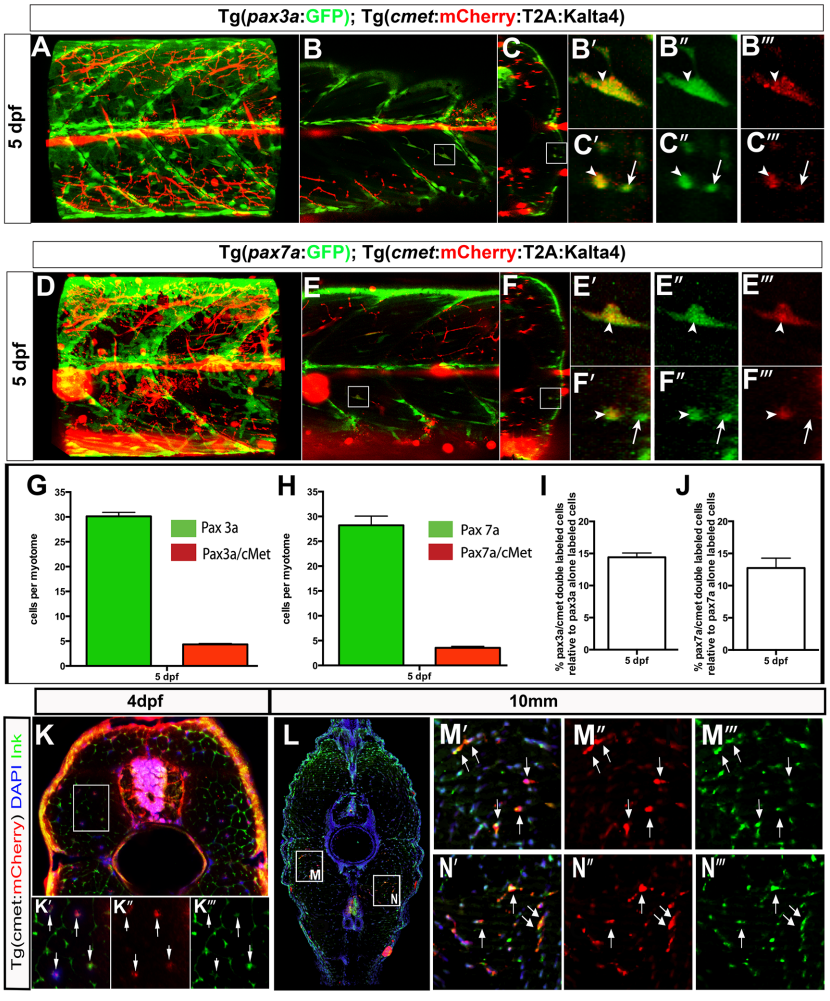

Fig. 3. *cmet* expression specifically marks satellite-like cells required for zebrafish muscle regeneration. (**A**) Maximum-projection confocal images of Tg(*pax3a*:GFP) (green) and Tg(*cmet*:mCherry-T2A-KALTA4) (red) double-transgenic fish. (**B** and **C**) Single confocal sections through the myotome show *pax3a* and *cmet* double-labeled cells [(B) parasagittal, (C) transverse]. (**B′** to **B‴** and **C′** to **C‴**) High-magnification views of regions boxed in (B) and (C), respectively (arrowheads, *pax3a*-high and *cmet*-high double-positive cells; arrows, *pax3a*-high and *cmet*-low–expressing cells). (**D**) Maximum-projection confocal images of Tg(*pax7a*:GFP) (green) and Tg(*cmet*:mCherry-T2A-KALTA4) (red) double-transgenic fish. (**E** and **F**) Single confocal sections through the myotome show *pax7a* and *cmet* double-labeled cells within the myotome [(E) parasagittal, (F) transverse]. (**E′** to **E‴** and **F′** to **F‴**) High-magnification views of regions boxed in (E) and (F), respectively (arrowheads, double-positive cells; arrows, single-positive cells). (**G** and **H**) Quantification of *pax3a*-only versus *pax3a* and *cmet* double-labeled cells (G) or *pax7a*-only versus *pax7a* and *cmet* double-labeled cells (H) per myotome. (**I** and **J**) Quantification of pax3a and cmet double-positive cells as a percentage of total *pax3a*-positive cells (I) or *pax7a* and *cmet* double-positive cells as a percentage of total *pax7a*-positive cells (J). For both pax3a and pax7a, cmet colabels 10 to 15% of the total population. Error bars indicate mean + SEM. (A to F″) Representative images were selected from n = 6 independent fish. (G to J) Numbers are derived from total myotomal counts of three individual larvae per transgene combination. (**K** to **N‴**) Cross section of 4-dpf [(K) to (K‴)] and 10-mm [(L) to (N‴)] Tg(*cmet*:mCherry-T2A-KALTA4) larvae costaining with an antibody against the cyclin-dependent kinase inhibitor ink4b. Arrows highlight colocalizing ink4b nuclear staining that occurs in *cmet*-positive cells (representative images from n = 8 sectioned embryos).

Asymmetric divisions generate clonally restricted progenitors

To examine how the *cmet*-positive cell population is activated during injury, we undertook continuous time-lapse analyses of the *cmet*-positive cells in several transgenic backgrounds that had undergone laser ablation injury. Analyses within injured animals double-transgenic for Tg(*myf5*:GFP) and Tg(*cmet*:mCherry-T2A-KALTA4) revealed that *cmet* and *myf5* double-positive cells are associated with the injury site and appear as doublets within *cmet*-only cells (Fig. 5, A to D, and fig. S9E, n = 6 time-lapse analyses of injured larvae, n = 35 doublets identified). These results suggest that *cmet*-positive cells are activated by injury to divide asymmetrically to produce a *myf5*-positive progenitor population that, in turn, generates the de novo myogenesis evident during muscle regeneration described above. Collectively, our results suggest that the *myf5*-positive cells observed in earlier experiments contained in this paper (Figs. 1H and 2A and movies S4 and S5) are, in fact, *cmet*-low/*myf5*-high daughter cells that are responding to signals from the injury site and from regenerating myofibers. Next, we undertook time-lapse imaging within injured animals double-transgenic for Tg(*pax7a*:GFP) and Tg(*cmet*:mCherry-T2A-KALTA4) to capture the earliest division of cmet-positive cells. *cmet* and *pax7a* double-positive cells migrate to the wound site and proliferate, indicating that cmet marks injury-responding cells during muscle regeneration. Division of activated *cmet* and *pax7a* cells was asymmetric, such that after each division a rounded *cmet*-high–/*pax7a*-low–expressing cell was maintained and a pax7a-high– or cmet-low–expressing progenitor population was created (Fig. 5E, movies S6 and S7, and fig. S9). Individual *cmet*-positive cells were identified that gave rise to multiple cmet-low– and pax7a-high–expressing progeny (n = 6 time lapses of injured larvae, n = 38 doublets identified; fig. S9 and movies S6 and S7). Furthermore, our analyses indicate that pax7 cells are proliferative within the wound site at 2 dpi, suggesting that *cmet*-low/*pax7a*-high cells proliferate, elongate, and undergo differentiation in the manner we have described above (Fig. 5E; movie S6; and fig. S6, D and H). Collectively, these observations suggest that the *cmet*-high/*pax7a*-low cells evident within our time-lapse analyses represent a regeneration-specific stem cell compartment that divides asymmetrically to self-renew the stem cell compartment and produce proliferative daughters cells required to effect regeneration.

In vitro studies have suggested that satellite cells divide in an apical-basal fashion relative to the plane of the muscle fiber, a process that subsequently dictates the fate of daughter cells (*5*). More recent analyses have defined a role for the dystrophin-associated glycoprotein complex in the control of this process whereby dystrophin localization

within the stem cell niche interacts with the PAR complex to regulate asymmetric division of the satellite cell (*37*). To determine whether a similar mechanism could control asymmetric division seen in our in vivo model, we used a gene-trap line driving the citrine fluorophore under the native dystrophin locus, Gt(*dmd*-citrine) (*38*), in combination with our Tg(*cmet*:mCherry-T2A-KALTA4) line. Examination of quiescent satellite cells showed us that dystrophin is specifically expressed on *cmet*-positive cells and is localized asymmetrically, but this asymmetry appears random relative to muscle fiber orientation (fig. S8, M to N‴), which suggests that the initial asymmetric cell divisions of the activated stem cell would likewise be in multiple orientations. This suggests that local "micro niches" could provide specific extracellular matrix cues that dictate the localization and polarity of the stem cell divisions initially.

Given the low number of these cells evident in the larval myotome (~15% of *pax7a*- or *pax3a*-positive cells in the myotome; Fig. 3, I and J), the asymmetric model of stem cell division indicates that a finite number of regeneration-specific stem cells, represented by *cmet* expression, are activated after injury, and that these cells would generate a limited set of clonally related lineages to effect repair. Clonality can also be predicted from several of the current models of satellite cell action in amniote muscle repair that propose the existence of a small subset of satellite cells with true stem cells properties (*7*–*9*, *14*). Specifically, the asymmetric model suggests that particular satellite

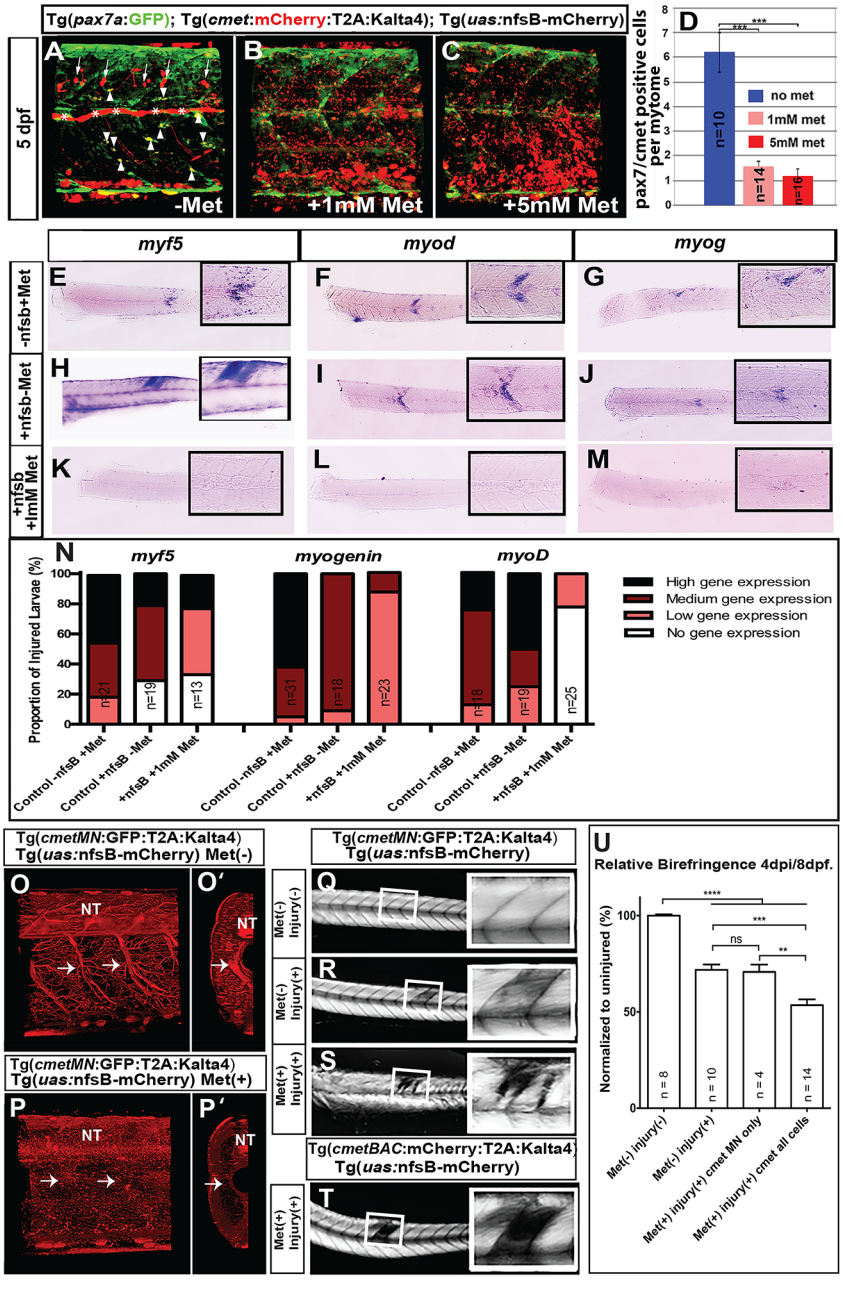

Fig. 4. *cmet*-positive cells are required for regeneration. (**A** to **C**) Maximum-projection confocal images of larvae transgenic for Tg(*pax7a*:GFP); Tg(*cmet*:KALTA4-T2A-mCherry); Tg(*uas*:E1b:Eco.NfsB-mCherry), which results in the expression of the nitroreductase enzyme specifically within *cmet*-positive cells. Addition of the prodrug metronidazole (Met) to these triple-transgenic larvae [(B) and (C)] results in ablation of *cmet*-expressing cells [arrowheads in (A)] but does not affect myoblasts expressing *pax7a* alone. The images from the *cmet* ablation are quantified in (**D**), indicating that 1 mM of Met is sufficient to induce significant reduction in *cmet*-positive cell numbers. mCherry-positive cellular debris collects superficially in metronidazole-treated larvae [(B) and (C)], which results not only from myoblast cell death but also degradation of the lateral line [asterisks in (A)] and motor neurons [arrows mark cell bodies in (A)], which also express *cmet*. The appearance of this mCherry-positive cellular debris is used as a positive control to show that the ablation has worked efficiently. Error bars in (D) indicate mean + SEM. ***$P < 0.001$. (**E** to **N**) Ablation of *cmet*-positive cells through metronidazole addition [(K) to (M)] results in a failure to initiate de novo myogenesis, which is indicated as failure to initiate the expression of myogenic regulatory factor gene expression at the wound site. Such a failure does not occur in control animals that have not received metronidazole [-Met, (H) to (J)] or those larvae that do receive metronidazole (+Met) but do not carry the Tg(*uas*:E1b:Eco.NfsB-mCherry) transgene and therefore do not express nitroreductase (-nfsb) [(E) to (G)]. Representative images of $n > 20$ animals per treatment group and probe. Insets show high-magnification views. (N) Quantitation of myogenic gene expression of ablated and nonablated larvae. Larvae were placed into arbitrary bins of expression (high, medium, low, or none), examples of which are shown in (E) to (M). (**O** to **U**) Ablation of *cmet*-positive motor neurons inhibits regeneration. (O) Transgenic line Tg(*cmetMN*:GFP-T2A-KALTA4) containing a subset of the *cmet*-regulatory regions evident in the full-length BAC clone expresses KALTA4 only within the motor neuron–expression domain. Crossing this line to Tg(*uas*:E1b:Eco.NfsB-mCherry) results in the expression of the nitroreductase enzyme (red) specifically within *cmet*-positive motor neurons. (**P**) Addition of Met to these embryos results in complete ablation of primary motor axons (positions marked by arrows) and their arbors, leaving only nonspecific mCherry cellular debris after ablation. NT, neural tube. (Q to U) Larval muscle regeneration is not impaired in motor neuron–ablated animals [+Met +injury, (S)] and is identical to injured nonablated controls [-Met +injury, (R)]. By contrast, ablation of both motor neurons and *cmet*-positive muscle stem cells in the *cmet* BAC transgenic line impairs regeneration (+Met +injury). (Q to T) Representative images of larvae under indicated conditions imaged for birefringence under polarized light. (U) Quantitation of birefringence levels relative to uninjured controls reveals that motor neuron–ablated larvae regenerate similarly to nonablated controls. However, ablation of both motor neurons and *cmet*-positive muscle stem cells in the cmet BAC transgenic line results in significantly lower birefringence, which points to impairment of muscle regeneration. Error bars indicate mean + SEM. Statistics: *t* test, two-tailed. ****$P < 0.0001$; ***$P < 0.001$; **$P < 0.01$.

cells maintain the ability to return to quiescence via asymmetric DNA segregation followed by differential gene expression, cell cycle entry, and metabolic status. Thus, this model indicates that all myogenic cells generated during repair would be clonally related to rare "stem" satellite cells (*7*–*9*, *14*). However, this clonal model of stem cell action lacks in vivo validation. To provide evidence for this mode of satellite cell action and validate our own observations, we crossed the Tg(*cmet*:mcherry-T2A-KALTA4) line with the ubiquitously expressed Tg(*ubi*:zebrabow) line (Fig. 5, F to H, n = 22 fish) (*39*). These double-transgenic embryos were further injected with a UAS:CreERT2 construct, which is responsive to the KALTA4 promoter. We then performed needle-stick injuries on these animals. Two outcomes were possible from this experiment. If *cmet* expression simply reflects a progenitor phase of muscle proliferation, then Cre-activated deletion in *cmet*-positive cells would result in multiple deletions within independently proliferating cells and, hence, a wide range of distinct zebrabow rearrangements leading to many different colored myoblast lineages. However, if *cmet* expression denotes a stem population that generates a clonally related progenitor compartment, Cre-mediated deletion would generate rearrangements within a limited number of stem cells. In turn, these stem cells would generate the bulk of proliferating myoblasts in the regenerate, with progeny of individual zebrabow-recombined stem cells all expressing an identical color upon differentiation into muscle cells. Upon needle-stick injury of the Tg(*cmet*:mcherry-T2A-KALTA4), Tg(*ubi*:zebrabow) double-transgenic line into which UAS:CreERT2 was injected, only a very few distinct colors are evident that cluster in homogeneously expressed and regionally localized clones of myoblasts and muscle cells produced during regeneration (Fig. 5, F to H, n = 22 fish). This result indicates that the *cmet*-positive cells represent the injury-responsive clonal stem cell compartment of the zebrafish myotome (fig. S10J).

To more broadly assay the clonal nature of muscle regeneration, independent of the *cmet* stem cell compartment, we performed needle-stick muscle injuries in animals that were doubly transgenic for Tg(*ubi*:zebrabow) and Tg(*msgn1*:CreERT2). The addition of tamoxifen to these fish during embryogenesis results in zebrabow rearrangements in all cells derived from the somites, as the *mesogenin* (*msgn1*) promoter is somite-specific (*40*). Because the somite is the embryonic compartment from which all muscle stem and progenitor cells derive, this combination of transgenes enables the generation of a "musclebow" fish, allowing the clonal relationships of muscle cells to be assessed (Fig. 5, J to Q; fig. S10, A to I, n = 13 fish; and movie S8) (*39*). Tamoxifen addition to uninjured embryos early during embryogenesis results in the labeling of muscle fibers within the embryo and reveals random deletions of the zebrabow array, leading to individual fibers expressing unique combinations of fluorophores (Fig. 5, I to M; fig. S10, A to I; and movies S8 and S10, n = 13 fish). No bias in any specific zebrabow deletion is detected by this analysis, with individual fibers displaying random spectral values upon differentiation (Fig. 5, I to M; fig. S10, A to I; and movies S8 and S10). Therefore, injury in these animals allows for global assay of the number of somite-derived lineages that contribute to zebrafish muscle regeneration. To statistically evaluate the clonal nature of regeneration, we manually determined the hue (radians) and saturation (percentage) values for each fiber and plotted them such that each coordinate represents the color identity of a particular fiber. We then calculated the distances between all coordinates to provide a statistically evaluated measure of clonality (Fig. 5I; see methods for computational methodology). Our analysis indicated that, in stark contrast to muscle fibers that result from growth, regenerated muscle fibers are highly clonal, as a limited numbers of recombined fluorescent phenotypes contribute to regeneration, consistent with a stem cell origin for these cells (Fig. 5, N to Q; fig. S10, A′ to I′; and movies S9 and S10). However, multiple clones, contributing individual single clonally restricted lineages, can contribute to regeneration of larger wounds, eliminating the possibility that a single clonal lineage marked early in development generates all satellite cells in zebrafish (e.g., fig. S10, E, E′, I, and I′). Furthermore, our analysis confirmed that the stem cells that contribute to regeneration derive from the somite, as these cells exhibit a recombined fluorescent phenotype generated from the expression of the somite-specific meosgenin Cre line. Collectively, our analyses, combined with previously published results (*7*–*9*, *14*), indicate that vertebrate muscle regeneration results from the activation of limited set of somite-derived stem cells that generate a clonally restricted proliferative myoblast population, which in turn differentiates to effect muscle repair.

Conclusion

We analyzed the morphological, cellular, and genetic basis for muscle regeneration in zebraish. Using transgenes that mark muscle stem and progenitor cells, in combination with long-term imaging modalities, we imaged the entire process of regeneration, from the initial injury to the formation of newly differentiated muscle fibers at the wound site in a vertebrate. We show that a stem cell niche equivalent to the mammalian satellite cell system operates within the zebrafish myotome. This observation suggests that the satellite cell is part of an evolutionary ancient stem cell system that is present throughout the vertebrate phylogeny and may well be a basal feature of gnathostomes.

Our time-lapse analyses enabled us to characterize a number of stereotypical phases of repair involving specific cell cohorts (Fig. 6 and fig. S10J). Although many of these morphogenetic events are canonical ones, in terms of known stem cell–driven regenerative processes (activation, proliferation of a progenitor population, and differentiation), the dynamic nature of the morphogenetic changes of both the activated stem cell and the proliferating progenitor population is surprising. Although migration of activated satellite cells on fibers has been documented in vitro (*41*), there has been no indication from such paradigms that the migration of activated muscle stem cells would deploy such a polarized phenotype. The polarized shape that *myf5*-positive cells adopt to migrate to the site of injury is therefore suggestive of a novel directional migratory mode. A recent examination of the role of activated pax7-positive cells during in vivo muscle repair in the mouse revealed similar polarized phenotypes for activated migrating murine myogenic cells (*10*), indicating the potential relevance of our observation to mammalian muscle biology. Due to current limitations of examining this process in vivo, little other information exists as to the mechanism used by migrating activated satellite cells to track to the wound site in amniotes. These limitations are largely overcome by use of the zebrafish larval system.

Furthermore, the interplay between the proliferating myogenic cells that enter the wound site with injured fibers in the initial contact phase of regeneration and secondarily with the undamaged remaining fibers at the injury site was also unexpected. A lack of information is available about how the injury site itself acts to direct the architecture and behavior of the regenerating fibers during skeletal muscle regeneration, as existing studies have almost exclusively focused on the factors that influence the stem cell compartment. However, the importance of the wound environment has been emphasized in recent in vivo investigations performed during early muscle repair in the mouse, which showed that myogenic progenitors at the injury site use the extracellular matrix left from dead and damaged muscle fibers to provide orientation cues for cell division and alignment (*10*). In this regard, the "lassoing" event that appears to guide differentiating cells at the wound by the surrounding uninjured fibers was an extension of these observations. It suggests that instead of being passive bystanders in the regenerative process, uninjured fibers themselves may play a role in directing differentiating progenitors to regions of the wound that are most in need of new fiber addition. It also suggests that the kinetics of repair at the wound, and even aspects of myocyte differentiation, may partly be dictated by the nature and availability of intact fibers to participate in this process.

Using the *cmet* and *pax7* transgenes as markers of the stem cell population, we have been able to examine activated cells immediately after injury by continuous time-lapse analyses. Our analyses detected the existence of two clonally related sets of cells during regeneration: a *cmet*-high/*pax7*-low stem cell population and a *pax7*-high/*cmet*-low progenitor population. Time-lapse analyses revealed that the *cmet*-high population divided asymmetrically to generate the differentiation-competent cmet-low population, as well as a *cmet*-high cell that maintained the ability of producing both *cmet*-low proliferative daughter cells and a self-renewing *cmet*-high undifferentiated stem cell. Previous analyses of murine single-fiber explants have suggested that the plane of division of a satellite cell, relative to the underlying basal lamina, dictates the fate of individual satellite cell daughters (*5*). Specifically, division of a satellite

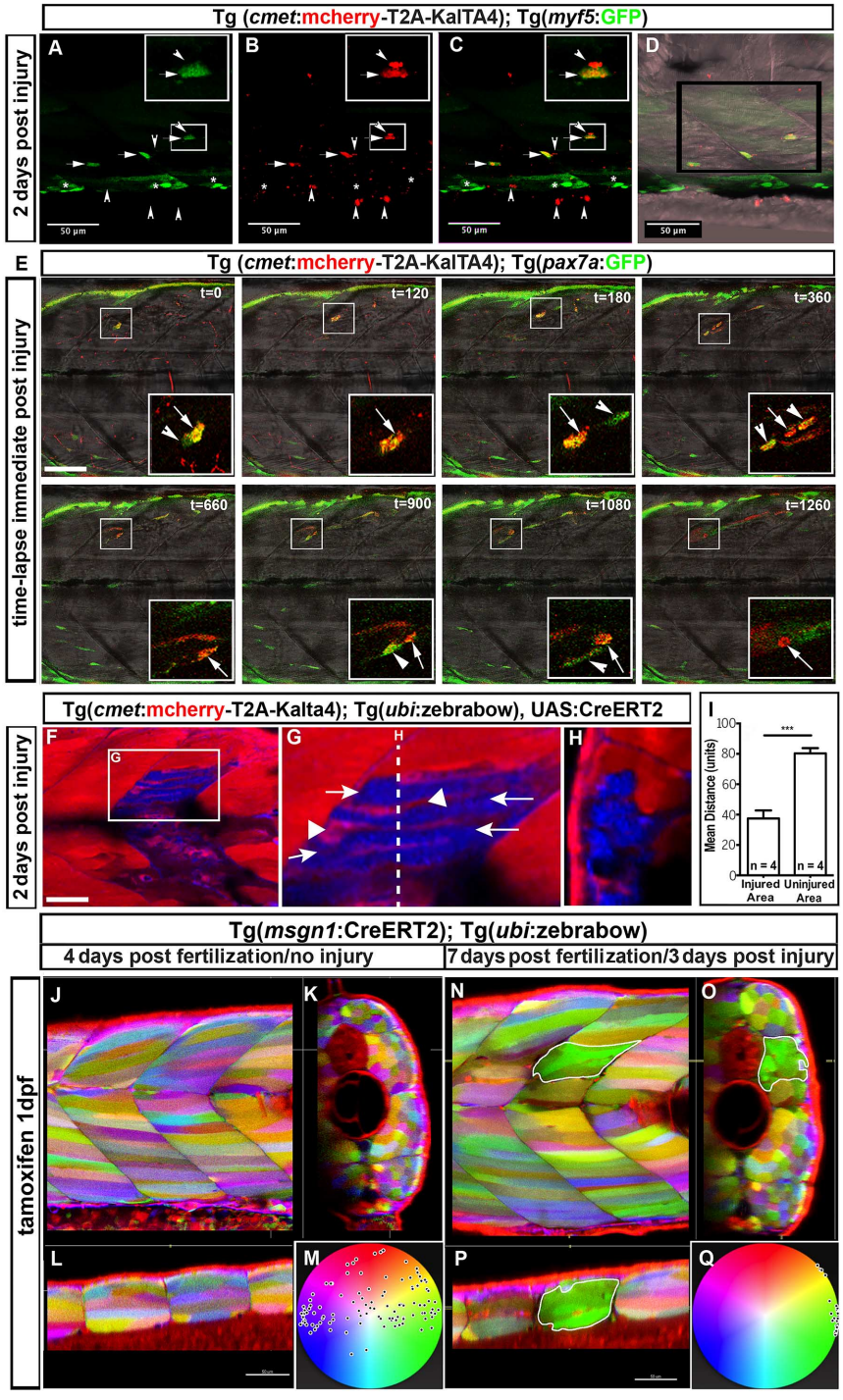

Fig. 5. Zebrafish satellite-like cells represent a lineage-restricted injury-responsive stem cell that undergoes asymmetric division during regeneration. (**A** to **D**) Maximum-intensity-projection confocal images of Tg(*myf5*:GFP) (green) and Tg(*cmet*:mCherry-T2A-KALTA4) (red) double-transgenic fish 2 days after needle injury. Double-positive cells (arrows), cells with Tg(*myf5*:GFP) alone (asterisks), and cells with Tg(*cmet*:mCherry-T2A-KALTA4) alone (arrowheads) are marked. Insets reveal the existence of cells with Tg(*cmet*:mCherry-T2A-KALTA4) alone and double-positive doublet cells associated with the injury site, illustrated in the region framed in the combined differential interference contrast image in (D). Representative images were taken from $n = 6$ independent fish. (**E**) Asymmetric division generates a *cmet*-high/*pax7*-low stem cell compartment and a *cmet*-low/*pax7*-high differentiation-competent progenitor population after laser ablation injury. Continuous confocal time-lapse imaging of 4-dpf larvae immediately after laser injury shows cells transgenic for Tg(*cmet*:mCherry-T2A-KALTA4) (red) and Tg(*pax7a*:GFP) (green), as well as those imaged in the brightfield channel (insets without brightfield). A single *cmet*-high/*pax7*-low cell (arrow) maintains *cmet* expression through several rounds of division that generate *cmet*-low/*pax7*-high cells (arrowheads), which subsequently elongate and differentiate. Time (t) is given in minutes. Scale bar, 50 µm. (**F** to **H**) Needle-stick injury of larvae transgenic for Tg(*ubi*:zebrabow) and Tg(*cmet*:mCherry-T2A-KALTA4) injected with a UAS:CreERT2 DNA construct. Tamoxifen addition results in limited recombination events generating a highly restricted set of colors in regenerating fibers and myoblasts. Red is the default expression color that appears in every cell; the expression of any other fluorophore represents a specific recombination. Only two regenerating lineages are evident: one from a recombination of the zebrabow cassette that generates "blue" fibers [marked by arrows in (G)] and myoblasts and a second that generates "pink" fibers [marked by arrowheads in (G)] and myoblasts. (G) High-magnification view of the region boxed in (F). (H) Cross section at the level marked in (G). Representative images are from $n = 14$ imaged larvae. Scale bar in (F), 50 µM. (**I** to **Q**) Injured larvae transgenic for Tg(*msgn1*:CreERT2) and Tg(*ubi*:zebrabow), to which tamoxifen addition results in clonal labeling of all somite-derived cells. (I) Quantitation of the clonality of muscle regeneration. To statistically evaluate the clonal nature of regeneration, the hue (radians) and saturation (percentage) values were manually determined for each fiber and plotted such that each coordinate represents the color identity of a particular fiber. Distances between all coordinates were then calculated to provide a statistically evaluated measure of clonality. Error bars indicate mean + SEM. Statistics: *t* test, two-tailed. ***$P < 0.001$. (J to M) Confocal sections through an uninjured larvae at 4 dpf, revealing the specific differentiated muscle fibers clonally marked by individual zebrabow rearrangements. (N to Q) The same larvae as in (J) to (M) (at 3 dpi and 7 dpf), revealing that regenerating fibers all express the same zebrabow green rearrangement (regenerated fibers bounded by white line), which indicates that regenerating fibers are clonally related and derive from a single stem cell {sagittal [(J) and (N)], coronal [(L) and (P)], and transverse [(K) and (O)] sections at the levels indicated}. Scale bars, 50 µm. Representative images were taken from $n = 13$ independent fish. (M and Q) Plotted spectral values (dots) of individual fibers from the same larvae within uninjured (M) and regenerated (Q) muscle, revealing the comparative clonality of regenerating fibers after injury.

cell in the apical-basal plane relative to the muscle fiber generates an apically positioned, differentiation-competent progenitor and a basally located self-renewing stem cell. A more recent imaging study of in vivo mouse muscle repair has suggested that activated myogenic progenitors at the wound site divide in a planar fashion, although this study was unable to assay the process of satellite cell activation (*10*). Although the highly migratory nature of the activated satellite cells in vivo precludes a definitive assignment of relative polarity of division, our observations suggest

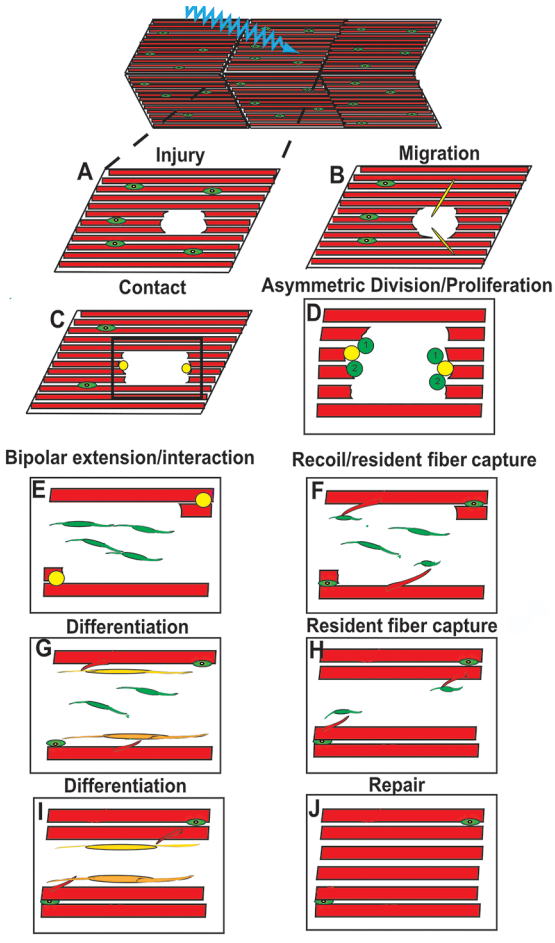

Fig. 6. A model for in vivo muscle regeneration. (**A** to **J**) In vivo repair of muscle from a defined stem population occurs through a number of stereotypical phases. The initial phase (migration and contact) is characterized by migration of the satellite-like cell populations into the wound area. Once in the wound, cells immediately associate as rounded cells with severed and dying fibers and remain in contact for several hours. In the second phase (proliferation and activation), activated stem cells undergo an asymmetric division to generate the proliferating compartment that undergoes further division. In the next phase (bipolar extension and interaction), proliferating cells extend to a bipolar shape and lose contact with the dying cells around them. Bipolar cells in the wound then actively migrate toward each other, extend filopodia to make contact, and then recoil and move rapidly apart from one another. Next, resident uninjured differentiated muscle cells extend filopodial-like membrane protrusions, which adhere and lasso the activated cells. Filopodial retraction guides the captured cell to align next to the differentiated muscle cell from which the filopodia extends. Cells then elongate and differentiate into muscle fibers, marking the end of the final phase (resident fiber capture and differentiation). Within 7 days, muscle fiber repair is complete, and the injury site is indistinguishable from surrounding uninjured fibers.

that the initial division of activated satellite cells probably occurs in a random polarity with respect to the plane of the muscle fiber in zebrafish. Furthermore, the clonality of regeneration we observe in response to muscle injury is a major finding of this work. Clonality is a direct prediction of the self-renewing immortal stem cell hypothesis generated from seminal in vitro observations (*5*–*9*), and our work provides direct in vivo validation of this hypothesis. We conclude that asymmetric divisions occur during muscle regeneration to generate the clonally related progenitors required for muscle repair, resolving a long-term debate surrounding the existence of this mechanism of stem cell self-renewal and muscle repair in vivo.

Materials and methods

Zebrafish strains and maintenance

Wild-type (WT) and transgenic lines Tg(-80.0*myf5*:eGFP) [referred to as Tg(*myf5*:GFP)] (*42*), Tg(*actc1b*:mCherry) (*43*), Tg(*actc1b*:BFP) (*43*), Tg(*actc1b*:mCherryCAAX) (*44*) ,Tg(*smyhc1*:GFP) (*45*), TgBAC (*pax7a*:GFP) [referred to as Tg(*pax7*:GFP)] (*12*), TgBAC(*pax3a*:GFP) [referred to as Tg(*pax3*:GFP)] (*12*), Tg(*ubi*:zebrabow) (*39*), Tg(*msgn1*:CreERT2) (*40*), Tg(UAS:nsfB-mCherry) (*46*), Tg(*cmetMN*:GFP-T2A-KALTA4) (*34*), Gt(dmd-citrine)^{ct90a} [(referred to as Gt(*dmd*-citrine)] (*38*), Tg(*actc1b*:Cre), and Tg(*ef1a1*:LOXP-eGFP-LOXP-mCherry) were maintained on TE WT background. Staging and husbandry were performed as previously described (*47*). A new transgenic line produced by microinjection into TE WT fish according to standard procedures (*48*) and used in this study is TgBAC_CH211-105D03(*cmet*:mCherry-T2A-KALTA4) [hereafter referred to as Tg(*cmet*:mCherry-T2A-KALTA4)], a BAC construct. Mutant strains used were *myf5*^{hu2022} (*28*), *myf6*^{hu2041} (*28*), *myog*^{fh265} (*27*), and *myod*^{hu2024} (*49*), all maintained on AB background. These mutants were genotyped by sequencing of polymerase chain reaction products amplified from fin clip or embryo genomic DNA using primers 5′-CATATAAGAAGGGCCGTATG-3′ and 5′-ATGCAGAGCTTCACTGTAGG-3′ for *myf5*, 5′-AAATGTTTAACTGTTATGCAAAG-3′ and 5′-TGTCGTTAAAGGTCGGATTC-3′ for *myod*, 5′-AGCGCTGGATAGAATTTCAC-3′ and 5′-CTGTGCGCAGAGTCAAAG-3′ for *myf6*, and 5′-AGG-CTCTGAAGAGGAGCACA-3′ and 5′-GTC-AGAAATAAAGCTGTCACTGAG-3′ for *myog*.

Gateway cloning and mosaic transgenesis

Gateway cloning was performed using the Gateway Tol2kit to create transgenic constructs, according to standard Invitrogen protocols (*50*). The *UAS*:CreERT2 and *actc1b*:nlsGFP constructs were created using the Gateway method. To generate mosaically transgenic zebrafish, individual plasmid DNA–containing constructs flanked by tol2 sites were delivered by microinjection into embryos at the single-cell stage, directly into the cell. The plasmid DNA concentration was typically at 25 ng/μl. The Tg(*actc1b*:Cre) and Tg(*ef1a1*:LOXP-eGFP-LOXP-mCherry) transgenic fish were generated from constructs also made using the Gateway method. To generate stable transgenic zebrafish, a mixture of mRNA-encoding tol2 recombinase and a DNA plasmid containing a construct flanked by tol2 sites was delivered by microinjection directly into the cell at the one-cell stage of development. mRNA was delivered at 20 ng/μl and the DNA construct at 25 ng/μl.

Needle-stick injury

For needle-stick injury induction, tricaine-anaesthetized 4-dpf larval zebrafish were placed on a 24.5 mm–by–76.2 mm glass slide in a drop of water and maneuvered into a lateral lying position with their heads pointing toward the left. A single needle-stick injury into the dorsal epaxial musculature above the cloaca was performed at an angle of 75°, using a 30-gauge needle. Subsequently, fish were immediately transferred to fresh embryo water (E3) to recover. The ventral side of the fish relative to the site of injury was used as an uninjured internal control.

Laser injury

For laser-induced injury, tricaine-anaesthetized 4-dpf larval zebrafish were placed in grooves on a specialized silicon block, similar to the one used for microinjection of embryos, mounted in a petri dish. A thin layer of low–melting point agarose [0.5% weight/volume agarose in E3 (Invitrogen)], maintained in a molten state at 36°C, was applied to each fish. As soon as the low–melting point agarose was set, the petri dish was filled with E3 containing tricaine to maintain the anaesthetized state throughout the injury procedure and for subsequent time-lapse photomicroscopy. A Micropoint laser connected to a Zeiss Axioplan microscope was used for injuring, as previously described (*51*), with a 40X water immersion objective and a laser pulse at a wavelength of 435 nm for cell ablation. Time-lapse recordings were generated on a Zeiss LSM 710 Live Duo confocal microscope (Carl Zeiss Microimaging).

Metronidazole ablation experiments

Cell ablation using this system was performed as previously described (*52*), with some modifications. Briefly, the prodrug metronidazole (Sigma) was dissolved in E3 water as a 5 or 1 mM working solution, as indicated, along with added 0.2% dimethyl sulfoxide and 0.003% 1-phenyl-2-thiourea in 10% Hank's saline (PTU). Transgenic zebrafish were incubated in this solution immediately after injury (4 dpf) at 28.5°C, solutions were changed every day, and fish were euthanized and fixed at 7 dpf for whole-mount in situ hybridization (WISH). Control fish were

subjected to the same injury and treatment procedure without metronidazole.

WISH and immunohistochemistry

In situ mRNA hybridization and immunohistochemistry were performed as previously described (*31*). The digoxigenin-tagged probes used were *pax7a* (*53*), *cmet* (*31*), *myf5* (*54*), *mrf4* (*55*), and *myod* and *myog* (*56*). Analyses of expression levels after in situ hybridization involved randomly mounting stained embryos, which were blinded to treatment group. Larvae were photographed and scored into arbitrary bins of "none," "low," "medium," and "high," on the basis of the experimental spread of expression. Images representative of the overall phenotype were then presented in the data. Primary antibodies used were rabbit anti-GFP [1:500 (Invitrogen)], mouse anti-Pax7 [1:10 (Developmental Studies Hybridoma Bank, DSHB)], mouse F59 anti–slow myosin heavy chain [1:10 (DSHB)], and rabbit anti-phospho-histone-H3 [1:1000 (Sigma)]. The p16 INK antibody (1:4) (*57*) probably recognizes proteins that are produced from a single locus ancestral to mammalian CDKN2A and -2B, as only a single syntenic gene is present in zebrafish. Hence, this antibody could recognize a range of potential cyclin inhibitors. Secondary antibodies used include goat anti-rabbit Alexa Fluor 488 [1:1000 (Invitrogen)], goat anti-rabbit Alexa Fluor 568 [1:1000 (Invitrogen)], goat anti-mouse Alexa Fluor 488 [1:1000 (Invitrogen)], goat anti-mouse Alexa Fluor 568 [1:1000, (Invitrogen)].

EdU labeling

Cell proliferation was determined by 5-ethynyl-2′-deoxyuridine EdU labeling according to established conditions (*58*), using 7 mM EdU (Invitrogen) dissolved in E3 medium. Briefly, larval fish were incubated for a 48-hour block before fixation. Fish were euthanized, fixed, and subsequently processed using the Click-iT EdU Imaging Kit (Invitrogen). This processing occurred after antibody staining, using the Click-iT solution.

TUNEL staining

Cell apoptosis was determined by terminal deoxynucleotidyl transferase–mediated deoxyuridine triphosphate biotin nick end labeling (TUNEL) staining, performed on whole larvae as previously described (*52*), with some modifications. To stain for apoptosis, a TMR Red In Situ Cell Detection Kit (Roche) was used according to manufacturer's specifications. Samples were incubated in stain solution in the dark for 2 hours at 37°C before processing and observation by fluorescence and confocal microscopy.

Birefringence imaging

Birefringence is the property of intact muscle tissue to diffract polarized light (damaged muscle tissue lacks this quality). Birefringence was measured as previously described (*59*). Briefly, anaesthetized zebrafish were placed on the Leica DMIRB (Leica Microsystems) microscope stage in a glass-bottom FluoroDish (World Precision Instruments). The exposure levels of the attached polarizing filters were automatically adjusted by the integrated Abrio Software [CRI (Hinds Instruments)], and the resulting final picture shows an averaged polarizing effect. The resultant birefringence images were analyzed for birefringence densitometry over the required area using the software FIJI.

Zebrabow analyses

Tamoxifen treatments were conducted as previously described for the Tg(*ubi*:zebrabow), Tg(*msgn1*:CreERT2) double-transgenic larvae (*40*). At 4 dpf, the fish were imaged and subsequently injured by needle stick. At 7 dpf, fish were reimaged at the injury site. Optical transverse cross sections were then generated from confocal stacks with Imaris (Bitplane), and color profiles of regenerated fibers at the injured site were measured in Photoshop (Adobe) as previously described (*39*). For clonal analysis, images were processed as described in (*39*), with modifications. Images were opened in Photoshop CS5.1, and the eyedropper tool (sample size set at 5 by 5 pixels) was used to measure the fiber of interest. Color display mode was set to hue saturation brightness, and the hue and saturation values in the color window were manually recorded. Hue (radians) and saturation (percentage) values were converted into x-y coordinates to be plotted on a Cartesian graph using basic trigonometry (hue, degrees; saturation, hypotenuse; adjacent or opposite side, point of interest). Each coordinate represented the color identity of a particular fiber. Distances between all clones were then calculated with following formula:

$$\text{Distance} = \sqrt{(x_1-x_2)^2 + (y_1-y_2)^2}.$$

Distance values were then imported into Prism software to conduct a Student's t test. For the Tg(*cmet*:mCherry-T2A-KALTA4); (*UAS*:CreERT2); Tg(*ubi*:zebrabow) transgenic larvae, tamoxifen was added at 4 dpf, immediately before injury, and samples were incubated postinjury for a further 8 hours before washing into embryo media.

REFERENCES AND NOTES

1. P. Seale *et al*., Pax7 is required for the specification of myogenic satellite cells. *Cell* **102**, 777–786 (2000). doi: 10.1016/S0092-8674(00)00066-0; pmid: 11030621
2. D. D. Cornelison, B. J. Wold, Single-cell analysis of regulatory gene expression in quiescent and activated mouse skeletal muscle satellite cells. *Dev. Biol.* **191**, 270–283 (1997). doi: 10.1006/dbio.1997.8721; pmid: 9398440
3. C. Lepper, T. A. Partridge, C. M. Fan, An absolute requirement for Pax7-positive satellite cells in acute injury-induced skeletal muscle regeneration. *Development* **138**, 3639–3646 (2011). doi: 10.1242/dev.067595; pmid: 21828092
4. C. A. Collins *et al*., Stem cell function, self-renewal, and behavioral heterogeneity of cells from the adult muscle satellite cell niche. *Cell* **122**, 289–301 (2005). doi: 10.1016/j.cell.2005.05.010; pmid: 16051152
5. S. Kuang, K. Kuroda, F. Le Grand, M. A. Rudnicki, Asymmetric self-renewal and commitment of satellite stem cells in muscle. *Cell* **129**, 999–1010 (2007). doi: 10.1016/j.cell.2007.03.044; pmid: 17540178
6. I. M. Conboy, T. A. Rando, The regulation of Notch signaling controls satellite cell activation and cell fate determination in postnatal myogenesis. *Dev. Cell* **3**, 397–409 (2002). doi: 10.1016/S1534-5807(02)00254-X; pmid: 12361602
7. V. Shinin, B. Gayraud-Morel, D. Gomès, S. Tajbakhsh, Asymmetric division and cosegregation of template DNA strands in adult muscle satellite cells. *Nat. Cell Biol.* **8**, 677–687 (2006). doi: 10.1038/ncb1425; pmid: 16799552
8. P. Rocheteau, B. Gayraud-Morel, I. Siegl-Cachedenier, M. A. Blasco, S. Tajbakhsh, A subpopulation of adult skeletal muscle stem cells retains all template DNA strands after cell division. *Cell* **148**, 112–125 (2012). doi: 10.1016/j.cell.2011.11.049; pmid: 22265406
9. A. Troy *et al*., Coordination of satellite cell activation and self-renewal by Par-complex-dependent asymmetric activation of p38α/β MAPK. *Cell Stem Cell* **11**, 541–553 (2012). doi: 10.1016/j.stem.2012.05.025; pmid: 23040480
10. M. T. Webster, U. Manor, J. Lippincott-Schwartz, C. M. Fan, Intravital imaging reveals ghost fibers as architectural units guiding myogenic progenitors during regeneration. *Cell Stem Cell* **18**, 243–252 (2016). doi: 10.1016/j.stem.2015.11.005; pmid: 26686466
11. S. Knappe, P. S. Zammit, R. D. Knight, A population of Pax7-expressing muscle progenitor cells show differential responses to muscle injury dependent on developmental stage and injury extent. *Front. Aging Neurosci.* **7**, 161 (2015). pmid: 26379543
12. C. Seger *et al*., Analysis of Pax7 expressing myogenic cells in zebrafish muscle development, injury, and models of disease. *Dev. Dyn.* **240**, 2440–2451 (2011). doi: 10.1002/dvdy.22745; pmid: 21954137
13. A. Rowlerson, G. Radaelli, F. Mascarello, A. Veggetti, Regeneration of skeletal muscle in two teleost fish: *Sparus aurata* and *Brachydanio rerio*. *Cell Tissue Res.* **289**, 311–322 (1997). doi: 10.1007/s004410050878; pmid: 9211834
14. D. Montarras, A. L'honoré, M. Buckingham, Lying low but ready for action: The quiescent muscle satellite cell. *FEBS J.* **280**, 4036–4050 (2013). doi: 10.1111/febs.12372; pmid: 23735050
15. R. J. Bryson-Richardson *et al*., Myosin heavy chain expression in zebrafish and slow muscle composition. *Dev. Dyn.* **233**, 1018–1022 (2005). doi: 10.1002/dvdy.20380; pmid: 15830374
16. S. H. Devoto, E. Melançon, J. S. Eisen, M. Westerfield, Identification of separate slow and fast muscle precursor cells in vivo, prior to somite formation. *Development* **122**, 3371–3380 (1996). pmid: 8951054
17. R. Matsuda, D. H. Spector, R. C. Strohman, Regenerating adult chicken skeletal muscle and satellite cell cultures express embryonic patterns of myosin and tropomyosin isoforms. *Dev. Biol.* **100**, 478–488 (1983). doi: 10.1016/0012-1606(83)90240-3; pmid: 6653881
18. U. Carraro, L. Dalla Libera, C. Catani, Myosin light and heavy chains in muscle regenerating in absence of the nerve: Transient appearance of the embryonic light chain. *Exp. Neurol.* **79**, 106–117 (1983). doi: 10.1016/0014-4886(83)90382-5; pmid: 6822248
19. S. Sartore, L. Gorza, S. Schiaffino, Fetal myosin heavy chains in regenerating muscle. *Nature* **298**, 294–296 (1982). doi: 10.1038/298294a0; pmid: 7045696
20. S. Schiaffino, A. C. Rossi, V. Smerdu, L. A. Leinwand, C. Reggiani, Developmental myosins: Expression patterns and functional significance. *Skelet. Muscle* **5**, 22 (2015). doi: 10.1186/s13395-015-0046-6; pmid: 26180627
21. D. T. Burnette, A. W. Schaefer, L. Ji, G. Danuser, P. Forscher, Filopodial actin bundles are not necessary for microtubule advance into the peripheral domain of *Aplysia* neuronal growth cones. *Nat. Cell Biol.* **9**, 1360–1369 (2007). doi: 10.1038/ncb1655; pmid: 18026092
22. E. W. Dent *et al*., Filopodia are required for cortical neurite initiation. *Nat. Cell Biol.* **9**, 1347–1359 (2007). doi: 10.1038/ncb1654; pmid: 18026093
23. J. C. Fierro-González, M. D. White, J. C. Silva, N. Plachta, Cadherin-dependent filopodia control preimplantation embryo compaction. *Nat. Cell Biol.* **15**, 1424–1433 (2013). doi: 10.1038/ncb2875; pmid: 24270889
24. E. Stanganello *et al*., Filopodia-based Wnt transport during vertebrate tissue patterning. *Nat. Commun.* **6**, 5846 (2015). doi: 10.1038/ncomms6846; pmid: 25556612
25. L. A. Megeney, B. Kablar, K. Garrett, J. E. Anderson, M. A. Rudnicki, MyoD is required for myogenic stem cell function in adult skeletal muscle. *Genes Dev.* **10**, 1173–1183 (1996). doi: 10.1101/gad.10.10.1173; pmid: 8675005
26. B. Gayraud-Morel *et al*., A role for the myogenic determination gene Myf5 in adult regenerative myogenesis. *Dev. Biol.* **312**, 13–28 (2007). doi: 10.1016/j.ydbio.2007.08.059; pmid: 17961534
27. Y. Hinits *et al*., Defective cranial skeletal development, larval lethality and haploinsufficiency in Myod mutant zebrafish. *Dev. Biol.* **358**, 102–112 (2011). doi: 10.1016/j.ydbio.2011.07.015; pmid: 21798255
28. Y. Hinits, D. P. Osborn, S. M. Hughes, Differential requirements for myogenic regulatory factors distinguish medial and lateral somitic, cranial and fin muscle fibre populations. *Development*

136, 403–414 (2009). doi: 10.1242/dev.028019; pmid: 19141670
29. P. Hasty *et al*., Muscle deficiency and neonatal death in mice with a targeted mutation in the *myogenin* gene. *Nature* **364**, 501–506 (1993). doi: 10.1038/364501a0; pmid: 8393145
30. K. Kikuchi *et al*., Primary contribution to zebrafish heart regeneration by *gata4*$^{+}$ cardiomyocytes. *Nature* **464**, 601–605 (2010). doi: 10.1038/nature08804; pmid: 20336144
31. G. E. Hollway *et al*., Whole-somite rotation generates muscle progenitor cell compartments in the developing zebrafish embryo. *Dev. Cell* **12**, 207–219 (2007). doi: 10.1016/j.devcel.2007.01.001; pmid: 17276339
32. F. Stellabotte, B. Dobbs-McAuliffe, D. A. Fernández, X. Feng, S. H. Devoto, Dynamic somite cell rearrangements lead to distinct waves of myotome growth. *Development* **134**, 1253–1257 (2007). doi: 10.1242/dev.000067; pmid: 17314134
33. M. T. Webster, C. M. Fan, c-MET regulates myoblast motility and myocyte fusion during adult skeletal muscle regeneration. *PLOS ONE* **8**, e81757 (2013). doi: 10.1371/journal.pone.0081757; pmid: 24260586
34. L. Haines *et al*., Met and Hgf signaling controls hypaxial muscle and lateral line development in the zebrafish. *Development* **131**, 4857–4869 (2004). doi: 10.1242/dev.01374; pmid: 15342468
35. T. E. Hall *et al*., The zebrafish *candyfloss* mutant implicates extracellular matrix adhesion failure in laminin α2-deficient congenital muscular dystrophy. *Proc. Natl. Acad. Sci. U.S.A.* **104**, 7092–7097 (2007). doi: 10.1073/pnas.0700942104; pmid: 17438294
36. H. Zhang, J. E. Anderson, Satellite cell activation and populations on single muscle-fiber cultures from adult zebrafish (*Danio rerio*). *J. Exp. Biol.* **217**, 1910–1917 (2014). doi: 10.1242/jeb.102210; pmid: 24577448
37. N. A. Dumont *et al*., Dystrophin expression in muscle stem cells regulates their polarity and asymmetric division. *Nat. Med.* **21**, 1455–1463 (2015). doi: 10.1038/nm.3990; pmid: 26569381
38. F. Ruf-Zamojski, V. Trivedi, S. E. Fraser, L. A. Trinh, Spatio-temporal differences in dystrophin dynamics at mRNA and protein levels revealed by a novel FlipTrap line. *PLOS ONE* **10**, e0128944 (2015). doi: 10.1371/journal.pone.0128944; pmid: 26083378
39. Y. A. Pan *et al*., Zebrabow: Multispectral cell labeling for cell tracing and lineage analysis in zebrafish. *Development* **140**, 2835–2846 (2013). doi: 10.1242/dev.094631; pmid: 23757414
40. P. D. Nguyen *et al*., Haematopoietic stem cell induction by somite-derived endothelial cells controlled by meox1. *Nature* **512**, 314–318 (2014). doi: 10.1038/nature13678; pmid: 25119043
41. A. L. Siegel, K. Atchison, K. E. Fisher, G. E. Davis, D. D. Cornelison, 3D timelapse analysis of muscle satellite cell motility. *Stem Cells* **27**, 2527–2538 (2009). doi: 10.1002/stem.178; pmid: 19609936
42. Y. H. Chen *et al*., Multiple upstream modules regulate zebrafish myf5 expression. *BMC Dev. Biol.* **7**, 1 (2007). doi: 10.1186/1471-213X-7-1; pmid: 17199897
43. N. J. Cole *et al*., Development and evolution of the muscles of the pelvic fin. *PLOS Biol.* **9**, e1001168 (2011). doi: 10.1371/journal.pbio.1001168; pmid: 21990962
44. J. Berger *et al*., Loss of Tropomodulin4 in the zebrafish mutant *träge* causes cytoplasmic rod formation and muscle weakness reminiscent of nemaline myopathy. *Dis. Model. Mech.* **7**, 1407–1415 (2014). doi: 10.1242/dmm.017376; pmid: 25288681
45. S. Elworthy, M. Hargrave, R. Knight, K. Mebus, P. W. Ingham, Expression of multiple slow myosin heavy chain genes reveals a diversity of zebrafish slow twitch muscle fibres with differing requirements for Hedgehog and Prdm1 activity. *Development* **135**, 2115–2126 (2008). doi: 10.1242/dev.015719; pmid: 18480160
46. H. Pisharath, J. M. Rhee, M. A. Swanson, S. D. Leach, M. J. Parsons, Targeted ablation of beta cells in the embryonic zebrafish pancreas using *E. coli* nitroreductase. *Mech. Dev.* **124**, 218–229 (2007). doi: 10.1016/j.mod.2006.11.005; pmid: 17223324
47. M. Westerfield, *The Zebrafish Book. A Guide for the Laboratory Use of Zebrafish (Danio rerio)* (Univ. of Oregen Press, ed. 3, 1995).
48. H. Kikuta, K. Kawakami, Transient and stable transgenesis using tol2 transposon vectors. *Methods Mol. Biol.* **546**, 69–84 (2009). doi: 10.1007/978-1-60327-977-2_5; pmid: 19378098
49. E. Busch-Nentwich *et al*., "Sanger Institute Zebrafish Mutation Resource targeted knock-out mutants phenotype and image data submission," ZFIN Direct Data Submission (Sanger Institute Zebrafish Mutation Resource, MPI Dresden, and Hubrecht laboratory, 2010).
50. K. M. Kwan *et al*., The Tol2kit: A multisite gateway-based construction kit for Tol2 transposon transgenesis constructs. *Dev. Dyn.* **236**, 3088–3099 (2007). doi: 10.1002/dvdy.21343; pmid: 17937395
51. C. Otten, S. Abdelilah-Seyfried, Laser-inflicted injury of zebrafish embryonic skeletal muscle. *J. Vis. Exp.* **71**, e4351 (2013). pmid: 23407156
52. H. Pisharath, M. J. Parsons, Nitroreductase-mediated cell ablation in transgenic zebrafish embryos. *Methods Mol. Biol.* **546**, 133–143 (2009). doi: 10.1007/978-1-60327-977-2_9; pmid: 19378102
53. H. C. Seo, B. O. Saetre, B. Håvik, S. Ellingsen, A. Fjose, The zebrafish *Pax3* and *Pax7* homologues are highly conserved, encode multiple isoforms and show dynamic segment-like expression in the developing brain. *Mech. Dev.* **70**, 49–63 (1998). doi: 10.1016/S0925-4773(97)00175-5; pmid: 9510024
54. J. A. Groves, C. L. Hammond, S. M. Hughes, Fgf8 drives myogenic progression of a novel lateral fast muscle fibre population in zebrafish. *Development* **132**, 4211–4222 (2005). doi: 10.1242/dev.01958; pmid: 16120642
55. Y. Hinits, D. P. S. Osborn, J. J. Carvajal, P. W. J. Rigby, S. M. Hughes, *Mrf4* (*myf6*) is dynamically expressed in differentiated zebrafish skeletal muscle. *Gene Expr. Patterns* **7**, 738–745 (2007). doi: 10.1016/j.modgep.2007.06.003; pmid: 17638597
56. E. S. Weinberg *et al*., Developmental regulation of zebrafish MyoD in wild-type, no tail and spadetail embryos. *Development* **122**, 271–280 (1996). pmid: 8565839
57. P. Chapouton *et al*., Notch activity levels control the balance between quiescence and recruitment of adult neural stem cells. *J. Neurosci.* **30**, 7961–7974 (2010). doi: 10.1523/JNEUROSCI.6170-09.2010; pmid: 20534844
58. M. Delous *et al*., Sox9b is a key regulator of pancreaticobiliary ductal system development. *PLOS Genet.* **8**, e1002754 (2012). doi: 10.1371/journal.pgen.1002754; pmid: 22719264
59. J. Berger, T. Sztal, P. D. Currie, Quantification of birefringence readily measures the level of muscle damage in zebrafish. *Biochem. Biophys. Res. Commun.* **423**, 785–788 (2012). doi: 10.1016/j.bbrc.2012.06.040; pmid: 22713473

ACKNOWLEDGMENTS

We thank P. Ingham, A. Schier, G. Lieschke, L. Bally-Cuif, and the Zebrafish International Resource Center for the supply of fish strains and reagents; R. Cheney for technical advice; N. Cole for technical assistance; and C. Marcelle and T. Rando for comments on the manuscript. This work was supported by a National Health and Medical Research Council of Australia grant to P.D.C. The Australian Regenerative Medicine Institute is supported by funds from the state government of Victoria and the Australian federal government. *cmet* transgenic lines are available from P.D.C. under a material transfer agreement with Monash University.

SUPPLEMENTARY MATERIALS

www.sciencemag.org/content/353/6295/aad9969/suppl/DC1
Figs. S1 to S10
References
Movies S1 to S10

8 December 2015; accepted 10 May 2016
Published online 19 May 2016
10.1126/science.aad9969

Asymmetric division of clonal muscle stem cells coordinates muscle regeneration in vivo
David B. Gurevich, Phong Dang Nguyen, Ashley L. Siegel, Ophelia V. Ehrlich, Carmen Sonntag, Jennifer M. N. Phan, Silke Berger, Dhanushika Ratnayake, Lucy Hersey, Joachim Berger, Heather Verkade, Thomas E. Hall and Peter D. Currie (May 19, 2016)
Science **353** (6295), . [doi: 10.1126/science.aad9969] originally published online May 19, 2016

Editor's Summary

Dividing asymmetrically to fix muscle

Resident tissue stem cells called satellite cells repair muscle after injury. However, how satellite cells operate inside living tissue is unclear. Gurevich *et al.* exploited the optical clarity of zebrafish larvae and used a series of genetic approaches to study muscle injury. After injury, satellite cells divide asymmetrically to generate a progenitor pool for muscle replacement and at the same time "self-renew" the satellite stem cell. This results in regeneration that is highly clonal in nature, validating many decades of in vitro analyses examining the regenerative capacity of skeletal muscle.

Science, this issue p. 136

Science (print ISSN 0036-8075; online ISSN 1095-9203) is published weekly, except the last week in December, by the American Association for the Advancement of Science, 1200 New York Avenue NW, Washington, DC 20005.

REPORTS

MICROPOROUS NETWORKS

A metal-organic framework–based splitter for separating propylene from propane

A. Cadiau,[1]* K. Adil,[1]* P. M. Bhatt,[1] Y. Belmabkhout,[1] M. Eddaoudi[1,2]†

The chemical industry is dependent on the olefin/paraffin separation, which is mainly accomplished by using energy-intensive processes. We report the use of reticular chemistry for the fabrication of a chemically stable fluorinated metal-organic framework (MOF) material (NbOFFIVE-1-Ni, also referred to as KAUST-7). The bridging of Ni(II)-pyrazine square-grid layers with $(NbOF_5)^{2-}$ pillars afforded the construction of a three-dimensional MOF, enclosing a periodic array of fluoride anions in contracted square-shaped channels. The judiciously selected bulkier $(NbOF_5)^{2-}$ caused the looked-for hindrance of the previously free-rotating pyrazine moieties, delimiting the pore system and dictating the pore aperture size and its maximum opening. The restricted MOF window resulted in the selective molecular exclusion of propane from propylene at atmospheric pressure, as evidenced through multiple cyclic mixed-gas adsorption and calorimetric studies.

Olefin/paraffin separation is a critical separation for the chemical industry. It is mainly accomplished by means of cryogenic distillation, which accounts for nearly 3% [120 tera–British thermal units (TBtu)/year] of the total energy used for separations (*1*). Exploratory olefin/paraffin separation studies that used conventional adsorbents such as zeolites and ultramicroporous carbon revealed the lack of a suitable adsorbent with the appropriate pore system (functionality and/or aperture size) that could selectively discriminate and separate the two relevant vapors with a noticeably reduced energy footprint (*2*).

Propylene is a prime olefin raw material for petrochemical production, second in importance to ethylene, and is an essential building block for the manufacturing of various chemicals, including polypropylene (*3*). Propylene purity guides its end use because polypropylene requires a high-purity propylene with 99.5 weight % (wt %) minimum (polymer-grade specifications), whereas chemical-grade specifications typically involve a propylene purity of 92% or more. The purity of propylene primarily depends on the removal of propane; this separation process is energy-intensive and conventionally dominated by the cryogenic distillation because of the close-boiling points and the slight variance in the condensabilities of the two components. Researchers have been exploring various separation methods, including (i) the π complexation–driven separation (as adsorbent or facilitated membrane) (*4*, *5*) or (ii) separation based on kinetics by using physical adsorbents (zeolites A) or membranes, driven mainly by the difference in diffusion rates into the pore system (*6*, *7*). Thus far, adsorbents and membranes reported for this task used a partial size-shape sieving–based separation process and displayed low to moderate separation factors, as exemplified in the case of zeolites (*8*, *9*) and carbon molecular sieves (*7*) encompassing contracted pore sizes. The full extraction of propylene from propane by using adsorbent-based separating agents has yet to be demonstrated and accomplished. This is due to (i) the close structural dimensions of propylene and propane molecules, in addition to their associated similar physical properties, and (ii) difficulties in fine-tuning the pore aperture size in 0.2 to 1 Å scale increments in a given ultramicropore adsorbent material with a suitable pore system size ranging between 3 and 5 to 6 Å.

Ideally, porous materials constructed by means of the molecular building block approach offer potential to attain the requisite separation through selective molecular exclusion, in which the molecular building blocks could be adopted in shape, size, and functionality so as to produce a suitable pore aperture size that can selectively separate molecules with almost identical physical properties. We recently succeeded in selectively separating branched paraffins from normal paraffins by fine-tuning a metal-organic framework (MOF) aperture size to completely exclude branched paraffins (*10*).

MOF materials represent a tunable class of hybrid solid-state materials that consist of metal nodes or metal clusters coordinated to multifunctional organic linkers (*11*–*13*). MOFs have received considerable attention as adsorbents for gas storage applications (*14*–*17*) and have demonstrated high potential for equilibrium- and/or kinetic-based gas separations, such as CO_2/N_2 or CO_2/H_2 (*18*–*22*). MOF chemistry has permitted the prospective fabrication of porous materials with a high degree of structural predictability and subsequently a precise control of window apertures size and shape at the molecular level, in contrast to those of zeolites, carbon, and polymeric-based materials (*10*).

We demonstrate a full molecular exclusion of propane from propylene at standard ambient temperature and pressure using a fluorinated porous MOF adsorbent, KAUST-7. The reticular chemistry (*23*) approach was used to construct this material based on pillared square-grids strategy—two-dimensional nets based on linked metal nodes that are pillared via a specific inorganic molecular building block in the third dimension so as to form a three-periodic net with a primitive cubic topology (Fig. 1).

Previously, we applied coordination chemistry principles to demonstrate that the introduction of specific cations—Zn^{2+}, Ni^{2+}, and Cu^{2+}—into the metal-pyrazine square-grid layers has an impact on the unit cell volume and more precisely on the pore size, which resulted in an enhancement of the CO_2-framework energy interaction. This family of materials possesses distinct CO_2 capture properties, especially at very low concentrations, which is ideal for postcombustion capture and air-capture application (*24*). Nevertheless, the SIFSIX-3-Ni (Fig. 1, C and E) was found to adsorb both propylene and propane.

Substitution of the metal node in the SIFSIX (*24*) platform permitted the fine-tuning of the aperture size and pore contraction and subsequent CO_2 capture properties. In order to explore the possibility of further tuning this platform, we closely examined the structural features of the SIFSIX platform (Figs. 1 and 2) (*24*) and identified an alternative pathway to potentially further fine-tune the pore aperture size. The hindered free rotation of the pyrazine-bridging ligands, by altering the nature, shape, and dimensions of the pillars used, dictates the pore aperture size and its maximum opening. This approach offers the potential to select for the passing or blocking of specific probe molecules.

To construct the targeted material with these envisioned structural features, we opted to maintain the Ni(II) as a six-connected node, connecting the pyrazine ligands in square grid–like layers, and to modify the inorganic pillars. We anticipated that using a pillar with a bigger cation (Nb^{5+} instead of Si^{4+}) would result in a relatively shorter proximal distance between the adjacent fluorine centers and consequently contract the aperture size of the channels (Fig. 2). Reactions between

[1]Division of Physical Sciences and Engineering, Advanced Membranes and Porous Materials Center, Functional Materials Design, Discovery and Development Research Group (FMD[3]), King Abdullah University of Science and Technology (KAUST), Thuwal 23955-6900, Kingdom of Saudi Arabia. [2]Department of Chemistry, University of South Florida, 4202 East Fowler Avenue, Tampa, FL 33620, USA.
*These authors contributed equally to this work. †Corresponding author. Email: mohamed.eddaoudi@kaust.edu.sa

$Ni(NO_3)_2$•$6H_2O$, Nb_2O_5, HF_{aq}, and pyrazine (pyr) in water yielded purple square-shaped crystals. The single-crystal x-ray diffraction data revealed the anticipated primitive-cubic structure, formulated as $NiNbOF_5(pyr)_2$•$2H_2O$, in good agreement with the elemental analysis and the thermal gravimetric analysis (TGA) results (supplementary materials, materials and methods, and fig. S6). The phase purity of resultant fluorinated MOF material, referred to as NbOFFIVE-1-Ni or KAUST-7, was confirmed by using a full pattern matching by means of the Le Bail method (fig. S1).

The assignment of fluorine atoms in equatorial positions within the pillar has been previously demonstrated in similar materials (*25*, *26*). The particular use of $(NbOF_5)^{2-}$ as the pillaring inorganic building block, instead of $(SiF_6)^{2-}$, resulted in a longer metal-fluorine distance (1.95 Å) and a subsequent tilting of pyrazine molecules (Figs. 1 and 2) (*19*, *24*). Analysis of the NbOFFIVE-1-Ni structure (collected at 100 K) revealed the plausible smallest pore window opening associated with the relatively hindered rotation of the $(NbOF_5)^{2-}$ pillars, reinforced by the presence of hydrogen bond interactions (Fig. 2 and fig. S3). As a result, the hydrogen atoms of the pyrazine linkers circumference the resultant square-shaped channels with a reduced pore aperture size of 3.0471(1) Å [versus 5.032(1) Å for SIFSIX-3-Ni] (Fig. 1B), prohibiting the diffusion of any molecule other than water (numbers in parentheses indicate the 1 SD uncertainty in the final digits). In order to gain a better insight on the plausible rotation and tilting of the pyrazine linker, and subsequently derive a relative maximum opening of the window, providing a gate limit for the largest molecule to pass through, we collected and analyzed the same structure at room temperature. No structural differences were detected from single-crystal x-ray data collected at room temperature and the cryogenic temperature. The thermal ellipsoids analysis revealed a certain degree of rotation of $(NbOF_5)^{2-}$ pillars, whereas the pyrazine molecules were crytallographically well localized. The $(NbOF_5)^{2-}$ pillars and pyrazine molecules were interconnected through a network of strong hydrogen bonding interactions [F–H 2.483(1) Å]. The noticeably small pore aperture size, derived from the crystal structure at room temperature, suggests that the passing of the propylene molecules is governed by the plausible gate opening associated with the extra tilting of the pyrazine molecules under propylene gas stimuli. The pore aperture size is regulated by the presence or omission of the steric hindrance between pyrazine molecules and $(NbOF_5)^{2-}$ pillars, and the lack of a precise kinetic diameter for propylene in the open literature makes precise quantification difficult. Presumably, the plausible complete omission of the occurring steric hindrance can afford a theoretical maximum pore aperture size of 4.752(1) Å (Fig. 1D).

To further confirm the restricted pore size opening owing to the hindered rotation of pyrazine ligands at low temperature, we performed adsorption studies on the fully evacuated NbOFFIVE-1-Ni. As anticipated, NbOFFIVE-1-Ni did not adsorb N_2 at 77 K, indicating the restricted access to N_2 at this low cryogenic temperature due to the contracted pore aperture size. On the other hand, adsorption studies performed at room temperature by using CO_2 as the adsorbate molecule revealed that NbOFFIVE-1-Ni is microporous,

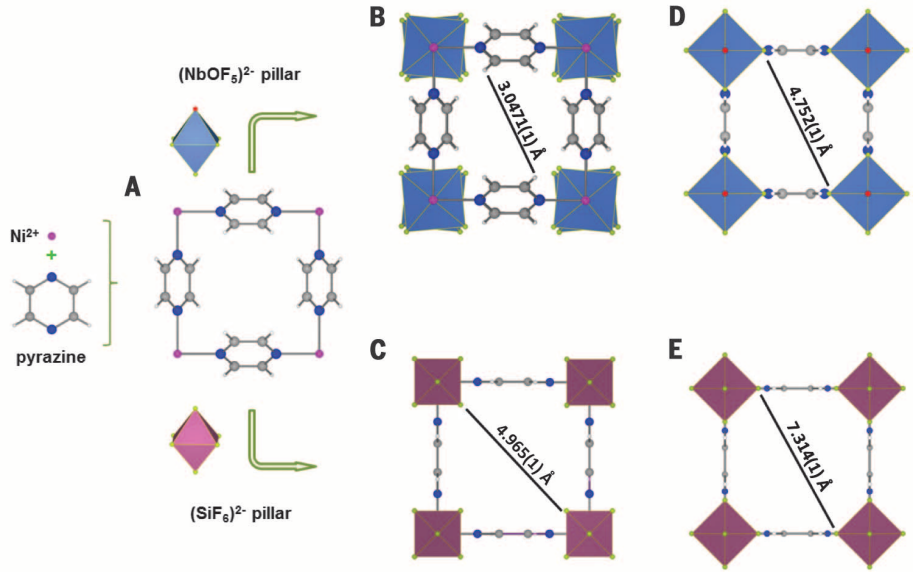

Fig. 1. Structure description of NbOFFIVE-1-Ni highlighting the building blocks arrangement and its comparison with the parent SIFSIX-3-Ni. (**A**) Illustration of the square-shaped arrangement in the Ni-pyrazine (4,4′) square grid that is further pillared by inorganic blocks [$(NbOF_5)^{2-}$ or $(SiF_6)^{2-}$] to generate a three-dimensional MOF with a primitive cubic topology. (**B**) Crystal structure of NbOFFIVE-1-Ni at 100 K, showing the titling of pyrazine molecules. (**C**) Crystal structure of SIFSIX-3-Ni at 298 K. (**D**) Simulation of the maximum open structure of NbOFFIVE-1-Ni, showing a theoretical window size of 4.752(1) Å. (**E**) Simulation of the maximum open structure of SIFSIX-3-Ni, showing a theoretical window size of 7.314(1) Å.

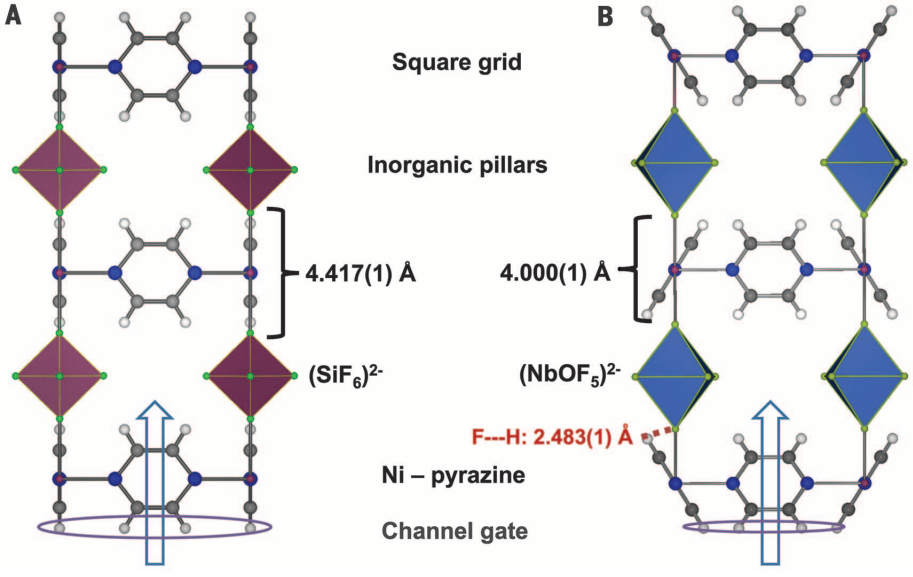

Fig. 2. Structure comparison between SIFSIX-3-Ni and NbOFFIVE-1-Ni showing the impact of the use of a relatively bigger inorganic pillar [$(NbOF_5)^{2-}$ instead of $(SiF_6)^{2-}$]. (**A**) [010]-projection view of SIFSIX-3-Ni, showing the perfectly aligned pyrazine molecules. (**B**) [010]-projection view of NbOFFIVE-1-Ni, showing the titling of pyrazine molecules due to the use of the bigger $(NbOF_5)^{2-}$ building block. The shorter distance between two $(NbOF_5)^{2-}$ building blocks from the two neighboring layers [4.000(1) Å versus 4.417(1) Å in the case of $(SiF_6)^{2-}$ pillars in the SIFSIX-3-Ni] induces a titling of pyrazine molecules and consequently a decrease in the pore aperture size, comparatively with that of SIFSIX-3-Ni.

with an apparent surface area of 280 m^2/g and an estimated pore volume of 0.095 cm^3/g (fig. S8).

The permanent porosity and the associated restricted pore aperture size [maximum 4.752(1) Å] prompted us to assess and evaluate the adsorption properties of NbOFFIVE-1-Ni for various key probe molecules characterized by different shapes and a comparatively larger kinetic diameter. Specifically, adsorption properties of molecules that are relevant to both industrial gases upgrading and the challenging olefin/paraffin separation—namely methane (CH_4), ethane (C_2H_6), ethylene (C_2H_4), propylene (C_3H_6), and propane (C_3H_8)—were evaluated at room temperature and atmospheric pressures.

Before assessing the NbOFFIVE-1-Ni as a potential separating agent, we evaluated its stability against water vapor and H_2S by monitoring the powder x-ray diffraction (PXRD) patterns upon exposure to various humidity levels and H_2S concentrations (Fig. 3A and fig. S4). Evidently, no loss of crystallinity and no phase change were observed during the exposure of the material to humidity from 5 to 95% (fig. S4), H_2O (fig. S7), or H_2S (up to 10%) (fig. S9). The hydrolytic stability of KAUST-7 is supported by the retention of the material CO_2 adsorption uptake and structural integrity after its immersion in aqueous solution for more than 6 months. The performance of the material was not altered as the maximum CO_2 uptake was reached (fig. S10). Moreover, the NbOFFIVE-1-Ni is proven to be highly thermal stable, as evidenced through thermogravimetric analysis (TGA) and variable temperature PXRD patterns (fig. S5 and S6).

Single-gas adsorption data revealed that the NbOFFIVE-1-Ni channels with restricted aperture size allowed the adsorption of C_3H_6 but did not permit the C_3H_8 to diffuse/adsorb into the pore system at 298 K up to ~1 bar (Fig. 3B). Considerably, C_3H_6/C_3H_8 50/50 mixed-gas adsorption data, collected at 298 K (up to 0.5 bar partial pressure of C_3H_6), overlaid with the pure C_3H_6 adsorption isotherm (Fig. 3B), which supports the molecular exclusion of propane from propylene. The concomitant pore aperture size and shape expressed in this MOF adsorbent provide the requisite size and shape cut-off in adsorption, resulting in the observed C_3H_6/C_3H_8 selectivity. The selectivity was further confirmed by performing C_3H_6/C_3H_8 50/50 mixed-gas column breakthrough experiments (Fig. 3C), imitating the real conditions for the C_3H_6/C_3H_8 separation process, at room temperature and 1 bar in a packed column bed of ~1.4 g of NbOFFIVE-1-Ni. By using 4 cm^3/min total gas flow, C_3H_8 was not adsorbed in the packed column bed, whereas pure C_3H_6 was retained for ~480 s (Fig. 3C). Additionally, mixed-gas column breakthrough experiments were performed in dilute conditions by using N_2 as a carrier inert gas, namely $C_3H_6/C_3H_8/N_2$ in 5/5/90 (fig. S25) and $C_3H_6/C_3H_8/N_2$ in 25/25/90 (fig. S26) mixtures. The pure C_3H_6 was retained in the packed column bed, whereas N_2 and C_3H_8 were not adsorbed or retained by NbOFFIVE-1-Ni. The regeneration and activation of the saturated adsorbent, desorption over a 10-min period, showed solely the propylene signal and thus confirmed the nonadsorption and nonretention of the propane in the bed (fig. S27).

To support and confirm the complete molecular exclusion of C_3H_8 and the sole adsorption of C_3H_6, simultaneous calorimetric and gravimetric measurements (thermogravimetry–differential scanning calorimetry) were performed at 1 bar. This confirmed the complete exclusion of propane from propylene, as evidenced by the lack of a detectable heat of adsorption in the case of C_3H_8, as compared with the heat of adsorption for C_3H_6 of 57.4 kJ/mol (Fig. 3D). High-pressure adsorption studies confirmed the nondetectable adsorption of C_3H_8 below 1.5 bar, and only minor propane uptake was observed at ~1.5 bar (~0.1 mol/kg) (fig. S11).

Prior C_3H_6/C_3H_8 adsorption studies—using zeolite, carbon molecular sieves (CMSs), or MOFs—revealed the plausible equilibrium- and/or kinetic-based separation but with low to moderate separation factors (*7*, *27*–*29*). Correspondingly, the evaluation of zeolite molecular sieves for the propylene/propane separation under similar experimental conditions as the NbOFFIVE-1-Ni adsorbent revealed (i) the very poor C_3H_6/C_3H_8 separation (fig. S12) for zeolite 4A at 1 bar total pressure, as a result of the very slow C_3H_6 adsorption kinetics (fig. S13), and (ii) the extremely low selectivity of nearly 2 for zeolite 5A, despite its associated fast adsorption kinetics relative to that of NbOFFIVE-1-Ni (fig. S13).

The deployment of NbOFFIVE-1-Ni as a splitter agent or adsorbent, permitting the complete sieving of C_3H_8 from C_3H_6, offers (i) a simplified separation process based on a concentration swing recycling mode (CSRM) or a vacuum swing recycling mode (VSRM), in which the ideal working C_3H_6 capacity can be accomplished by performing a desorption step with an inert gas (such as He or N_2) purge at 1.2 bar or by simply reducing the pressure from 1.2 bar to 0.01 bar (Fig. 3B); and (ii) the ability to eliminate the energy-demanding high-pressure steps used in the case of the zeolite 4A adsorbent—pressurization (step 2), purge (with N_2, step 3), and cocurrent blow down (step 4) will not be required in the projected concentration swing adsorption (CSA) or vacuum swing adsorption (VSA) system when using the NbOFFIVE-1-Ni adsorbent (Fig. 4B). The implementation of the VSA system based on NbOFFIVE-1-Ni as an

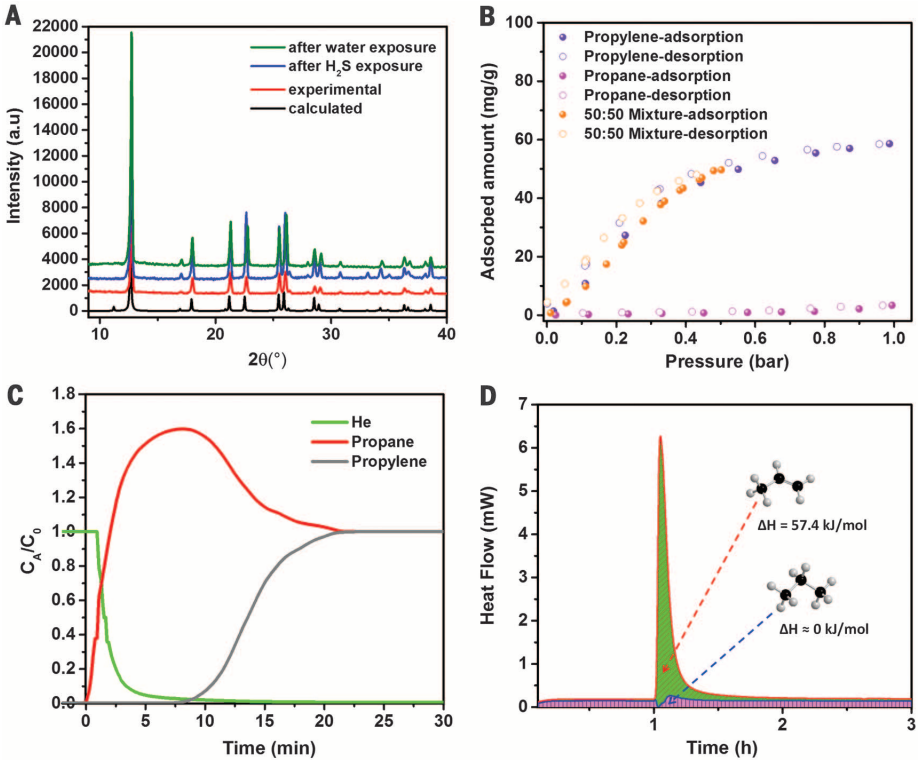

Fig. 3. Evaluation of the chemical stability and propylene/propane separation ability of NbOFFIVE-1-Ni. (**A**) Powder x-ray diffraction experiments showing the stability of NbOFFIVE-1-Ni after exposure to water and H_2S. (**B**) The pure C_3H_8 (pink), pure C_3H_6 (purple), and equimolar mixture of C_3H_6/C_3H_8 50/50 (orange) isotherms of NbOFFIVE-1-Ni have been collected at 298 K, demonstrating the full propylene from propane sieving ability of this adsorbent at 1 bar. (**C**) C_3H_6/C_3H_8 50/50 mixed-gas experiment using a packed column bed at 298 K and a 1 bar total pressure and 4 cm^3/min total flow, confirming the infinite C_3H_6/C_3H_8 separation factor. (**D**) Calorimetric measurements of C_3H_8 and C_3H_6 adsorption on NbOFFIVE-1-Ni were performed so as to quantify the heat of adsorption of propylene and to reaffirm the exclusion/no adsorption of propane.

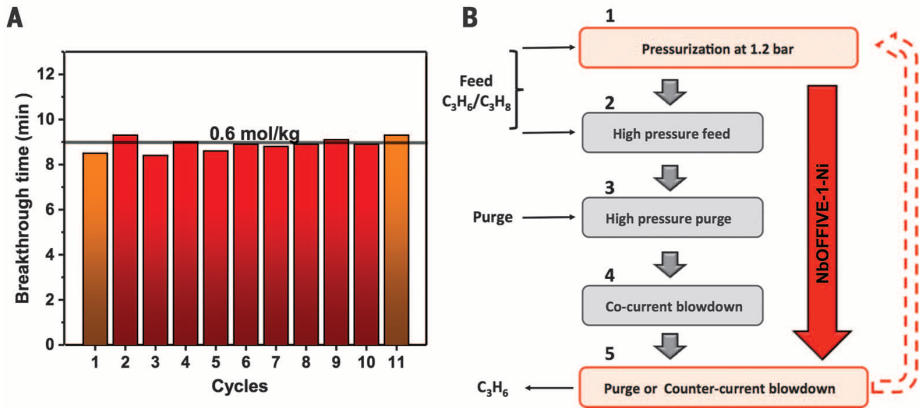

Fig. 4. Separation process based on concentration swing recycling mode and a simplified CSA or VSA system for the NbOFFIVE-1-Ni molecular sieve. (**A**) C_3H_6/C_3H_8 50/50 mixed-gas 11 cyclic experiments for NbOFFIVE-1-Ni at 298 K and 1 bar, with 4 cm^3/min total flow and using a CSRM system, with He as a purge gas for cycles 2 to 10, whereas the sample was activated for 8 hours at 105°C under vacuum for cycle 1 and cycle 11. (**B**) Principle of using NbOFFIVE-1-Ni as a C_3H_8 sieve in two-step CSA or VSA (red line, steps 1 and 5) as compared with a pressure swing adsorption (PSA) system using the zeolite 4A (steps 1 through 5).

adsorbent offers the potential to considerably reduce the energy penalty associated with the conventional C_3H_6/C_3H_8 separation, and valuably recover both C_3H_6 and C_3H_8 separately in a high-purity grade.

Correspondingly, we performed subsequent mixed-gas (C_3H_6/C_3H_8 at 50/50) column breakthrough measurements in order to corroborate the preservation of the adsorption properties and separation performance of the NbOFFIVE-1-Ni—the propylene adsorption uptake and the full molecular exclusion of propane from propylene at standard ambient temperature and pressure. The multiple adsorption/desorption measurements (over 10 cycles) by use of CSRM revealed that NbOFFIVE-1-Ni maintained its propylene adsorption capacity and its full molecular exclusion of propane (Fig. 3C and figs. S14 to S23). Conversely, the deployment of the aforementioned CSRM protocol under the same operating conditions in the case of the evaluated zeolite molecular sieves revealed a noticeable decrease in the C_3H_6 retention time by the zeolite 5A, which is equivalent to a 300% reduction after only four adsorption/desorption cycles (fig. S24). In the case of zeolite 4A, the low propylene uptake associated with its very slow diffusion limited the scope of zeolite 4A for the C_3H_6/C_3H_8 separation under atmospheric conditions.

Detailed analysis of the data, for the C_3H_6/C_3H_8 50/50 mixed-gas adsorption cycles in a bed composed of 1.4 g of NbOFFIVE-1-Ni, indicated a C_3H_6 uptake of ~0.6 mol/kg for a given cycle based on an 8-min adsorption followed by a 10-min desorption (Fig. 3C) when using CSRM. This result pinpoints the appropriateness of the NbOFFIVE-1-Ni as a stable separating agent for propylene/propane, with a pronounced propylene uptake/recovery of ~2 mol/kg/hour. The NbOFFIVE-1-Ni adsorbent offers potential to effectively separate propylene from propane with a reduced energy footprint by using a CSA. The zeolite 4A, when using VSA at high pressure and 423 K, offers only a limited 26% recovery for a propylene capacity of 1.03 mol/kg/hour (0.13 mol/kg per cycle), with a 97% purity (*30*).

We have demonstrated the successful use of reticular chemistry to deliberately fabricate a fluorinated MOF adsorbent, with controlled pore aperture size and shape, for the selective molecular exclusion of propane from propylene at standard ambient temperature and pressure, up to 1.5 bar. This complete molecular sieving of propane from propylene was supported by a combined comprehensive study on the basis of single-gas, mixed-gas adsorption and calorimetric-gravimetric experiments. The NbOFFIVE-1-Ni adsorbent possesses a noticeably high chemical stability—as demonstrated by its tolerance to water vapor and hydrogen sulfide—and high thermal stability. The full molecular exclusion of propane by NbOFFIVE-1-Ni adsorbent provides the potential to deploy a simplified and energy-efficient concentration swing adsorption system that does not require energy-demanding steps such as pressurization, high-pressure purge, or cocurrent blow down.

This study illustrates the merit of the molecular building block approach in MOF chemistry for the ultrafine-tuning of the pore aperture size and shape to address important gas separations. Evidently, high porosity is not a sorbent perquisite for an effective and efficient gas separation; a nonporous material to the N_2 adsorbate at cryogenic temperature—a routine probe to assess the microporosity of a given adsorbent such as KAUST-7—can possess distinctive gas separation properties that can be revealed and disclosed through the close examination of the material structural features and the subsequent deeper examination and evaluation of its gas adsorption properties at room temperature.

REFERENCES AND NOTES

1. U.S. Department of Energy (DOE), *Materials for Separation Technology: Energy and Emission Reduction Opportunities* (DOE, 2005).
2. P. Bai *et al.*, *Nat. Commun.* **6**, 5912 (2015).
3. A. Chauvel, G. Lefebvre, in *Petrochemical Processes* (Gulf Publishing, 1989), pp. 199–208.
4. D. J. Safarik, R. B. Eldridge, *Ind. Eng. Chem. Res.* **37**, 2571–2581 (1998).
5. R. T. Yang, E. S. Kikkinides, *AIChE J.* **41**, 509–517 (1995).
6. M. C. Campo *et al.*, *Separ. Purif. Tech.* **103**, 60–70 (2013).
7. J. Liu *et al.*, *Carbon* **85**, 201–211 (2015).
8. C. A. Grande, J. Gascon, F. Kapteijn, A. E. Rodrigues, *Chem. Eng. J.* **160**, 207–214 (2010).
9. C. A. Grande, A. E. Rodrigues, *Ind. Eng. Chem. Res.* **44**, 8815–8829 (2005).
10. A. H. Assen *et al.*, *Angew. Chem. Int. Ed. Engl.* **54**, 14353–14358 (2015).
11. G. Férey, *Chem. Soc. Rev.* **37**, 191–214 (2008).
12. S. Kitagawa, R. Kitaura, S. Noro, *Angew. Chem. Int. Ed. Engl.* **43**, 2334–2375 (2004).
13. M. Eddaoudi *et al.*, *Acc. Chem. Res.* **34**, 319–330 (2001).
14. A. R. Millward, O. M. Yaghi, *J. Am. Chem. Soc.* **127**, 17998–17999 (2005).
15. D. Fairen-Jimenez *et al.*, *Chem. Commun.* **48**, 10496–10498 (2012).
16. Y. Peng *et al.*, *J. Am. Chem. Soc.* **135**, 11887–11894 (2013).
17. Q. Yang *et al.*, *Chem. Commun.* **48**, 9831–9833 (2012).
18. D.-X. Xue *et al.*, *J. Am. Chem. Soc.* **137**, 5034–5040 (2015).
19. P. Nugent *et al.*, *Nature* **495**, 80–84 (2013).
20. K. Sumida *et al.*, *Chem. Rev.* **112**, 724–781 (2012).
21. S. Xiang *et al.*, *Nat. Commun.* **3**, 954 (2012).
22. Z. R. Herm, R. Krishna, J. R. Long, *Micropor. Mesopor. Mater.* **151**, 481–487 (2012).
23. O. M. Yaghi *et al.*, *Nature* **423**, 705–714 (2003).
24. O. Shekhah *et al.*, *Nat. Commun.* **5**, 4228 (2014).
25. H. K. Izumi, J. E. Kirsch, C. L. Stern, K. R. Poeppelmeier, *Inorg. Chem.* **44**, 884–895 (2005).
26. R. Gautier, M. D. Donakowski, K. R. Poeppelmeier, *J. Solid State Chem.* **195**, 132–139 (2012).
27. O. Shekhah *et al.*, *Chem. Commun.* **50**, 2089–2092 (2014).
28. E. D. Bloch *et al.*, *Science* **335**, 1606–1610 (2012).
29. X. Yang, B. H. Toby, M. A. Camblor, Y. Lee, D. H. Olson, *J. Phys. Chem. B* **109**, 7894–7899 (2005).
30. F. A. Da Silva, A. E. Rodrigues, *Ind. Eng. Chem. Res.* **40**, 5758–5774 (2001).

ACKNOWLEDGMENTS

Research reported in this publication was solely performed in KAUST and exclusively supported by KAUST funds and the KAUST center collaborative funding grants CCF/1/1972-02-01 and CCF/1/1972-8-01. The data reported in the paper are presented in the supplementary materials. Crystal structures of NbOFFIVE-1-Ni collected at 100 K and room temperature are available free of charge from the Cambridge Crystallographic Data Centre under reference nos. CCDC 1477136 and 1447953. A.C., K.A., Y.B., M.E., and KAUST have filed provisional patent applications (4053-023PCT1 and 4053-024PCT1) that relate to highly stable fluorinated MOF absorbents as tunable platforms for gas/vapor separation.

SUPPLEMENTARY MATERIALS

www.sciencemag.org/content/353/6295/137/suppl/DC1
Materials and Methods
Supplementary Text
Figs. S1 to S29
Tables S1 and S2
References (*31*–*35*)
CIF Files (Crystal Structure)

7 March 2016; accepted 25 May 2016
10.1126/science.aaf6323

MICROPOROUS NETWORKS

Pore chemistry and size control in hybrid porous materials for acetylene capture from ethylene

Xili Cui,[1]* Kaijie Chen,[2]* Huabin Xing,[1]† Qiwei Yang,[1] Rajamani Krishna,[3] Zongbi Bao,[1] Hui Wu,[4] Wei Zhou,[4] Xinglong Dong,[5] Yu Han,[5] Bin Li,[6] Qilong Ren,[1] Michael J. Zaworotko,[2]† Banglin Chen[6]†

The trade-off between physical adsorption capacity and selectivity of porous materials is a major barrier for efficient gas separation and purification through physisorption. We report control over pore chemistry and size in metal coordination networks with hexafluorosilicate and organic linkers for the purpose of preferential binding and orderly assembly of acetylene molecules through cooperative host-guest and/or guest-guest interactions. The specific binding sites for acetylene are validated by modeling and neutron powder diffraction studies. The energies associated with these binding interactions afford high adsorption capacity (2.1 millimoles per gram at 0.025 bar) and selectivity (39.7 to 44.8) for acetylene at ambient conditions. Their efficiency for the separation of acetylene/ethylene mixtures is demonstrated by experimental breakthrough curves (0.73 millimoles per gram from a 1/99 mixture).

An urgent demand for efficient solutions to challenges in gas separation, sensing, and storage (*1*–*7*) has spurred research on custom-designed porous materials, termed metal-organic frameworks (MOFs) and/or porous coordination polymers (PCPs) (*8*), in which open lattices are formed from inorganic centers (nodes) and organic linking groups. These materials can be designed from first principles and, thanks to their inherent diversity, afford precise control over pore chemistry and pore size.

Ideal porous materials for gas separation should exhibit high selectivity and optimal adsorption capacity for the target gas molecules at relevant conditions. However, the design of new materials that improve upon existing benchmarks poses a daunting challenge to materials scientists (*9*–*12*). For example, porous materials are needed for acetylene (C_2H_2) capture and separation from ethylene (C_2H_4) (*13*–*17*), industrial processes that are relevant for the production of polymer-grade C_2H_2 and C_2H_4 (the most produced organic compound in the world, at over 140 million metric tons in 2014). The MOF-74 family of compounds has a high density of open metal sites that drive high uptake of C_2H_2 but displays low separation selectivities (*18*). The M′MOF (mixed metal–organic framework) family has ultramicropores that enable sieving effects and high separation selectivities but relatively low uptake of C_2H_2 (*19*).

We report that metal coordination networks with preformed inorganic and organic linkers—SIFSIX-2-Cu-i [SIFSIX, hexafluorosilicate (SiF_6^{2-}); 2, 4,4′-dipyridylacetylene; i, interpenetrated)] (*20*) and SIFSIX-1-Cu (1, 4,4′-bipyridine) (*21*)—can exhibit exceptional C_2H_2 capture performance because the geometric disposition of SiF_6^{2-} moieties enables preferential binding of C_2H_2 molecules. Both materials have pore spaces that enable extremely high C_2H_2 capture under low pressures, and they unexpectedly represent new benchmarks for the highly efficient removal of minor amounts of C_2H_2 from C_2H_4 gas (SIFSIX-2-Cu-i) and mass separation of C_2H_2/C_2H_4 mixtures under ambient conditions (SIFSIX-1-Cu). We attribute this unprecedented performance to the existence of "sweet spots" in pore chemistry and pore size that enable highly specific recognition and high uptake of C_2H_2 to occur in the same material.

In these SIFSIX materials, two-dimensional (2D) nets of organic ligand and metal node are pillared with SiF_6^- anions in the third dimension to form 3D coordination networks that have primitive cubic topology and, importantly, pore walls lined by inorganic anions (*20*–*23*). The pore sizes within this family of materials can be systematically tuned by changing the length of the organic linkers, the metal node, and/or the framework interpenetration. SIFSIX-1-Cu, SIFSIX-2-Cu, SIFSIX-2-Cu-i, SIFSIX-3-Cu (3, pyrazine), SIFSIX-3-Zn, and SIFSIX-3-Ni have already been studied for their exceptional CO_2 capture performance, but here we report a study of their C_2H_2 and C_2H_4 adsorption from 283 to 303 K. Figure 1, A and B, and figs. S2 to S7 show dramatically different adsorption behaviors for C_2H_2 than those observed for CO_2 (figs. S8 and S9) (*24*). SIFSIX-2-Cu-i rapidly adsorbs C_2H_2 at very low pressure (≤0.05 bar). Its C_2H_2 uptake reaches 2.1 mmol/g at 298 K and 0.025 bar (Fig. 1B), compared with an uptake of 1.78 mmol/g by UTSA-100a (*17*). This performance at low pressure indicates that SIFSIX-2-Cu-i has promise for capturing C_2H_2 when it is a minor component in a gas mixture. SIFSIX-1-Cu exhibits exceptionally high C_2H_2 uptake (8.5 mmol/g) at 298 K and 1.0 bar. This is not only the highest uptake of any of the SIFSIX materials, but is also even higher than that of the previous benchmark, FeMOF-74 (table S1) (*18*, *24*). As detailed herein, we attribute the unprecedented performance of these materials to their hybrid pore chemistry and optimal pore sizes for binding C_2H_2.

To understand the C_2H_2 adsorption isotherms in these materials, we conducted detailed modeling studies using first-principles DFT-D (dispersion-corrected density functional theory) calculations. In SIFSIX-1-Cu, C_2H_2 molecules are bound through strong C–H···F hydrogen (H) bonding (2.017 Å) and van der Waals (vdW) interactions with the 4,4′-bipyridine linkers (Fig. 1C and fig. S10) (*24*). The DFT-D–calculated static adsorption energy (ΔE) is 44.6 kJ/mol. Each unit cell of SIFSIX-1-Cu contains four equivalent exposed F atoms, and each exposed F atom binds one C_2H_2 molecule. The distance between neighboring adsorbed C_2H_2 molecules is ideal for them to synergistically interact with each other through multiple $H^{\delta+}\cdots C^{\delta-}$ dipole-dipole interactions (Fig. 1C), further enhancing the energy of adsorption. Because four C_2H_2 molecules are adsorbed per unit cell, the ΔE of C_2H_2 increases to 47.0 kJ/mol. The strong binding of C_2H_2 at F atoms and the geometric arrangement of SiF_6^{2-} anions enable the efficient packing of four C_2H_2 molecules per unit cell and very high C_2H_2 uptake at 298 K and 1.0 bar (about 4.4 C_2H_2 molecules per unit cell).

C_2H_2 adsorption is weaker in the wider-pore material SIFSIX-2-Cu (10.5 Å × 10.5 Å cavity) than in SIFSIX-1-Cu (ΔE, 34.6 versus 44.6 kJ/mol; uptake, 5.3 versus 8.5 mmol/g). The C–H···F H-bonding interaction from SiF_6^{2-} sites is of the same nature in these isoreticular networks (Fig. 1, C and D). However, the vdW interaction between C_2H_2 and the organic linker in SIFSIX-2-Cu is weak compared with that in SIFSIX-1-Cu. We attribute this difference to the former's larger pore size and weaker vdW potential overlap (figs. S10 and S11) (*24*). Moreover, at high gas uptake, the C_2H_2 molecules adsorbed on adjacent F sites are too far separated to have synergistic guest-guest interactions. However, in the twofold interpenetrated structure of SIFSIX-2-Cu-i, one C_2H_2 molecule can be simultaneously bound by two F atoms from different nets through cooperative C–H···F H-bonding (2.013 and 2.015 Å; Fig. 1E), which enables the strongest energy of C_2H_2 binding yet observed in SIFSIX materials (ΔE, 52.9 kJ/mol). The strong adsorption energy of SIFSIX-2-Cu-i contributes to its extremely high uptake capacity at low pressure. In SIFSIX-3-Zn and SIFSIX-3-Ni, which are

[1]Key Laboratory of Biomass Chemical Engineering of Ministry of Education, College of Chemical and Biological Engineering, Zhejiang University, Hangzhou 310027, China. [2]Department of Chemical and Environmental Sciences, University of Limerick, Limerick, Republic of Ireland. [3]Van 't Hoff Institute for Molecular Sciences, University of Amsterdam, Science Park 904, 1098 XH Amsterdam, Netherlands. [4]Center for Neutron Research, National Institute of Standards and Technology, Gaithersburg, MD 20899-6102, USA. [5]Advanced Membranes and Porous Materials Center, Physical Sciences and Engineering Division, King Abdullah University of Science and Technology, Thuwal 23955-6900, Saudi Arabia. [6]Department of Chemistry, University of Texas–San Antonio, One UTSA Circle, San Antonio, TX 78249-0698, USA.

*These authors contributed equally to this work. †Corresponding author. Email: xinghb@zju.edu.cn (H.X.); michael.zaworotko@ul.ie (M.J.Z.); banglin.chen@utsa.edu (B.C.)

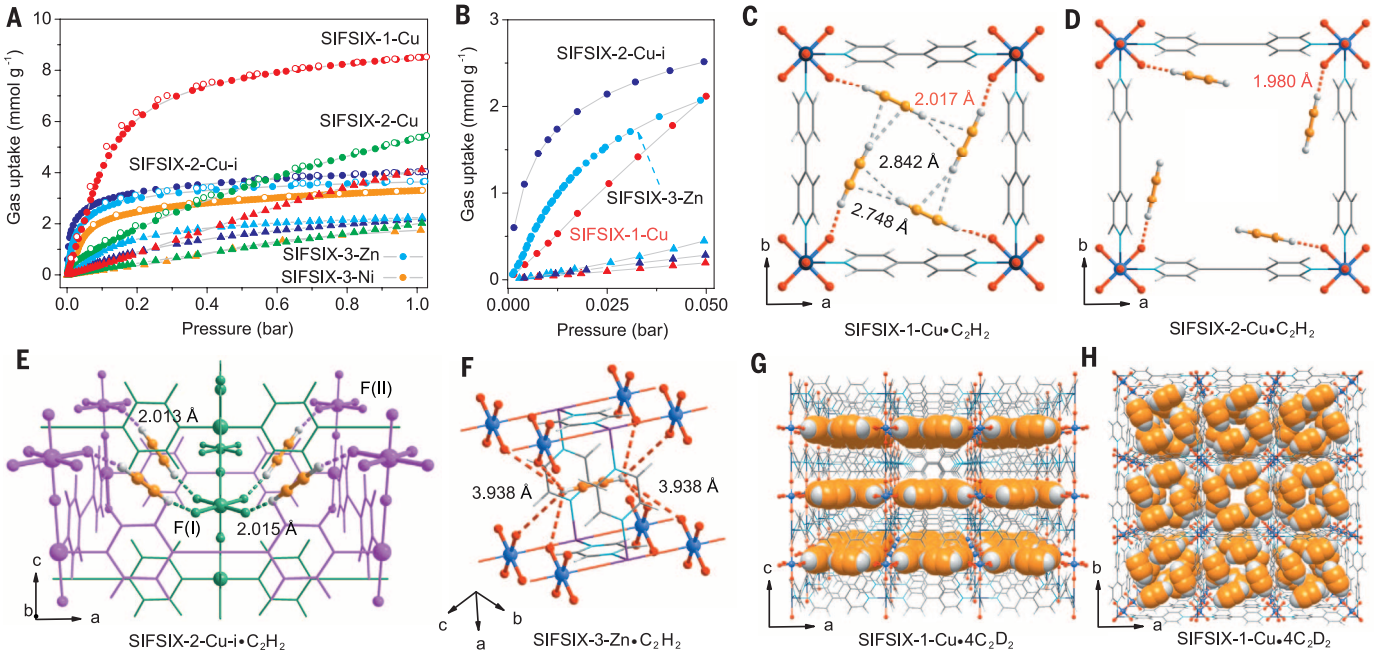

Fig. 1. C_2H_2 and C_2H_4 adsorption isotherms of the MOFs, DFT-D–simulated optimized C_2H_2 adsorption sites of the MOFs, and neutron crystal structure of SIFSIX-1-Cu·4C_2D_2. (**A** and **B**) Adsorption isotherms of C_2H_2 (filled circles) and C_2H_4 (triangles) in SIFSIX-1-Cu (red), SIFSIX-2-Cu (green), SIFSIX-2-Cu-i (blue), SIFSIX-3-Zn (light blue), and SIFSIX-3-Ni (orange) at 298 K in two pressure regions, 0 to 1.0 bar (A) and 0 to 0.05 bar (B). Open circles in (A) are desorption isotherms of C_2H_2 (**C** to **F**) DFT-D–calculated C_2H_2 adsorption binding sites in SIFSIX-1-Cu (C), SIFSIX-2-Cu (D), SIFSIX-2-Cu-i (E) (the different nets are highlighted in magenta and green for clarity), and SIFSIX-3-Zn (F). Color code: F, red; Si, light blue; C, gray; H, light gray; N, sky blue; Cu, dark teal; Zn, violet; C (in C_2H_2 or C_2D_2), orange. (**G** and **H**) Neutron crystal structure of SIFSIX-1-Cu·4C_2D_2 at 200 K, determined from Rietveld analysis.

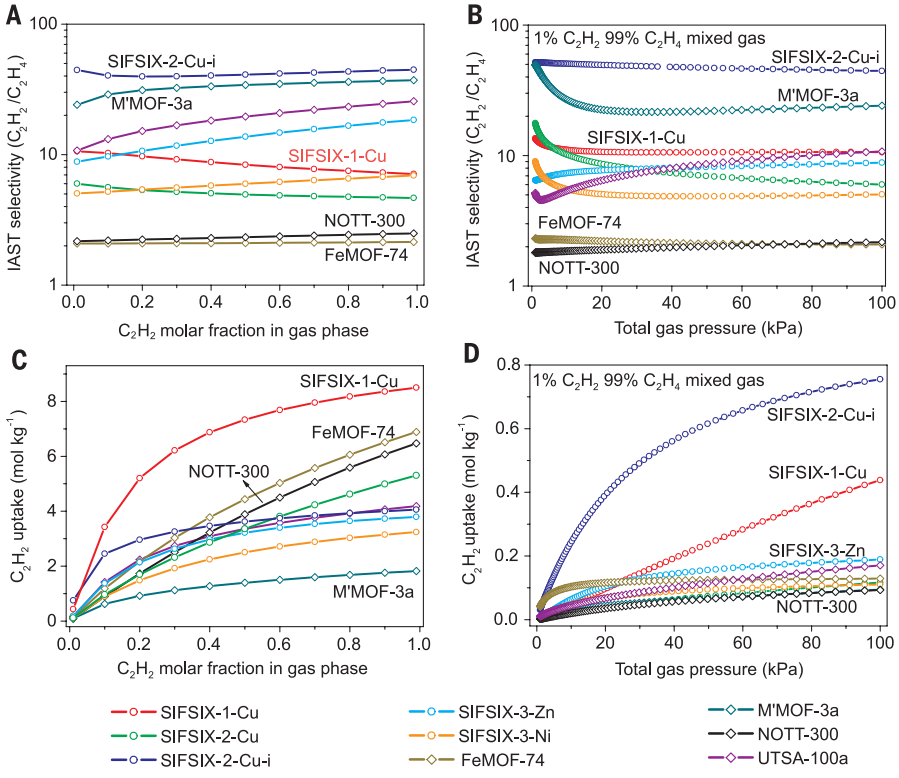

Fig. 2. IAST calculations for MOF performance with C_2H_2/C_2H_4 mixtures. (**A** and **B**) Comparison of the IAST selectivities of SIFSIX materials versus those of previously reported best-performing materials for C_2H_2/C_2H_4 mixtures. Results for varying C_2H_2 molar fractions at 100 kPa are shown in (A), and results at varying pressures for a 1% C_2H_2 mixture are shown in (B). (**C** and **D**) MOF capacity to uptake C_2H_2 from C_2H_2/C_2H_4 mixtures. Results for varying C_2H_2 molar fractions at 100 kPa are shown in (C), and results at varying pressures for a 1% C_2H_2 mixture are shown in (D).

the strongest CO_2 adsorbents, the pore size is smallest, and C_2H_2 molecules are primarily adsorbed at a different site in the 1D channel along the *c* axis (ΔE, 50.3 kJ/mol; Fig. 1F). The secondary adsorption site in SIFSIX-3-Zn (fig. S12) (*24*) exhibits a much smaller adsorption energy (25.9 kJ/mol), which results in lower C_2H_2 uptake compared with that of SIFSIX-2-Cu-i.

The weakly basic nature of the SiF_6^{2-} sites (acid dissociation constant pK_a, 1.92) and their geometric disposition enable strong binding with weakly acidic C_2H_2 molecules. Because C_2H_2 is more acidic than C_2H_4 (pK_a, 25 versus 44) (*17*), and the geometry of the SIFSIX materials is more optimal for C_2H_2 binding, there are much stronger interactions with C_2H_2 than with C_2H_4 (ΔE in SIFSIX-1-Cu, 44.6 versus 27.2 kJ/mol; ΔE in SIFSIX-2-Cu-i, 52.9 versus 39.8 kJ/mol). The calculated H-bond distances between C_2H_4 and SiF_6^{2-} sites are 2.541 and 2.186 Å in SIFSIX-1-Cu and SIFSIX-2-Cu-i, respectively, which are longer than those between C_2H_2 and SiF_6^{2-} sites (figs. S13 and S14) (*24*).

To establish the structure of the C_2H_2 binding sites through Rietveld structural refinements, high-resolution neutron powder diffraction data were collected on C_2D_2-loaded samples of SIFSIX-1-Cu·4C_2D_2 and SIFSIX-2-Cu-i·1.7C_2D_2 at 200 K (figs. S15 and S16) (*24*). Each unit cell of SIFSIX-1-Cu is filled with four C_2D_2 molecules that are arranged in an ordered planar structure (Fig. 1, G and H), consistent with the DFT-D modeling results. C–D···F H-bonding occurs between C_2D_2 and SiF_6^- anions (2.063 Å), and $D^{\delta+}\cdots C^{\delta-}$ distances between neighboring C_2D_2 molecules are 3.063 and 3.128 Å. In SIFSIX-2-Cu-i, each C_2H_2

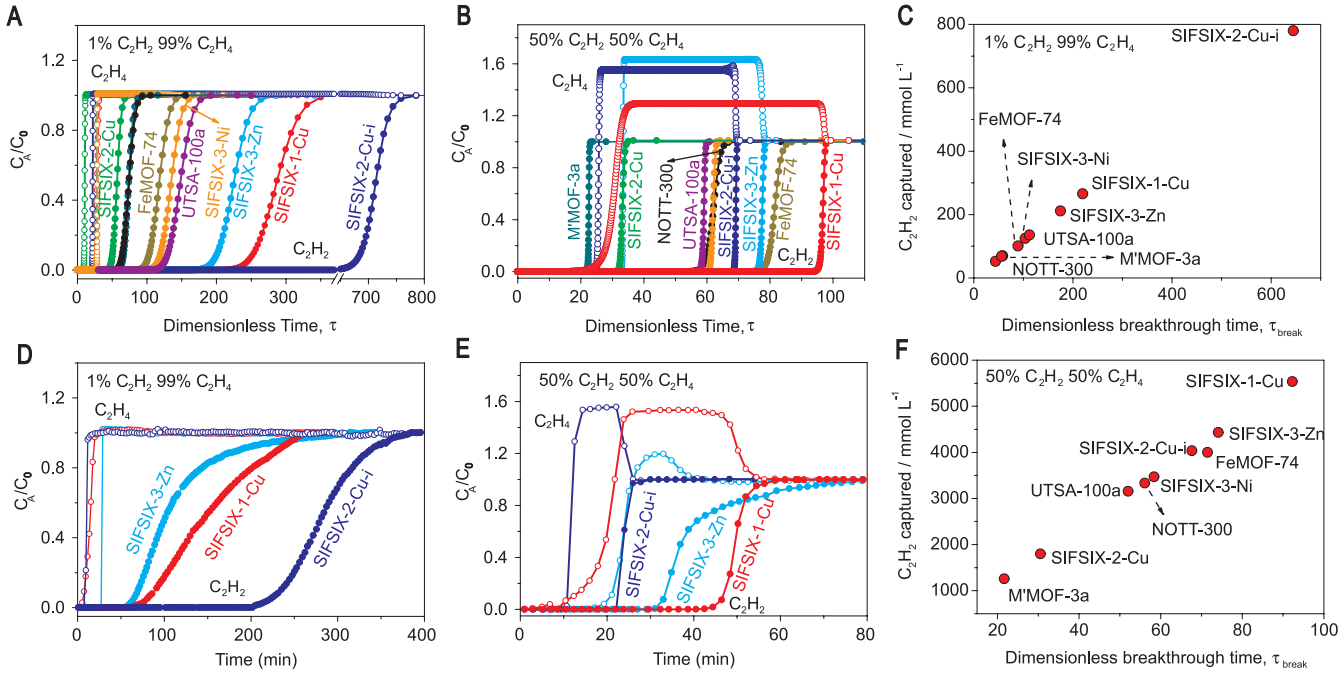

Fig. 3. Simulated and experimental column breakthrough results. (**A** and **B**) Simulated column breakthrough curves for C_2H_2/C_2H_4 separations with SIFSIX materials and previously reported best-performing materials [(A), 1/99 mixture; (B), 50/50 mixture]. (**C** and **F**) Plots of the amount of C_2H_2 captured as a function of τ_{break} in the simulated column breakthrough [(C), 1/99 mixture; (F), 50/50 mixture]. (**D** and **E**) Experimental column breakthrough curves for C_2H_2/C_2H_4 separations with SIFSIX-1-Cu, SIFSIX-2-Cu, and SIFSIX-3-Zn at 298 K and 1.01 bar [(D), 1/99 mixture; (E), 50/50 mixture]. In (A), (B), (D), and (E), open circles are for C_2H_4, and filled circles are for C_2H_2. C_A/C_0, outlet concentration/feed concentration.

interacts with two SiF_6^- anions via dual C–D···F H-bonding (2.134 Å; fig. S17) (*24*).

The separation of C_2H_2 from C_2H_4 is necessary for the production of high-purity C_2H_4 and C_2H_2. In the production of polymer-grade C_2H_4, removal of trace C_2H_2 (about 1%) from C_2H_4 gas must meet the requirement of <40 parts per million (ppm) C_2H_2 in the downstream polymerization reaction (*17*). Similarly, in the production of polymer-grade C_2H_2 by pyrolysis of coal and biomass, the capture of C_2H_2 from C_2H_2/C_2H_4 mixtures (90/10 to 50/50, v/v) is a crucial step. Existing methods, such as solvent absorption and partial hydrogenation of C_2H_2 (*25*), are energy intensive, so there is an urgent need to develop efficient porous materials for C_2H_2 capture from C_2H_4.

To address gas mixture separations, we first determined the C_2H_2/C_2H_4 separation selectivities of the SIFSIX materials by means of ideal adsorbed solution theory (IAST) calculations (Fig. 2 and fig. S20) (*24*, *26*). SIFSIX-2-Cu-i exhibits record C_2H_2/C_2H_4 selectivities (39.7 to 44.8; Fig. 2A), even greater than those of M'MOF-3a (table S1). Because SIFSIX-2-Cu-i adsorbs a high amount of C_2H_2 under very low pressures, it not only has the highest C_2H_2/C_2H_4 selectivities (Fig. 2B) but also the highest C_2H_2 uptake (Fig. 2D) for C_2H_2/C_2H_4 (1/99) mixtures. SIFSIX-1-Cu displays moderately high C_2H_2/C_2H_4 separation selectivities (7.1 to 10.6), which are greater than those of FeMOF-74 (2.1) (*18*) and NOTT-300 (2.2 to 2.5) (*14*) (Fig. 2A). For C_2H_2/C_2H_4 (1/99) mixtures, SIFSIX-1-Cu exhibits greater selectivities (10.6) than SIFSIX-3-Zn (8.8) and SIFSIX-3-Ni (5.0) (Fig. 2B). Its C_2H_2 uptake from the 1/99 mixture is the second highest of the compounds investigated (Fig. 2D). Given that SIFSIX-1-Cu has a relatively large surface area, it should also be very efficient for C_2H_2/C_2H_4 (1/99) separation. SIFSIX-1-Cu exhibits higher C_2H_2 uptakes than benchmark MOFs, including FeMOF-74, NOTT-300, and UTSA-100a. Its high C_2H_2/C_2H_4 selectivities (Fig. 2A) make SIFSIX-1-Cu most suitable for C_2H_2/C_2H_4 (50/50) separation (Fig. 2C and fig. S20) (*24*). Some further comparisons of how these MOFs perform with respect to C_2H_2/C_2H_4 separations are shown in table S1 (*24*).

Transient breakthrough simulations (*27*) were conducted to demonstrate the C_2H_2/C_2H_4 separation performances of the SIFSIX materials in column adsorption processes. Two C_2H_2/C_2H_4 mixtures (1/99 and 50/50) were used as feeds to mimic the industrial process conditions. Clean separations were realized with all five SIFSIX MOFs; C_2H_4 first eluted through the bed to yield a polymer-grade gas, then C_2H_2 broke through from the bed at a certain time τ_{break} (Fig. 3A and figs. S21 and S22) (*24*). The dimensionless τ_{break} values for SIFSIX-1-Cu (1/99 and 50/50 mixtures) and SIFSIX-2-Cu-i (1/99 mixture) exceed those of the other SIFSIX materials and MOFs that we studied (Fig. 3, A and B). The amount of C_2H_2 captured from the 1/99 mixture in SIFSIX-1-Cu and SIFSIX-2-Cu-i was as high as 265.3 and 780.0 mmol/liter, respectively, which compares favorably with state-of-art adsorbents such as UTSA-100a (135.5 mmol/liter), FeMOF-74 (100.7 mmol/liter), and NOTT-300 (68.3 mmol/liter). SIFSIX-2-Cu-i efficiently removes trace C_2H_2 from C_2H_4 gas (1/99 mixture), whereas SIFSIX-1-Cu demonstrates excellent C_2H_2 capacity with an uptake of 5533 mmol/liter from the 50/50 mixture, ~37% greater than that of FeMOF-74 (Fig. 3F).

Through experimental breakthrough studies, we further examined these materials in actual adsorption processes for both 1/99 and 50/50 mixtures. Highly efficient separations for C_2H_2/C_2H_4 mixtures were realized (Fig. 3, D and E). For the capture of C_2H_2 from the 1/99 mixture, the concentration of C_2H_2 in the gas exiting the adsorber for up to 140 min was below 2 ppm, and the purity of C_2H_4 was >99.998% (fig. S23) (*24*). The hierarchy of breakthrough times for the 1/99 mixture was, from longest to shortest, SIFSIX-2-Cu-i, SIFSIX-1-Cu, then SIFSIX-3-Zn; for the 50/50 mixture, it was SIFSIX-1-Cu, SIFSIX-3-Zn, then SIFSIX-2-Cu-i (Fig. 3, D and E). These experiments are consistent with simulated breakthrough results. Although the uptake of C_2H_2 by SIFSIX-3-Zn at low pressure for the 1/99 mixture is higher than that by SIFSIX-1-Cu (Fig. 1B), SIFSIX-1-Cu exhibits a longer breakthrough time for C_2H_2, presumably because of its higher selectivity (Fig. 2B). The amounts of C_2H_2 captured by SIFSIX-1-Cu, SIFSIX-2-Cu-i, and SIFSIX-3-Zn from the 1/99 mixture (0.38, 0.73, and 0.08 mmol/g, respectively) and from the 50/50 mixture (6.37, 2.88, and 1.52 mmol/g, respectively) during the breakthrough process are in excellent agreement with the simulated results, except in the case of SIFSIX-3-Zn (tables S12 and S13) (*24*).

In the production of high-purity C_2H_4, the feed gases for the C_2H_2 removal unit are contaminated with trace levels of CO_2 (<50 ppm), H_2O (<5 ppm), and O_2 (<5 ppm). We conducted breakthrough experiments for the 1/99 mixture with SIFSIX-2-Cu-i, the best-performing material for capturing trace

amounts of C_2H_2. These experiments indicate that the presence of CO_2 has only a slight (1000 ppm CO_2) or no (10 ppm CO_2) effect on the separation of C_2H_2 from C_2H_4 (fig. S24) (*24*). Moisture (6 to 1340 ppm) and oxygen (2200 ppm) do not affect the C_2H_2 capture ability of SIFSIX-2-Cu-i (figs. S25 and S26) (*24*). The breakthrough performances of SIFSIX-2-Cu-i and SIFSIX-3-Zn for the 1/99 mixture did not decline during 16 and 3 cycles, respectively (figs. S28 and S29) (*24*), and the SIFSIX materials retained their stability after breakthrough experiments (figs. S1 and S30) (*24*).

The SIFSIX materials that we studied exhibit excellent C_2H_2 storage performance. The volumetric uptake of C_2H_2 by SIFSIX-1-Cu at 298 K and 1.0 bar is the highest among these SIFSIX materials (0.191 g/cm^3; table S14) (*24*). The C_2H_2 storage densities in the pores of SIFSIX-1-Cu, SIFSIX-2-Cu-i, and SIFSIX-3-Zn at 298 K are 0.388, 0.403, and 0.499 g/cm^3, respectively.

The basic principles outlined here are likely to be applicable to other gas mixtures. Primary binding sites will be necessary for recognition of specific gas molecules, whereas suitable pore sizes and spacing will be needed to enforce synergistic binding to multiple sites in order to form the so-called "gas clusters" through intermolecular guest-guest interactions. This work not only reveals a path forward for industrial C_2H_2/C_2H_4 separations, but also facilitates a design or crystal engineering approach to the development of porous materials for other gas separations.

REFERENCES AND NOTES

1. S. Kitagawa, *Angew. Chem. Int. Ed.* **54**, 10686–10687 (2015).
2. R. Vaidhyanathan *et al.*, *Science* **330**, 650–653 (2010).
3. N. T. T. Nguyen *et al.*, *Angew. Chem. Int. Ed.* **53**, 10645–10648 (2014).
4. N. L. Rosi *et al.*, *Science* **300**, 1127–1129 (2003).
5. Y. Peng *et al.*, *J. Am. Chem. Soc.* **135**, 11887–11894 (2013).
6. J. A. Mason *et al.*, *Nature* **527**, 357–361 (2015).
7. S. Ma *et al.*, *J. Am. Chem. Soc.* **130**, 1012–1016 (2008).
8. H. Furukawa, K. E. Cordova, M. O'Keeffe, O. M. Yaghi, *Science* **341**, 1230444 (2013).
9. S. J. Datta *et al.*, *Science* **350**, 302–306 (2015).
10. Z. J. Zhang, Z.-Z. Yao, S. Xiang, B. Chen, *Energy Environ. Sci.* **7**, 2868–2899 (2014).
11. Q. Lin, T. Wu, S. T. Zheng, X. Bu, P. Feng, *J. Am. Chem. Soc.* **134**, 784–787 (2012).
12. J.-R. Li, R. J. Kuppler, H.-C. Zhou, *Chem. Soc. Rev.* **38**, 1477–1504 (2009).
13. R. Matsuda *et al.*, *Nature* **436**, 238–241 (2005).
14. S. Yang *et al.*, *Nat. Chem.* **7**, 121–129 (2014).
15. H. Wu, Q. Gong, D. H. Olson, J. Li, *Chem. Rev.* **112**, 836–868 (2012).
16. J.-P. Zhang, X.-M. Chen, *J. Am. Chem. Soc.* **131**, 5516–5521 (2009).
17. T. L. Hu *et al.*, *Nat. Commun.* **6**, 7328–7335 (2015).
18. E. D. Bloch *et al.*, *Science* **335**, 1606–1610 (2012).
19. M. C. Das *et al.*, *J. Am. Chem. Soc.* **134**, 8703–8710 (2012).
20. P. Nugent *et al.*, *Nature* **495**, 80–84 (2013).
21. S. Noro *et al.*, *J. Am. Chem. Soc.* **124**, 2568–2583 (2002).
22. O. Shekhah *et al.*, *Nat. Commun.* **5**, 4228–4234 (2014).
23. A. Kumar *et al.*, *Angew. Chem. Int. Ed.* **54**, 14372–14377 (2015).
24. Materials and methods are available as supplementary materials on *Science* Online.
25. F. Studt *et al.*, *Science* **320**, 1320–1322 (2008).
26. K. S. Walton, D. S. Sholl, *AIChE J.* **61**, 2757–2762 (2015).
27. R. Krishna, *RSC Adv.* **5**, 52269–52295 (2015).

ACKNOWLEDGMENTS

This work is supported by the National Natural Science Foundation of China (grants 21222601, 21436010, and 21476192), Zhejiang Provincial Natural Science Foundation of China (grant LR13B060001), Ten Thousand Talent Program of China (to H.X.), the Welch Foundation (grant AX-1730), King Abdullah Science and Technology University Office of Competitive Research Funds (grant URF/1/1672-01-01), and the Science Foundation Ireland (award 13/RP/B2549 to M.Z.). We thank T. L. Hu, Y. F. Zhao, W. D. Shan, and M. D. Jiang for their help and arrangement of the breakthrough experiments; A. Kumar for help with sample characterization; and Z. G. Zhang and B. G. Su for discussions of the experiments. Metrical data for the solid-state structures of SIFSIX-2-Cu-i·C_2D_2 and SIFSIX-1-Cu·C_2D_2 are available free of charge from the Cambridge Crystallographic Data Centre under reference numbers CCDC 1471795 and 1471796.

The authors and their affiliated institutions have filed a patent application related to the results presented here.

SUPPLEMENTARY MATERIALS

www.sciencemag.org/content/353/6295/141/suppl/DC1
Materials and Methods
Figs. S1 to S32
Tables S1 to S15
References (*28*–*34*)

12 January 2016; accepted 5 May 2016
Published online 19 May 2016
10.1126/science.aaf2458

ORGANIC CHEMISTRY

Copper-catalyzed asymmetric addition of olefin-derived nucleophiles to ketones

Yang Yang,[1] Ian B. Perry,[1] Gang Lu,[2] Peng Liu,[2]* Stephen L. Buchwald[1]*

Enantioenriched alcohols found in an array of bioactive natural products and pharmaceutical agents are often synthesized by asymmetric nucleophilic addition to carbonyls. However, this approach generally shows limited functional-group compatibility, requiring the use of preformed organometallic reagents in conjunction with a stoichiometric or substoichiometric amount of chiral controller to deliver optically active alcohols. Herein we report a copper-catalyzed strategy for the stereoselective nucleophilic addition of propargylic and other alkyl groups to ketones, using easily accessible (poly)unsaturated hydrocarbons as latent carbanion equivalents. Our method features the catalytic generation of highly enantioenriched organocopper intermediates and their subsequent diastereoselective addition to ketones, allowing for the effective construction of highly substituted stereochemical dyads with excellent stereocontrol. Moreover, this process is general, scalable, and occurs at ambient temperature.

Stereochemically complex alcohols in optically pure form are commonly encountered structural elements in a diverse range of pharmaceutical drugs and biologically active natural products (Fig. 1A). Consequently, general methods that allow for the stereoselective assembly of highly substituted alcohols have long been sought (*1*). The discovery of Grignard reagents and their subsequent addition to ketones and aldehydes have been widely considered as milestones in synthetic chemistry, giving rise to a general synthesis of alcohols from preformed organomagnesium reagents and broadly available carbonyl compounds (*2*). Since then, extensive efforts have been devoted to the development of asymmetric variants of nucleophilic addition reactions to carbonyls, using preformed organometallic reagents (*1*, *3*–*7*). These synthetic endeavors have proven to be exceptionally fruitful, culminating in a variety of protocols for enantioselective additions to carbonyls, using either a chiral auxiliary-modified organometallic reagent or a substoichiometric amount of chiral controller to achieve excellent levels of stereocontrol. Compared with aldehydes, however, the asymmetric nucleophilic addition to ketones has been studied to a lesser extent (*5*–*7*).

Although numerous advances have been made in this area, considerable hurdles have impeded the further adaptation of these methods by the synthetic community. The requirement to prepare and use a stoichiometric quantity of an organometallic reagent complicates most of the existing methods. In addition, the highly nucleophilic and basic nature of organometallic reagents has posed substantial limitations with respect to the functional-group compatibility of these processes. As a consequence, these methods are typically not amenable to the transformation of late-stage intermediates and other highly functionalized molecules. Furthermore, an additional synthetic operation is required to prepare these organometallic reagents from organic halide or unsaturated hydrocarbon precursors, imposing further constraints on the types of nucleophiles suitable for carbonyl addition.

In this context, a catalytic method for stereoselective additions to carbonyls, using easily accessible olefins as latent carbanion equivalents in

[1]Department of Chemistry, Massachusetts Institute of Technology (MIT), Cambridge, MA 02139, USA. [2]Department of Chemistry, University of Pittsburgh, Pittsburgh, PA 15260, USA.
*Corresponding author. Email: pengliu@pitt.edu (P.L.); sbuchwal@mit.edu (S.L.B.)

lieu of preformed organometallic reagents, would circumvent these issues and greatly expand the scope of stereochemically well-defined alcohols accessible from carbonyl addition processes. In elegant work using Ru-, Rh-, and Ir-based noble metal catalysts, Krische and co-workers have pioneered the development of a range of synthetically versatile stereoselective coupling reactions of olefins and carbonyls under hydrogenation and transfer hydrogenation conditions (*8*–*10*). To date, however, the synthesis of sterically demanding tertiary alcohols from simple ketones remains challenging with these processes, in part because of the increased steric hindrance and the attenuated electrophilicity of ketones relative to aldehydes. In a mechanistically distinct approach, Montgomery, Jamison, and colleagues have devised novel Ni-based methods for the enantioselective reductive coupling of alkynes and aldehydes (*11*–*14*). Additionally, Hoveyda and co-workers have developed exceptional copper-catalyzed borylative processes for the addition of olefin-derived nucleophiles bearing a boryl moiety to carbonyls. This chemistry has been highly successful in the enantioselective preparation of secondary alcohols from aldehydes (*15*, *16*), although ketones represent more challenging substrates for this enantioselective process (*16*). Alkenes and ketones constitute two of the most widely available building blocks for organic synthesis. Nevertheless, a broadly applicable and highly enantioselective catalyst system for the coupling of these orthogonal feedstocks remains elusive.

We have recently become interested in the development of copper(I) hydride (CuH) catalysis

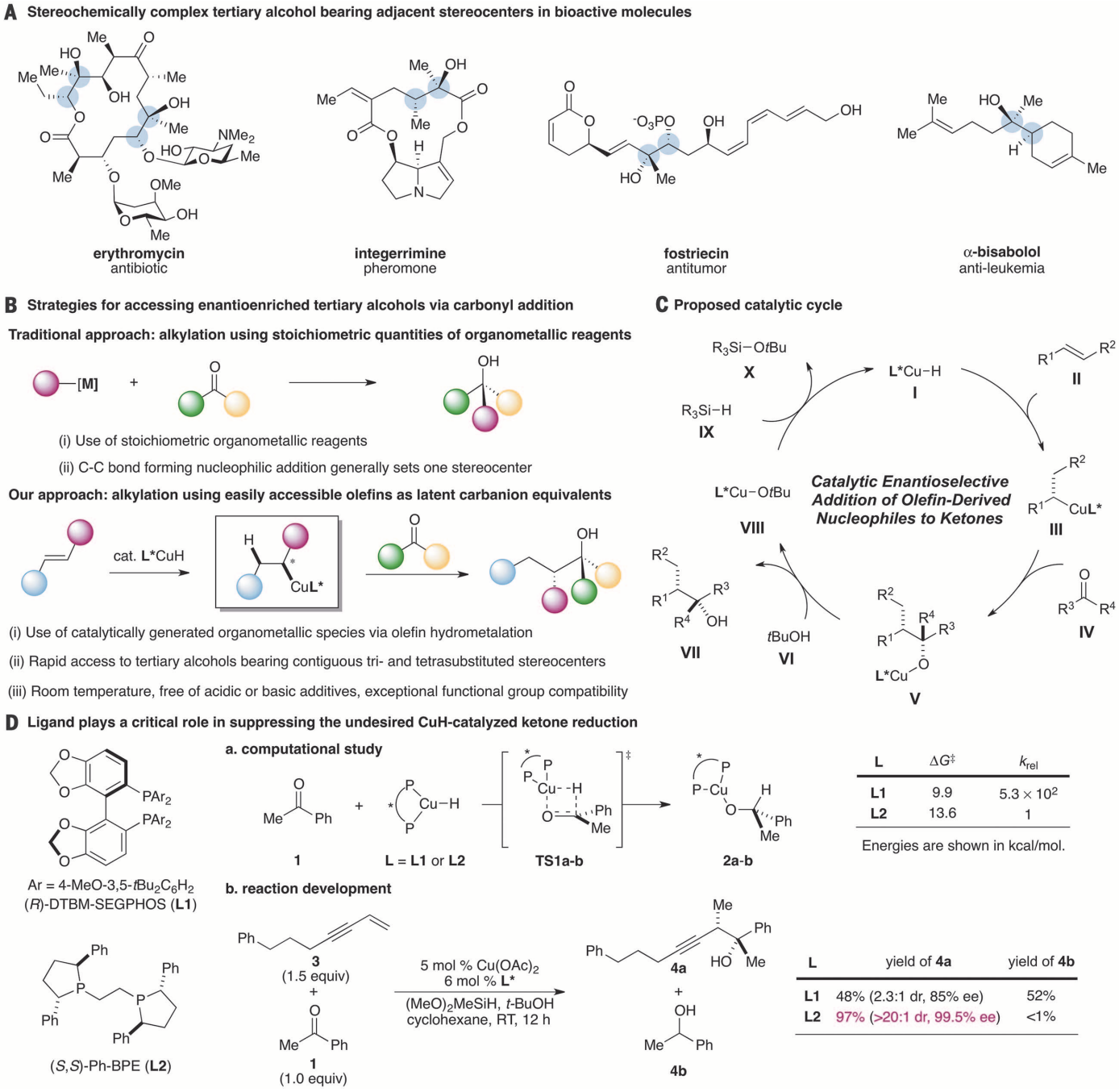

Fig. 1. (A to D) Asymmetric addition of olefin-derived nucleophiles to ketones, using a copper-hydride catalyst. M, metal; L, ligand; R^1 to R^4, generic substituent; *t*Bu, *tert*-butyl; Ph, phenyl; RT, room temperature; k_{rel}, relative rate constant.

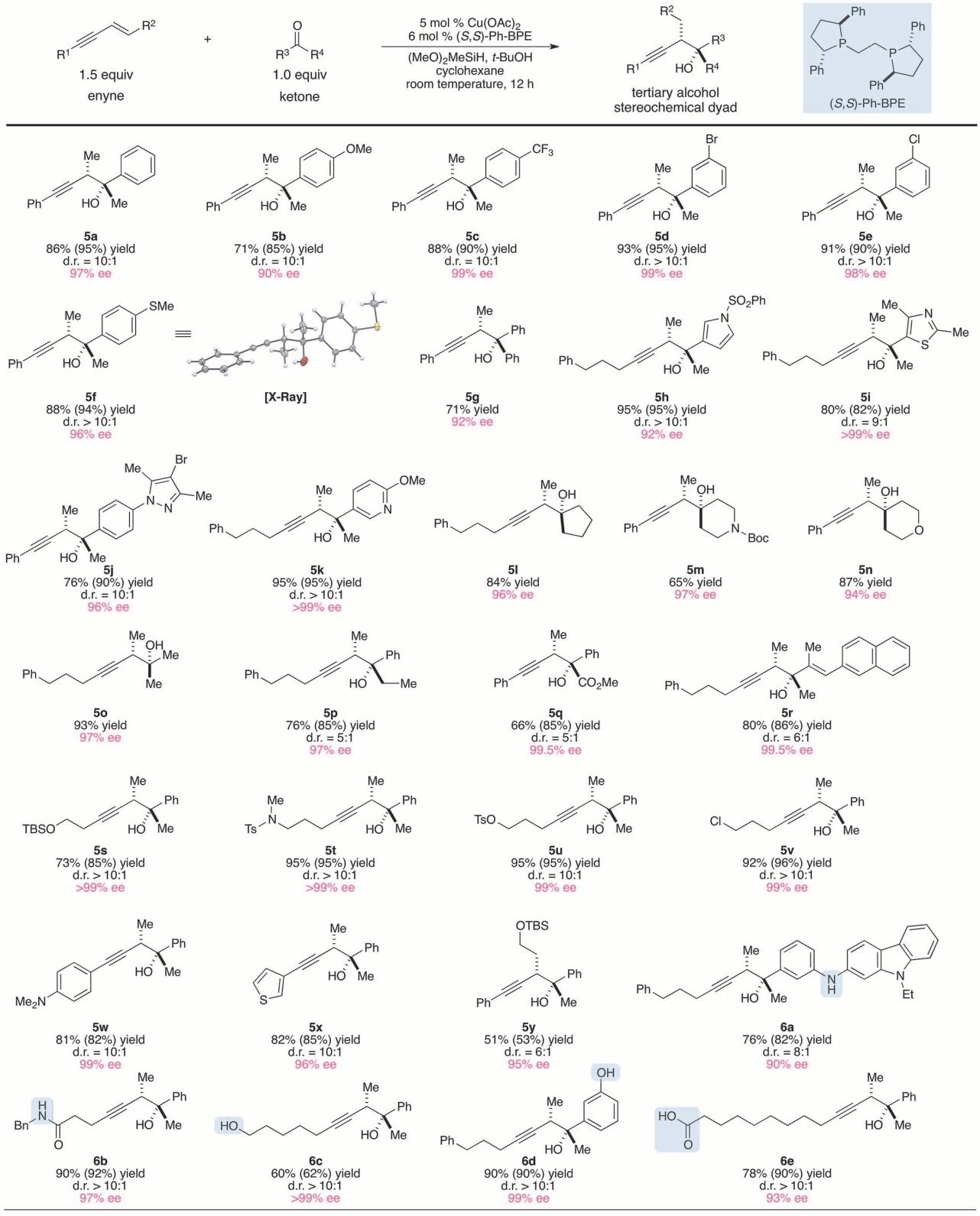

Fig. 2. Substrate scope of the copper-catalyzed diastereo- and enantioselective addition of enyne-derived nucleophiles to ketones. Reaction conditions: $Cu(OAc)_2$ (0.5 mol %), (*S*,*S*)-Ph-BPE (6 mol %), ketone [0.5 mmol, 1.0 equivalents (equiv)], enyne (0.75 mmol, 1.5 equiv), *t*-BuOH (0.5 mmol, 1 equiv), $(MeO)_2MeSiH$ (2.5 mmol, 5 equiv), RT, 12 hours. Yields refer to isolated yields of the major diastereomer (>10:1 dr). Yields in parentheses refer to the combined yields of two diastereomers determined by ^1H nuclear magnetic resonance (NMR) spectroscopy calibrated using an internal standard. The dr values were determined by ^1H NMR spectroscopic analysis of the crude reaction mixture, and the ee values were determined by chiral high-performance liquid chromatography analysis. TBS, *tert*-butyldimethylsilyl; Ts, tosyl; Et, ethyl. Blue shading highlights the functional group present in the starting material.

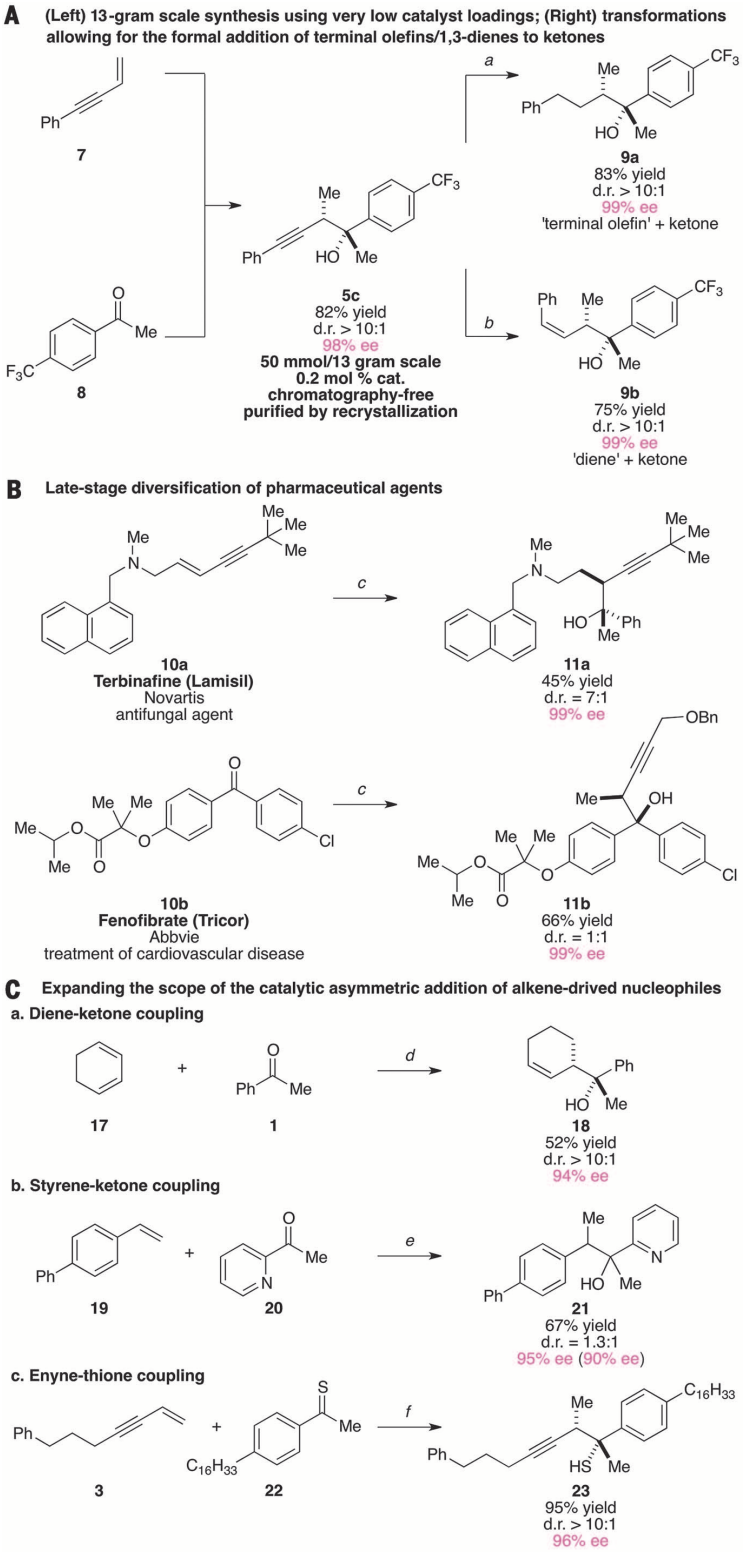

Fig. 3. Application and further extension of the copper-catalyzed asymmetric addition of olefin-derived nucleophiles. (**A**) *a*: $Pd(OH)_2$/C, H_2 (balloon pressure), MeOH, RT, 12 hours. *b*: 5 mol % IPrCuCl, 6 mol % Li*O*tBu, $(MeO)_2MeSiH$, *t*-BuOH, toluene, RT, 48 hours. (**B**) *c*: 5 mol % $Cu(OAc)_2$, 6 mol % (*S*,*S*)-Ph-BPE, $(MeO)_2MeSiH$, *t*-BuOH, cyclohexane, RT, 12 hours. (**C**) *d*: 5 mol % $Cu(OAc)_2$, 6 mol % (*S*,*S*)-Ph-BPE, **17** (2.0 equiv), **1** (1.0 equiv), $(MeO)_2MeSiH$, tetrahydrofuran, RT, 12 hours. *e*: 5 mol % $Cu(OAc)_2$, 6 mol % (*S*,*S*)-Ph-BPE, **19** (2.0 equiv), **20** (1.0 equiv), $(MeO)_2MeSiH$, methyl *tert*-butyl ether, RT, 12 hours. *f*: 5 mol % $Cu(OAc)_2$, 6 mol % (*S*,*S*)-Ph-BPE, **3** (1.5 equiv), **22** (1.0 equiv), $(MeO)_2MeSiH$, *t*-BuOH, cyclohexane, RT, 12 hours.

as a general means of accessing enantioenriched alkylcopper intermediates from readily available olefin precursors. By employing a class of electrophilic aminating reagents established by Berman and Johnson (*17*) to intercept these organometallic intermediates, our laboratory (*18*) and Miura, Hirano, and colleagues (*19*–*21*) have independently developed a CuH-catalyzed approach for the enantioselective hydroamination of olefins (*22*). On the basis of these studies and notable contributions from other groups in the area of copper-catalyzed enantioselective reductive aldol reactions (*6*, *7*, *23*–*26*), we envisioned the development of CuH chemistry as a general platform for the use of simple olefins as latent carbon nucleophiles in carbonyl addition (Fig. 1B). In particular, we were interested in investigating the coupling of (poly)unsaturated hydrocarbons and ketones via the diastereoselective addition of catalytically generated chiral organocopper intermediates to the carbonyl group. If successful, our proposed strategy would enable the use of an earth-abundant first-row transition metal catalyst for the diastereo- and enantioselective synthesis of alcohols, including those possessing vicinal tri- and tetrasubstituted stereogenic centers from olefins and carbonyls.

Our proposed catalytic cycle is illustrated in Fig. 1C. Enantioselective addition of a phosphine-bound copper hydride catalyst (**I**) across the C=C double bond of an olefin (**II**) would lead to the formation of an alkylcopper intermediate (**III**). Interception of this nascent alkylcopper intermediate with a ketone (**IV**) would provide the alkoxycopper species **V**. Ligand exchange of **V** with *tert*-butanol (**VI**) would furnish the asymmetric addition product (**VII**) and release copper *tert*-butoxide (**VIII**). Upon undergoing a σ-bond metathesis with hydrosilane **IX**, **VIII** would then regenerate the copper hydride catalyst (**I**) and complete the catalytic cycle. The mechanistic proposal outlined herein does not require the use of any exogenous acidic or basic additives for substrate or catalyst activation, thereby potentially allowing for a range of sensitive functional groups to be tolerated. Mechanistically, in contrast to the majority of previously developed transition metal–catalyzed reductive couplings (*8*–*14*), the strategy we envisioned does not involve redox processes at the copper(I) center while allowing for the polar and nonpolar building blocks to couple in a reductive fashion. Additionally, inexpensive and mild silane reagents are used as the reductant for the catalytic generation of organocopper intermediates.

At the outset, we recognized that the successful implementation of our proposed strategy would depend on unprecedented chemo- and stereoselectivity with respect to the copper catalyst. The competitive hydrocupration of the carbonyl coupling partner is known to be a facile process and would lead to its unproductive reduction. Moreover, important work by Lipshutz and coworkers has demonstrated that the copper hydride species based on DTBM-SEGPHOS [DTBM, 3,5-di-*tert*-butyl-4-methoxyphenyl; SEGPHOS, 4,4′-bi-1,3-benzodioxole-5,5′-diylbis(diphenylphosphane)]

(**L1**), our optimal catalyst for olefin hydroamination (*18*), is highly robust and efficient for the asymmetric reduction of a variety of carbonyls, including ketones (*27*). On the other hand, the alkylcopper intermediate generated from olefin hydrometalation would need to be nucleophilic enough to facilitate the alkylation of a range of unactivated ketones, a process that has proven challenging with other transition metal catalysts. Nevertheless, we reasoned that judicious choice of the copper catalyst could suppress the undesired ketone reduction while still allowing for the effective olefin hydrocupration, as well as ketone alkylation. Furthermore, we postulated that it would be feasible to access a catalyst capable of imposing effective stereochemical facial discrimination on the prochiral olefin and the ketone to achieve high levels of enantio- and diastereoselectivity.

We focused our initial investigation on the transformation of enynes, a subset of olefins that could be conveniently prepared from terminal alkynes in a single operation. Previous work on the use of enynes for transition metal–catalyzed reductive and borylative transformations (*15*, *28*–*30*) led us to postulate that these enyne substrates could serve as a suitable starting point for our investigations, because hydrocupration of these substrates might be facilitated by the formation of an alkylcopper species stabilized by a neighboring alkynyl group. From the standpoint of utility, the enantioselective coupling of enynes to ketones would furnish synthetically versatile homopropargyl alcohol products (*31*–*33*). Prior to our experimental studies, we carried out density functional theory (DFT) calculations to gain some insight into the ligand effects on the ketone reduction and olefin hydrocupration processes (Fig. 1D). Our computational studies revealed that, although the hydrocupration of ketones is a kinetically facile and highly exergonic process, the choice of the ancillary phosphine ligand could dramatically influence the reactivity of the **L***CuH species. In particular, although the reduction of ketone **1** with a catalyst generated from DTBM-SEGPHOS requires a low activation energy ($\Delta G^{\ddagger}$) of 9.9 kcal/mol, the same process is less facile when other commercially available ligands are employed. In particular, the use of a catalyst derived from Ph-BPE {(*S*,*S*)-Ph-BPE, (−)-1,2-bis[(2*S*,5*S*)-2,5-diphenylphospholano]ethane} (**L2**), another ligand previously employed in CuH chemistry (*20*, *34*), results in a higher activation energy ($\Delta G^{\ddagger}$ = 13.6 kcal/mol). Furthermore, our calculations suggested that the activation barrier for the hydrocupration of enyne **3** is 1.3 kcal/mol lower than that of ketone **1** with this Ph-BPE–based

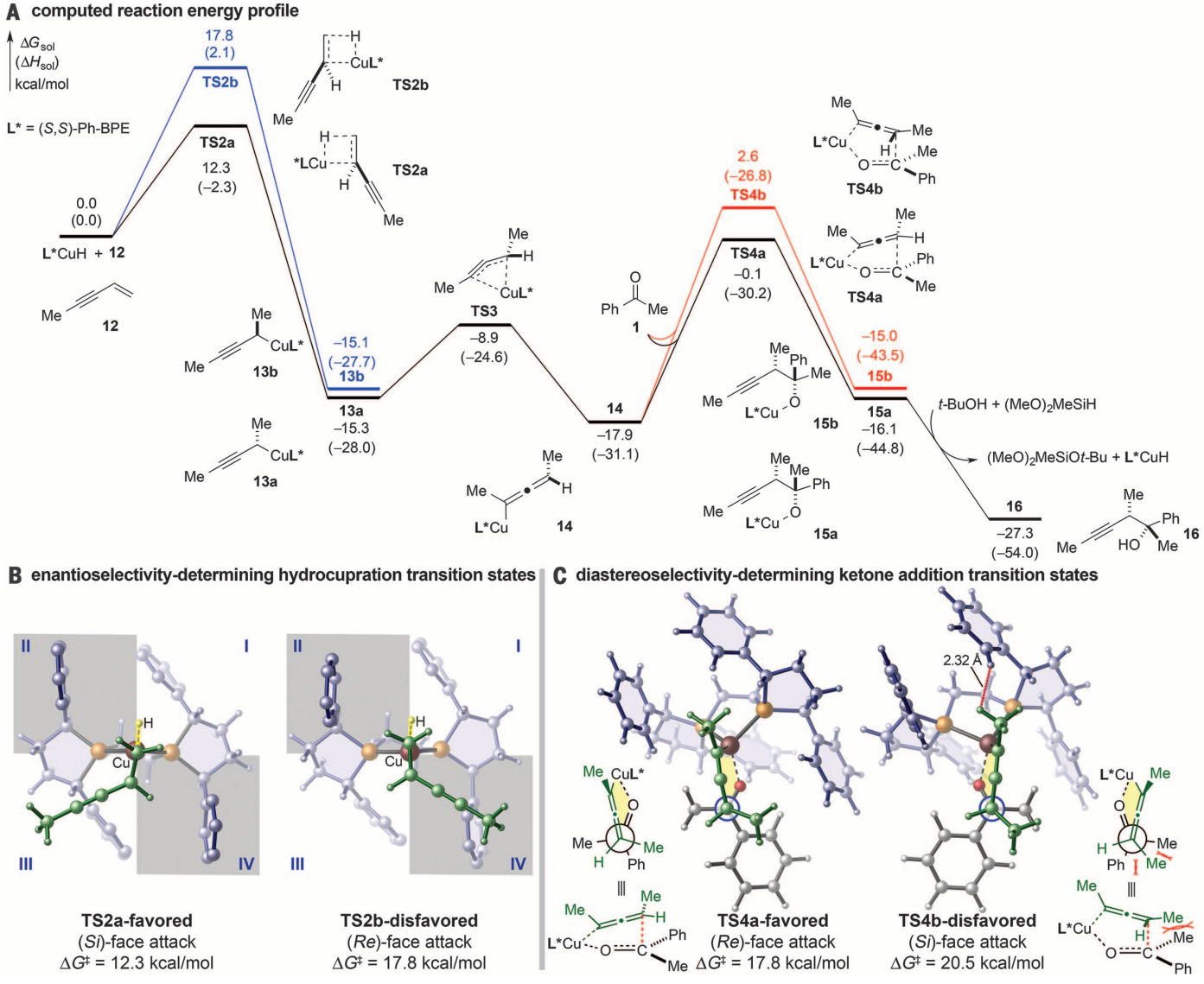

Fig. 4. DFT-calculated enantio- and diastereochemical–determining transition states for the copper-catalyzed addition of an enyne (12)–derived nucleophile to ketone 1. (**A** to **C**) Energies were calculated at the M06/SDD–6-311+G(d,p)/SMD(cyclohexane) level of theory with geometries optimized at the B3LYP/SDD–6-31G(d) level. ΔG_{sol}, free energy of activation; ΔH_{sol}, enthalpy of activation. In (B), roman numerals denote the four quadrants of the coordination space; green indicates the enyne substrate; yellow indicates the hydride of LCuH. In (C), green indicates the chiral allenyl moiety; yellow indicates a six-membered ring.

catalyst, indicating the feasibility of chemoselective enyne hydrocupration in the presence of ketones. These computational trends were corroborated by our experimental efforts to identify suitable conditions for the enantioselective addition of enyne-derived nucleophiles to ketones. The use of a catalyst based on DTBM-SEGPHOS produced the coupled product **4a** in only 48% yield with moderate stereoselectivity [2.3:1 diastereomeric ratio (dr), 85% enantiomeric excess (ee)], along with a substantial amount of reduction product **4b** (52% yield). In contrast, under the optimized reaction conditions employing Ph-BPE as the ligand, the coupled product bearing adjacent tertiary and quaternary stereocenters (**4a**) formed in 97% yield with excellent diastereo- and enantiocontrol (>20:1 dr, 99.5% ee).

We next set out to examine the substrate scope of this enyne-ketone coupling process (Fig. 2). Electron-rich and electron-deficient acetophenones were successfully transformed into the corresponding tertiary alcohols (**5b** and **5c**) in good yield with excellent diastereo- and enantioselectivity. Ketones bearing aryl bromide (**5d**) and chloride (**5e**) functional groups were also compatible with our protocol, permitting further transformations of the alcohol product using cross-coupling technologies. Additionally, a variety of nitrogen heterocycles that are frequently found in medicinally active agents, including a pyrrole (**5h**), a thiazole (**5i**), a pyrazole (**5j**), a pyridine (**5k**), a thiophene (**5x**), and a carbazole (**6a**), could be applied with this stereoselective coupling. Appreciably less reactive aliphatic ketones could also be effectively converted into tertiary aliphatic alcohols with excellent enantioselectivity (**5l** to **5o**), further highlighting the excellent reactivity exhibited by this Ph-BPE–based alkylcopper intermediate. An α-ketoester (**5q**) and an enone (**5r**) also underwent the asymmetric carbonyl addition with outstanding enantiocontrol. Moreover, the current process displayed a broad scope with respect to the enyne fragment. In addition to enynes bearing aromatic substituents, aliphatic enynes were also readily accommodated under these reaction conditions (**5h**, **5i**, **5r** to **5v**, and **6a** to **6e**). Finally, substitution at the olefinic terminus of the enyne component (**5y**) was found to be compatible with our protocol.

The mildness of the reaction conditions required for the current asymmetric nucleophilic addition allowed for the use of substrates possessing sensitive functional groups that are incompatible with preformed organometallic reagents. A variety of sensitive functional groups, such as a thioether (**5f**), a sulfonamide (**5t**), a methyl ester (**5q**), an alkyl tosylate (**5u**), an alkyl chloride (**5v**), and a tertiary amine (**5w**), were tolerated under these reaction conditions. Most usefully, various basic and acidic functional groups, including a secondary amine (**6a**), a secondary amide (**6b**), an alcohol (**6c**), a phenol (**6d**), and a carboxylic acid (**6e**), were compatible with our protocol, thereby eliminating the need for inefficient protection and deprotection sequences often required by traditional carbonyl alkylation methodologies that use stoichiometric organometallic reagents. The relative and absolute stereochemistry of the addition product were determined by x-ray crystallographic analysis of **5f**.

In addition, this copper-catalyzed enantioselective coupling process proved to be scalable and required a very low catalyst loading (Fig. 3A). We were able to perform a 50-mmol-scale (13-g-scale) reaction to prepare **5c**, using only 0.2 mole % (mol %) $Cu(OAc)_2$ (OAc, acetate) and 0.4 mol % (*S*,*S*)-Ph-BPE without lowering the yield or the stereoselectivity of the transformation (82% yield, 10:1 dr, 98% ee). The scalability and robustness of this copper-catalyzed asymmetric transformation illustrate its potential application in the manufacture of highly enantioenriched fine chemicals on an industrial scale. Furthermore, these synthetically versatile homopropargyl alcohols prepared by our method could easily be transformed into a variety of useful molecular architectures. For example, hydrogenation and CuH-catalyzed cis-selective semireduction of alkyne **5c** (*35*) furnished saturated alcohol **9a** and homoallylic alcohol **9b** as a single stereoisomer, respectively. These reactions allowed for the synthetic equivalent of asymmetric addition to ketones with nucleophiles derived from terminal aliphatic olefins and 1,3-dienes in a highly regio-, diastereo-, and enantioselective fashion.

The late-stage modification of medicinally relevant molecules allows for the rapid generation of analogous bioactive compounds and facilitates structure-activity relationship studies. To further demonstrate the synthetic utility of our method in this context, we selected two widely prescribed pharmaceutical agents, terbinafine (Lamisil, **10a**) and fenofibrate (Tricor, **10b**) and subjected them to our coupling protocol (Fig. 3B). Both substrates were effectively converted into the tertiary alcohol adduct with excellent levels of enantioselectivity (99% ee for each), further highlighting the utility of our method in a more complex setting.

We also performed DFT calculations to investigate the mechanism and the origin of stereoselectivity of this copper-catalyzed enyne-ketone coupling. The computed free energy profile of the overall catalytic cycle is shown in Fig. 4A (see supplementary materials for a detailed discussion). Our computational studies suggest that the initial enyne hydrocupration is irreversible and thus constitutes the enantio-determining step for this reaction. The hydrocupration involves a four-membered transition state in which the delivery of the hydride and the formation of the Cu–C bond take place simultaneously. To better understand the enantioinduction that occurs during the hydrocupration event, we divided the coordination space of this C_2 symmetric copper catalyst into four quadrants (Fig. 4B). The phenyl substituents on the ligand's phospholane moieties in quadrants II and IV point out of the plane of the paper, rendering these two quadrants sterically inaccessible for a substrate coming toward this plane. In contrast, quadrants I and III are relatively unencumbered, with the two phenyl groups pointing away from the plane of the paper. In **TS2a**, the unfavorable repulsion between the olefin's alkynyl substituent and the catalyst's sterically crowded quadrant IV is avoided, thereby leading to the preferential formation of the (*S*)-propargylcopper intermediate **13a**, with an activation free energy that is 5.5 kcal/mol lower than the disfavored transition state **TS2b**.

Subsequent 1,3-isomerization of the highly enantioenriched propargylcopper **13a** proceeds in a stereospecific fashion, affording an axially chiral allenylcopper intermediate **14** as a single diastereomer. Furthermore, this 1,3 shift is found to be facile and exergonic (ΔG = −2.6 kcal/mol), thus setting the stage for the ketone addition involving a six-membered cyclic transition state (Fig. 4C). In the lowest-energy transition states of this diastereoselectivity-determining step (**TS4a** and **TS4b**), the phenyl group of the ketone is oriented anti to the allenylcopper [i.e., gauche to the methyl (Me) and H substituents on the distal terminus of the allenyl moiety] to avoid close contact with the Ph-PBE ligand (see supplementary materials for details). In the preferred diastereomeric transition state **TS4a**, the chiral allenyl moiety (highlighted in green) attacks the (*Re*)-face of the ketone, placing the hydrogen atom of the allene gauche to the methyl and the phenyl groups flanking the carbonyl group. In the disfavored transition state **TS4b** [(*Si*)-face attack], the bulkier Me group of the allene is oriented gauche to the two carbonyl substituents. In addition, **TS4b** is also destabilized by the proximity of the allenyl moiety with the Ph-BPE ligand, as evidenced by a relatively short H···H distance of 2.32 Å. Taken together, the substrate-substrate and ligand-substrate interactions combine to confer high levels of diastereocontrol in the C–C bond forming event leading to the homopropargyl copper alkoxide (**15a**) and, eventually, the homopropargyl alcohol product (**16**).

In preliminary studies, we have demonstrated that a range of other structurally diversified olefins could also be employed in this mode of catalysis in a highly enantioselective fashion (Fig. 3C). By applying slightly modified reaction conditions, a related process with a cyclic diene (**17**) and acetophenone (**1**) afforded tertiary alcohols possessing contiguous tertiary and quaternary stereocenters in >10:1 dr and 94% ee. Styrenes (**19**), a class of abundant feedstock chemicals possessing moderate levels of reactivity toward hydrometalation, were also effectively converted into the tertiary alcohol adduct with excellent enantiocontrol (95% ee). Furthermore, thione **22**, which could easily be synthesized from the parent ketone, was also suitable for this coupling process. The highly enantioselective preparation of tertiary thiol **23** (>10:1 dr, 96% ee) using our strategy represents a synthetically valuable advance, given that enantioenriched thiols are prevalent structural motifs in a variety of small-molecule therapeutics, and only a handful of enantioselective methods are available for their preparation (*36*).

Our strategy represents a departure from the use of preformed organometallic reagents in classic carbonyl addition chemistry. Furthermore, this C–C bond forming process readily accommodates a wide range of olefin and ketone coupling partners, allowing for the highly stereoselective

preparation of alcohols bearing adjacent tri- and tetrasubstituted stereogenic centers. We anticipate that the design of optimal ligand scaffolds will enable the transformation of a broader range of unactivated olefins, ultimately delivering a powerful tool for the asymmetric addition of olefin-derived nucleophiles to carbonyls that will be of broad synthetic utility.

REFERENCES AND NOTES

1. E. J. Corey, L. Kürti, *Enantioselective Chemical Synthesis: Methods, Logic and Practice* (Direct Book Publishing, 2010).
2. P. Knochel *et al*., *Angew. Chem. Int. Ed.* **42**, 4302–4320 (2003).
3. R. Noyori, M. Kitamura, *Angew. Chem. Int. Ed. Engl.* **30**, 49–69 (1991).
4. L. Pu, H.-B. Yu, *Chem. Rev.* **101**, 757–824 (2001).
5. J. L. Stymiest, V. Bagutski, R. M. French, V. K. Aggarwal, *Nature* **456**, 778–782 (2008).
6. O. Riant, J. Hannedouche, *Org. Biomol. Chem.* **5**, 873–888 (2007).
7. M. Shibasaki, M. Kanai, *Chem. Rev.* **108**, 2853–2873 (2008).
8. H.-Y. Jang, M. J. Krische, *Acc. Chem. Res.* **37**, 653–661 (2004).
9. E. Skucas, M.-Y. Ngai, V. Komanduri, M. J. Krische, *Acc. Chem. Res.* **40**, 1394–1401 (2007).
10. J. F. Bower, I. S. Kim, R. L. Patman, M. J. Krische, *Angew. Chem. Int. Ed.* **48**, 34–46 (2009).
11. M. R. Chaulagain, G. J. Sormunen, J. Montgomery, *J. Am. Chem. Soc.* **129**, 9568–9569 (2007).
12. E. P. Jackson *et al*., *Acc. Chem. Res.* **48**, 1736–1745 (2015).
13. K. M. Miller, W.-S. Huang, T. F. Jamison, *J. Am. Chem. Soc.* **125**, 3442–3443 (2004).
14. R. M. Moslin, K. Miller-Moslin, T. F. Jamison, *Chem. Commun.* **2007**, 4441–4449 (2007).
15. F. Meng, F. Haeffner, A. H. Hoveyda, *J. Am. Chem. Soc.* **136**, 11304–11307 (2014).
16. F. Meng, H. Jang, B. Jung, A. H. Hoveyda, *Angew. Chem. Int. Ed.* **52**, 5046–5051 (2013).
17. A. M. Berman, J. S. Johnson, *J. Am. Chem. Soc.* **126**, 5680–5681 (2004).
18. M. T. Pirnot, Y.-M. Wang, S. L. Buchwald, *Angew. Chem. Int. Ed.* **55**, 48–57 (2016).
19. Y. Mikki, K. Hirano, T. Satoh, M. Miura, *Angew. Chem. Int. Ed.* **52**, 10830–10834 (2013).
20. Y. Mikki, K. Hirano, T. Satoh, M. Miura, *Org. Lett.* **16**, 1498–1501 (2014).
21. D. Nishikawa, K. Hirano, M. Miura, *J. Am. Chem. Soc.* **137**, 15620–15623 (2015).
22. Y. Xi, T. W. Butcher, J. Zhang, J. F. Hartwig, *Angew. Chem. Int. Ed.* **55**, 776–780 (2016).
23. J. Deschamp, O. Chuzel, J. Hannedouche, O. Riant, *Angew. Chem. Int. Ed.* **45**, 1292–1297 (2006).
24. D. Zhao, K. Oisaki, M. Kanai, M. Shibasaki, *J. Am. Chem. Soc.* **128**, 14440–14441 (2006).
25. B. H. Lipshutz, B. Amorelli, J. B. Unger, *J. Am. Chem. Soc.* **130**, 14378–14379 (2008).
26. A. Saxena, B. Choi, H. W. Lam, *J. Am. Chem. Soc.* **134**, 8428–8431 (2012).
27. B. H. Lipshutz, K. Noson, W. Chrisman, A. Lower, *J. Am. Chem. Soc.* **125**, 8779–8789 (2003).
28. L. M. Geary, S. K. Woo, J. C. Leung, M. J. Krische, *Angew. Chem. Int. Ed.* **51**, 2972–2976 (2012).
29. V. Komanduri, M. J. Krische, *J. Am. Chem. Soc.* **128**, 16448–16449 (2006).
30. Y. Sasaki, Y. Horita, C. Zhong, M. Sawamura, H. Ito, *Angew. Chem. Int. Ed.* **50**, 2778–2782 (2011).
31. C.-H. Ding, X.-L. Hou, *Chem. Rev.* **111**, 1914–1937 (2011).
32. S.-L. Shi, L.-W. Xu, K. Oisaki, M. Kanai, M. Shibasaki, *J. Am. Chem. Soc.* **132**, 6638–6639 (2010).
33. K. R. Fandrick *et al*., *J. Am. Chem. Soc.* **133**, 10332–10335 (2011).
34. E. Ascic, S. L. Buchwald, *J. Am. Chem. Soc.* **137**, 4666–4669 (2015).
35. A. M. Whittaker, G. Lalic, *Org. Lett.* **15**, 1112–1115 (2013).
36. J. Clayden, P. Maclellan, *Beilstein J. Org. Chem.* **7**, 582–595 (2011).

ACKNOWLEDGMENTS

We are grateful to the NIH (grant GM 46059 to S.L.B.), the Undergraduate Research Opportunities Program at MIT (I.B.P.), and the University of Pittsburgh (P.L.) for financial support. The content in this paper is solely the responsibility of the authors and does not necessarily represent the official views of the NIH. We thank Y.-M. Wang and M. T. Pirnot (MIT) for advice on the preparation of this manuscript and P. Müller (MIT) for x-ray crystallographic analysis of **5f**. Cambridge Crystallographic Data Centre accession number 1470340 contains the supplementary crystallographic data for **5f**. Calculations were performed at the Center for Simulation and Modeling at the University of Pittsburgh and the Extreme Science and Engineering Discovery Environment (XSEDE) supported by the NSF.

SUPPLEMENTARY MATERIALS

www.sciencemag.org/content/353/6295/144/suppl/DC1
Materials and Methods
Figs. S1 to S12
Table S1
References (*37*–*50*)
NMR Spectra
HPLC Traces

28 March 2016; accepted 20 May 2016
Published online 9 June 2016
10.1126/science.aaf7720

CATALYSIS

Thermally stable single-atom platinum-on-ceria catalysts via atom trapping

John Jones,[1]* Haifeng Xiong,[1]* Andrew T. DeLaRiva,[1] Eric J. Peterson,[1] Hien Pham,[1] Sivakumar R. Challa,[1] Gongshin Qi,[2] Se Oh,[2] Michelle H. Wiebenga,[2] Xavier Isidro Pereira Hernández,[3] Yong Wang,[3,4] Abhaya K. Datye[1]†

Catalysts based on single atoms of scarce precious metals can lead to more efficient use through enhanced reactivity and selectivity. However, single atoms on catalyst supports can be mobile and aggregate into nanoparticles when heated at elevated temperatures. High temperatures are detrimental to catalyst performance unless these mobile atoms can be trapped. We used ceria powders having similar surface areas but different exposed surface facets. When mixed with a platinum/aluminum oxide catalyst and aged in air at 800°C, the platinum transferred to the ceria and was trapped. Polyhedral ceria and nanorods were more effective than ceria cubes at anchoring the platinum. Performing synthesis at high temperatures ensures that only the most stable binding sites are occupied, yielding a sinter-resistant, atomically dispersed catalyst.

Diesel oxidation catalysts (DOCs) are used in the automotive industry to oxidize harmful emissions that contain CO, NO, and hydrocarbons. Pt is very active for such oxidation reactions (*1*, *2*). Under oxidizing conditions at high temperatures, the Pt nanoparticles on the oxide support sinter to form large particles, which leads to a loss of surface area and hence decreased catalytic activity, so there is commercial interest in developing sinter-resistant catalysts that can maintain activity over long-term operation. We previously found that the mechanism of activity loss involves the emission of mobile species from small particles and their capture by large particles—a process called Ostwald ripening (*3*, *4*). Here, we show that the conditions under which nanoparticles emit mobile species are also ideally suited to generating atomically dispersed catalysts if the mobile species can be effectively trapped. Platinum group metals can be trapped in ionic form in complex oxides (*5*), but they can be lost inside the bulk oxide, where they are no longer effective as a catalyst. An ideal support for trapping metal species is one in which the mobile species stay at the surface so that they retain catalytic activity.

Our studies were performed at 800°C in oxidizing ambient conditions typically used for accelerated testing of DOCs. Under these conditions, Pt can be emitted as volatile PtO_2 (*6*) which can lead to transport of Pt from the DOC catalyst to the downstream selective catalytic reduction (SCR) catalyst (*7*). A vapor-phase approach for the synthesis of catalysts—specifically, transferring Pt from a metal foil to alumina—was reported previously (*8*), but the ability of supports such as ceria to trap atomically dispersed Pt was not recognized. In industry, the vapor-phase transport of metal oxides is regarded as a leading cause of catalyst degradation (*9*). Thus, we set out to find materials that could effectively trap the mobile species. In previous work, we found that PdO was able to trap mobile PtO_2, forming metallic Pt-Pd particles (*10*). The remarkable efficiency of PdO for trapping Pt suggests that other oxides could play a similar role. McVicker *et al*. (*11*) had implied that CaO, SrO, and BaO may slow the rates of Ir sintering through the presence of acid sites on the support.

We worked with ceria as a support because Ce-Zr-Y was shown by Nagai *et al*. (*12*) to be effective for inhibiting the sintering of Pt by

[1]Department of Chemical and Biological Engineering and Center for Micro-Engineered Materials, University of New Mexico, Albuquerque, NM 87131, USA. [2]General Motors Global R&D, 30500 Mound Road, Warren, MI 48090, USA. [3]Voiland School of Chemical Engineering and Bioengineering, Washington State University, Pullman, WA 99164, USA. [4]Institute for Integrated Catalysis, Pacific Northwest National Laboratory, Richland, WA 99354, USA.
*These authors contributed equally to this work. **†Corresponding author. Email: datye@unm.edu**

forming a surface complex. The ability of ceria to improve the sinter resistance of metals in automotive catalysts has been explained in terms of lowering the surface energy of nanoparticles (enhanced wetting) (*13*). However, as we show here, an additional benefit is the ability of ceria to trap Pt in an atomically dispersed state. Other catalyst supports have been shown to stabilize Pt in the form of isolated atoms—for example, penta-coordinated Al^{3+} sites on alumina (*14*), FeO_x (*15*), and the (111) surface of $MgAl_2O_4$ (*16*). However, when these catalysts are aged at 800°C in air (*16*, *17*), the formation of large crystalline Pt particles can be detected via x-ray diffraction (XRD). The complete absence of an XRD peak for Pt demonstrates that the sample contains only atomically dispersed species, which can be confirmed by reactivity measurements, energy-dispersive spectroscopy (EDS), aberration-corrected scanning transmission electron microscopy (AC-STEM), and diffuse reflectance infrared Fourier transform spectroscopy (DRIFTS).

Exposing ceria powders with different surface facets allowed us to determine the most effective surface for trapping Pt. Ceria can be synthesized in well-defined shapes, specifically nanorods, cubes, and octahedra (*18*). The similar specific reactivity of octahedra and nanorods for the water-gas shift reaction (*19*) suggests that the rods expose dominant (111) facets, contrary to the previously reported morphology of the nanorods (*18*). Ceria nanoshapes have been studied for their role in Pt sintering and redispersion (*20*). Density functional theory (DFT) calculations by Bruix *et al.* (*21*) suggested that CeO_2 (100) surfaces provide the right geometry to stabilize Pt^{2+} by bonding to O^{2-} in square pockets. Neitzel *et al.* (*22*) showed that the Pt cations are stable on the surface rather than diffusing into the ceria bulk. However, the highest temperature achieved in these previous studies was much lower than the aging temperature of DOCs (*21*).

We sought to determine the effectiveness of various ceria surface facets for trapping Pt at typical DOC aging conditions, 800°C in air. We introduced ceria powders as a separate phase by simple physical mixing. Three different ceria shapes were used: cubes (50 m^2/g), nanorods (90 m^2/g), and what we refer to as polyhedral ceria (89 m^2/g). The latter, obtained by calcination of cerium nitrate, consists of nanoparticles of truncated octahedra, which expose (111) surface facets, because they constitute the most stable low-index surface of ceria (*23*). The rounded nature of these polyhedral particles indicates that other less prominent surfaces, as well as step edges, must also be exposed (figs. S1 and S2).

The STEM image of the as-prepared Pt/La-Al_2O_3 catalyst, nominally 1 weight percent (wt %) (Fig. 1A), shows small Pt particles on the alumina support. After the sample was aged at 800°C for 10 hours in flowing air, large Pt crystallites were formed (Fig. 1B). After aging, EDS analysis in a scanning electron microscope (SEM) showed ~0.8 wt % Pt (table S1), which was confirmed via XRD analysis (*24*). XRD patterns corroborated the rapid sintering, as evident from the well-defined, sharp reflections for face-centered cubic (fcc) Pt in Fig. 1C; the broad reflections and the background in this pattern come from the alumina support.

The as-prepared 1 wt % Pt/La-Al_2O_3 catalyst was physically mixed with ceria powders in a weight ratio of 2:1 (33 wt % ceria) and then subjected to aging in flowing air. TEM/STEM images of the physical mixtures after aging show that the Al_2O_3 and CeO_2 phases in the mixture are attached to each other (fig. S3). Furthermore, the STEM image revealed that no Pt was present on the alumina because it had migrated to the CeO_2 phase (figs. S3 and S4) and was trapped, forming subnanometer Pt species. XRD patterns of the physically mixed catalysts after aging at 800°C for 10 hours in air are shown in Fig. 1D, curves a to c. The size of the Pt(111) peak gets smaller in samples a to c, suggesting improved efficiency for trapping Pt (decrease in the amount of the crystalline Pt phase). The sample aged for 1 week in air (Fig. 1D, curve d) shows no Pt peak at all, indicating the complete absence of large Pt particles. Because ceria can scatter x-rays, it causes a decrease in the size of Pt peak. This effect of ceria is seen by comparing the XRD pattern of the aged Pt/La-Al_2O_3 (Fig. 1C) with the XRD pattern of the same sample after mixing with ceria (2 parts Pt/La-Al_2O_3:1 part ceria) (Fig. 1D, curve e).

The inset in Fig. 1D shows magnified views of the Pt(111) reflection. The size and sharpness of this peak are indicative of the crystallite size of Pt. The splitting of the peak into a doublet, the $K_{\alpha1}$ and $K_{\alpha2}$, is further evidence of large Pt crystallites. With such large particles, XRD cannot be used to estimate crystallite dimensions because size-induced broadening is smaller than the instrumental broadening. The size of the Pt peak gives us a visual indication of the amount of crystalline Pt in these samples. The Rietveld refinement method (fig. S5) was used to quantify the amount of crystalline Pt visible to XRD, which is reported for each of these samples in table S2. The calculated value of 0.81 wt % Pt in the reference sample (Fig. 1D, curve e) agrees with independent EDS analysis of the overall composition of this sample (table S1). The excellent agreement between XRD-derived composition and elemental analysis allows us to estimate the amount of crystalline Pt visible to XRD in each of these samples. Subtracting the amount of crystalline Pt from the total Pt gives us the amount of atomically dispersed Pt in each sample (table S2).

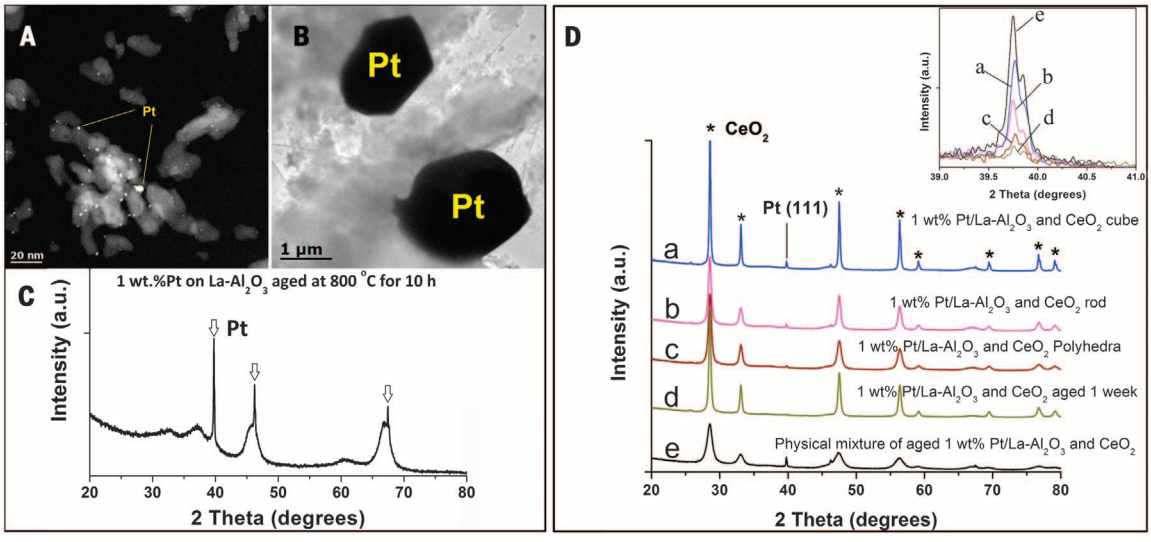

Fig. 1. The transfer of Pt from alumina to ceria leads to a decrease in size of the Pt(111) XRD peak. (**A**) HAADF STEM image of 1 wt % Pt/La-Al_2O_3 after calcination in air at 350°C for 5 hours. (**B**) TEM image of this catalyst after aging at 800°C in air for 10 hours. (**C**) XRD pattern of this catalyst after aging in air at 800°C for 10 hours. The sharp Pt reflections (vertical arrows) arise from the large particles seen in the TEM image (B), whereas the broad peaks come from the alumina support. (**D**) XRD patterns of physical mixtures of 1 wt % Pt/La-Al_2O_3 and ceria powders (weight ratio 2:1) after aging at 800°C for 10 hours in flowing air [(a) to (c)], aged for 1 week with polyhedral ceria (d), and a reference sample (e) where the Pt/La-alumina catalyst was first aged as in (C), then mixed with polyhedral ceria in the same weight ratio. The asterisks show the CeO_2 reflections whose peak widths vary as a result of changes in crystallite sizes due to aging. The inset shows a higher-magnification view of the Pt(111) reflection; the size of the peak corresponds to the amount of crystalline Pt in the sample.

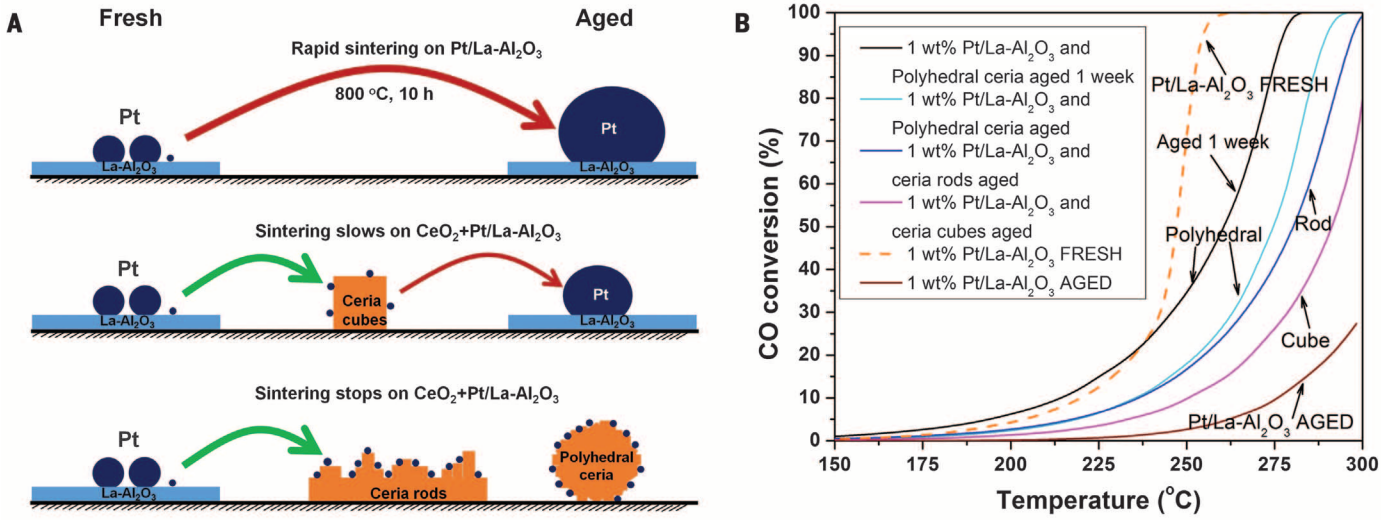

Fig. 2. Physically mixing ceria with Pt/La-Al_2O_3 leads to enhanced reactivity. (**A**) Illustration of Pt nanoparticle sintering, showing how ceria can trap the mobile Pt to suppress sintering. Cubes appear to be less effective than rods or polyhedral ceria. (**B**) Light-off curves for CO oxidation on the 1 wt % Pt/La-Al_2O_3 sample (20 mg of catalyst in the reactor) and the samples physically mixed with ceria (20 mg of 1 wt % Pt/La-Al_2O_3 mixed with 10 mg of ceria powder) and then aged at 800°C in air. The higher reactivity of the samples containing ceria correlates with the smaller Pt peak in the XRD patterns (inset in Fig. 1).

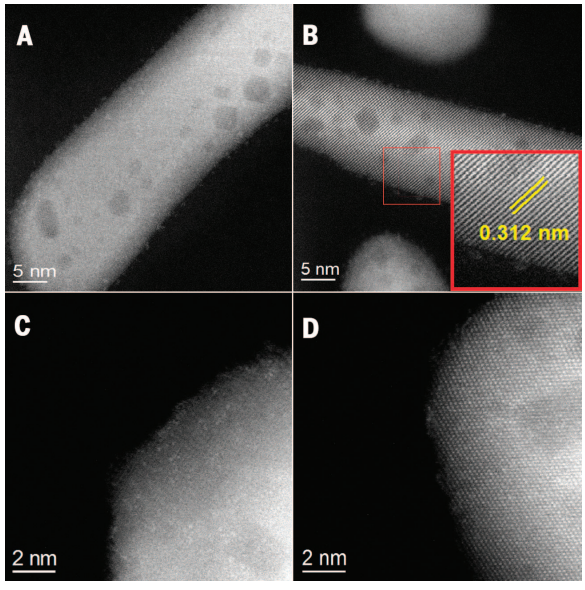

Fig. 3. Heating in air at 800°C allows mobile Pt species to be trapped on ceria. (**A** to **D**) Representative AC-STEM images of 1 wt % Pt/CeO_2-rod [(A) and (B)] and 1 wt % Pt/CeO_2-polyhedra [(C) and (D)] after aging at 800°C for 10 hours in flowing air. The darker objects within the ceria particles are internal voids. The bright dots on the surface of CeO_2 represent mononuclear Pt species that are stable to treatment in flowing air at 800°C. When the ceria lattice is aligned with the electron beam [(B) and (D)], it is more difficult to distinguish the Pt because of the strong contrast from the ceria. The Pt species reside on the surface of ceria rather than being embedded within it.

Figure 2A provides a schematic illustration of how physically mixed ceria traps Pt emitted from the alumina catalyst, thereby helping to improve the reactivity for CO oxidation (Fig. 2B). The smaller the Pt peak in the inset in Fig. 1D, the more atomically dispersed Pt that is present on the sample, which leads to higher catalytic activity. The aged Pt/La-alumina had such large Pt crystallites that there was negligible CO oxidation reactivity at 225°C. Among the nanoshapes, the physically mixed polyhedral ceria and the nanorods show similar performance, with the lowest reactivity seen with the ceria cubes. When the physically mixed polyhedral ceria was aged for 1 week with the Pt/La-Al_2O_3, the reactivity was comparable to that of the fresh catalyst (per gram of catalyst), indicating remarkable sinter resistance (Fig. 2B).

On the basis of the CO oxidation activity shown in Fig. 2, we calculated the specific reactivity [turnover frequency (TOF)] for the Pt (table S2 and fig. S6). Chemisorption of H_2, O_2, and CO was performed on these catalysts (*24*) after oxidative pretreatments similar to those used for the reactivity measurements. No H_2 or O_2 uptake was detected; the ratio of chemisorbed CO/Pt was 0.18. The low CO uptake would suggest a particle size of ~5 nm, but high-angle annular dark-field (HAADF) AC-STEM imaging showed only atomically dispersed Pt species on the polyhedral ceria and on the ceria rod samples (Fig. 3). The ceria underwent sintering after being heated at 800°C in air, as seen from the peak widths of the ceria XRD peaks highlighted with asterisks in Fig. 1D. As a result, the rods and cubes changed shape and became more rounded (Fig. 3 and fig. S7). The effect of high-temperature treatment was most severe on the ceria cubes, as seen from the $K_{\alpha1}$-$K_{\alpha2}$ splitting of the high-angle ceria XRD reflections (Fig. 1D, curve a) indicating large crystallite sizes. We could not image any single-atom Pt species on the ceria cubes; hence, the concentration of atomically dispersed Pt on the cubes is apparently much lower (fig. S7).

Because chemisorption of CO was not useful for counting the number of Pt sites, we used the amount of atomically dispersed Pt derived from the XRD measurements (*24*). The TOF derived in this manner is remarkably similar for all of these catalysts, within experimental error (0.12 ± 0.04 s^{-1} at 225°C). Surprisingly, the TOF is also close to that reported for single crystals of Pt(100) (*25*) at this temperature (0.12 s^{-1}), even though the atomically dispersed Pt is very different from a monolithic single crystal in morphology and nearest neighbors. These TOF values are lower than those reported on the most active Pt/CeO_2 catalysts (*26*, *27*), but the latter contain metallic Pt nanoparticles while our catalysts contain atomically dispersed Pt that is present in ionic form, most likely Pt^{2+}. A reaction mechanism based on DFT calculations was proposed for single isolated Pt^{2+} on alumina, and although the mechanism differs from that on metallic Pt, the TOF for CO oxidation was comparable to that on 1 wt % Pt/alumina (*28*).

Because Pt was deposited through the vapor phase in physically mixed ceria samples, we prepared a second set of catalysts directly on the same ceria powders using a conventional method, impregnation of chloroplatinic acid. These 1 wt % Pt/ceria samples were then aged at similar

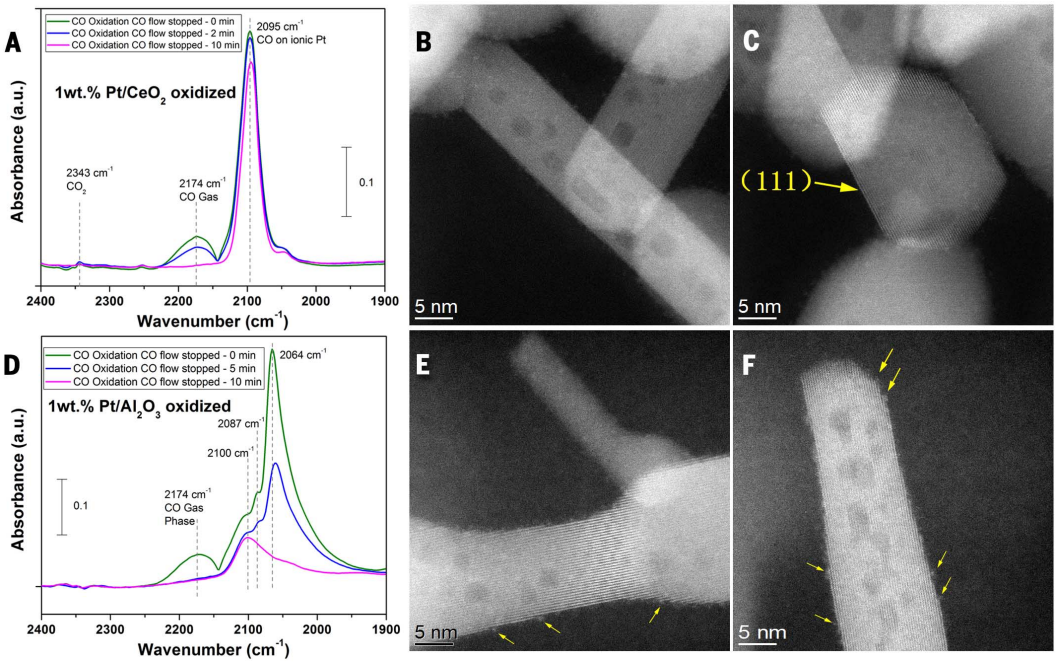

Fig. 4. The atomic dispersion of Pt is preserved during CO oxidation measurements. (**A**) DRIFTS of the 1 wt % Pt/CeO_2 polyhedra during CO oxidation at 125°C after oxidative pretreatment in 10% O_2 at 450°C. After 30 min of CO oxidation, the CO flow was stopped and spectra recorded at 0, 2, and 10 min while the oxygen flow continued. There is negligible drop in the symmetrical feature at 2095 cm^{-1} that is assigned to isolated ionic Pt sites on the ceria. (**B**, **C**, **E**, and **F**) HAADF AC-STEM images of Pt/ceria rods treated at 800°C in flowing air for 10 hours, before [(B) and (C)] and after three cycles of CO oxidation [(E) and (F)] to 300°C, showing that the catalyst is stable after reaction and the Pt species remain atomically dispersed. The arrows point to step edges that appear to be sites where the Pt species are present, rather than the smooth well-defined (111) facets. (**D**) DRIFTS of a 1 wt % Pt/Al_2O_3 catalyst after similar pretreatment as in (A) and after 30 min of CO oxidation at 125°C. Spectra were recorded after CO was switched off while the oxygen continued to flow for 0, 5, and 10 min. The band of CO on metallic Pt (2087 cm^{-1} and 2064 cm^{-1}) disappeared rapidly, leaving behind a feature at ~2100 cm^{-1} that corresponds to oxidized Pt.

conditions (800°C in air for 10 hours). The XRD patterns of these aged Pt/ceria samples (fig. S8) show that a well-defined Pt(111) reflection is seen only on the Pt/ceria cube sample, but no Pt(111) reflection is seen on the nanorods or the polyhedral ceria. SEM images (fig. S9) show large Pt particles on the cube sample, but no such large particles were detected on the rod or polyhedral ceria samples. The conversion of CO was marginally higher on the rod samples than on the polyhedral ceria; the cubes were less reactive (fig. S10). TEM images of the Pt species in the physically mixed ceria after aging (fig. S3) are similar to the Pt/ceria prepared by impregnation (fig. S11). The method of Pt deposition does not seem to matter as long as the sample is aged at elevated temperatures in air. The similarity in TOF for Pt/alumina and Pt/ceria suggests that the Pt is not lost into the bulk of the ceria. Solid-solution substitution of platinum for cerium in bulk ceria is unfavorable, given the smaller ionic radii of Pt^{2+} or Pt^{4+}. Platinum cations prefer six-fold octahedral coordination with surrounding oxygens, in contrast to the eight-fold cube coordination of oxygens surrounding cerium cations in CeO_2.

We examined the Pt/ceria rod samples after three cycles of CO oxidation going up to 300°C. The Pt was atomically dispersed before (Fig. 4, B and C) and after reaction (Fig. 4, E and F). To examine the nature of the Pt during reaction, we performed DRIFTS of the 1 wt % Pt/polyhedral CeO_2 sample (Fig. 4A) and compared the results with a 1 wt % Pt/Al_2O_3 sample (Fig. 4D). Both samples were subjected to an oxidative treatment (10% O_2 in He at 450°C) before exposure to reaction conditions at 125°C ($CO:O_2$ = 1.5:1). A prominent symmetrical band at 2095 cm^{-1} was the only feature seen on the Pt/CeO_2 support (Fig. 4A), whereas on Pt/alumina we observed multiple CO adsorption features typical of metallic Pt nanoparticles, including a band on ionic Pt at ~2100 cm^{-1} (which is seen most clearly when the CO is switched off while oxygen continues to flow for 10 min) (Fig. 4D). The coexistence of Pt ionic species and Pt nanoparticles on alumina and other oxide supports was also noted by Ding *et al.* (*29*). To prepare a sample that contained exclusively ionic Pt (and showing a CO adsorption band similar to Fig. 4A), they used a ZSM-5 support and low metal loading (0.5 wt %). The Pt/ZSM-5 was not stable beyond 1 min during electron microscope imaging, forming Pt nanoparticles (*29*). As seen from the images in Figs. 3 and 4 (*24*), the Pt/ceria is stable in the TEM and during repeated CO oxidation tests. The 2095 cm^{-1} band is the only feature seen even at 350°C during CO oxidation (fig. S12), indicating that Pt nanoparticles do not form under these conditions. As reported by Ding *et al.* (*29*), CO on ionic Pt (2095 cm^{-1}) is not reactive at low temperatures (Fig. 4A), whereas CO on metallic Pt (2064 cm^{-1}) reacts readily with flowing oxygen (Fig. 4D). Despite the transient activity seen on metallic Pt nanoparticles, both of these catalysts exhibit very low steady-state activity at this temperature (Fig. 2 and figs. S13 and S14) due to strongly bound CO. It is only at higher temperatures that the Pt nanoparticles on alumina and the single-atom Pt on ceria become active (Fig. 2) and exhibit similar specific activity for CO oxidation (table S2).

While ceria helps to trap atomically dispersed Pt, the strong interaction between Pt and ceria also helps preserve the surface area of polyhedral ceria (table S3). We estimate a surface atom concentration of 1.1 Pt atoms/nm^2 in the aged sample (table S3). A recent study (*30*) suggests that step edges on the ceria (111) surface provide stable sites for Pt^{2+}. By engineering the density of surface steps, 80% of the Pt loading of 0.18 monolayer (1 monolayer = 7.9 atoms/nm^2) could be stabilized in the form of Pt^{2+}. This corresponds to 1.2 atoms/nm^2, which is similar to the loading of atomically dispersed Pt that we observed. The high step density was achieved by Dvořák *et al.* (*30*) through deposition of ceria on their CeO_2 (111) thin films or via heat treatment. The AC-STEM images, especially those in Fig. 4, suggest that the Pt occupies step edges (arrowed) on the ceria rod sample. On the other hand, the well-defined (111) facet in Fig. 4C does not show any Pt species. DFT calculations suggest that the binding energy of Pt to surface steps on CeO_2 (*30*) exceeds that of Pt on CeO_2 (111) and also the cohesive energy of bulk Pt. The images in

Figs. 3 and 4 show Pt species located randomly on the ceria surfaces (not embedded in the ceria), with no preference for specific facets.

Atom trapping should be broadly applicable as a method for preparing single-atom catalysts. The approach requires a supply of mobile atoms and a support that can bind the mobile species. Conditions that are conducive to Ostwald ripening, which normally is implicated in the degradation of catalysts (*3*), are ideal because mobile species are continually being generated. In our work, at the aging temperature of 800°C in air, mobile PtO_2 is rapidly emitted; the estimated lifetime is only a few seconds for a 5-nm Pt crystallite (*24*). Surface species such as hydroxyls and carbonates, which could prevent the trapping of mobile species, would have desorbed at high temperatures, providing a clean surface for the formation of covalent metal oxide bonds that are needed to stabilize single atoms. Trapping of atoms provides a plausible explanation for the role of ceria in slowing the rates of Ostwald ripening and may help to explain how other supports modify the rates of catalyst sintering.

REFERENCES AND NOTES

1. G. W. Graham *et al.*, *Catal. Lett.* **116**, 1–8 (2007).
2. M. H. Wiebenga *et al.*, *Catal. Today* **184**, 197–204 (2012).
3. T. W. Hansen, A. T. Delariva, S. R. Challa, A. K. Datye, *Acc. Chem. Res.* **46**, 1720–1730 (2013).
4. T. R. Johns *et al.*, *J. Catal.* **328**, 151–164 (2015).
5. J. A. Kurzman, L. M. Misch, R. Seshadri, *Dalton Trans.* **42**, 14653–14667 (2013).
6. C. B. Alcock, G. W. Hooper, *Proc. R. Soc. London Ser. A* **254**, 551–561 (1960).
7. G. Cavataio *et al.*, *SAE Int. J. Fuels Lubr.* **2**, 204–216 (2009).
8. Y.-F. Yu-Yao, J. T. Kummer, *J. Catal.* **106**, 307–312 (1987).
9. J. G. McCarty, K.-H. Lau, D. L. Hildenbrand, *Stud. Surf. Sci. Catal.* **111**, 601–607 (1997).
10. C. Carrillo *et al.*, *J. Phys. Chem. Lett.* **5**, 2089–2093 (2014).
11. G. B. McVicker, R. L. Garten, R. T. K. Baker, *J. Catal.* **54**, 129–142 (1978).
12. Y. Nagai *et al.*, *J. Catal.* **242**, 103–109 (2006).
13. J. A. Farmer, C. T. Campbell, *Science* **329**, 933–936 (2010).
14. J. H. Kwak *et al.*, *Science* **325**, 1670–1673 (2009).
15. B. Qiao *et al.*, *Nat. Chem.* **3**, 634–641 (2011).
16. W.-Z. Li *et al.*, *Nat. Commun.* **4**, 2481 (2013).
17. T. R. Johns *et al.*, *ChemCatChem* **5**, 2636–2645 (2013).
18. H.-X. Mai *et al.*, *J. Phys. Chem. B* **109**, 24380–24385 (2005).
19. S. Agarwal *et al.*, *ChemSusChem* **6**, 1898–1906 (2013).
20. T. Wu *et al.*, *J. Phys. Chem. Lett.* **5**, 2479–2483 (2014).
21. A. Bruix *et al.*, *Angew. Chem. Int. Ed.* **53**, 10525–10530 (2014).
22. A. Neitzel *et al.*, *J. Phys. Chem. C* **120**, 9852–9862 (2016).
23. Z. L. Wang, X. Feng, *J. Phys. Chem. B* **107**, 13563–13566 (2003).
24. See supplementary materials on *Science* Online.
25. P. J. Berlowitz, C. H. F. Peden, D. W. Goodman, *J. Phys. Chem.* **92**, 5213–5221 (1988).
26. R. Kopelent *et al.*, *Angew. Chem. Int. Ed.* **54**, 8728–8731 (2015).
27. M. Cargnello *et al.*, *Science* **341**, 771–773 (2013).
28. M. Moses-DeBusk *et al.*, *J. Am. Chem. Soc.* **135**, 12634–12645 (2013).
29. K. Ding *et al.*, *Science* **350**, 189–192 (2015).
30. F. Dvořák *et al.*, *Nat. Commun.* **7**, 10801 (2016).

ACKNOWLEDGMENTS

Supported by NSF GOALI grant CBET-1438765 (J.J., H.X., S.R.C., A.K.D.), General Motors Global R&D (G.Q., S.O., and M.H.W.), U.S. Department of Energy grant DE-FG02-05ER15712 (A.T.D., E.J.P., A.K.D., X.I.P.H., and Y.W.), and the Center for Biorenewable Chemicals funded by NSF grant EEC-0813570 (H.X., H.P., and A.K.D.). This work made use of the JEOL JEM-ARM200CF at the University of Illinois at Chicago. We thank A. Nicholls for recording the AC-STEM images and D. Kunwar for assistance in catalyst preparation.

SUPPLEMENTARY MATERIALS

www.sciencemag.org/content/353/6295/150/suppl/DC1
Materials and Methods
Figs. S1 to S14
Tables S1 to S3
References (*31*–*35*)

26 April 2016; accepted 13 June 2016
10.1126/science.aaf8800

ANIMAL ROBOTICS

Tail use improves performance on soft substrates in models of early vertebrate land locomotors

Benjamin McInroe,[1]* Henry C. Astley,[1]* Chaohui Gong,[2] Sandy M. Kawano,[3] Perrin E. Schiebel,[1] Jennifer M. Rieser,[1] Howie Choset,[2] Richard W. Blob,[4] Daniel I. Goldman[1,5]†

In the evolutionary transition from an aquatic to a terrestrial environment, early tetrapods faced the challenges of terrestrial locomotion on flowable substrates, such as sand and mud of variable stiffness and incline. The morphology and range of motion of appendages can be revealed in fossils; however, biological and robophysical studies of modern taxa have shown that movement on such substrates can be sensitive to small changes in appendage use. Using a biological model (the mudskipper), a physical robot model, granular drag measurements, and theoretical tools from geometric mechanics, we demonstrate how tail use can improve robustness to variable limb use and substrate conditions. We hypothesize that properly coordinated tail movements could have provided a substantial benefit for the earliest vertebrates to move on land.

During the vertebrate invasion of land, 385 to 360 million years ago, early tetrapods and relatives faced a variety of challenges (*1*), including locomotion in terrestrial environments. Terrestrial locomotion relies on interactions between the body and substrate to generate propulsive forces, but the interaction between the organism and some substrates may be complex. Fossil evidence indicates that tetrapods emerged from water in near-shore habitats, where they likely encountered flowable soft substrates such as sands and muds (*2*, *3*). These substrates exhibit properties of solids and fluids, either jamming or yielding (plastic deformation of the material) depending on how they are loaded (*4*) and sloped (*5*).

The challenge of movement on flowable substrates therefore arises from the complexity of interactions between the substrate and the organism. Even on level deformable substrates, subtle variations in limb morphology (*6*) and kinematics (*7*) can lead to substantial differences in performance. Furthermore, interactions between appendages and these substrates leave local disturbances, which can influence subsequent interactions, sometimes leading to deteriorating locomotor performance and eventual total locomotor failure (*8*). As substrate slope increases, yield forces decrease and downhill material flow becomes important, reducing the range of effective locomotor strategies (*5*).

The use of an additional locomotor structure that can be independently coordinated may allow a greater range of effective behaviors, even in the absence of derived limb morphology and sophisticated motor patterns. We propose that the tail could have been a critical locomotor structure for early tetrapods. In addition to being a primary driver of aquatic locomotion, tails play major roles in the propulsion of many modern fishes during terrestrial locomotion (*9*–*12*) and can be used as inertial reorientation appendages in some tetrapods (*13*, *14*). Thus, the use of a prominent tail [as seen in fossil taxa (*15*–*17*) (Fig. 1A)] may have increased locomotor robustness to environmental and kinematic variables.

Evaluating locomotor performance for extinct taxa is challenging (*18*, *19*), in part because the sensitivity of locomotion on complex substrates to kinematics and control strategies cannot necessarily be inferred from range of motion and morphology (*7*). Therefore, to test our hypothesis, we used three complementary modeling methods (Fig. 1): a model organism, a robophysical model, and a mathematical model. We made several choices governing our modeling approaches. In our locomotors, we modeled symmetrical, forelimb-driven

[1]School of Physics, Georgia Institute of Technology, Atlanta, GA, USA. [2]Robotics Institute, Carnegie Mellon University, Pittsburgh, PA, USA. [3]National Institute for Mathematical and Biological Synthesis, University of Tennessee, Knoxville, TN, USA. [4]Department of Biological Sciences, Clemson University, Clemson, SC, USA. [5]School of Biology, Georgia Institute of Technology, Atlanta, GA, USA.
*These authors contributed equally to this work. †Corresponding author. Email: daniel.goldman@physics.gatech.edu

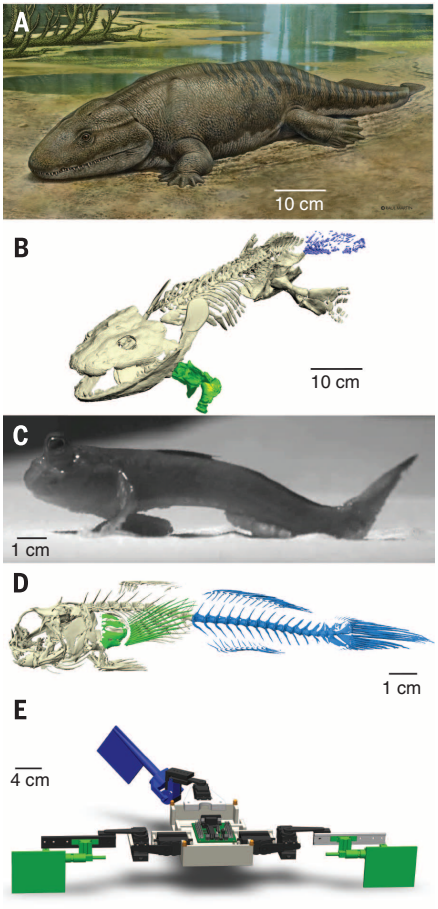

Fig. 1. Target and model systems for understanding early tetrapod locomotion on granular media. (**A**) A reconstruction of *Ichthyostega* (~360 million years ago), an example of an early tetrapod body plan, by Raul Martin. (**B**) Skeletal reconstruction of *Ichthyostega*, an example of an early tetrapod body plan [from (*20*)], highlighting the pectoral limbs (green) and tail (blue). (**C**) The mudskipper (*Periophthalmus barbarus*), a biological model for early terrestrial locomotors. (**D**) A micro–computed tomography scan reconstruction of a mudskipper skeleton, highlighting the pectoral fin (green) and tail (blue). (**E**) The MuddyBot, a 3D printed robot developed to model the locomotion of crutching early tetrapods. Limbs are in green and the tail is in blue.

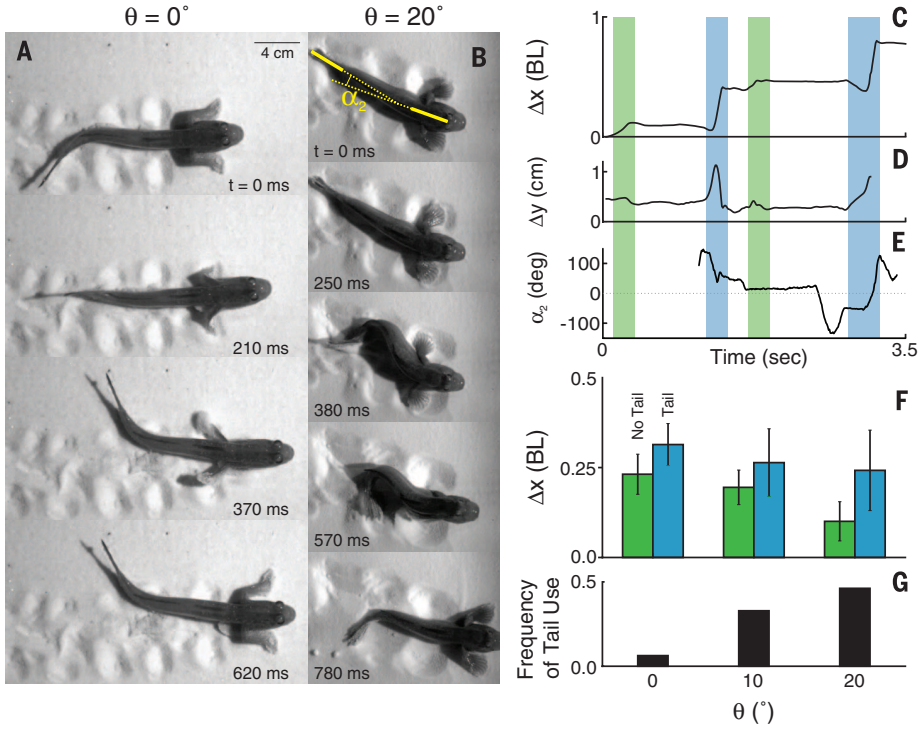

Fig. 2. Mudskipper locomotion on granular media at different substrate inclines (θ). (**A** and **B**) Dorsal-view video frames of a mudskipper fish on dry, loose sand inclined at 0° (A) and 20° (B) (movies S1 and S2). Yellow solid lines along the longest tail fin ray and from between the eyes to the anterior edge of the dorsal fin are used to compute the tail angle (α_2) in (E). The tail is not used propulsively in (A), although it moves slightly; in (B), the tail is used for propulsion. (**C** to **E**) Horizontal forward displacement per cycle (Δx) in body lengths (BL) for a single trial (C), vertical displacement (Δy, measured from eye) (D), and tail angle (α_2) (E) of mudskippers on sand at 20° incline. Cycles without tail use are indicated by green regions; cycles with tail use are indicated by blue regions (determined from video inspection). Missing values of α_2 are when the tail fin was out of view. (**F**) Δx at all inclines (θ) for steps without (green) and with (blue) tail use. Error bars denote SD. (**G**) Percentage of cycles with propulsive tail use across substrate inclines.

crutching locomotion (rather than salamander-like movement) in accordance with recent studies of *Ichthyostega* (*20*, *21*); this choice enabled simplicity of control (coordinating two appendages rather than four) and obviated the need for continuous, stable support of an elevated body. We note that we are not strictly modeling *Ichthyostega*, nor any specific fossil taxon associated with the water-land transition, but are instead seeking general principles underlying limbed, crutching locomotion on yielding media.

Our biological model is the mudskipper (*Periophthalmus barbarus*) (*12*, *18*, *20*–*24*), a small fish that frequently moves terrestrially using synchronous motions of the pectoral fins, although these animals can use their tails for rapid jumping despite unspecialized tail morphology (*25*). Our robophysical model (Fig. 1E) (*26*) was designed with morphology representing the simplest possible version of a crutching locomotor, allowing us to systematically explore performance over a range of locomotor movements, including those movements not used by our biological model. Our mathematical model relies on the framework of geometric mechanics (*27*, *28*) and allows us to understand how certain aspects of performance relate to coordination of limbs and tail. Our use of dry granular media was another modeling choice: The first vertebrates to move on land likely did so in wet shoreline habitats (such as mudflats) with properties that differ from those of dry granular media, but these media are united in displaying plastic deformation once the yield stress is exceeded (*29*–*31*). Although partially wet soils can display cohesion that increases yield stresses and results in larger "memory" effects, these rheological similarities [combined with the difficulty of preparing large volumes of standardized wet granular media (*30*)] led us to use dry media to model flowable substrates in our trials (*30*, *31*).

Mudskippers ($N = 6$) were capable of effective locomotion over a level ($\theta = 0°$) granular substrate [loose-packed dry oolite sand (table S1)] using a crutching gait actuated by synchronous retraction of the pectoral fins with the tail angle (α_2) almost straight (21° ± 22°; all measurements are means ± SD) (Fig. 2A and movie S1), moving an average forward distance per cycle (Δx) of 0.21 ± 0.03 body lengths (BL) (Fig. 2F). During locomotion, mudskippers were able to fold the fin rays of the caudal and anal fins away from the substrate, allowing terrestrial locomotion without damage to or interference from these structures (Fig. 2B).

In some locomotor cycles, mudskippers used their tails (Fig. 2B and movie S2), bending the tail and planting the distal end of the tail and fin rays in the sand approximately orthogonal to the body axis (119° ± 21°) (Fig. 2E) before retracting the pectoral fins and straightening the tail during the propulsive phase (Fig. 2B). Tracks left by these trials typically consisted of a series of paired impressions from the pectoral fins (sometimes obscured by yielding flow from subsequent steps, especially on inclines), with tail use leaving an additional impression offset to the right or left and overlapping the previous fin impressions (Fig. 2, A and B, and movies S1 and S2). Steps using the tail resulted in a higher displacement of 0.28 ± 0.08 BL on horizontal media (Fig. 2, C, D, and F).

As substrate incline angle increased, crutching with only the pectoral fins became less effective (Fig. 2F) and the frequency of steps for which the tail was used propulsively increased, from 6% on level substrate to 36% on substrate inclined at 10° and to 55% on substrate inclined at 20° (Fig. 2G). In addition to increasing displacement per cycle, tail use prevented downhill slip on inclined media when the tail was planted. The disparity in forward displacement increased between steps with and without tail use as substrate angle increased (Fig. 2F). At a 10° incline, mudskippers moved forward an average of 0.16 ± 0.03 BL with each step, versus 0.18 ± 0.08 BL when the tail was used (Fig. 2F). When the substrate was inclined to 20°, displacement was 0.07 ± 0.03 BL without tail use, increasing to 0.14 ± 0.07 BL with tail use (Fig. 2F). Further, mudskippers would occasionally jump clear of the test arena via tail-powered movements, indicating that the use of tails during crutching locomotion is controlled and submaximal.

A robophysical model of a crutching locomotor with limbs (Fig. 3A) allowed systematic testing of how locomotor performance in realistic granular environments was affected by variations in foot placement, limb adduction, and tail use (*7*). We elected to use a highly simplified morphology (a pair of laterally positioned, synchronously moving forelimbs and a posterior tail) (Fig. 3A) in order to focus on overarching locomotor control principles ("templates") as opposed to the details of their anatomical implementation ("anchors") (*32*). Although this model is simplified, it possesses some of the degrees of freedom seen in the mudskippers, namely the ability to control both body lifting (via limb adduction) and the interface with the substrate (limb supination) as well as use of the tail.

In addition to varying the incline (θ = 0°, 10°, and 20°) of the granular material, we varied three parameters of the robot: limb adduction angle (ψ), limb supination angle (ϕ), and presence or absence of tail use (Fig. 3). Adduction angle and the resultant lifting of the body is known to affect locomotor performance in similar robots on granular media (*8*) and may have been critical to terrestrial locomotion in early tetrapods (*20*). Supination angle, a simplified model of differences in limb placement, varied from a vertical limb insertion into the media (0°) to nearly flat (60°) in 15° increments. The tail was either used or not used, and was lifted clear of the media when not in use (resulting in the posterior portion of the robot dragging in the media). In all cases, tail use induced alternating lateral rotations and displacements; although these yaw movements were often small (<10°), they explain the few instances in which tail use was detrimental. To prevent damage to the motors, instead of sand we used two granular materials, loosely packed poppy seeds and spherical plastic particles (table S1) (*33*); prior work has shown that these substrates function well as models of more natural granular media (*8*, *33*). Although the robot's movements were slower than those of the mudskippers, all three substrates showed no dependence of force on speed over the ranges observed (~5 to 10 cm/s) (fig. S6).

In each trial, the robot performed a total of six limb cycles, the maximum number possible for the size of the bed. Insufficient first-step displacement has been shown to produce interactions with the previously disturbed media, resulting in lower displacement and further interactions until complete failure (stranding) (*8*). Conversely, if the first step is sufficient to prevent this interaction, the likelihood of failure decreases. In our experiments, few configurations produced intermediate displacements that led to decaying performance; most were either consistently successful or immediate failures (fig. S1). These trials were not sufficiently numerous to determine whether tail use altered the rate of decay, although it may do so indirectly if it increases first-step displacement. Consequently, we present data for only the first step (Δx_1).

To characterize how the adduction, supination, and tail use parameters affected the robot's locomotion in undisturbed media, we measured Δx_1 for three trials per configuration (Fig. 3, D and E). During these trials, high values of adduction (which resulted in lifting much of the body clear of the substrate) and use of the tail improved first-step displacement, although not in a simple, additive manner; supination angle had an additional, minor influence (Fig. 3, D and E). On the level substrate, increasing adduction angle led to the largest performance increase, with supination angles of 30° and tail use resulting in modest improvements at lower adduction angles but offering minimal improvement over performance at the highest adduction angle (Fig. 3, B and D). At higher substrate angles with consequently lower granular yield forces, the role of the tail became dominant; effective locomotion without the tail was possible only at the highest adduction and lowest supination angles, but the use of the tail allowed locomotion over a wide range of limb kinematics (Fig. 3, C and E). In many of these cases, the use of the tail was the difference between success and failure [at θ = 20°, there were 15 failures among the 30 different configurations of ϕ and ψ (Fig. 3, D and E)]. Thus, the tail was not simply a uniform addition of propulsive force conferring a uniform advantage, as it did little to improve performance under near-optimal conditions. Instead, the tail had the greatest benefit when locomotion was otherwise compromised or ineffective as a result of low adduction angle or high substrate angle. A second set of trials

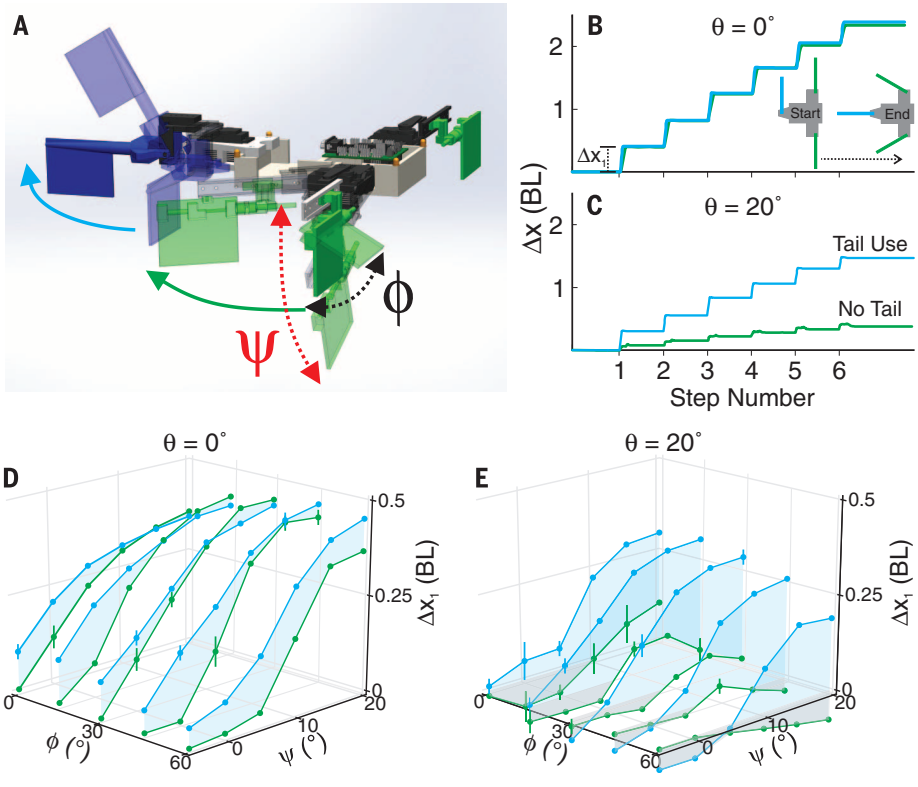

Fig. 3. Robophysical experiments on granular media at various substrate inclines (θ). (**A**) 3D model of MuddyBot, showing ranges of motion for limb retraction (green arrow, 60°) and tail motion (blue arrow, 90°). Limb adduction (ψ, −5° to 20°, where 0° is horizontal) and limb supination (ϕ, 0° to 60°, where 0° is vertical to the limb) are labeled, with other arrows showing directions of limb and tail motion during thrust phase. (**B** and **C**) Kinematics of a single trial of MuddyBot (ϕ = 15°, ψ = 15°) moving for six cycles, without tail use (green) and with tail use (blue), on level (θ = 0°) (B) and inclined (θ = 20°) (C) poppy seeds. (**D** and **E**) First-step net displacement versus adduction and supination angles on θ = 0° (D) and θ = 20° (E) poppy seeds. Blue shading shows regions of identical supination angle for clarity. Vertical lines denote SD > 0.01. Gray shading indicates negative values.

conducted using a different granular material showed qualitatively similar results [spherical plastic particles (table S1)], indicating that these results are robust to different granular media of different particle size and friction (figs. S2 and S5).

To gain insight into effective coordination of locomotor structures, we created a mathematical planar model of the robot using geometric mechanics. This method, developed as a theoretical framework to elucidate principles of movement (*27*), describes how the self-deformation of the body (in our case, limb or tail movements) (Fig. 4A) generates net translation (or rotation) of the body. Geometric mechanics has been useful for understanding robot swimming (cyclic self-deformation due to traveling-wave body undulation) within granular media in which inertial forces were small relative to frictional forces (*28*).

The geometric mechanics framework relies on construction of a "local connection" (*34*), which can be visualized as vector fields representing the link between small self-deformations (changes in the locomotor's shape space, the set of internal shapes the mechanism can assume, here defined by planar limb and tail angles; Fig. 4A) and the resulting movement in world space (Fig. 4, D and E). For any given body configuration (a point in the diagrams in Fig. 4, D and E), the corresponding vector indicates the body deformation pattern that results in maximal forward movement. That is, if the robot begins from an arbitrary limb and tail angle combination (Fig. 4A), which corresponds to a horizontal and vertical location on the vector field (Fig. 4, D and E), a self-deformation parallel to the vector at that location will produce the greatest world-space incremental displacement, whereas self-deformations perpendicular to that vector will produce zero displacement. The overall pattern of a vector field allows visualization of how a time-varying pattern of self-deformations—represented as a path in the shape space—results in translation (or rotation). The net movement for a given sequence of limb and tail movements can be evaluated via a line integral in the vector field, with more effective motor patterns represented as paths that locally align more closely with vectors and pass through vectors of larger magnitudes (Fig. 4, D and E) (*24*).

Construction of local connection vector fields requires knowledge of how limb and tail segments experience drag forces. Because fundamental equations of motion for granular drag in the regime relevant to our robot studies do not exist, we generated the vector fields in Fig. 4, D and E, by empirically estimating the forces acting on a robot limb moving through granular media in plate drag experiments (figs. S3, S5, and S6) [assuming the material was continuously deforming and thus in the "frictional fluid" regime (*33*, *35*)]. Similar to previous studies (*5*, *33*, *35*), the measured force was a function of the drag angle between the limb tangent and velocity vectors (Fig. 4B, inset), depth of intrusion into the media, and media incline, and was insensitive to speed (within the relevant range).

In such non-inertial limb- and tail-driven locomotion, the interaction between the granular media and the limb is governed by the ratio of the perpendicular thrust forces to parallel drag forces. These ratios collapsed to a single curve across inclines, depths (Fig. 4B), and granular media (fig. S5 and supplementary materials). This collapse suggests that the change in performance on granular slopes in the crutching locomotion may be a consequence of the effect of gravity on the body. Because our drag measurements were made in freshly prepared media, and because we could not model the possible interactions with the footprints of previous steps (*8*), we confined our analysis to the first step, as with the robot. Further, only high adduction angles were considered, so that we could avoid the effects of an accumulating pile of granular media at the front of the robot

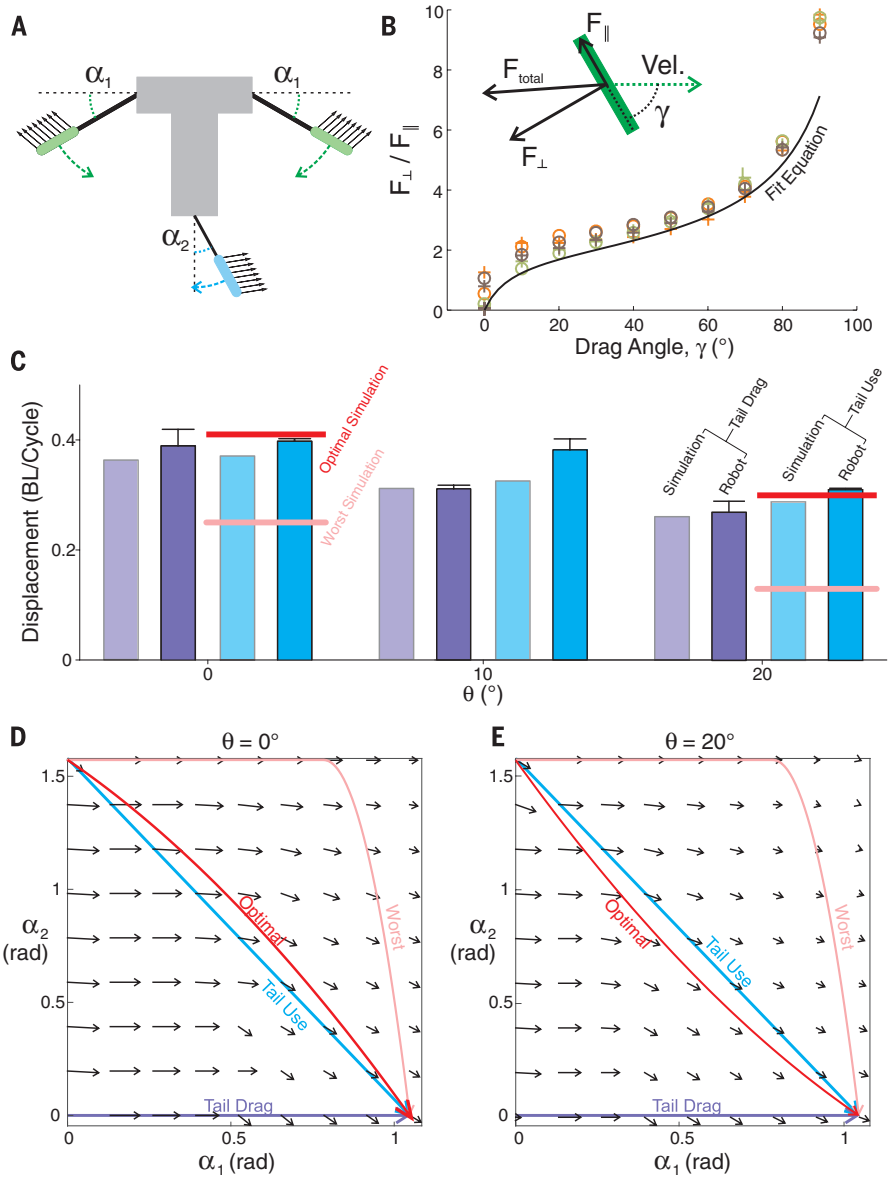

Fig. 4. Geometric mechanics model of MuddyBot locomotion. (**A**) A diagram of the simulation, showing the limb angle (α_1) and tail angle (α_2) as well as the reaction forces used to compute the local connection (see supplementary materials) between body deformation and body displacement. (**B**) The ratio of forces parallel and perpendicular to the limb surface during poppy seed drag experiments at various drag angles to the direction of motion, insertion depths, and substrate slopes. Intrusion depths are 1 cm (crosses) and 3 cm (circles), with θ = 0° (brown), 20° uphill (orange), and 20° downhill (green). The black line represents the ratio of perpendicular and parallel equations (fitted independently; see supplementary materials). (**C**) First-step displacement (without slip) of the robot and simulation at all inclines (ψ = 20°, ϕ = 0°), showing close agreement between the simulation and robot performance. Red and pink bars indicate the optimal and worst gaits, respectively. (**D** and **E**) Local connection vector field for θ = 0° (D) and θ = 20° (E) media, showing the limb only with tail dragging (purple) and tail gaits (light blue), as well as calculated optimal (red) and worst (pink) gaits.

when the body was insufficiently lifted. Additionally, when the tail was lifted clear of the media in robot experiments, the posterior motor and mounting structures intruded into and dragged through the media, resulting in an intrusion that was difficult to model; therefore, we simulated trials with the tail intruding into the media in the same configuration as at the end of tail-thrusting behavior, which yielded similar performance. To test these assumptions, we compared results to a subset of robot trials, and obtained good agreement between simulation and experiment (Fig. 4C and fig. S4).

The change in the patterns of the local connection vector fields revealed how limbs and tail could coordinate to produce movement (Fig. 4, C to E). For example, these fields demonstrated that the tail was not uniformly beneficial in all situations, nor even substantially beneficial in horizontal movement, in which the vertical component of the vectors (tail contribution) was small. However, as surface incline angle increased, the horizontal magnitudes of connection vectors decreased, indicating reduced efficacy of limb-only tail-dragging gaits (a horizontal path across the vector field). The relatively larger vertical component across more of the shape space indicated the increased importance of the tail to forward movement. The optimal gait for both inclines was close to the synchronous thrusting used by the robot and mudskipper, yielding similar displacements (Fig. 4, C to E); phase lag between initiation of limb and tail movement was suboptimal and, in one case per incline, yielded the worst possible gait (Fig. 4, D and E). Improper use of the tail resulted in substantially lower performance than simply allowing it to drag (Fig. 4, C to E). Additionally, the generally downward direction of the vectors in both fields demonstrate that purely tail-powered locomotion (a vertical path down the right of the vector field) can produce forward motion, as seen in some extant fish (*12*).

Our results from a biological analog of early tetrapods and robophysical and mathematical models demonstrate that the tail can play an important role in limb-driven crutching locomotion on inclined granular substrates by making locomotors more robust to suboptimal kinematics and substrate conditions. This suggests that the sizable, well-ossified (and presumably well-muscled) tails of early tetrapods (*15*–*17*), originally used for swimming, may have been co-opted to promote reliable locomotion over challenging substrates, providing an exaptation (*36*) that facilitated their invasion of land. Although evidence of tail use is absent among the few fossil trackways attributed to early tetrapods (*37*, *38*), tail use might be evident in trackways formed on inclined shores.

REFERENCES AND NOTES

1. J. A. Clack, *Gaining Ground: The Origin and Evolution of Tetrapods* (Indiana Univ. Press, 2002).
2. E. B. Daeschler, N. H. Shubin, F. A. Jenkins Jr., *Nature* **440**, 757–763 (2006).
3. A. Blieck *et al.*, *Geol. Soc. London Spec. Publ. 278*, 219–235 (2007).
4. N. Gravish, P. B. Umbanhowar, D. I. Goldman, *Phys. Rev. Lett.* **105**, 128301 (2010).
5. H. Marvi *et al.*, *Science* **346**, 224–229 (2014).
6. F. Qian *et al.*, *Bioinspir. Biomim.* **10**, 056014 (2015).
7. C. Li, P. B. Umbanhowar, H. Komsuoglu, D. E. Koditschek, D. I. Goldman, *Proc. Natl. Acad. Sci. U.S.A.* **106**, 3029–3034 (2009).
8. N. Mazouchova, P. B. Umbanhowar, D. I. Goldman, *Bioinspir. Biomim.* **8**, 026007 (2013).
9. J. Davenport, A. K. M. A. Matin, *J. Fish Biol.* **37**, 175–184 (1990).
10. A. G. Johnels, *Oikos* **8**, 122 (1957).
11. C. M. Pace, A. C. Gibb, *J. Exp. Biol.* **214**, 530–537 (2011).
12. C. M. Pace, A. C. Gibb, *J. Fish Biol.* **84**, 639–660 (2014).
13. A. Jusufi, D. I. Goldman, S. Revzen, R. J. Full, *Proc. Natl. Acad. Sci. U.S.A.* **105**, 4215–4219 (2008).
14. T. Libby *et al.*, *Nature* **481**, 181–184 (2012).
15. E. Jarvik, *Medd. Gronl.* **114**, 1–90 (1952).
16. E. Jarvik, *The Devonian Tetrapod* Ichthyostega (Indiana Univ. Press, 1996).
17. M. I. Coates, *Trans. R. Soc. Edinb. Earth Sci.* **87**, 363–421 (1996).
18. R. W. Blob, *Paleobiology* **27**, 14–38 (2001).
19. M. A. Ashley-Ross, S. T. Hsieh, A. C. Gibb, R. W. Blob, *Integr. Comp. Biol.* **53**, 192–196 (2013).
20. S. E. Pierce, J. A. Clack, J. R. Hutchinson, *Nature* **486**, 523–526 (2012).
21. S. E. Pierce, J. R. Hutchinson, J. A. Clack, *Integr. Comp. Biol.* **53**, 209–223 (2013).
22. E. M. Standen, T. Y. Du, H. C. E. Larsson, *Nature* **513**, 54–58 (2014).
23. S. M. Kawano, R. W. Blob, *Integr. Comp. Biol.* **53**, 283–294 (2013).
24. V. A. Harris, *Proc. Zool. Soc. London* **134**, 107–135 (1960).
25. B. O. Swanson, A. C. Gibb, *J. Exp. Biol.* **207**, 4037–4044 (2004).
26. J. Aguilar, D. I. Goldman, *Nat. Phys.* **12**, 278 (2016).
27. A. Shapere, F. Wilczek, *Phys. Rev. Lett.* **58**, 2051–2054 (1987).
28. R. L. Hatton, Y. Ding, H. Choset, D. I. Goldman, *Phys. Rev. Lett.* **110**, 078101 (2013).
29. N. Mitarai, F. Nori, *Adv. Phys.* **55**, 1–45 (2006).
30. S. S. Sharpe, R. Kuckuk, D. I. Goldman, *Phys. Biol.* **12**, 046009 (2015).
31. H. Askari, K. Kamrin, http://arxiv.org/abs/1510.02966 (2015).
32. K. Nishikawa *et al.*, *Integr. Comp. Biol.* **47**, 16–54 (2007).
33. C. Li, T. Zhang, D. I. Goldman, *Science* **339**, 1408–1412 (2013).
34. S. D. Kelly, R. M. Murray, *J. Robot. Syst.* **12**, 417–431 (1995).
35. R. D. Maladen, Y. Ding, C. Li, D. I. Goldman, *Science* **325**, 314–318 (2009).
36. S. J. Gould, E. S. Vrba, *Paleobiology* **8**, 4–15 (1982).
37. J. Clack, *Palaeogeogr. Palaeoclimatol. Palaeoecol.* **130**, 227–250 (1997).
38. S. Curth, M. S. Fischer, J. A. Nyakatura, *Ichnos* **21**, 32–43 (2014).

ACKNOWLEDGMENTS

Supported by NSF grants PoLS PHY-1205878, PHY-1150760, and CMMI-1361778, Army Research Office (ARO) grant W911NF-11-1-0514, and the ARL MAST CTA (D.I.G.); ARO Robotics CTA and NSF National Robotics Initiative IIS-1426655 (H.C.); NSF grants IOS-0517340 and IOS-0817794 (R.W.B.); GT UROP and the GT PURA Travel Grant (B.M.); a Clemson University Wade Stackhouse Fellowship, NSF award DBI-1300426, and the University of Tennessee, Knoxville (S.M.K.); and the U.S. Department of Defense, Air Force Office of Scientific Research, National Defense Science and Engineering Graduate (NDSEG) Fellowship, 32 CFR 168a (P.E.S.). The authors declare no conflicts of interest. Data are available from the corresponding author upon request.

SUPPLEMENTARY MATERIALS

www.sciencemag.org/content/353/6295/154/suppl/DC1
Materials and Methods
Supplementary Text
Figs. S1 to S6
Table S1
Movies S1 to S6
References (*39*, *40*)

16 December 2015; accepted 26 May 2016
10.1126/science.aaf0984

ROBOTICS

Phototactic guidance of a tissue-engineered soft-robotic ray

Sung-Jin Park,[1] Mattia Gazzola,[2]* Kyung Soo Park,[3,4]† Shirley Park,[5]‡ Valentina Di Santo,[6] Erin L. Blevins,[6]§ Johan U. Lind,[1] Patrick H. Campbell,[1] Stephanie Dauth,[1] Andrew K. Capulli,[1] Francesco S. Pasqualini,[1] Seungkuk Ahn,[1] Alexander Cho,[1] Hongyan Yuan,[1]|| Ben M. Maoz,[1] Ragu Vijaykumar,[5] Jeong-Woo Choi,[3,4] Karl Deisseroth,[5,7] George V. Lauder,[6] L. Mahadevan,[2,8] Kevin Kit Parker[1,4]¶

Inspired by the relatively simple morphological blueprint provided by batoid fish such as stingrays and skates, we created a biohybrid system that enables an artificial animal—a tissue-engineered ray—to swim and phototactically follow a light cue. By patterning dissociated rat cardiomyocytes on an elastomeric body enclosing a microfabricated gold skeleton, we replicated fish morphology at $^{1}/_{10}$ scale and captured basic fin deflection patterns of batoid fish. Optogenetics allows for phototactic guidance, steering, and turning maneuvers. Optical stimulation induced sequential muscle activation via serpentine-patterned muscle circuits, leading to coordinated undulatory swimming. The speed and direction of the ray was controlled by modulating light frequency and by independently eliciting right and left fins, allowing the biohybrid machine to maneuver through an obstacle course.

Bioinspired design, as applied to robotics, aims at implementing naturally occurring features such as soft materials, morphologies, gaits, and control mechanisms in artificial settings in order to improve performance (*1*–*4*). For example, recent soft-robotics studies raised awareness on the importance of material properties (*3*, *4*), shifting the focus from rigid elements to soft materials, whereas other investigations report successful mimicry of gaits or morphological features inspired by insects (*5*, *6*), fish (*7*, *8*), snakes (*9*), salamanders (*10*), and cheetahs (*11*). Although recent advances have the promise of bridging the performance gap with animals,

the current soft-robotic actuators based on, for instance, electroactive polymers, shape memory alloys, or pressurized fluids are yet to mature to the point of replicating the high-resolution complex movements of biological muscles (*3*, *4*).

In this context, biosensors and bioactuators (*12*) are intriguing alternatives because they can intrinsically respond to a number of control inputs (such as electric fields and optical stimulation). Thanks to recent advances in genetic tools (*13*) and tissue engineering (*12*), these responses can be altered and tuned across a wide range of time and length scales. Some pioneering studies have exploited these technologies for self-propulsion, developing miniaturized walking machines (*14*–*16*) and flagellar (*17*) or jellyfish-inspired (*18*) swimming devices. These biohybrid systems operate at high energy efficiency and harvest power from energy-dense, locally available nutrients, although at present they require specialized environments (physiological solutions) that may limit their applicability. Moreover, these biohybrid locomotors lack the reflexive control (*9*, *19*) necessary to enable adaptive maneuvering and thus the ability to respond to spatiotemporally varying external stimuli.

We designed, built, and tested a tissue-engineered analog of a batoid fish such as stingrays and skates. By combining soft materials and tissue engineering with optogenetics, we created an integrated sensory-motor system that allowed for coordinated undulating fin movement and phototactically controlled locomotion that is guided via light stimuli. We drew from fish morphology, neuromuscular dynamics, and gait control to implement a living, biohybrid system that leads to robust and reproducible locomotion and turning maneuvers. Batoid fish are ideal biological models in robotics (*8*) because their nearly planar bauplan is characterized by a broad dorsoventral disk, with a flattened body and extended pectoral fins, that enhances stability against roll (*20*). They swim with high energy efficiency (*21*) by generating spanwise bending deformations and chordwise front-to-rear undulatory motion (Fig. 1A and movie S1) (*20*, *22*) via the sequential activation of pectoral fin muscles. This undulatory gait allows slender aquatic animals to channel body movement into forward motion by exchanging momentum with the fluid (*7*, *22*) and is a convergent mode of aquatic propulsion (*23*). Moreover, batoids can use these undulatory modes for fine maneuvering and turning by independently and asymmetrically actuating their pectoral fins (*24*). Inspired by batoids, we reverse-engineered their musculoskeletal structure (Fig. 1B and fig. S1) via a four-layered architecture (Fig. 1C): a three-dimensional elastomer [polydimethylsiloxane (PDMS)] body, cast via a titanium mold (fig. S2A and movie S2); a chemically neutral skeleton fabricated by means of thermal evaporation of gold through a custom designed shadow mask; a thin interstitial elastomer layer obtained by spin-coating; and last, a layer of aligned rat cardiomyocytes generated via microcontact printing of fibronectin (fig. S3) (*25*).

This design yielded a tissue-engineered ray with a single muscle layer capable of downward contraction (Fig. 1, C and D). Upward contraction would require a second layer of muscle that acts antagonistically to the upper layer. To minimize the complexity of our design, we instead used an asymmetrical stiff gold skeleton that stores elastic energy during the downstroke and rebounds during the subsequent relaxation phase. Inspired by histological analysis (fig. S1) as well as theoretical considerations (*26*), we channeled muscular work and elastic energy into forward motion by breaking fore-aft symmetry through a varying body rigidity along the anterior-posterior axis. This was achieved via a thicker body and a denser and radially further reaching skeleton pattern in the front (Figs. 1, C and D, and 2A and fig. S2A). Likewise, along the proximal-distal axis, flexibility of the fins was enhanced by gradually reducing their thickness (fig. S2A). Last, the PDMS mixture was adjusted (*25*) to provide body rigidity and fin flexibility while conserving overall neutral buoyancy (fig. S2).

The composite supporting structure described above was coupled to a tissue-engineered muscle layer, which captured the salient musculoskeletal features of batoid fish (Fig. 2B). At the mesoscale (50 μm to 5 mm), batoid myofibers are tightly bundled and are aligned in the radial direction parallel to the rays of the skeleton (Fig. 2B). At the microscale (1 to 10 μm), the Z-lines of the sarcomeres (the cell force–generating units) (Fig. 2C) present strong nematic alignment perpendicular to individual myofibers so as to focus contraction forces. Following this layout, the muscles and sarcomeres of the tissue-engineered ray were designed to orient radially from the body and parallel to the gold skeleton rays (Fig. 2B and fig. S4), and the Z-lines of the sarcomeres were engineered to be perpendicular to the skeleton rays through microscale patterning of fibronectin (Fig. 2C and fig. S4).

Last, to mimic the sensory-somatic nervous system that controls the sequential activation of fin muscles in the batoid fish, we recast the neurocontrol problem as a design problem. A possible solution is given by serpentine-patterned muscle circuits that physically determine the propagation of muscle contraction in space and time (Figs. 1D and 2, D and E), leading to hardwired coordination that could be triggered with external

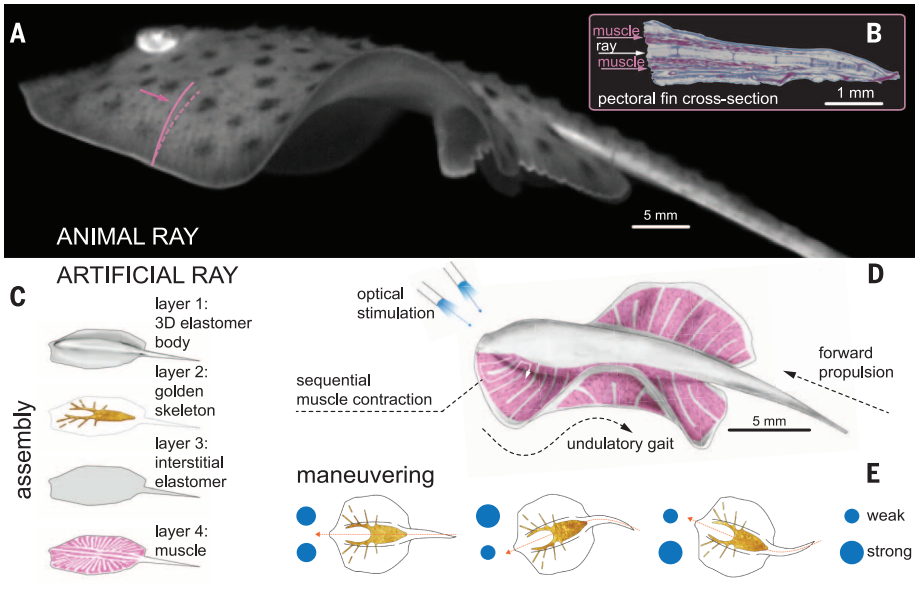

Fig. 1. Bioinspired concept design of the tissue-engineered ray. (**A**) A live Little skate, *Leucoraja erinacea*, swimming and (**B**) its musculoskeletal structure. (**C** to **E**) Tissue-engineered ray with (C) four layers of body architecture, (D) concept, and (E) phototactic control. Upon optical stimulation, the tissue-engineered ray induces sequential muscle activation via serpentine-patterned muscle tissues, generates undulatory locomotion, and sustains steady forward swimming. It changes direction by generating asymmetric undulating motion between left and right fins, modulated by light pulse frequency.

[1]Disease Biophysics Group, Wyss Institute for Biologically Inspired Engineering, John A. Paulson School of Engineering and Applied Sciences, Harvard University, Cambridge, MA 02138, USA. [2]John A. Paulson School of Engineering and Applied Sciences, Harvard University, Cambridge, MA 02138, USA. [3]Department of Chemical and Biomolecular Engineering, Sogang University, Seoul 121-742, Korea. [4]Sogang-Harvard Research Center for Disease Biophysics, Sogang University, Seoul 121-742, Korea. [5]Department of Bioengineering, Stanford University, Stanford, CA 94305, USA. [6]Museum of Comparative Zoology, Harvard University, Cambridge, MA 02138, USA. [7]Department of Psychiatry and Behavioral Sciences and the Howard Hughes Medical Institute, Stanford University, Stanford, CA 94305, USA. [8]Department of Organismic and Evolutionary Biology, Department of Physics, Wyss Institute for Biologically Inspired Engineering, Kavli Institute for Nanobio Science and Technology, Harvard University, Cambridge, MA 02138S, USA.
*Present address: Department of Mechanical Science and Engineering, University of Illinois at Urbana-Champaign, Urbana, IL 61801, USA. †Present address: Department of Biomedical Engineering, University of Michigan, Ann Arbor, MI 48109, USA. ‡Present address: Department of Cardiovascular Medicine, Stanford University Medical Center, Stanford, CA 94305, USA. §Present address: The Winsor School, Boston, MA 02215, USA. ||Present address: Department of Mechanical, Industrial and Systems Engineering, University of Rhode Island, Kingston, RI 02881, USA.
¶Corresponding author. Email: kkparker@seas.harvard.edu

stimuli. This design was implemented by overlaying onto anisotropic tissue a layer of cardiomyocytes that were electrically coupled with gap junctions (fig. S4H). These myocytes were engineered to respond to optical stimuli (Fig. 1D) by expressing a light-sensitive ion channel [channelrhodopsin-2 (ChR2)] (*27*). Thus, a point light stimulus directed at the front of the ray triggers the propagation of an action potential that is spatially and temporally modulated by the gap junctions between muscle cells without the need for neural coupling and coordination (Fig. 2, D and E). The expression of ChR2 was obtained via lentiviral transduction mediated by the truncated cardiac troponin T promoter cTnT (fig. S5) (*25*, *28*). This approach led to an 88% transduction rate of cardiomyocytes and maximized the sensitivity to blue light at powers of ~10 mW (fig. S5).

Optical stimulation of the circuits initiated sequential activation waves that propagated along the anterior-posterior axis as revealed by means of calcium imaging (*25*) for three different circuit designs (Fig. 2D, fig. S6, and movies S3 and S4). Dense serpentine patterns enhanced activation localization, whereas rarefied ones increased propagation speed (figs. S7 and S8). To allow for maneuverability, we ensured that each pectoral fin could be independently actuated by pacing left and right optical stimuli at different frequencies (fig. S6 and movie S5). Among the various designs considered, the circuit of choice was characterized by the intermediate serpentine pattern density (Fig. 2E). This circuit represented the best tradeoff between overlap with batoids' operating range and contraction time reproducibility (low standard error) in order to minimize desynchronization and undesired turning (Fig. 2E). The final overall design of our ray consists of ~200,000 live cardiomyocytes in an elastomeric body of 16.3 mm length and 10.18 ± 0.43 mg mass.

When immersed in a 37°C Tyrode's physiological salt solution containing glucose as energy reservoir, and upon optical stimulation, the fabricated ray was propelled by producing forward thrust via the undulatory motion of its fins (Fig. 3 and movie S6). Video-tracking analysis (*25*) showed that during each swimming cycle, as the calcium signal propagated (fig. S9), the anterior region bent downward, while the posterior one lifted upward (Fig. 3, A and B), conferring a small downward orientation (–10°) to the ray's longitudinal axis (fig. S9). Both regions reached their maximum displacement around ~200 ms (Fig. 3B), when their motion gradually inverted until ~340 ms

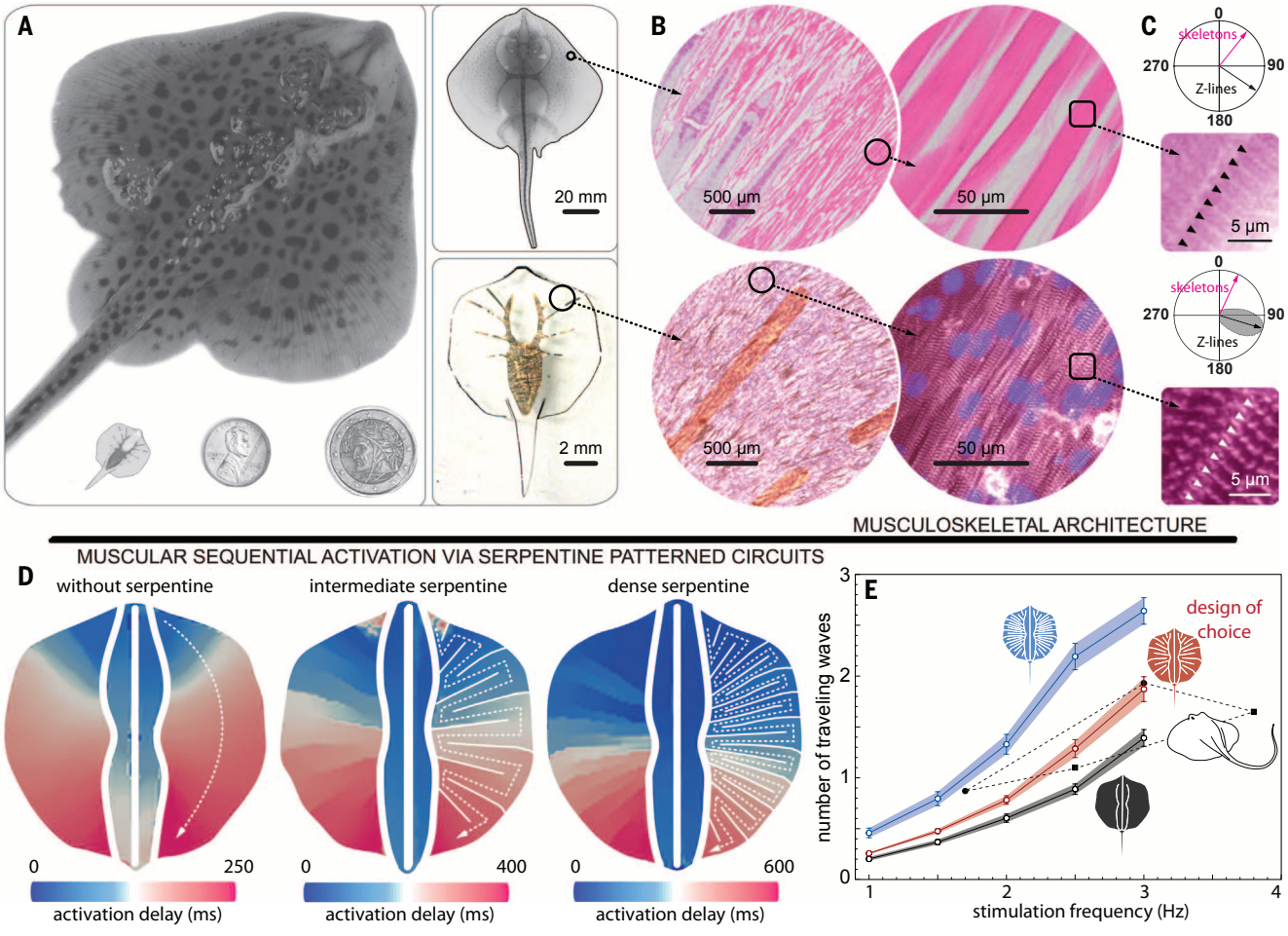

Fig. 2. Engineering solutions. (**A**) System-level design for skate (top) and tissue-engineered ray (bottom left) comparable with one penny and a two Euros coin (bottom middle and right). (**B** and **C**) Musculoskeletal (B) meso- and (C) micro-architecture of a skate, *L. erinacea* (top), is replicated in a tissue-engineered ray (bottom). Horizontal sections of the skate were stained with hematoxylin and eosin (top), and the engineered tissue was immunostained with a light-sensitive membrane protein, ChR2 (red, bottom left), sarcomeric α-actinin [red, (B), bottom right, and (C)], and nuclei (blue, (B), bottom right). (C) Orientation of the Z-lines (skate, black arrow and black triangles, top; and tissue-engineered ray, black arrow with gray distribution and white triangles, bottom). In both cases, Z-lines are perpendicular to the skeleton rays (pink arrows). (**D**) Muscle circuits with preprogrammed activation pattern. A point light stimulus directed at the front of the fins with 1.5 Hz frequency triggers the calcium wave that propagates along the predefined serpentine patterns. (**E**) Operating range of the muscle circuits. The circuit with intermediate serpentine pattern density represents the best tradeoff between contraction time reproducibility (SEM) and overlap with batoids' operating range [*Taeniura lymma* (*20*) and *Potamotrygon orbignyi* (*22*), black symbols]. Black, red, and blue indicates muscle circuit without serpentine patterns and with intermediate and dense serpentine patterns, respectively. Each colored band indicates SEM of number of traveling waves.

(Fig. 3, C and D). At this point, the calcium wave had traveled ~70% of the ray body and approached the flexible tail region (Fig. 3E and fig. S9). This signal caused a rapid, strong downward contraction of the rear of the body, a quick upward recoil of the head region (presumably mediated by the stiff skeleton) (Fig. 3), a 30° upward reorientation of the longitudinal axis (fig. S9), and a spike in forward swimming speed (Fig. 3E). After 340 ms, the calcium wave vanishes, and the ray relaxes (Fig. 3E and fig. S9), gliding until its forward momentum dissipates.

A periodical optical stimulation leads to a rhythmically sustained forward displacement (Fig. 3F). To test the benefits of spatiotemporally modulated undulatory locomotion relative to pulsatile locomotion (typical of jellyfish), we stimulated our design of choice via a global electrical field (*25*). The latter, unlike optical point stimulation, induces a global, synchronized contraction of the entire muscle layer, leading to jet-like propulsion (movie S7). Although pulsatile actuation also produced forward motion, undulatory gaits were found to be twice as fast at 1.5 Hz pacing (Fig. 3G).

We compared the kinematics (Fig. 3, H and I) and hydrodynamics (Fig. 3, J to M) of bioinspired and live rays. Both rays exhibit asymmetric deformation patterns in which the deflection amplitude progressively increases in the radially outward and anterior-posterior directions. This similarity shows that our asymmetric composite structure compensates for the lack of the upper muscle layer (Fig. 3, B and D), leading to the coordinated undulatory locomotion. Our design of choice was found to outperform a symmetric design (by 5.7×, as measured by distance traveled per unit time) as well as asymmetric designs without gold skeleton (2.7×), with denser gold skeleton (8.2×), and with thinner (1.5×) and thicker fins (3.3×) (fig. S10 and movie S8 and S9). Particle image velocimetry (PIV) (*25*) images of the hydrodynamic footprint of the tissue-engineered ray (Fig. 3, A to D) show that body contractions generate vortices of alternating sign that are sequentially shed downstream in the wake (Fig. 3, A to D, and movie S10), which is the hallmark of inertial undulatory swimming (*29*). Indeed, PIV of live skates (Fig. 3, K to M, and fig. S11) reveals a qualitatively similar alternation of positive and negative vortices, respectively generated in concave and convex regions of the body.

We emphasize here that our ray is a 10-fold scaled-down version of a live skate and moves in a laminar flow regime, as opposed to batoid fish that operate in turbulent conditions. Thus, a direct performance comparison is not meaningful, but it is instructive to contextualize artificial and natural solutions in terms of a recent scaling framework (*23*, *30*). All inertial undulatory swimmers hew to two scaling laws, $Re = Sw^{4/3}$ in the laminar regime and $Re = Sw$ in the turbulent regime, where the Swimming number $Sw = 2\pi fAL/\upsilon$ (L is the characteristic length of the swimmer, f is the undulation frequency, A is the amplitude, and υ is the fluid viscosity) captures input kinematics, and the Reynolds number $Re = UL/\upsilon$ (where U is the forward speed) captures output speed. By fitting extant biological data (*23*), the average swimming "roofline" was determined, thus providing an objective way to assess swimming performance. In this analysis, our tissue-engineered rays reached up to 63% of the Re of comparable natural solutions at the given Sw (Fig. 3J).

For gait control, we first determined a set of gait protocols for speed and direction control by modulating light frequency and by synchronously or asynchronously triggering the right and left serpentine circuits (figs. S11 and S12 and movies S12 to S18). Synchronous pacing on both fins resulted in straight, forward displacement (figs. S11 and S12 and movies S12 and S13), whereas stimulation frequency determined the swimming speed range (maximum at 1.5 to 2 Hz, minimum at 1 or 3 Hz) (fig. S10E and movies S14 to S16). Asynchronous pacing instead resulted in directional

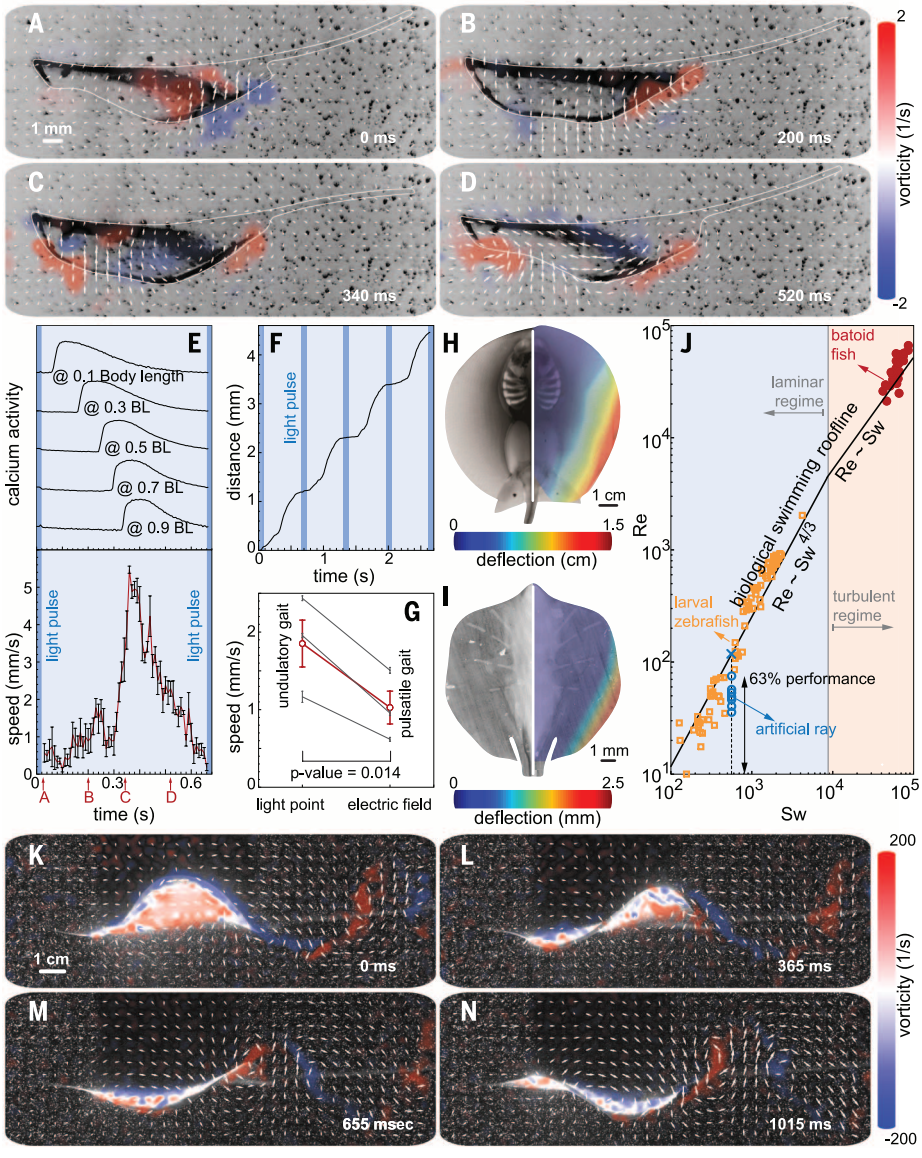

Fig. 3. Kinematics and hydrodynamics. (**A** to **D**) PIV flow measurements highlight the production of alternated positive and negative vortices by the tissue-engineered ray. The viscosity associated with the relatively small *Re* is responsible for the dissipation of the vortex street in the wake. (**E**) Correlation between calcium activity and undulatory locomotion. (**F**) The moving distance during four strokes. (**G**) Comparison of swimming speed between the tissue-engineered rays stimulated by point and field stimulations. Undulatory locomotion produced by sequential muscle activation (point, 1.85 mm/s) improved swimming speed significantly compared with pulsatile propulsion generated by global muscle activation (field, 1.03 mm/s; matched pairs test, $P = 0.014$, $n = 3$ rays). Gray and red lines indicate the speed of individual rays and their average, respectively. (**H** and **I**) Out-of-plane fin deflection in both (H) a live stingray, *P. orbignyi*, and (I) a tissue-engineered ray (maximum amplitude, 2.54 ± 0.02 mm). (**J**) Comparison of swimming performance between tissue-engineered rays ($n = 7$ rays) and aquatic swimmers [batoid fish (*20*) and larval zebrafish (*32*)] following the scaling analysis (*23*). [Figure adapted from (*23*).] (**K** to **N**) PIV analysis of live Little skate, *L. erinacea*.

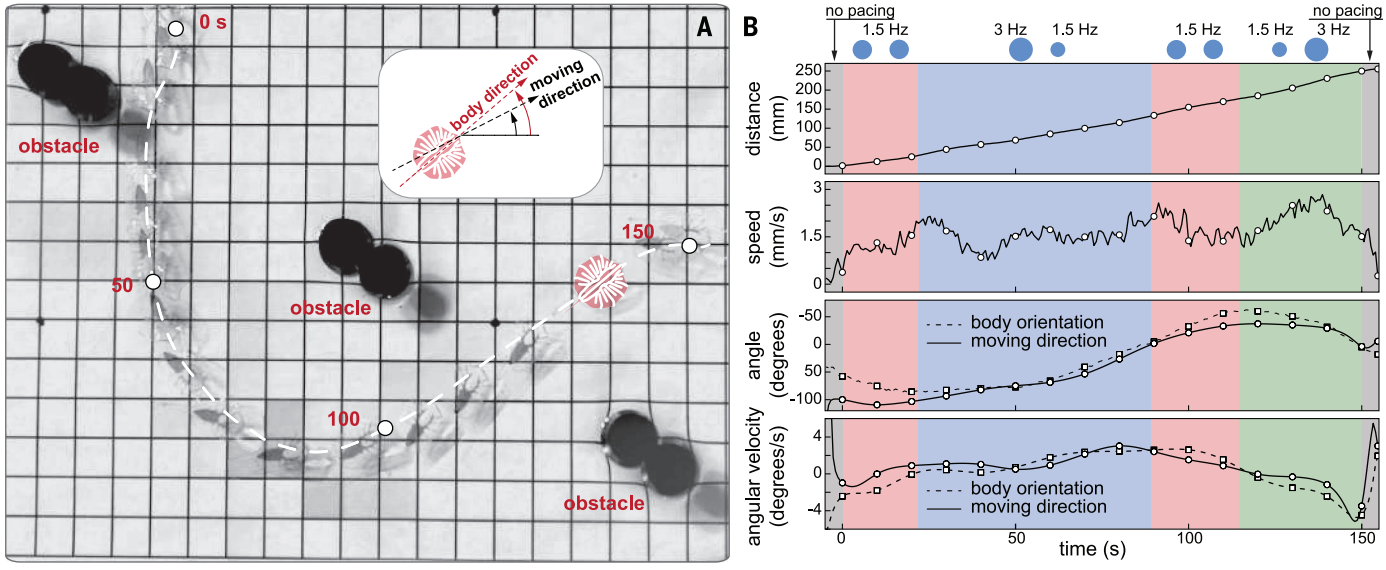

Fig. 4. Phototactic steering of the tissue-engineered ray through an obstacle course. (**A**) The ray completed a course that required complex coordination and maneuvering. Motion began with a forward protocol (at 0 s) to gain acceleration. A following left turn protocol allowed the ray to overcome forward momentum, making a left turn (at ~50 s). Next, another forward protocol was used to dissipate counterclockwise angular momentum and regain directionality (at ~100 s). While the ray made its way back to the other side of the obstacles, a final right turn protocol was given to make a right turn, winding the last obstacle. Grids, 1 cm. (**B**) Corresponding kinematic analysis relative to light frequency modulation protocols used for guidance.

turns (fig. S12, B, C, and F). In order to minimize the turning radius, we paired stimulation frequencies (1/1.5 Hz in movie S17, or 3/1.5 Hz in movie S18) to maximize the actuation difference between fins. Our ray turned in either clockwise or counterclockwise directions by generating asymmetric undulating motion between left and right fins, as in batoid fishes (*24*).

Last, we challenged the tissue-engineered ray to swim through an obstacle course. Using the above gait and turning protocols, we guided the ray along a curved path by alternating forward motion and turning maneuvers, at an average speed of ~1.5 mm/s over a distance of ~250 mm, 15 times longer than its body length (Fig. 4 and movie S19). Furthermore, the ray was found able to maintain 80% of its initial speed for up to 6 consecutive days (fig. S13 and movie S20). Therefore, our ray outperformed existing locomotive biohybrid systems in terms of speed [3.2 mm/s in movie S16, 1.3× over jellyfish (*18*)], distance traveled [~250 mm, 35× over cantilever-like walkers (*15*)], and durability (6 days), demonstrating the potential of self-propelled, phototactically activated tissue-engineered robots.

With dissociated cells, naturally equipped with biosensors and bioactuators, as a programmable, actuating building material, we used optogenetics and tissue engineering to build an adaptive swimming animal. Our study is but a first step in engineering multilevel systems that link neurodynamics, mechanics, and complex controllable gaits—coupling sensory information to motor coordination and movement that leads to behavior. This work paves the way for the development of autonomous and adaptive artificial creatures able to process multiple sensory inputs and produce complex behaviors in distributed systems and may represent a path toward soft-robotic "embodied cognition" (*4*, *31*).

REFERENCES AND NOTES

1. R. Pfeifer, M. Lungarella, F. Iida, *Science* **318**, 1088–1093 (2007).
2. M. Haberland, S. Kim, *Bioinspir. Biomim.* **10**, 016010 (2015).
3. S. Kim, C. Laschi, B. Trimmer, *Trends Biotechnol.* **31**, 287–294 (2013).
4. D. Rus, M. T. Tolley, *Nature* **521**, 467–475 (2015).
5. K. Y. Ma, P. Chirarattananon, S. B. Fuller, R. J. Wood, *Science* **340**, 603–607 (2013).
6. J. S. Koh *et al.*, *Science* **349**, 517–521 (2015).
7. M. S. Triantafyllou, G. S. Triantafyllou, *Sci. Am.* **272**, 64–70 (1995).
8. K. W. Moored, F. E. Fish, T. H. Kemp, H. Bart-Smith, *Mar. Technol. Soc. J.* **45**, 99–109 (2011).
9. H. C. Astley *et al.*, *Proc. Natl. Acad. Sci. U.S.A.* **112**, 6200–6205 (2015).
10. A. J. Ijspeert, A. Crespi, D. Ryczko, J. M. Cabelguen, *Science* **315**, 1416–1420 (2007).
11. D. J. Hyun, S. Seok, J. Lee, S. Kim, *Int. J. Robot. Res.* **33**, 1417–1445 (2014).
12. V. Chan, H. H. Asada, R. Bashir, *Lab Chip* **14**, 653–670 (2014).
13. J. D. Sander, J. K. Joung, *Nat. Biotechnol.* **32**, 347–355 (2014).
14. A. W. Feinberg *et al.*, *Science* **317**, 1366–1370 (2007).
15. V. Chan *et al.*, *Sci Rep* **2**, 857 (2012).
16. R. Raman *et al.*, *Proc. Natl. Acad. Sci. U.S.A.* **113**, 3497–3502 (2016).
17. B. J. Williams, S. V. Anand, J. Rajagopalan, M. T. A. Saif, *Nat. Commun.* **5**, 3081 (2014).
18. J. C. Nawroth *et al.*, *Nat. Biotechnol.* **30**, 792–797 (2012).
19. V. Braitenberg, *Vehicles: Experiments in Synthetic Psychology* (MIT Press, 1986).
20. L. J. Rosenberger, M. W. Westneat, *J. Exp. Biol.* **202**, 3523–3539 (1999).
21. V. Di Santo, C. P. Kenaley, *J. Exp. Biol.* **219**, 1804–1807 (2016).
22. E. L. Blevins, G. V. Lauder, *J. Exp. Biol.* **215**, 3231–3241 (2012).
23. M. Gazzola, M. Argentina, L. Mahadevan, *Nat. Phys.* **10**, 758–761 (2014).
24. J. M. Parson, F. E. Fish, A. J. Nicastro, *J. Exp. Mar. Biol. Ecol.* **402**, 12–18 (2011).
25. Materials and methods are available as supplementary materials on *Science* Online.
26. M. Gazzola, M. Argentina, L. Mahadevan, *Proc. Natl. Acad. Sci. U.S.A.* **112**, 3874–3879 (2015).
27. E. S. Boyden, F. Zhang, E. Bamberg, G. Nagel, K. Deisseroth, *Nat. Neurosci.* **8**, 1263–1268 (2005).
28. H. Ma, C. M. Sumbilla, I. K. G. Farrance, M. G. Klein, G. Inesi, *Am. J. Physiol. Cell Physiol.* **286**, C556–C564 (2004).
29. W. M. van Rees, M. Gazzola, P. Koumoutsakos, *J. Fluid Mech.* **722**, R3 (2013).
30. A. J. Cote, P. W. Webb, *Integr. Comp. Biol.* **55**, 662–672 (2015).
31. R. Pfeifer, H. G. Marques, F. Iida, Soft robotics: The next generation of intelligent machines. *Proceedings of the Twenty-Third International Joint Conference on Artificial Intelligence*, 3–9 August 2013, Beijing, China, pp. 5–11 (2013).
32. U. K. Müller, J. L. van Leeuwen, *J. Exp. Biol.* **207**, 853–868 (2004).

ACKNOWLEDGMENTS

Data reported in the paper are included in the supplementary materials. We thank A. P. Nesmith, M. McKenna, and A. Chandler for discussion on design and K. Hudson and Margherita Gazzola for photography and illustrations. This work was funded by the Harvard Paulson School of Engineering and Applied Sciences, the Wyss Institute for Biologically Inspired Engineering, the National Center for Advancing Translational Sciences grant UH3TR000522, subcontract 312659 from Los Almos National Laboratory under prime DTRA contract DE-AC52-06NA25396, the National Science Foundation (NSF) grant EFRI-0938043, NSF Materials Research Science and Engineering Center grant DMR-1420570, Office of Naval Research Multidisciplinary University Research Initiative grant N000141410533, the Swiss National Science Foundation, the MacArthur Foundation, the Radcliffe Institute, the National Research Foundation of Korea grant 2013K1A4A3055268, and the U.S. Army Research Laboratory and Office contract W911NF-12-2-0036. The views and conclusions contained in this Report are those of the authors and should not be interpreted as representing official policies, expressed or implied, of the Army Research Office or Laboratory, the U.S. government, or any other funding agencies. The U.S. government is authorized to reproduce and distribute reprints for government purposes notwithstanding any copyright notation hereon. Portions of this work were performed at the Harvard Center for Nanoscale Systems (NSF 1541959) and at the Neurobiology Imaging Facility (NINDS P30 Core Center NS072030). Certain aspects of the paper are described in U.S. patent 8,492,150 and U.S. patent application 20150182679.

SUPPLEMENTARY MATERIALS

www.sciencemag.org/content/353/6295/158/suppl/DC1
Materials and Methods
Supplementary Text
Figs. S1 to S15
References (*33*–*44*)
Movies S1 to S20

6 February 2016; accepted 19 May 2016
10.1126/science.aaf4292

NETWORK SCIENCE

Higher-order organization of complex networks

Austin R. Benson,[1] David F. Gleich,[2] Jure Leskovec[3]*

Networks are a fundamental tool for understanding and modeling complex systems in physics, biology, neuroscience, engineering, and social science. Many networks are known to exhibit rich, lower-order connectivity patterns that can be captured at the level of individual nodes and edges. However, higher-order organization of complex networks—at the level of small network subgraphs—remains largely unknown. Here, we develop a generalized framework for clustering networks on the basis of higher-order connectivity patterns. This framework provides mathematical guarantees on the optimality of obtained clusters and scales to networks with billions of edges. The framework reveals higher-order organization in a number of networks, including information propagation units in neuronal networks and hub structure in transportation networks. Results show that networks exhibit rich higher-order organizational structures that are exposed by clustering based on higher-order connectivity patterns.

Networks are a standard representation of data throughout the sciences, and higher-order connectivity patterns are essential to understanding the fundamental structures that control and mediate the behavior of many complex systems (*1*–*7*). The most common higher-order structures are small network subgraphs, which we refer to as network motifs (Fig. 1A). Network motifs are considered building blocks for complex networks (*1*, *8*). For example, feed-forward loops (Fig. 1A, M_5) have proven fundamental to understanding transcriptional regulation networks (*9*); triangular motifs (Fig. 1A, M_1–M_7) are crucial for social networks (*4*); open bidirectional wedges (Fig. 1A, M_{13}) are key to structural hubs in the brain (*10*); and two-hop paths (Fig. 1A, M_8–M_{13}) are essential to understanding air traffic patterns (*5*). Although network motifs have been recognized as fundamental units of networks, the higher-order organization of networks at the level of network motifs largely remains an open question.

Here, we use higher-order network structures to gain new insights into the organization of complex systems. We develop a framework that identifies clusters of network motifs. For each network motif (Fig. 1A), a different higher-order clustering may be revealed (Fig. 1B), which means that different organizational patterns are exposed, depending on the chosen motif.

Conceptually, given a network motif M, our framework searches for a cluster of nodes S with two goals. First, the nodes in S should participate in many instances of M. Second, the set S should avoid cutting instances of M, which occurs when only a subset of the nodes from a motif are in the set S (Fig. 1B). More precisely, given a motif M, the higher-order clustering framework aims to find a cluster (defined by a set of nodes S) that minimizes the following ratio:

$$\phi_M(S) = \mathrm{cut}_M(S, \bar{S}) / \min[\mathrm{vol}_M(S), \mathrm{vol}_M(\bar{S})] \quad (1)$$

where $\bar{S}$ denotes the remainder of the nodes (the complement of S), $\mathrm{cut}_M(S,\bar{S})$ is the number of instances of motif M with at least one node in S and one in $\bar{S}$, and $\mathrm{vol}_M(S)$ is the number of nodes in instances of M that reside in S. Equation 1 is a generalization of the conductance metric in spectral graph theory, one of the most useful graph partitioning scores (*11*). We refer to $\phi_M(S)$ as the motif conductance of S with respect to M.

Finding the exact set of nodes S that minimizes the motif conductance is computationally infeasible (*12*). To approximately minimize Eq. 1 and, hence, to identify higher-order clusters, we developed an optimization framework that provably finds near-optimal clusters [supplementary materials (*13*)]. We extend the spectral graph clustering methodology, which is based on the eigenvalues and eigenvectors of matrices associated with the graph (*11*), to account for higher-order structures in networks. The resulting method maintains the properties of traditional spectral graph clustering: computational efficiency, ease of implementation, and mathematical guarantees on the near-optimality of obtained clusters. Specifically, the clusters identified by our higher-order clustering framework satisfy the motif Cheeger inequality (*14*), which means that our optimization framework finds clusters that are at most a quadratic factor away from optimal.

The algorithm (illustrated in Fig. 1C) efficiently identifies a cluster of nodes S as follows:

- Step 1: Given a network and a motif M of interest, form the motif adjacency matrix W_M whose entries (i, j) are the co-occurrence counts of nodes i and j in the motif M: $(W_M)_{ij}$ = number of instances of M that contain nodes i and j.

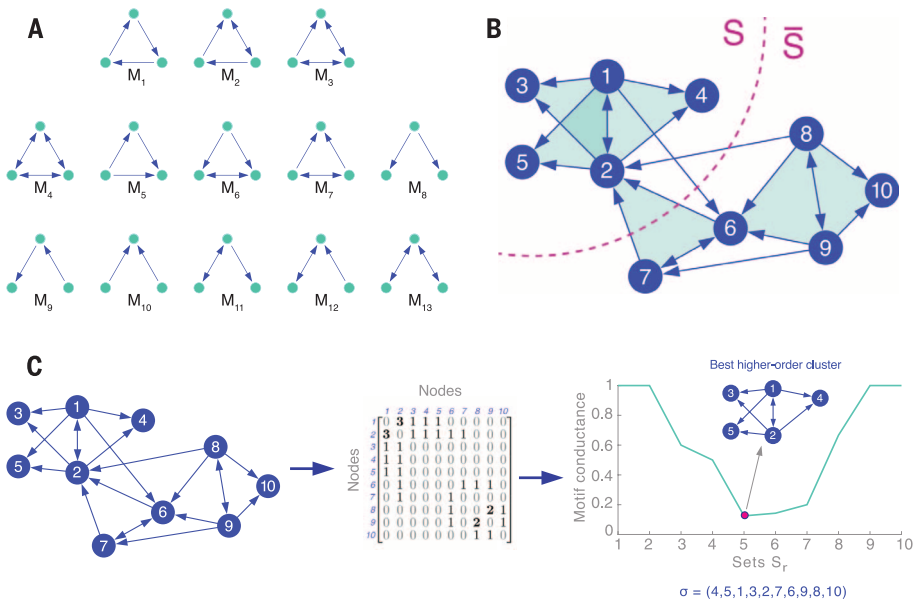

Fig. 1. Higher-order network structures and the higher-order network clustering framework. (**A**) Higher-order structures are captured by network motifs. For example, all 13 connected three-node directed motifs are shown here. (**B**) Clustering of a network based on motif M_7. For a given motif M, our framework aims to find a set of nodes S that minimizes motif conductance, $\phi_M(S)$, which we define as the ratio of the number of motifs cut (filled triangles cut) to the minimum number of nodes in instances of the motif in either S or $\bar{S}$ (*13*). In this case, there is one motif cut. (**C**) The higher-order network clustering framework. Given a graph and a motif of interest (in this case, M_7), the framework forms a motif adjacency matrix (W_M) by counting the number of times two nodes co-occur in an instance of the motif. An eigenvector of a Laplacian transformation of the motif adjacency matrix is then computed. The ordering σ of the nodes provided by the components of the eigenvector (*15*) produces nested sets $S_r = \{\sigma_1, \ldots, \sigma_r\}$ of increasing size r. We prove that the set S_r with the smallest motif-based conductance, $\phi_M(S_r)$, is a near-optimal higher-order cluster (*13*).

[1]Institute for Computational and Mathematical Engineering, Stanford University, Stanford, CA 94305, USA. [2]Department of Computer Science, Purdue University, West Lafayette, IN 47906, USA. [3]Computer Science Department, Stanford University, Stanford, CA 94305, USA.
*Corresponding author. Email: jure@cs.stanford.edu

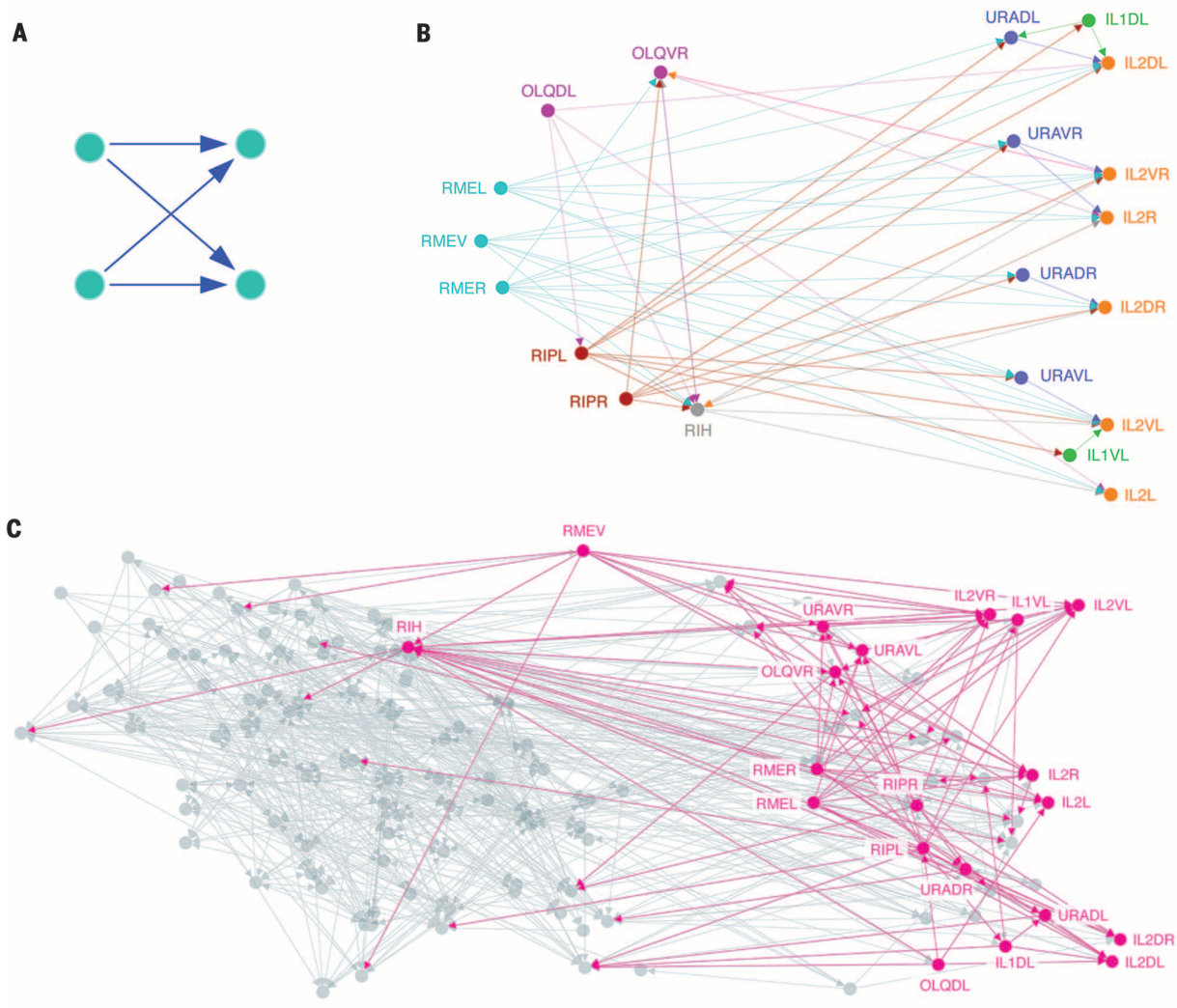

Fig. 2. Higher-order cluster in the *C. elegans* neuronal network. [See (*29*).] (**A**) The four-node bi-fan motif, which is overexpressed in neuronal networks (*1*). Intuitively, this motif describes a cooperative propagation of information from the nodes on the left to the nodes on the right. (**B**) The best higher-order cluster in the *C. elegans* frontal neuronal network based on the motif in (A). The cluster contains three ring motor neurons (RMEL, -V, and -R; cyan) with many outgoing connections, which serve as the source of information; six inner labial sensory neurons (IL2DL, -VR, -R, -DR, -VL, and -L; orange) with many incoming connections, serving as the destination of information; and four URA motor neurons (purple) acting as intermediaries. These RME neurons have been proposed as pioneers for the nerve ring (*21*), whereas the IL2 neurons are known regulators of nictation (*22*), and the higher-order cluster exposes their organization. The cluster also reveals that RIH serves as a critical intermediary of information processing. This neuron has incoming links from three RME neurons, outgoing connections to five of the six IL2 neurons, and the largest total number of connections of any neuron in the cluster. (**C**) Illustration of the higher-order cluster in the context of the entire network. Node locations are the true two-dimensional spatial embedding of the neurons. Most information flows from left to right, and we see that RMEV, -R, and -L and RIH serve as sources of information to the neurons on the right.

• Step 2: Compute the spectral ordering σ of the nodes from the normalized motif Laplacian matrix constructed via W_M (*15*).

• Step 3: Find the prefix set of σ with the smallest motif conductance (the argument of the minimum), formally, $S := \arg\min_r \phi_M(S_r)$, where $S_r = \{\sigma_1, \ldots, \sigma_r\}$.

For triangular motifs, the algorithm scales to networks with billions of edges and, typically, only takes several hours to process graphs of such size. On smaller networks with hundreds of thousands of edges, the algorithm can process motifs up to size 9 (*13*). Although the worst-case computational complexity of the algorithm for triangular motifs is $\Theta(m^{1.5})$, where m is the number of edges in the network, in practice, the algorithm is much faster. By analyzing 16 real-world networks where the number of edges m ranges from 159,000 to 2 billion, we found the computational complexity to scale as $\Theta(m^{1.2})$. Moreover, the algorithm can easily be parallelized, and sampling techniques can be used to further improve performance (*16*).

The framework can be applied to directed, undirected, and weighted networks, as well as motifs (*13*). Moreover, it can also be applied to networks with positive and negative signs on the edges, which are common in social networks (friend versus foe or trust versus distrust edges) and metabolic networks (edges signifying activation versus inhibition) (*13*). The framework can be used to identify higher-order structure in networks where domain knowledge suggests the motif of interest. In the supplementary materials, we also show that when a domain-specific higher-order pattern is not known in advance, the framework can also serve to identify which motifs are important for the modular organization of a given network (*13*). Such a general framework allows complex higher-order organizational structures in a number of different networks by using individual motifs and sets of motifs. The framework and mathematical theory immediately extend to other spectral methods, such as localized algorithms that find clusters around a seed node (*17*) and

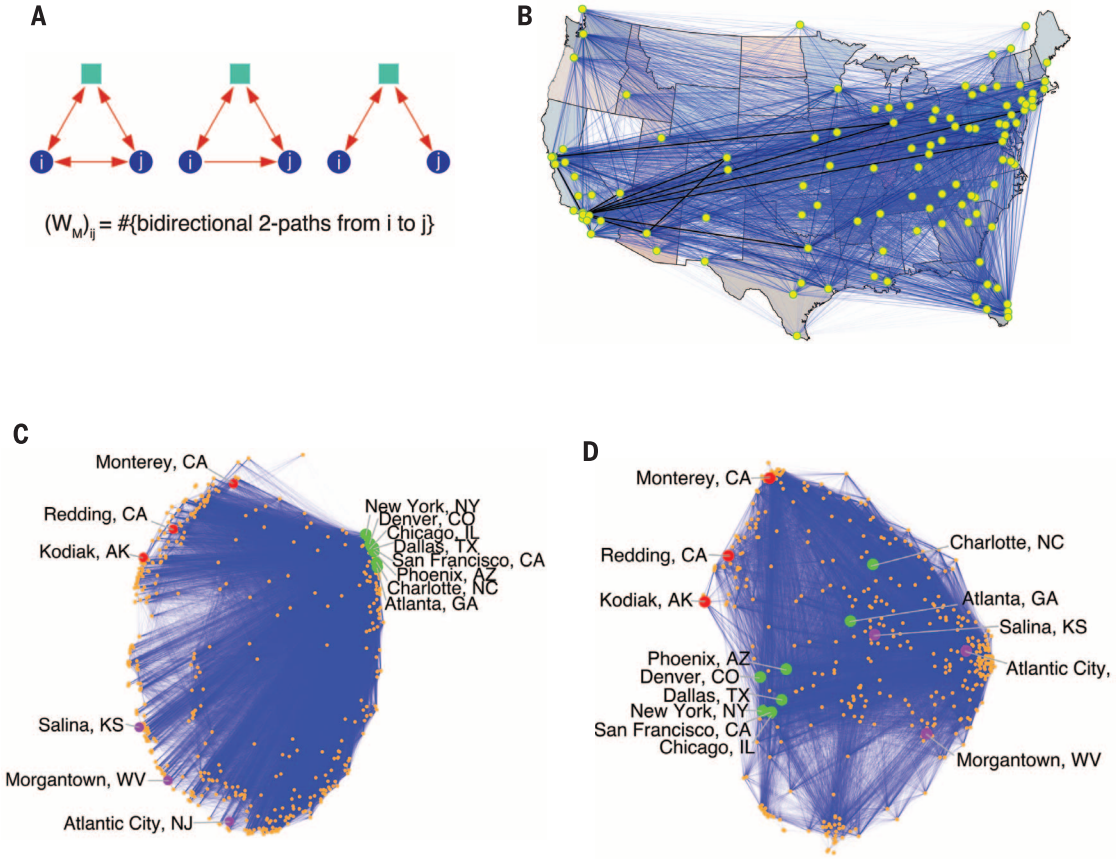

Fig. 3. Higher-order spectral analysis of a network of airports in Canada and the United States. [See (*23*).] (**A**) The three higher-order structures used in our analysis. Each motif is "anchored" by the blue nodes *i* and *j*, which means our framework only seeks to cluster together the blue nodes. Specifically, the motif adjacency matrix adds weight to the (*i*, *j*) edge on the basis of the number of third intermediary nodes (green squares). The first two motifs correspond to highly connected cities, and the motif on the right connects nonhubs to nonhubs. (**B**) The top 50 most populous cities in the United States, which correspond to nodes in the network. The edge thickness is proportional to the weight in the motif adjacency matrix W_M. The thick, dark lines indicate that large weights correspond to popular mainline routes. (**C**) Embedding of nodes provided by their corresponding components of the first two nontrivial eigenvectors of the normalized Laplacian for W_M. The marked cities are eight large U.S. hubs (green), three West Coast nonhubs (red), and three East Coast nonhubs (purple). The primary spectral coordinate (left to right) reveals how much of a hub the city is, and the second spectral coordinate (top to bottom) captures west-east geography (*13*). (**D**) Embedding of nodes provided by their corresponding components in the first two nontrivial eigenvectors of the standard, edge-based (non–higher-order) normalized Laplacian. This method does not capture the hub and geography found by the higher-order method. For example, Atlanta, the largest hub, is in the center of the embedding, next to Salina, a nonhub.

algorithms for finding overlapping clusters (*18*). To find several clusters, one can use embeddings from multiple eigenvectors and *k*-means clustering (*13*, *19*) or can apply recursive bipartitioning (*13*, *20*).

The framework can serve to identify a higher-order modular organization of networks. We apply the higher-order clustering framework to the *Caenorhabditis elegans* neuronal network, where the four-node "bi-fan" motif (Fig. 2A) is overexpressed (*1*). The higher-order clustering framework then reveals the organization of the motif within the *C. elegans* neuronal network. We find a cluster of 20 neurons in the frontal section with low bi-fan motif conductance (Fig. 2B). The cluster shows a way that nictation is controlled. Within the cluster, ring motor neurons (RMEL, -V, or -R), proposed pioneers of the nerve ring (*21*), propagate information to inner labial sensory neurons, regulators of nictation (*22*), through the neuron RIH (Fig. 2C). Our framework contextualizes the importance of the bi-fan motif in this control mechanism.

The framework also provides new insights into network organization beyond the clustering of nodes based only on edges. Results on a transportation reachability network (*23*) demonstrate how it finds the essential hub interconnection airports (Fig. 3). These appear as extrema on the primary spectral direction (Fig. 3C) when two-hop motifs (Fig. 3A) are used to capture highly connected nodes and nonhubs. [The first spectral coordinate of the normalized motif Laplacian embedding was positively correlated with the airport city's metropolitan population with Pearson correlation 99% confidence interval (0.33, 0.53).] The secondary spectral direction identified the west-east geography in the North American flight network [it was negatively correlated with the airport city's longitude with Pearson correlation 99% confidence interval (−0.66, −0.50)]. On the other hand, edge-based methods conflate geography and hub structure. For example, Atlanta, a large hub, is embedded next to Salina, a nonhub, with an edge-based method (Fig. 3D).

Our higher-order network clustering framework unifies motif analysis and network partitioning—two fundamental tools in network science—and reveals new organizational patterns and modules in complex systems. Prior efforts along these lines do not provide worst-case performance guarantees on the obtained clustering (*24*) and do not reveal which motifs organize the network (*25*) but rely on expanding the size of the network (*26*, *27*). Theoretical results in the supplementary materials (*13*) also explain why classes of hypergraph partitioning methods are more general than previously assumed and how motif-based clustering provides a rigorous framework for the special case of partitioning directed graphs. Finally, the higher-order network clustering framework is generally applicable to a wide range of network types, including directed, undirected, weighted, and signed networks.

REFERENCES AND NOTES

1. R. Milo *et al.*, *Science* **298**, 824–827 (2002).
2. S. Mangan, A. Zaslaver, U. Alon, *J. Mol. Biol.* **334**, 197–204 (2003).
3. J. Yang, J. Leskovec, *Proc. IEEE* **102**, 1892–1902 (2014).
4. P. W. Holland, S. Leinhardt, *Am. J. Sociol.* **76**, 492–513 (1970).
5. M. Rosvall, A. V. Esquivel, A. Lancichinetti, J. D. West, R. Lambiotte, *Nat. Commun.* **5**, 4630 (2014).
6. N. Pržulj, D. G. Corneil, I. Jurisica, *Bioinformatics* **20**, 3508–3515 (2004).
7. J. Leskovec, K. J. Lang, A. Dasgupta, M. W. Mahoney, *Internet Math.* **6**, 29–123 (2009).
8. Ö. N. Yaveroğlu *et al.*, *Sci. Rep.* **4**, 4547 (2014).
9. S. Mangan, U. Alon, *Proc. Natl. Acad. Sci. U.S.A.* **100**, 11980–11985 (2003).

10. C. J. Honey, R. Kötter, M. Breakspear, O. Sporns, *Proc. Natl. Acad. Sci. U.S.A.* **104**, 10240–10245 (2007).
11. S. E. Schaeffer, *Comput. Sci. Rev.* **1**, 27–64 (2007).
12. Minimizing $\phi_M(S)$ is nondeterministic polynomial-time hard (NP-hard), which follows from the NP-hardness of the traditional definition of conductance (*28*).
13. See the supplementary materials on *Science* Online.
14. Formally, when the motif has three nodes, the selected cluster S satisfies $\phi_M(S) \le 4\sqrt{\phi_M^*} \le 1$, where ϕ_M^* is the smallest motif conductance of any possible node set S. This inequality is proved in the supplementary materials.
15. The normalized motif Laplacian matrix is $L_M = D^{-1/2}(D - W_M)D^{-1/2}$, where D is a diagonal matrix with the row-sums of W_M on the diagonal [$D_{ii} = \Sigma_j (W_M)_{ij}$], and $D^{-1/2}$ is the same matrix with the inverse square roots on the diagonal [$D_{ii}^{-1/2} = 1/\sqrt{\Sigma_j (W_M)_{ij}}$]. The spectral ordering σ is the by-value ordering of $D^{-1/2}z$, where z is the eigenvector corresponding to the second smallest eigenvalue of L_M, i.e., σ_i is the index of $D^{-1/2}z$ with the ith smallest value.
16. C. Seshadhri, A. Pinar, T. G. Kolda, *Stat. Anal. Data Min.* **7**, 294–307 (2014).
17. R. Andersen, F. Chung, K. Lang, in *Proceedings of the 47th Annual IEEE Symposium on Foundations of Computer Science, FOCS'06*, Berkeley, California, 21 to 25 October 2006 (Institute of Electrical and Electronics Engineers, Piscataway, NJ, 2006), pp. 475–486.
18. J. J. Whang, I. S. Dhillon, D. F. Gleich, in *Proceedings of the 2015 SIAM International Conference on Data Mining*, Vancouver, British Columbia, Canada, 30 April to 2 May 2015, S. Venkatasubramanian, J. Ye, Eds. (Society for Industrial and Applied Mathematics, Philadelphia, PA, 2015), pp. 936–944.
19. A. Y. Ng, M. I. Jordan, Y. Weiss, *Adv. Neural Inf. Process. Syst.* **14**, 849–856 (2002).
20. D. Boley, *Data Min. Knowl. Discov.* **2**, 325–344 (1998).
21. D. L. Riddle *et al.*, Eds., *C. elegans II* (Cold Spring Harbor Laboratory Press, Cold Spring Harbor, NY, ed. 2, 1997).
22. H. Lee *et al.*, *Nat. Neurosci.* **15**, 107–112 (2011).
23. B. J. Frey, D. Dueck, *Science* **315**, 972–976 (2007).
24. B. Serrour, A. Arenas, S. Gómez, *Comput. Commun.* **34**, 629–634 (2011).
25. T. Michoel, A. Joshi, B. Nachtergaele, Y. Van de Peer, *Mol. Biosyst.* **7**, 2769–2778 (2011).
26. A. R. Benson, D. F. Gleich, J. Leskovec, in *Proceedings of the 2015 SIAM International Conference on Data Mining*, Vancouver, British Columbia, Canada, 30 April to 2 May 2015, S. Venkatasubramanian, J. Ye, Eds. (SIAM, Philadelphia, 2015), pp. 118–126.
27. F. Krzakala *et al.*, *Proc. Natl. Acad. Sci. U.S.A.* **110**, 20935–20940 (2013).
28. D. Wagner, F. Wagner, in *Mathematical Foundations of Computer Science 1993, Proceedings of the 18th International Symposium on Mathematical Foundations of Computer Science, MFCS'93*, Gdańsk, Poland, 30 August to 3 September 1993, A. M. Borzyszkowski, S. Sokolowski, Eds. (Lecture Notes in Computer Science, Springer, New York, 1993), pp. 744–750.
29. M. Kaiser, C. C. Hilgetag, *PLOS Comput. Biol.* **2**, e95 (2006).

ACKNOWLEDGMENTS

The authors thank R. Sosič for insightful comments. A.R.B. was supported by a Stanford Graduate Fellowship; D.F.G. was supported by NSF (CCF-1149756 and IIS-1422918), J.L. was supported by NSF (IIS-1149837 and CNS-1010921), trans-NIH initiative Big Data to Knowledge (BD2K), Defense Advanced Research Projects Agency [XDATA and Simplifying Complexity in Scientific Discovery (SIMPLEX)], Boeing, Lightspeed, and Volkswagen. Software implementations and the data sets used to obtain the results in this manuscript are available at http://snap.stanford.edu/higher-order/.

SUPPLEMENTARY MATERIALS

www.sciencemag.org/content/353/6295/163/suppl/DC1
Materials and Methods
Supplementary Text
Figs. S1 to S13
Tables S1 to S12
References (*30*–*84*)

18 November 2015; accepted 18 May 2016
10.1126/science.aad9029

PLANT SCIENCE

S-Acylation of the cellulose synthase complex is essential for its plasma membrane localization

Manoj Kumar,[1] Raymond Wightman,[2] Ivan Atanassov,[1]* Anjali Gupta,[1] Charlotte H. Hurst,[3,4] Piers A. Hemsley,[3,4]† Simon Turner[1]†

Plant cellulose microfibrils are synthesized by a process that propels the cellulose synthase complex (CSC) through the plane of the plasma membrane. How interactions between membranes and the CSC are regulated is currently unknown. Here, we demonstrate that all catalytic subunits of the CSC, known as cellulose synthase A (CESA) proteins, are S-acylated. Analysis of *Arabidopsis* CESA7 reveals four cysteines in variable region 2 (VR2) and two cysteines at the carboxy terminus (CT) as S-acylation sites. Mutating both the VR2 and CT cysteines permits CSC assembly and trafficking to the Golgi but prevents localization to the plasma membrane. Estimates suggest that a single CSC contains more than 100 S-acyl groups, which greatly increase the hydrophobic nature of the CSC and likely influence its immediate membrane environment.

Cellulose in plants is synthesized at the plasma membrane by the cellulose synthase complex (CSC), which contains at least 18 catalytic CESA protein subunits (*1*). The direction of CSC movement and the orientation of cellulose microfibril deposition are determined by cortical microtubules (*2*). Movement of the CSC through the plane of the plasma membrane is likely to cause severe disruption to the lipid bilayer (*3*), which suggests that membrane partitioning of this process may be important. Here, we describe the modifications of CESA proteins and demonstrate their importance to the functioning of the CSC.

S-Acylation involves reversible addition of an acyl group, often palmitate or stearate, to a cysteine residue, which can affect protein structure or localization (*4*). A recent study identified many S-acylated proteins in plants (*5*), including CESA1 and CESA3, which are essential for cellulose synthesis in the primary cell wall (*6*). We used acyl–resin-assisted capture (acyl-RAC) assays (*7*) to confirm that CESA1 is S-acylated (fig. S1) and showed that CESA6 is also S-acylated (Fig. 1A). Furthermore, all three CESAs required for cellulose synthesis in the secondary cell wall, CESA4, CESA7, and CESA8, are S-acylated (Fig. 1A), which demonstrates that S-acylation is a common feature of CESA proteins involved in cellulose synthesis in both primary and secondary cell walls.

CESA7 has 26 cysteines (fig. S2A). In order to identify S-acylated cysteines, we mutated individual CESA7 cysteines to serines and tested their ability to complement the *cesa7$^{irx3\text{-}1}$* mutant. None of the eight cysteines in the zinc finger domain (ZR) showed any significant complementation (Fig. 2A and figs. S3 and S4). The structure of the RING-type zinc-finger domain from CESA7 [Protein Data Bank (PDB) ID: 1WEO] shows that all eight cysteines are involved in coordinating two zinc atoms, which makes them unlikely to be S-acylated. Consequently, we focused our subsequent analysis on other regions of CESA7. Two highly conserved cysteines in the short C terminus (table S1) are also essential for CESA protein function (Fig. 2A). None of the remaining 16 single cysteine mutants showed a substantial effect on cellulose content (Fig. 2A).

A cysteine-rich region lies within VR2 (*8*). The number of VR2 cysteines is conserved among orthologous CESAs from different species but varies between paralogous CESAs (table S1). There are four VR2 cysteines in CESA7 (fig. S2), and mutating them individually has no effect on cellulose biosynthesis (Fig. 2, A and C). We hypothesized that if VR2 is a site of CESA S-acylation, the remaining VR2 cysteines may support sufficient S-acylation for CESA7 function. Consequently, we mutated all four VR2 cysteines in CESA7 ($VR2_{C/S}$). The $VR2_{C/S}$ mutant exhibited no complementation of *cesa7$^{irx3\text{-}1}$* (Fig. 2C). Thus, the cysteines in this region appear to be functionally redundant.

Having identified the VR2 and CT cysteines as potential S-acylation sites, we proceeded to determine if these sites were S-acylated. We generated a mutant in which both CT cysteines were mutated ($CT_{C/S}$). The $CT_{C/S}$ mutant did not complement the *cesa7$^{irx3\text{-}1}$* mutant (Fig. 2B). Using Acyl-RAC assays we consistently found that S-acylation was dramatically reduced in the $VR2_{C/S}$ mutant, although some signal remained. The $CT_{C/S}$ mutants exhibited a smaller decrease in S-acylation (Fig. 1, B and C). We then constructed a mutant in which both the VR2 and CT cysteines were mutated

[1]Faculty of Life Sciences, The University of Manchester, Michael Smith Building, Oxford Road, Manchester M13 9PT, UK. [2]Microscopy Core Facility, Sainsbury Laboratory, University of Cambridge, Bateman Street, Cambridge CB2 1LR, UK. [3]Division of Plant Sciences, School of Life Sciences, University of Dundee, Dow Street, Dundee, DD1 5EH, Scotland, UK. [4]Cell and Molecular Sciences, The James Hutton Institute, Invergowrie, DD2 5DA, Scotland, UK.
*Present address: AgroBioInstitute, 8 Dragan Tzankov Boulevard, 1164 Sofia; Bulgaria. **†Corresponding author. Email: simon.turner@manchester.ac.uk (S.T.); p.a.hemsley@dundee.ac.uk (P.A.H.)**

(VR2/$CT_{C/S}$). The VR2/$CT_{C/S}$ mutant exhibited no complementation (Fig. 2B) and CESA7 S-acylation was effectively abolished (Fig. 1, B and C), consistent with the hypothesis that both the VR2 and CT cysteines are S-acylated.

In order to determine whether some of the VR2 cysteines were more important than the others, these cysteines were mutated in all possible double and triple combinations. All 10 of these double and triple VR2 cysteine mutants had a lower cellulose content than the single VR2 cysteine mutants (Fig. 2C), which indicated that all four cysteines are important. In order to explore sequence specificity around the VR2 cysteines, we replaced the six–amino acid–long motif containing four cysteines of CESA7 with a motif from the same region of either CESA8 ($CESA7_{CESA8VRC}$), which contains only three cysteines, or CESA4 ($CESA7_{CESA4VRC}$), which contains six cysteines in a 12–amino acid–long motif (fig. S2B). The $CESA7_{CESA4VRC}$ construct complemented the *cesa7*$^{irx3-7}$ mutant, but $CESA7_{CESA8VRC}$ did not (Fig. 2D and fig. S3D). We also observed that wild-type levels of CESA7 S-acylation were restored in $CESA7_{CESA4VRC}$ but only partially in $CESA7_{CESA8VRC}$ (fig. S5). Restoration of activity in $CESA7_{CESA4VRC}$ would suggest that the lack of acylation in the $VR2_{C/S}$ mutant is not a result of changes to protein conformation caused by mutating the cysteines in this region.

To investigate the effect of S-acylation on the trafficking of the CSC, we performed live-cell imaging of CESA7 in the developing xylem of intact roots (Fig. 3). During vessel differentiation, CSCs can be seen both moving around the cell in the Golgi, where they exhibit a characteristic ring-shaped morphology, and as transverse bands at the plasma membrane that correspond to sites of secondary cell-wall deposition and cortical microtubule localization (*9*, *10*). Using wild-type yellow fluorescent protein (YFP)–labeled CESA7 (YFP-CESA7), this banded pattern can be seen in single images, movie projections (Fig. 3, A and C), and movies (movie S1) and colocalizes with bands of cortical microtubules (fig. S6). In contrast, neither of the $VR2_{C/S}$ or $CT_{C/S}$ mutants exhibited the banded pattern (Fig. 3, A and C, and movies S2 and S3). Furthermore, we did not observe colocalization of CESA7 with cortical microtubules in the $VR2_{C/S}$ mutant (fig. S6). The banded pattern of CESA7 localization is only apparent during later stages of vessel differentiation. At earlier stages, YFP-CESA7 is localized mainly within the Golgi, a distribution that resembles those seen in the $VR2_{C/S}$ and $CT_{C/S}$ mutants. Similarly, mechanical perturbation of the seedlings during the imaging process can lead to a loss of the banded pattern. In plants that contained both cyan fluorescent protein (CFP)–tagged wild-type CESA7 and YFP-tagged $VR2_{C/S}$, we were able to see bands with CFP-CESA7, indicative of localization at the plasma membrane, but not with YFP-$VR2_{C/S}$ (Fig. 3B). Although we always observed banding in the lines containing only the CFP-CESA7, banding was not observed in additional lines with high levels of YFP-$VR2_{C/S}$ expression, which indicated that this construct has a dominant-negative effect on CFP-CESA7 localization. Trafficking of the CSC to the plasma membrane is known to occur from the Golgi via particles known as microtubule-associated cellulose synthase compartments (MASCs) or small CESA compartments (SmaCCs) (*11*, *12*). We analyzed the movement of the Golgi and found no differences in trafficking dynamics between the wild-type and either the CESA7 $VR2_{C/S}$ or $CT_{C/S}$ mutants (fig. S7A). The imaging data are consistent with the hypothesis that the defective

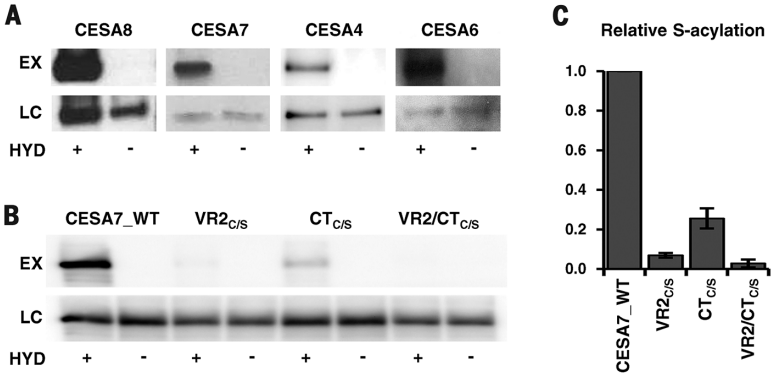

Fig. 1. Analysis of *Arabidopsis* CESA protein S-acylation. S-Acylation of various CESA proteins from wild-type (WT) plants assayed using biotin exchange or acyl-RAC assays (**A**) and CESA7 cysteine cluster mutants measured by acyl-RAC (**B**). For each assay, the experimental sample (EX) was compared with the loading control (LC) with or without (+/-) hydroxylamine (HYD) for hydroxylamine-dependent capture of S-acylated proteins. Individual CESA proteins were detected with specific antibodies. (**C**) The genotypes shown in (B) were tested in four independent experiments. Relative levels of S-acylation are expressed as a percentage of the wild type. Error bars represent SEMs.

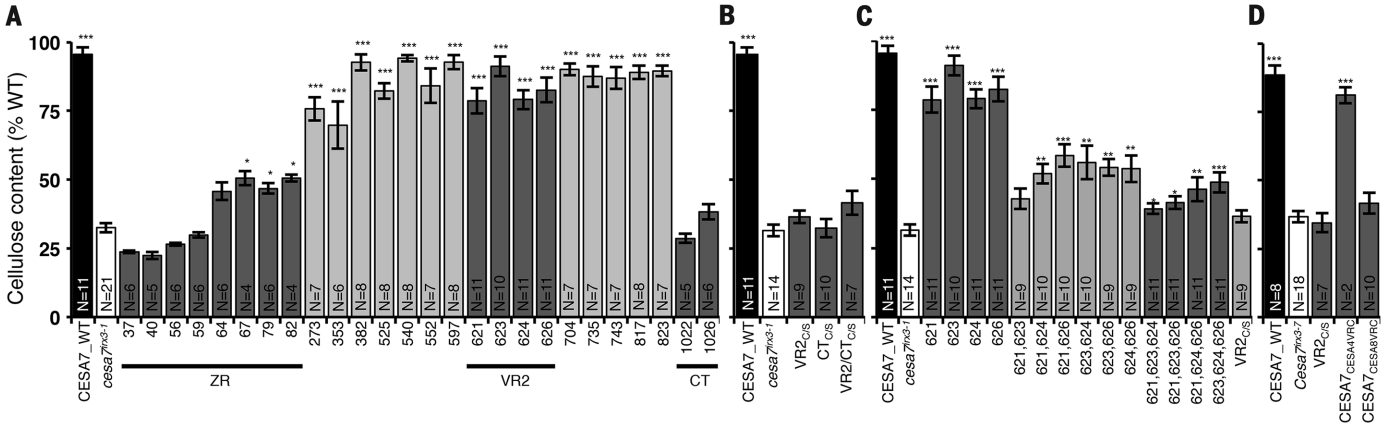

Fig. 2. Cellulose content of the CESA7 cysteine mutants. Cellulose content of single cysteine mutants (**A**), cysteine cluster mutants (**B**), VR2 cysteines mutant combinations (**C**), and mutants with CESA7 VR2 cysteines replaced with those of CESA4 and CESA8 (**D**). The numbers on the horizontal axis in (A) and (C) refer to the CESA7 residue number of the mutated cysteines. ZR, VR2, and CT domains mentioned in text are highlighted with black lines in (A). Cellulose content is expressed as percentage of the wild type by using Landsberg *erecta* (Ler-0) for *cesa7*$^{irx3-1}$ [(A), (B), (C)] or Colombia (Col-0) for *cesa7*$^{irx3-7}$ (D). Error bars are SEM. Significance values are for comparison of each genotype to the mutant control in a univariate analysis of variance (ANOVA) test. Significance at ***$P < 0.001$, **$P < 0.01$, or *$P < 0.05$ levels are indicated.

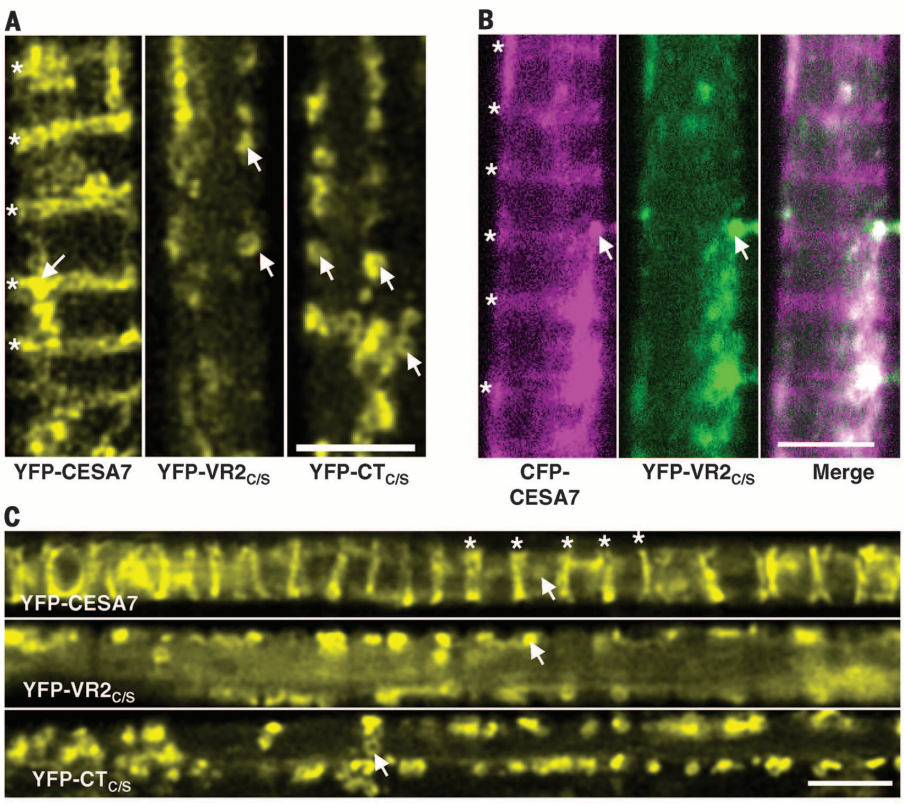

Fig. 3. Loss of acylation affects CSC localization at the plasma membrane. In live-cell imaging of the CSC in developing xylem vessels of intact roots using YFP-CESA7, CSCs at the plasma membrane appear as lateral bands (asterisks); whereas in the Golgi, CSCs are visualized as ring-shaped particles (arrows). (**A**) Single-frame images showing localization of YFP-tagged wild-type CESA7 and the $VR2_{C/S}$ and $CT_{C/S}$ mutants. (**B**) Single-frame images showing CFP-CESA7 (magenta) and YFP-$VR2_{C/S}$ (green) within the same cell. (**C**) Average projections taken from movies showing YFP-tagged WT CESA7 and the $VR2_{C/S}$ and $CT_{C/S}$ mutants. Scale bars, 5 μm.

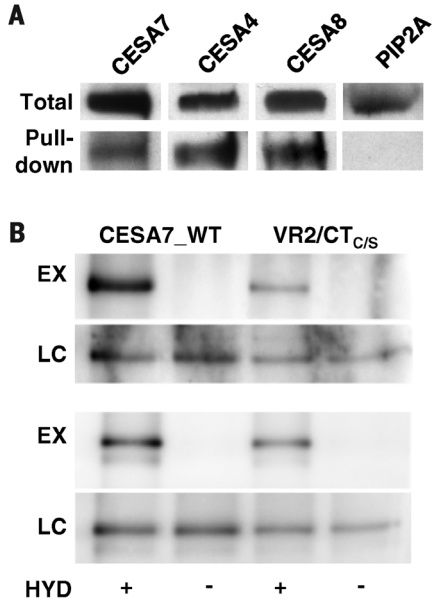

Fig. 4. Loss of CESA7 acylation does not affect the CSC subunit association or S-acylation of other CESAs in the complex. (**A**) Total protein and Ni^{2+} affinity purified CESA7 samples from CESA7 $VR2/CT_{C/S}$ mutant were probed with the CESA antibodies as indicated. PIP2 was used as a control. (**B**) S-Acylation status of CESA4 (top) and CESA8 (bottom) was determined in CESA7_WT and CESA7 $VR2/CT_{C/S}$ plants by using Acyl-RAC. For each assay, the experimental samples (EX) were compared with the loading control (LC) with or without (+/-) hydroxylamine (HYD) for hydroxylamine-dependent capture of S-acylated proteins. Blots were probed with either CESA4- or CESA8-specific antibodies.

S-acylation of the $VR2_{C/S}$ mutant interferes with Golgi to plasma membrane trafficking of the CSC. In both the CESA7 $VR2_{C/S}$ and $CT_{C/S}$ mutants, we were able to observe particles that resemble MASCs (fig. S7B), but using the intact root system, we were unable to track their movement or observe individual insertion events. Consequently, we cannot exclude the possibility of S-acylation–defective CSCs being transiently inserted into the plasma membrane and rapidly recycled or plasma membrane insertion occurring at a much-reduced rate, nor can we exclude the possibility that S-acylation affects the ability of CSC complexes to associate with cortical microtubules. In the future, it will be interesting to determine exactly at what point the trafficking is defective in the acylation-deficient mutant and whether interactions between the MASC and microtubules or other markers for the sites of cell-wall deposition are altered.

To explore how the trafficking of CESA is altered in the S-acylation–deficient mutant, we examined the interactions of CESA subunits, because mutations in one CESA protein can affect the association among the remaining CESAs in the complex (*13*). We used the tag on the $VR2/CT_{C/S}$ mutant in a pull-down assay of CESA7 and found that both CESA4 and CESA8 could be coprecipitated. This suggests that all three CESAs are still able to associate as part of a complex, even in the absence of normal CESA7 S-acylation (Fig. 4A). S-Acylation of CESA4 and CESA8 remained intact in the CESA7 $VR2/CT_{C/S}$ mutant (Fig. 4B) which indicated that an S-acylation defect in one subunit does not affect the S-acylation states of the others. Acylation of membrane proteins often causes conformation changes that may be essential for targeting and/or interactions with other proteins (*4*); so, whereas CESA proteins still associate in CESA7 $VR2/CT_{C/S}$ mutants, potentially they may have altered confirmations that could affect the correct assembly of the CSC.

VR2 encompasses a region known as the class-specific region (CSR) (*8*). Modeling studies have suggested that the CSR loops away from the catalytic core, which makes it a candidate for subunit interactions (*14*). S-Acylation of VR2 cysteines would alter the conformational prediction for this region by placing the beginning of the CSR adjacent to the plasma membrane, which suggests further structural data for this region is required. The acyl groups are likely to be inserted into the plasma membrane close to the transmembrane region, in a region that is occupied by the bacterial cellulose synthase B (BcsB) in the BcsA/B crystal structure from *Rhodobacter* (*6*, *14*, *15*). One of the major differences between the way in which bacteria and plants make cellulose is the mobile nature of the plant CSC, which must be able to move through the plane of the plasma membrane as it makes cellulose. We speculate that this process may be facilitated by the S-acylation of plant CESA proteins.

Up to six cysteines are likely to be S-acylated in each of CESA7, CESA4, and CESA8. Thus, a functional CSC, with at least 18 CESA proteins, would contain more than 100 S-acyl groups. The hydrophobic nature of S-acylation can make some proteins resistant to solubilization even by ionic detergents such as SDS (*16*). S-Acyl groups can be removed by treatment with dithiothreitol (DTT) (*17*), which also reduces aggregation of CESA proteins during SDS-polyacrylamide gel electrophoresis (*18*). Using mass spectrometry, we have only been able to identify VR2 peptides from DTT-treated samples. The very high level of S-acylation and hydrophobicity of the CSC and/or the requirement for a specialized membrane environment is likely to make the CSC susceptible to aggregation and

may explain why it has not been possible to purify an intact, active CSC. Although S-acylation is known to affect partitioning of proteins into membrane microdomains, it has also been suggested that the crowding of S-acyl groups within a membrane may actually facilitate the formation of lipid microdomains (*19*). The high level of S-acylation found in the CSC would make it a very good candidate for a protein complex capable of generating lipid microdomains that may facilitate the colocalization of proteins with similar properties. We note that a recent proteomic study of S-acylated proteins also identified the endoglucanase KORRIGAN, a known CESA-binding protein (*5*).

REFERENCES AND NOTES

1. A. N. Fernandes *et al.*, *Proc. Natl. Acad. Sci. U.S.A.* **108**, E1195–E1203 (2011).
2. A. R. Paredez, C. R. Somerville, D. W. Ehrhardt, *Science* **312**, 1491–1495 (2006).
3. F. Diotallevi, B. Mulder, *Biophys. J.* **92**, 2666–2673 (2007).
4. P. A. Hemsley, *New Phytol.* **205**, 476–489 (2015).
5. P. A. Hemsley, T. Weimar, K. S. Lilley, P. Dupree, C. S. Grierson, *New Phytol.* **197**, 805–814 (2013).
6. M. Kumar, S. Turner, *Phytochemistry* **112**, 91–99 (2015).
7. M. T. Forrester *et al.*, *J. Lipid Res.* **52**, 393–398 (2011).
8. C. E. Vergara, N. C. Carpita, *Plant Mol. Biol.* **47**, 145–160 (2001).
9. R. Wightman, S. R. Turner, *Plant J.* **54**, 794–805 (2008).
10. Y. Watanabe *et al.*, *Science* **350**, 198–203 (2015).
11. E. F. Crowell *et al.*, *Plant Cell* **21**, 1141–1154 (2009).
12. R. Gutierrez, J. J. Lindeboom, A. R. Paredez, A. M. C. Emons, D. W. Ehrhardt, *Nat. Cell Biol.* **11**, 797–806 (2009).
13. N. G. Taylor, R. M. Howells, A. K. Huttly, K. Vickers, S. R. Turner, *Proc. Natl. Acad. Sci. U.S.A.* **100**, 1450–1455 (2003).
14. L. Sethaphong *et al.*, *Proc. Natl. Acad. Sci. U.S.A.* **110**, 7512–7517 (2013).
15. J. L. W. Morgan, J. Strumillo, J. Zimmer, *Nature* **493**, 181–186 (2013).
16. S. Monier, D. J. Dietzen, W. R. Hastings, D. M. Lublin, T. V. Kurzchalia, *FEBS Lett.* **388**, 143–149 (1996).
17. O. Batistic, N. Sorek, S. Schültke, S. Yalovsky, J. Kudla, *Plant Cell* **20**, 1346–1362 (2008).
18. I. I. Atanassov II, J. K. Pittman, S. R. Turner, *J. Biol. Chem.* **284**, 3833–3841 (2009).
19. S. S. A. Konrad, T. Ott, *Trends Plant Sci.* **20**, 351–361 (2015).

ACKNOWLEDGMENTS

We thank J. Ogas for a critical reading of the manuscript. H. Höfte kindly provided antibodies against CESA1 and CESA6. The work was funded by Biotechnology and Biological Sciences Research Council grants BB/H012923/1 and BB/M004031/1 to S.T. and BB/M024911/1 to P.A.H. The Microscopy Facility at the Sainsbury Laboratory is supported by the Gatsby Charitable Foundation. The authors declare no conflict of interest. M.K., R.W., I.A., A.G., C.H.H., and P.A.H. carried out the experimental work. M.K., P.A.H., and S.T. wrote the manuscript and conceived the experiments. Supplementary materials contain additional data. S.T. would like to dedicate this manuscript to physicist Roy Turner (1931–2016) for his support, encouragement, and help with advanced mathematics.

SUPPLEMENTARY MATERIALS

www.sciencemag.org/content/353/6295/166/suppl/DC1
Materials and Methods
Figs. S1 to S8
Tables S1 and S2
Movies S1 to S3
References (*20*–*25*)

5 February 2016; accepted 6 June 2016
10.1126/science.aaf4009

CLIMATE CHANGE

Climate-driven regime shift of a temperate marine ecosystem

Thomas Wernberg,[1]*† Scott Bennett,[1,2,3]† Russell C. Babcock,[1,4] Thibaut de Bettignies,[1,5] Katherine Cure,[1,6] Martial Depczynski,[6] Francois Dufois,[7] Jane Fromont,[8] Christopher J. Fulton,[9] Renae K. Hovey,[1] Euan S. Harvey,[2] Thomas H. Holmes,[1,10] Gary A. Kendrick,[1] Ben Radford,[6,11] Julia Santana-Garcon,[1,2,3] Benjamin J. Saunders,[2] Dan A. Smale,[1,11] Mads S. Thomsen,[1,12] Chenae A. Tuckett,[1] Fernando Tuya,[13] Mathew A. Vanderklift,[7] Shaun Wilson[1,10]

Ecosystem reconfigurations arising from climate-driven changes in species distributions are expected to have profound ecological, social, and economic implications. Here we reveal a rapid climate-driven regime shift of Australian temperate reef communities, which lost their defining kelp forests and became dominated by persistent seaweed turfs. After decades of ocean warming, extreme marine heat waves forced a 100-kilometer range contraction of extensive kelp forests and saw temperate species replaced by seaweeds, invertebrates, corals, and fishes characteristic of subtropical and tropical waters. This community-wide tropicalization fundamentally altered key ecological processes, suppressing the recovery of kelp forests.

Broad-scale losses of species that provide the foundations for habitats cause dramatic shifts in ecosystem structure, because they support core ecological processes (*1*–*3*). Such habitat loss can lead to a regime shift, in which reinforcing feedback mechanisms intensify to provide resilience to an alternate community configuration, often with profound ecological, social, and economic consequences (*4*–*6*). Benthic marine regime shifts have been associated with the erosion of ecological resilience through overfishing or eutrophication, altering the balance between consumers and resources, rendering ecosystems vulnerable to major disturbances (*1*, *2*, *6*, *7*). Now, climate change is also contributing to the erosion of resilience (*8*, *9*), because increasing temperatures are modifying key physiological, demographic, and community-scale processes (*8*, *10*), driving species redistribution at a global scale and rapidly breaking down long-standing biogeographic boundaries (*11*, *12*). These processes culminate in novel ecosystems where tropical and temperate species interact, with unknown implications (*13*). Here we document how a marine heat wave caused the loss of kelp forests across ~2300 km^2 of Australia's Great Southern Reef, forcing a regime shift to seaweed turfs. We describe a rapid 100-km range contraction of kelp forests and a community-wide shift toward warm-water species, with ecological processes suppressing kelp forest recovery.

To document ecosystem changes, we surveyed kelp forests, seaweeds, fish, mobile invertebrates, and corals at 65 reefs across a ~2000-km tropical-to-temperate transition zone in western Australia (*14*). Surveys were conducted between 2001 and 2015, covering the years before and after an extreme marine heat wave affected the region.

The Indian Ocean adjacent to western Australia is a "hot spot" where the rate of ocean warming is in the top 10% globally (*15*), and isotherms are shifting poleward at a rate of 20 to 50 km per decade (*16*). Until recently, kelp forests were dominant along >800 km of the west coast (*8*), covering 2266 km^2 of rocky reefs between 0 and 30 m depth south of 27.7°S (Fig. 1). Kelp forests along the midwest section of this coast (27.7° to 30.3°S) have experienced steadily increasing ocean temperatures since the 1970s, recently punctuated by three of the warmest summers in the past 215 years (Fig. 2) (*17*, *18*, *19*). In December 2010, immediately before an extreme marine heat wave, kelp forests covered over ~70% of shallow rocky reefs in the midwest (Fig. 2 and fig. S1), with no differences in kelp cover or biomass among reefs along the west coast (Fig. 1 and figs. S1 and S2) (*8*). During this time, seaweed and fish communities in the

[1]School of Plant Biology and Oceans Institute, The University of Western Australia, 39 Fairway, Crawley, Western Australia 6009, Australia. [2]Department of Environment and Agriculture, School of Science, Curtin University, Bentley, Western Australia 6102, Australia. [3]Department of Global Change Research, Institut Mediterrani d'Estudis Avançats (Universitat de les Illes Balears–Consejo Superior de Investigaciones Científicas), Esporles, Spain. [4]Commonwealth Scientific and Industrial Research Organisation (CSIRO) Oceans and Atmosphere, General Post Office Box 2583, Brisbane, Queensland 4001, Australia. [5]Service du Patrimoine Naturel, Muséum National d'Histoire Naturelle, 36 Rue Geoffroy Saint-Hilaire CP41, Paris 75005, France. [6]Australian Institute of Marine Science, 39 Fairway, Crawley, Western Australia 6009, Australia. [7]CSIRO Oceans and Atmosphere Flagship, Private Bag 5, Wembley, Western Australia 6913, Australia. [8]Western Australian Museum, Locked Bag 49, Welshpool DC, Western Australia 6986, Australia. [9]Research School of Biology, The Australian National University, Canberra, Australian Capital Territory 2601, Australia. [10]Marine Science Program, Science Division, Department of Parks and Wildlife, Kensington, Western Australia 6151, Australia. [11]School of Geography and Environmental Science, The University of Western Australia, 39 Fairway, Crawley, Western Australia 6009, Australia. [12]Marine Biological Association of the United Kingdom, The Laboratory, Citadel Hill, Plymouth PL1 2PB, UK. [13]Marine Ecology Group, School of Biological Sciences, The University of Canterbury, Private Bag 4800, Christchurch, New Zealand. [14]Instituto Universitario Ecoaqua, Universidad de Las Palmas de Gran Canaria, 35017 Canary Islands, Spain.
***Corresponding author. Email: thomas.wernberg@uwa.edu.au**
†These authors contributed equally to this work. The other authors are arranged alphabetically.

midwest were similar to those of the temperate southwest (~500 km farther south) and clearly distinct from those of tropical reefs in the (~500 km farther north) (Fig. 3, A and B, and fig. S3) (*17*).

By early 2013, only 2 years later, our extensive surveys found a 43% (963 km^2) loss of kelp forests on the west coast (Fig. 1). Previously dense kelp forests north of 29°S had disappeared (Fig. 2 and fig. S1) or been severely reduced (>90% loss, Fig. 1), representing a ~100-km range contraction and functional extinction from 370 km^2 of reef (a reduction in abundance severe enough to delete ecological function). Instead, we found a dramatic increase in the cover of turf-forming seaweeds (Fig. 2) and a community-wide shift from species characteristic of temperate waters to species and functional groups characteristic of subtropical and tropical waters [Figs. 3 and 4 and fig. S3, mean square contingency coefficient ($\varphi_{2,52}$) = −0.70, P < 0.001]. Compared to the composition of the heavily affected midwest reef communities in Kalbarri before the 2011 marine heat wave, differences in community structure (Bray-Curtis dissimilarity) from reefs in Perth in the temperate southwest increased by 91 and 28% for seaweeds and fishes, respectively, whereas differences from Ningaloo Reef in the tropical northwest decreased by 32 and 16%, respectively. This broad-scale community-wide reef transformation reflected consistent decreases in the abundance of taxa characteristic of temperate reefs, coinciding with increases in the abundance of species characteristic of subtropical and tropical reefs, for both seaweeds (Fig. 3C and table S2, $\varphi_{2,20}$ = −0.81, P < 0.001) and fishes (Fig. 3D and table S3, $\varphi_{2,20}$ = −0.64, P = 0.008). Similar changes were seen for sessile and mobile invertebrates in the southern part of the midwest region, where small hermatypic coral colonies increased almost sixfold in abundance and doubled in species richness (Fig. 4 and table S5), while the abundances of sea urchins and gastropods also increased and decreased in accordance with their thermal affinities (Fig. 4 and tables S4 and S5, $\varphi_{2,12}$ = −0.68, P < 0.045).

Even though the acute climate stressor has abated (Fig. 2 and fig. S1), as of late 2015, almost 5 years after the heat wave, we have observed no signs of kelp forest recovery on the heavily affected reefs north of 29°S. Instead, concurrent with an 80% reduction in standing seaweed biomass (fig. S2), we have recorded subtropical and tropical fish feeding rates on canopy seaweeds that are three times higher than on comparable coral reef systems. Similarly, we have found a 400% increase in the biomass of scraping and grazing fishes, a functional group characteristic of coral reefs, which now display grazing rates on seaweed turfs that are comparable to those observed on healthy coral reefs worldwide (table S6) (*10*). High herbivore pressure now suppresses the recovery of kelp forests by cropping turfs and kelp recruits (*10*).

We deduce that extreme temperatures beginning in 2011 exceeded a physiological tipping point for kelp forests north of 29°S, and now reinforcing feedback mechanisms have become established that support a new kelp-free state. Similar ecosystem changes have not been observed in the southwest, where heat wave temperatures remained within the thermal tolerance of kelps (*17*), and the greater distance to tropical bioregions limited the incursion of tropical species. Threshold temperatures for kelp forests appear close to 2.5°C above long-term summer maximum temperatures, consistent with other seaweeds in the region (*20*). However, the partial loss of kelp forests on reefs between 29° and 32°S suggests that there is variation in threshold temperatures within and between kelp populations.

The consistent responses of both cool- and warm-water species clearly illustrate the important role of temperature. However, the transition in community structure and subsequent persistence of the new regime would have been augmented

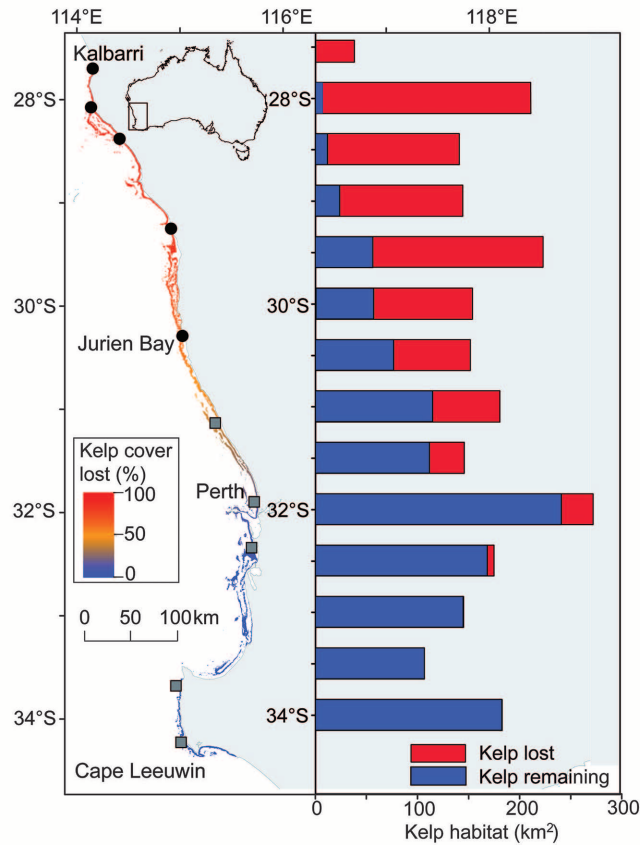

Fig. 1. Extent of kelp forests in western Australia before and after the 2011 marine heat wave. (**Left**) The extent of kelp forests from 0 to 30 m depth before 2011 is shown (map), with a color scale indicating the proportion lost by 2013. (**Right**) The area of kelp forests before 2011 in 0.5° bins (bars). Before 2011, kelp forests covered 2266 km^2 along the >800 km of coastline. However, by 2013, 43% of these kelp forests had disappeared (red bars). On the left side of the map, gray squares (southwest region) and black circles (midwest region) mark locations where reefs were surveyed by scuba divers to establish proportional kelp loss (table S1).

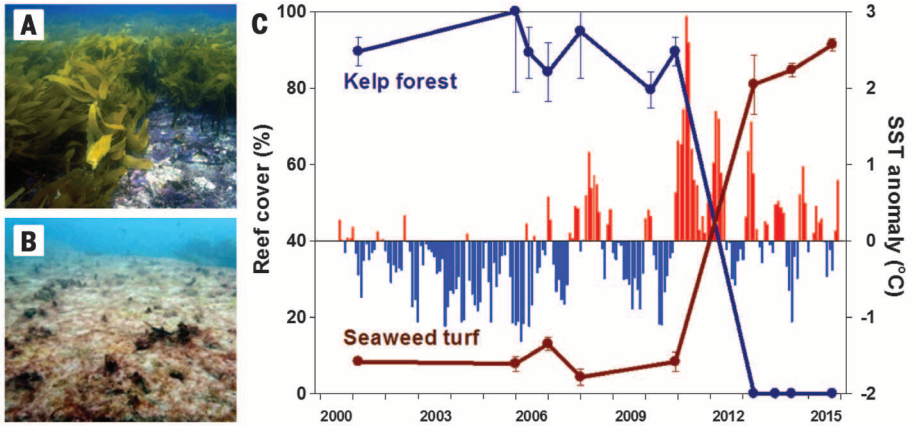

Fig. 2. Regime shift from kelp forests to seaweed turfs after the 2011 marine heat wave. Kelp forests were dense in Kalbarri until 2011 (**A**), when they disappeared from ~100 km of coastline (Fig. 1) and were replaced by seaweed turfs (**B**). (**C**) The habitat transition (lines) coincided with exceptionally warm summers in 2011, 2012, and 2013 (red bars), punctuating gradually increasing mean ocean temperatures over the past decades (*17*). Shown are mean (± SE, n = 3 reefs) kelp forest cover (dark blue circles and line) and seaweed turf cover (dark red circles and line), chronologically aligned with monthly sea surface temperature (SST) anomalies (blue and red bars) relative to monthly climatological means for 1981–2015 (table S1).

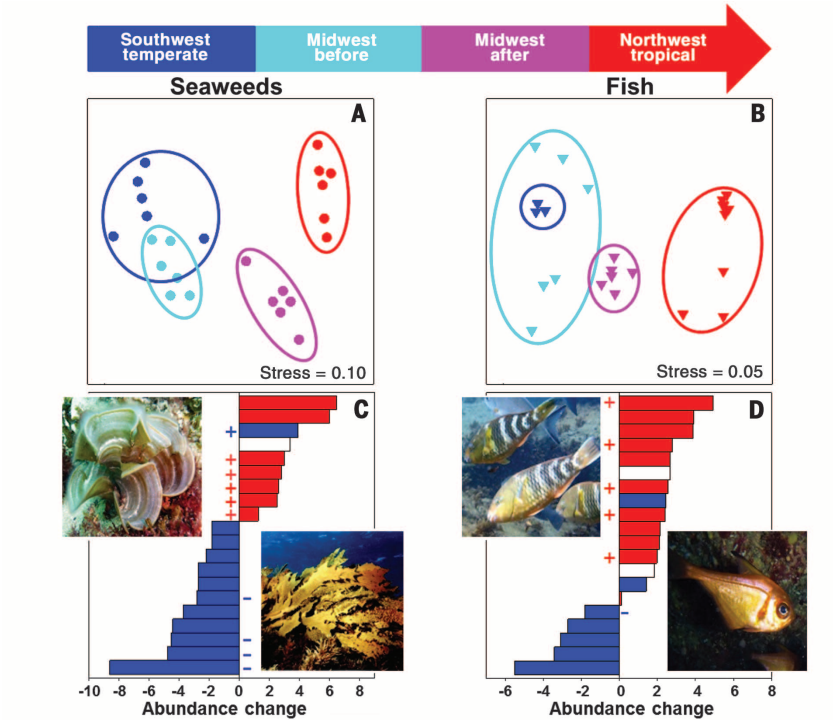

Fig. 3. Changes in seaweed and fish communities on affected reefs after the 2011 marine heat wave. Ordinations (nonmetric multidimensional scaling) of seaweed (**A**) and fish (**B**) communities show how community structure on reefs north of 29°S shifted from a close resemblance to temperate reefs farther south to a greater resemblance to tropical reefs to the north. Dark blue = Perth (2005–2007), light blue = Kalbarri before (2005–2007), pink = Kalbarri after (2013–2015), red = Ningaloo Reef (2010) (table S1). Each symbol represents an individual reef. Ordinations are based on Bray-Curtis dissimilarities calculated from ln(x + 1)–transformed data. (**C** and **D**) Change in ln(x + 1)–transformed abundance of seaweeds [(C) grams of fresh weight per 1.5 m^2] and fish [(D) individuals per 2500 m^2] in Kalbarri (2005–2007 versus 2013–2015) clearly show the decline in cool-water species (blue bars) and concurrent increase in warm-water species (red bars), with several species not previously recorded (+) or now absent from the samples (–). Each bar represents an average across six reefs for an individual species. White bars indicate taxa with ambiguous distributions. Species are listed in tables S2 and S3.

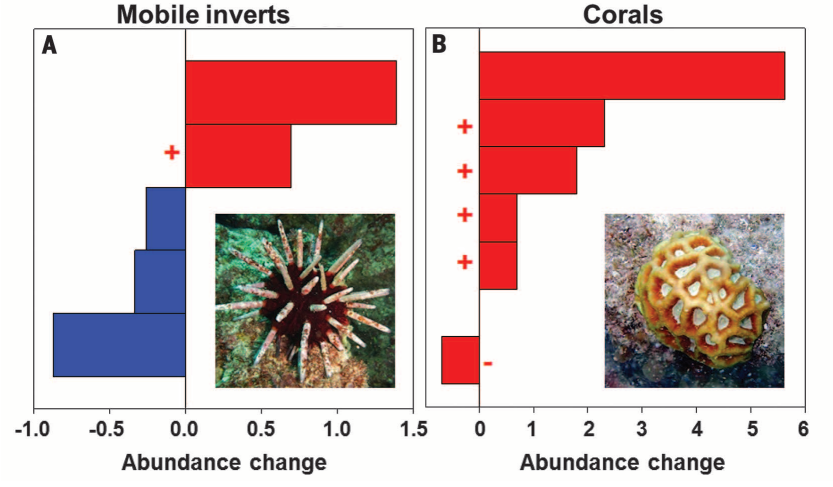

Fig. 4. Changes in benthic invertebrate abundances in the midwest after the 2011 marine heat wave. (**A** and **B**) Change in ln(x + 1)–transformed abundance of common mobile invertebrates (inverts) [(A) individuals per 30 m^2] and small (<6 cm) hermatypic corals [(B) colonies per 1000 m^2]. Colors and symbols are as in Fig. 3. Each bar represents an average across 6 and 23 reefs for an individual species of mobile invertebrates and corals, respectively. Mobile invertebrates were counted in Jurien Bay (2005, 2011 versus 2013 and 2014), and corals were counted between Cervantes and Dongara (30.6° to 29.3°S) (2005–2006 versus 2013) (table S1). Species are listed in tables S4 and S5.

by the low and high availability of temperate and tropical propagules and immigrants, respectively, as well as changes in competitive interactions after the loss of kelp canopies (*21*). The oceanography of the region is dominated by the poleward-flowing Leeuwin Current, which delivers warm nutrient-poor water and tropical species into the temperate region, while limiting the supply of propagules, including kelp zoospores from higher-latitude kelp forests (*22*, *23*). Indeed, healthy coral reefs already occur at the Houtman-Abrolhos Islands, 60 km offshore from Kalbarri, directly in the path of the Leeuwin Current. Until now, however, cooler coastal waters have enabled kelp forests to dominate nearshore reefs.

The Leeuwin Current is strongly influenced by the El Niño–Southern Oscillation (*24*). The strength of the Leeuwin Current and the flow of warm tropical water down the west coast of Australia increase during the La Niña phase of this cycle. These La Niña conditions drive warming anomalies such as the 2011 marine heat wave (*24*) and are predicted to double in frequency and intensity in the near future (*25*). Moreover, the southeast Indian Ocean has gradually warmed by at least 0.65°C over the past five decades and will continue to warm until the end of the century and beyond (*19*). Kelp forest recovery from disturbances can be slow in the nutrient-poor west coast waters, even in the cool southwest (*8*, *26*), providing time for populations of herbivorous fish to become established and seaweed turfs to proliferate. Consequently, the probability of prolonged cool conditions that could reset community structure and ecological processes to facilitate the recovery of kelp forests is becoming increasingly unlikely, while the risk of more heat waves that will exacerbate and expand the new tropicalized ecosystem state is increasing (*25*).

Short-term climate variability has previously precipitated large-scale destruction of kelp forests (*27*, *28*), which have mostly recovered as environmental conditions returned to normal. The future of kelp forest communities in western Australia is, however, grim. Warming, more frequent heat waves, and the intrusion of tropical species into temperate habitats are unequivocal (*13*, *19*, *25*). The current velocity of ocean warming is pushing kelp forests toward the southern edge of the Australian continent (*29*), where they are at risk of rapid local extinction over thousands of kilometers, due to the east-west orientation of the continent's poleward coastline and west-to-east flow of surface currents (*12*). This would devastate lucrative fishing and tourism industries worth more than $10 billion (Australian) per year (*30*) and have catastrophic consequences for the thousands of endemic species (*30*) supported by the kelp forests of Australia's Great Southern Reef.

REFERENCES AND NOTES

1. T. P. Hughes, *Science* **265**, 1547–1551 (1994).
2. R. S. Steneck *et al.*, *Environ. Conserv.* **29**, 436–459 (2002).
3. M. S. Thomsen *et al.*, *Integr. Comp. Biol.* **50**, 158–175 (2010).
4. M. Scheffer, S. Carpenter, J. A. Foley, C. Folke, B. Walker, *Nature* **413**, 591–596 (2001).
5. N. A. J. Graham *et al.*, *Front. Ecol. Environ* **11**, 541–548 (2013).
6. R. S. Steneck, A. Leland, D. C. McNaught, J. Vavrinec, *Bull. Mar. Sci.* **89**, 31–55 (2013).

7. S. D. Ling, C. R. Johnson, S. D. Frusher, K. R. Ridgway, *Proc. Natl. Acad. Sci. U.S.A.* **106**, 22341–22345 (2009).
8. T. Wernberg *et al.*, *Ecol. Lett.* **13**, 685–694 (2010).
9. N. A. J. Graham, S. Jennings, M. A. MacNeil, D. Mouillot, S. K. Wilson, *Nature* **518**, 94–97 (2015).
10. S. Bennett, T. Wernberg, E. S. Harvey, J. Santana-Garcon, B. J. Saunders, *Ecol. Lett.* **18**, 714–723 (2015).
11. E. S. Poloczanska *et al.*, *Nat. Clim. Change* **3**, 919–925 (2013).
12. T. Wernberg *et al.*, *Curr. Biol.* **21**, 1828–1832 (2011).
13. A. Vergés *et al.*, *Proc. Biol. Sci.* **281**, 20140846 (2014).
14. Materials and methods are available as supplementary materials on *Science* Online.
15. A. Hobday, G. Pecl, *Rev. Fish Biol. Fish.* **24**, 415–425 (2014).
16. M. T. Burrows *et al.*, *Science* **334**, 652–655 (2011).
17. T. Wernberg *et al.*, *Nat. Clim. Change* **3**, 78–82 (2013).
18. J. Zinke *et al.*, *Nat. Commun.* **5**, 3607 (2014).
19. J. Lough, A. Sen Gupta, A. J. Hobday, in *Report Card of Marine Climate Change for Australia: Detailed Scientific Assessment*, E. S. Poloczanska, A. J. Hobday, A. J. Richardson, Eds. (Hobart, Tasmania, 2012); www.oceanclimatechange.org.au.
20. S. Bennett, T. Wernberg, B. Arackal Joy, T. de Bettignies, A. H. Campbell, *Nat. Commun.* **6**, 10280 (2015).
21. D. P. Thomson, R. C. Babcock, M. A. Vanderklift, G. Symonds, J. R. Gunson, *Estuar. Coast. Shelf Sci.* **96**, 105–113 (2012).
22. M. Feng, D. Slawinski, L. E. Beckley, J. K. Keesing, *Mar. Freshw. Res.* **61**, 1259–1267 (2010).
23. M. A. Coleman *et al.*, *J. Ecol.* **99**, 1026–1032 (2011).
24. M. Feng, M. J. McPhaden, S.-P. Xie, J. Hafner, *Scientific Reports* **3**, 1277 (2013).
25. W. Cai *et al.*, *Nat. Clim. Change* **5**, 132–137 (2015).
26. B. D. Toohey, G. A. Kendrick, E. S. Harvey, *Oikos* **116**, 1618–1630 (2007).
27. P. K. Dayton, M. J. Tegner, *Science* **224**, 283–285 (1984).
28. E. A. Martinez, L. Cardenas, R. Pinto, *J. Phycol.* **39**, 504–508 (2003).
29. M. T. Burrows *et al.*, *Nature* **507**, 492–495 (2014).
30. S. Bennett *et al.*, *Mar. Freshw. Res.* **67**, 47–56 (2016).

ACKNOWLEDGMENTS

This work was funded by the Australian Research Council (T.W., G.A.K.), the Hermon Slade Foundation (T.W., S.B.), a U.K. Natural Environment Research Council Independent Research Fellowship (D.A.S.), the Australian Institute of Marine Science (T.W., M.D., B.R.), the Australian National University (C.J.F.), the Western Australian Museum (J.F.), the Department of Parks and Wildlife (T.H.H., S.W.), CSIRO Oceans and Atmosphere (R.C.B., F.D., M.A.V.), Fisheries Research and Development Corporation project no. 2008/013 (R.K.H., G.A.K.), The Marsden Fund of The Royal Society of New Zealand (M.S.T.), and the WA Strategic Research Fund for the Marine Environment (R.B., M.A.V., J.F.). T.W. and S.B. conceptualized and wrote the manuscript; T.W., S.B., R.B., T.dB., K.C., M.D., F.D., J.F., C.J.F., J.S.-G., R.K.H., E.S.H., T.H.H., G.K., B.R., B.J.S., D.K.S., M.T., C.T., F.T., M.A.V., and S.W. provided data; and T.W., S.B., R.K.H., J.S.-G., and D.A.S. performed analyses and modeling. All authors discussed the results and commented on the manuscript. The data are provided in the supplementary materials. Additional information can be obtained from T.W. All authors declare no conflicting interests.

SUPPLEMENTARY MATERIALS

www.sciencemag.org/content/353/6295/169/suppl/DC1
Materials and Methods
Figs. S1 to S3
Tables S1 to S6
References (*31*–*70*)

18 January 2016; accepted 31 May 2016
10.1126/science.aad8745

STRUCTURAL BIOLOGY

Structural basis for membrane anchoring of HIV-1 envelope spike

Jyoti Dev,[1,2]* Donghyun Park,[3]* Qingshan Fu,[1] Jia Chen,[3,4] Heather Jiwon Ha,[3,4] Fadi Ghantous,[5] Tobias Herrmann,[2] Weiting Chang,[3] Zhijun Liu,[6] Gary Frey,[3,4] Michael S. Seaman,[5] Bing Chen,[3,4]† James J. Chou[1,6]

HIV-1 envelope spike (Env) is a type I membrane protein that mediates viral entry. We used nuclear magnetic resonance to determine an atomic structure of the transmembrane (TM) domain of HIV-1 Env reconstituted in bicelles that mimic a lipid bilayer. The TM forms a well-ordered trimer that protects a conserved membrane-embedded arginine. An amino-terminal coiled-coil and a carboxyl-terminal hydrophilic core stabilize the trimer. Individual mutations of conserved residues did not disrupt the TM trimer and minimally affected membrane fusion and infectivity. Major changes in the hydrophilic core, however, altered the antibody sensitivity of Env. These results show how a TM domain anchors, stabilizes, and modulates a viral envelope spike and suggest that its influence on Env conformation is an important consideration for HIV-1 immunogen design.

HIV-1 envelope spike [Env; trimeric $(gp160)_3$, cleaved to $(gp120/gp41)_3$] fuses viral and host cell membranes to initiate infection (*1*). Binding of gp120 to receptor (CD4) and co-receptor (e.g., CCR5 or CXCR4) trigger large conformational changes, leading to a cascade of refolding events in gp41 and ultimately to membrane fusion (*2*–*4*). Mature Env spikes, $(gp120/gp41)_3$, are the sole antigens on the virion surface; they often induce strong antibody responses in infected individuals (*5*, *6*). A vast amount of structural information is available for the ectodomain of Env, a primary target of the host immune system, but much less for its transmembrane domain (TMD), membrane-proximal external region (MPER), and cytoplasmic tail (CT), in the context of lipid bilayer. The cryo-EM (electron microscopy) structure of a detergent-solubilized clade B JR-FL EnvΔCT construct without the CT has been described recently (*7*), but its MPER and TMD are disordered, probably because detergent micelles failed to mimic a membrane environment.

The HIV-1 TMD is more conserved than a typical membrane anchor (fig. S1). Previous studies showed that mutations and truncations in the TMD indeed affect membrane fusion and viral infectivity (*8*–*11*). Presence of a GxxxG motif, often implicated in oligomeric assembly of TM helices (*12*), suggests clustering of TMDs in membrane (fig. S1). The presence of a conserved, positively charged residue (usually arginine) near the middle of the TMD suggests functions other than just spanning a bilayer. TM helices of many cell surface receptors are not merely inert anchors but play essential roles in receptor assembly and signal transmission. For example, we have shown that CT truncation affects the antigenic surface of the ectodomain of HIV-1 Env on the opposite side of the membrane (*13*). Thus, understanding the physical coupling (conformation and/or dynamics) between the CT and the ectodomain mediated by the TMD may guide design of immunogens that mimic native, functional Env and induce broadly neutralizing antibodies (bnAbs).

To characterize the TMD structure by nuclear magnetic resonance (NMR), we used a fragment of gp41 (residues 677 to 716; HXB2 numbering, fig. S1), derived from a clade D HIV-1 isolate 92UG024.2 (*14*). This construct, $gp41^{HIV1D(677\text{-}716)}$, contains a short stretch of MPER (residues 677 to 683); the TM segment (residues 684 to 705), defined by hydrophobicity; and a fragment previously assigned to the CT domain [residues 706 to 716, containing a tyrosine-based sorting motif (*15*, *16*)]. The $gp41^{HIV1D(677\text{-}716)}$ protein was purified and reconstituted into bicelles (fig. S2, A and B) (*17*–*19*) with an expected lipid-bilayer diameter of ~44 Å (fig. S2C) (*20*, *21*), thereby incorporating the refolded $gp41^{HIV1D(677\text{-}716)}$ into a membrane-like environment. The bicelle-reconstituted $gp41^{HIV1D(677\text{-}716)}$ migrated on SDS–polyacrylamide gel electrophoresis (SDS-PAGE) with a size close to that of a trimer (theoretical molecular mass 14.1 kDa) (fig. S2D), suggesting that the protein was trimeric and resistant to SDS denaturation. The reconstituted $gp41^{HIV1D(677\text{-}716)}$ protein in bicelles generated an NMR spectrum with excellent chemical-shift dispersion (fig. S3A). The equivalent protein constructs from isolates 92BR025.9 (clade C) and 92RU131.16 (clade G) gave similar NMR spectra (fig. S3, B and C), suggesting that the TMDs of most HIV-1 Envs have similar structures when reconstituted in bicelles. We completed the NMR structure of $gp41^{HIV1D(677\text{-}716)}$ using a previously described protocol (figs. S4 and S5) (*22*, *23*). The final ensemble of structures converged to a root mean

[1]Department of Biological Chemistry and Molecular Pharmacology, Harvard Medical School, 250 Longwood Avenue, Boston, MA 02115, USA. [2]Virology Program, Harvard Medical School, 260 Longwood Avenue, Boston, MA 02115, USA. [3]Division of Molecular Medicine, Boston Children's Hospital, 3 Blackfan Street, Boston, MA 02115, USA. [4]Department of Pediatrics, Harvard Medical School, 300 Longwood Avenue, Boston, MA 02115, USA. [5]Center for Virology and Vaccine Research, Beth Israel Deaconess Medical Center, 330 Brookline Avenue, Boston, MA 02215, USA. [6]State Key Laboratory of Molecular Biology, National Center for Protein Science Shanghai, Shanghai Institute of Biochemistry and Cell Biology, Chinese Academy of Sciences, Shanghai 200031, China.
*These authors contributed equally to this work. †Corresponding author. Email: bchen@crystal.harvard.edu

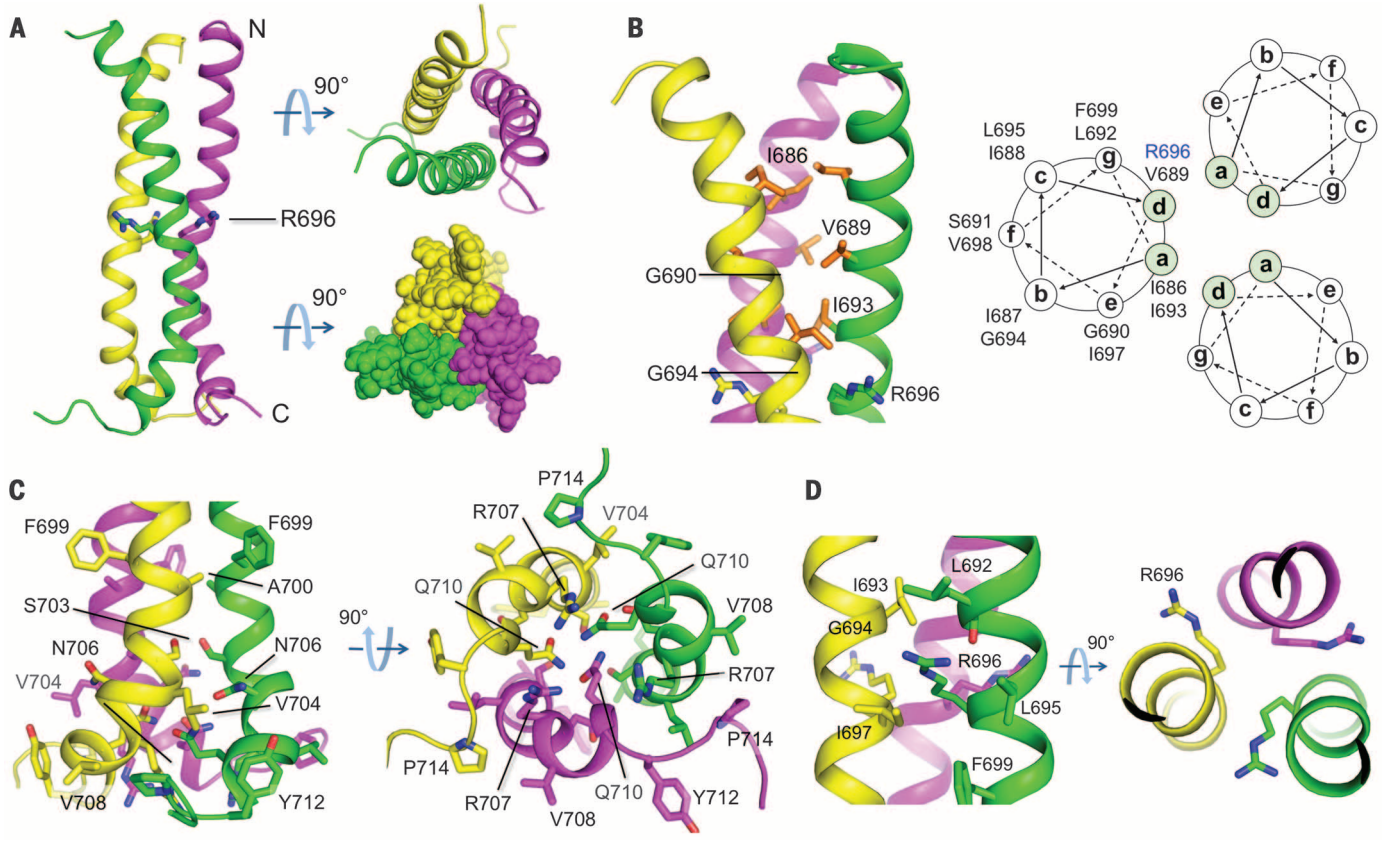

Fig. 1. NMR structure of the gp41$^{HIV1D(677-716)}$ trimer in bicelles. (**A**) Ribbon representation of the lowest-energy structure from the calculated ensemble. The sphere representation of the top view (lower right) shows that the trimer has no ion-permeable holes. (**B**) The N-terminal half of the structure with hydrophobic residues (orange) arranged in the coiled-coil pattern (right panel). (**C**) The C-terminal half of the structure showing an array of polar residues that form the C-terminal hydrophilic core. The network of polar contacts is hypothesized to stabilize the trimer. (**D**) Enlarged middle region of the structure showing the intramembrane R696 and its surrounding hydrophobic residues, as well as the backbone oxygen of L692. Single-letter abbreviations for the amino acid residues are as follows: A, Ala; C, Cys; D, Asp; E, Glu; F, Phe; G, Gly; H, His; I, Ile; K, Lys; L, Leu; M, Met; N, Asn; P, Pro; Q, Gln; R, Arg; S, Ser; T, Thr; V, Val; W, Trp; and Y, Tyr.

square deviation of 0.95 and 1.44 Å for backbone and all heavy atoms, respectively (fig. S6 and table S1).

gp41$^{HIV1D(677-716)}$ is a tightly assembled trimer ~54 Å long, with the conserved arginine (R696) near its midpoint (Fig. 1A). It shows a packing arrangement not seen in any other known TM helix dimers or trimers: Its N- and C-terminal halves have different modes of assembly, with an intervening kink. The N-terminal region is a conventional three-chain coiled-coil formed by residues 686 to 696 (Fig. 1B), including the GxxxG motif. The C-terminal half does not show classic "knobs-into-holes" interactions, but instead is held together by a network of polar contacts, mainly involving R707 and Q710, at the trimer interface of the kinked helical segments (residues 704 to 712) (Fig. 1C). We call this interface the "hydrophilic core."

R696, near the middle of each TM helix (Fig. 1D), produces three unbalanced charges at the center of the membrane. This residue occupies a "d" position in the heptad sequence (Fig. 1B). Its C^{β} points toward the threefold axis of the trimer, while the rest of the side chain bends away from the axis, placing the guanidinium group in a peripheral hydrophobic pocket formed by L692, L695, and I697 (Fig. 1D). The backbone carbonyl of L692 may form a hydrogen bond with one of the guanidinium NH_2 group of R696. H^{ε} of R696 showed a water nuclear Overhauser effect (NOE) in a ^{15}N-edited NOE spectrum (fig. S4), indicating the presence of an adjacent structured water. Thus, the guanidinium group, presumably charged at pH 6.7 under the NMR conditions, is partially neutralized by hydrogen bonding with the electronegative backbone oxygen of L692 and the water molecule. The polarizability of the hydrophobic pocket that surrounds the guanidinium may also lower its pK_a (acid dissociation constant) from its value in aqueous solution. Although well accommodated in the TMD trimer, the intramembrane R696 may modulate the stability of the helical trimer if the helices dissociate at any stage in assembly or fusion. The ^{1}H-^{15}N correlation spectrum of the gp41$^{HIV1D(677-716)}$ trimer showed inhomogeneous peak linewidth, with the N-terminal half near R696 having the most severe peak broadening, consistent with conformational fluctuation (fig. S7).

To confirm membrane partition of the TMD trimer, we used a paramagnetic probe, Gd(DOTA) (*24*), to measure solvent exposure of the four arginine residues in the gp41$^{HIV1D(677-716)}$ trimer. These arginines are distributed at different positions along the TM helices and thus serve as four depth markers. We measured intensity decrease of the arginine Hε-Nε correlation peaks at increasing concentrations of Gd(DOTA). The most solvent-exposed R707 showed the highest sensitivity to Gd(DOTA), whereas the most buried R696 was the least sensitive (Fig. 2A). R683 and R709 are near opposite lipid headgroup regions in the structure. R709 showed a greater resonance broadening than did R683, indicating that the latter is more deeply buried. We placed the gp41$^{HIV1D(677-716)}$ trimer in the lipid bilayer so that the four arginine positions were consistent with their respective sensitivity to Gd(DOTA) (Fig. 2B). This placement, which is consistent with the surface distribution of hydrophobic, polar, and charged residues (Fig. 2C), places R696 in a fully hydrophobic environment, slightly closer to the cytoplasmic side of the membrane. The MPER segment is in the headgroup region of the outer leaflet. The C-terminal segment, previously assigned to the CT, is at the headgroup-water interface of the inner leaflet.

To assess the contribution of specific residues to TMD stability, we generated 12 gp41$^{HIV1D(677-716)}$ mutants with single or double mutations, mainly

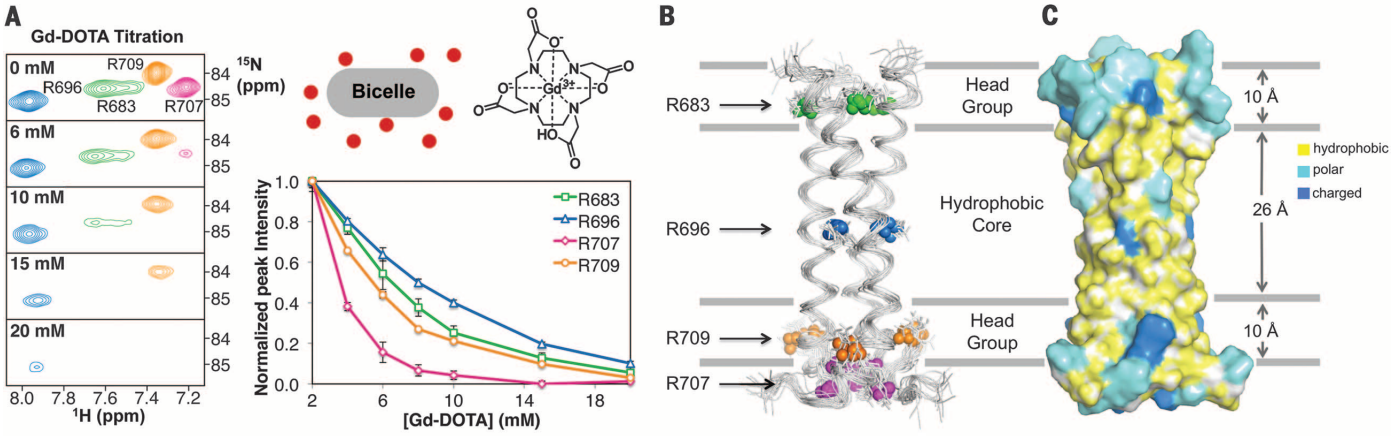

Fig. 2. Partition of the gp41$^{HIV1D(677-716)}$ trimer in lipid bilayer. (**A**) Measurement of membrane immersion depth of the four arginines using the water-soluble and membrane-inaccessible paramagnetic probe Gd-DOTA. The ^{1}H-^{15}N correlation peaks of the arginine Hε-Nε recorded in q = 0.5 bicelles (left) showed reduced peak intensity with increasing Gd-DOTA concentration (right) due to paramagnetic relaxation enhancement (PRE). R683 is shown in green, R696 in blue, R707 in magenta, and R709 in orange. Error bars represent spectra noise level normalized against maximum reference peak intensity. (**B**) Placement of the trimer structure in the presumed DMPC lipid bilayer, which is slightly thinner than the characterized thickness of DOPC bilayer (*35*), such that the positions of the four arginines are in accordance with the PRE results in (A). The positions of the arginine side chains are indicated by the Hε (spheres) in the ensemble of 15 low-energy structures. The color scheme is the same as in (A). (**C**) Surface representation of the lowest-energy structure positioned in DMPC bilayer as in (B) for showing the surface distribution of hydrophobic, polar, and charged amino acids. The hydrophobic residues (yellow) include A, I, L, F, V, P, and G; the polar residues (cyan) include Q, N, H, S, T, Y, C, M, and W; the charged residues (blue) include K, R, D, and E.

in the trimer interface. To introduce large-scale changes in the hydrophilic core, we also created mutants Δ(705–716) and G690L/Δ(705–716) with residues 705 to 716 deleted, and mutants 704–713 and G690L/704–713 with residues 704 to 713 mutated (Fig. 3 and table S2). We analyzed these mutants by SDS-PAGE after reconstitution in bicelles (fig. S8). Most simple mutations, including I686A, I693A, and R696N, did not disrupt the trimer completely, but only shifted the band to molecular mass positions lower than that of the wild type, indicating only partial trimer destabilization (fig. S8). We observed a similar pattern for mutants 704–713, G690L/704–713, and Δ705–716. The only mutant that migrated as a monomer was G690L/Δ705–716, with the GxxxG motif mutated and the entire hydrophilic-core region truncated (fig. S8). Thus, both the coiled-coil and the hydrophilic core contribute to the extraordinary stability of the TMD, and either one of them is sufficient to prevent the trimer from complete dissociation in bicelles.

To elucidate functional roles of the structural elements in the TMD, we mutated each of them in the intact Env spike and analyzed the effect on Env biogenesis, membrane fusion, and viral infectivity. We generated 27 Env mutants, using the sequence of a clade A isolate 92UG037.8, with single, double, or triple mutations in the coiled-coil region, R696 and its protecting residues, the kink, the hydrophilic core, or combinations of these elements (table S2). We also produced mutants 704–713 and G690L/704–713. When transiently transfected in 293T cells, all mutants expressed comparable levels of Env, with similar extents of cleavage between gp120 and gp41, as well as similar cell-surface levels (figs. S9 and S10). At a high Env expression level, at which cell-cell fusion was resistant to most neutralizing antibodies, the fusion activity of the TMD mutants was indistinguishable (93 to 109%) from that of the wild type (fig. S11). When the expression level was reduced to mimic the low surface density on HIV-1 virions (*25*), several TMD mutants, including R696A, had significantly lower cell-cell fusion activity than did the wild type (table S2 and fig. S12). Likewise, when these mutations were introduced into pseudoviruses, there were no major differences in Env incorporation and processing, but limited changes in infectivity for most of them (table S2 and figs. S13 and S14). R696A had almost full wild-type infectivity, whereas 704–713 and G690L/704–713 had substantially less—just the opposite of their effects on cell-cell fusion (table S2 and fig. S14).

To determine whether mutations in the TMD can influence the antigenic structure of the Env ectodomain and whether they might affect its antibody sensitivity, we used the cell-cell fusion assay to test inhibition of each Env mutant by a trimer-specific bnAb PG16 and by a nonneutralizing V3 antibody 3791 (table S3). Most mutants were essentially identical to the wild type in their sensitivity to either antibody; mutants I686A, Y712A, P714N, G690L/Y712A, G690L/P714N, G690L/P714K, and G690L/P714H exhibited detectable differences (fig. S15). We observed the most pronounced differences for mutants 704–713 and G690L/704–713, for which PG16 and 3791 switched phenotypes—the former became inactive and the latter inhibitory (fig. S15). All mutations that affect antibody inhibition are located in either the coiled-coil or the hydrophilic core. We infer that changes in TMD stability influence the antigenic structure of the ectodomain of the functional Env. When tested in a pseudovirus-based neutralization assay with bnAbs PG9 (trimer specific), 3BNC117 (CD4 binding site), 10-1074 (glycan- and V3-dependent), 10E8 (MPER), and 3791 (table S3), most mutants, except for 704–713 and G690/704–713, were unchanged in their sensitivity to PG9, 3BNC117, 10-1074 and 3791, but most became more sensitive to 10E8 (table S4). This result suggests that the changes produced by all the mutations tested, except for 704–713 and G690/704–713, are limited to local structure. In contrast, the mutants 704–713 and G690/704–713 became resistant to PG9 and sensitive to 3791—reflecting their properties in the cell-cell fusion assay. Mutant 704–713 was analyzed with additional antibodies. For cell-cell fusion, wild-type Env is sensitive to trimer-specific bnAbs PG9, PG16, and PGT145 and resistant to nonneutralizing antibodies b6 (CD4 binding site), 3791, and 17b (CD4-induced) (table S3, Fig. 3A, and fig. S16). The antibody inhibition pattern is reversed, however, for the fully functional mutant 704–713, indicating that the hydrophilic core of the TMD plays an important role in stabilizing and modulating the antigenic structure of the Env spike. Similar phenotypes were also observed with a 704–713 mutant derived from a clade C strain C97ZA012 (fig. S17). The pseudovirus neutralization assay gave similar, but less pronounced, results for the mutant 704–713 (Fig. 3B and table S4).

The most important finding from this study relevant to vaccine development is how the TMD modulates the antigenic surfaces of the Env spike. We reported previously that truncation of the CT domain of HIV-1 Env reshapes the antigenic surfaces of its ectodomain (*13*). We now show that mutations destabilizing the hydrophilic core of the TMD trimer resemble the CT deletion in altering the sensitivity of the functional Env to both nonneutralizing and trimer-specific neutralizing antibodies. In particular, the trimer-specific bnAbs, which neutralize by stabilizing the native

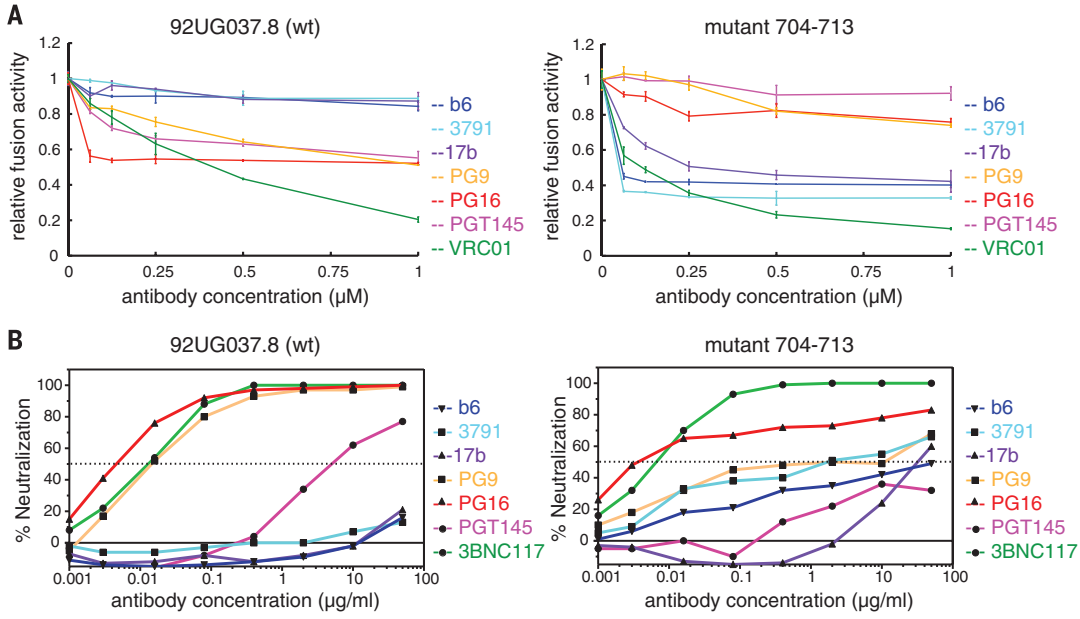

Fig. 3. Effect of mutations in the TMD of HIV-1 Env on its antibody sensitivity. (**A**) Antibody inhibition of cell-cell fusion mediated by the wild-type 92UG037.8 Env (left) and the TMD mutant 704–713 [right; residues 704 to 713 (VINRVRQGYS) were mutated to SSAASAAGSA] was analyzed with both nonneutralizing antibodies—including b6 (CD4 binding site; blue), 3791 (V3; cyan), and 17b (CD4-induced; purple)—and trimer-specific bnAbs, including PG9 (orange), PG16 (red), and PGT145 (magenta). The CD4 binding site bnAb VRC01 (green) was a control antibody. The experiment was carried out in triplicate and repeated at least twice with similar results. Error bars indicate the SD calculated by the Excel STDEV function. (**B**) Antibody neutralization of pseudoviruses containing either the 92UG037.8 Env (left) or the TMD mutant 704–713 (right) was determined with antibodies b6, 3791, 17b, PG9, PG16, and PGT145, shown in the same color scheme as in (A). The CD4 binding site bnAb 3BNC117 was a control antibody (green). The experiment was performed in duplicate.

conformation of Env (*26*, *27*), do not recognize the Env spike when its TMD has been destabilized. We suggest that the TMD mediates conformational coupling between the ectodomain and the CT and that the trimeric structure seen by NMR represents the conformation of the TMD adopted by a native Env spike in a membrane.

The placement of gp41$^{HIV1D(677-716)}$ in a lipid bilayer reveals clear boundaries of the TM segment and settles a contentious issue (*10*, *28*). Part of the 10E8 epitope (residues 677 to 683) is embedded in the headgroup layer of the outer leaflet, consistent with lack of accessibility of this epitope on the native Env (*13*, *29*). The hydrophilic core, which was thought to be part of the CT, is similarly protected by the headgroup layer of the inner leaflet. This hydrophilic region contains a tyrosine-based sorting signal (^{712}YSPL^{715}), which may participate in Env internalization by endocytosis (*15*, *16*, *30*). Our structure indicates that Y712 and P714 in this motif on one TM protomer interact with L704 and V708 of the adjacent protomer, respectively, thereby also contributing to trimer stability.

The TMD is required not only for membrane anchoring and fusion, but also for stability of the entire Env spike. This observation can explain why most soluble Env preparations with the TMD deleted, except for those of a few selected strains (*31*, *32*), are unstable and conformationally heterogeneous, unless they have specific, stabilizing modifications (*26*, *33*, *34*). To design immunogens that mimic optimally native viral spikes, one must not ignore structural constraints imposed by the TMD on the ectodomain. The high-resolution structure of the HIV-1 Env TMD trimer presented here can be a guide for engineering more effective immunogens.

REFERENCES AND NOTES

1. S. C. Harrison, *Nat. Struct. Mol. Biol.* **15**, 690–698 (2008).
2. D. C. Chan, D. Fass, J. M. Berger, P. S. Kim, *Cell* **89**, 263–273 (1997).
3. W. Weissenhorn, A. Dessen, S. C. Harrison, J. J. Skehel, D. C. Wiley, *Nature* **387**, 426–430 (1997).
4. M. Pancera *et al.*, *Nature* **514**, 455–461 (2014).
5. X. Wei *et al.*, *Nature* **422**, 307–312 (2003).
6. D. D. Richman, T. Wrin, S. J. Little, C. J. Petropoulos, *Proc. Natl. Acad. Sci. U.S.A.* **100**, 4144–4149 (2003).
7. J. H. Lee, G. Ozorowski, A. B. Ward, *Science* **351**, 1043–1048 (2016).
8. R. J. Owens, C. Burke, J. K. Rose, *J. Virol.* **68**, 570–574 (1994).
9. L. Shang, L. Yue, E. Hunter, *J. Virol.* **82**, 5417–5428 (2008).
10. L. Yue, L. Shang, E. Hunter, *J. Virol.* **83**, 11588–11598 (2009).
11. E. Helseth *et al.*, *J. Virol.* **64**, 6314–6318 (1990).
12. M. G. Teese, D. Langosch, *Biochemistry* **54**, 5125–5135 (2015).
13. J. Chen *et al.*, *Science* **349**, 191–195 (2015).
14. F. Gao *et al.*, *J. Virol.* **70**, 1651–1667 (1996).
15. J. F. Rowell, P. E. Stanhope, R. F. Siliciano, *J. Immunol.* **155**, 473–488 (1995).
16. M. Boge, S. Wyss, J. S. Bonifacino, M. Thali, *J. Biol. Chem.* **273**, 15773–15778 (1998).
17. M. E. Call *et al.*, *Cell* **127**, 355–368 (2006).
18. M. E. Call, K. W. Wucherpfennig, J. J. Chou, *Nat. Immunol.* **11**, 1023–1029 (2010).
19. To produce the protein, we expressed the His-tagged TrpLE-gp41$^{HIV1D(677-716)}$ fusion protein in *Escherichia coli* as inclusion bodies, purified the solubilized protein by Ni-affinity chromatography, removed the TrpLE tag with cyanogen bromide, and separated the product by reverse-phase high-performance liquid chromatography. Bicelles were made of 1,2-dimyristoyl-sn-glycero-3-phosphocholine (DMPC; lipid) and 1,2-dihexanoyl-sn-glycero-3-phosphocholine (DHPC; detergent) at a ratio (*q*) of 0.5. In this report, we use gp41$^{HIV1D(677-716)}$ and TMD interchangeably for convenience.
20. K. J. Glover *et al.*, *Biophys. J.* **81**, 2163–2171 (2001).
21. C. R. Sanders 2nd, J. P. Schwonek, *Biochemistry* **31**, 8898–8905 (1992).
22. B. OuYang *et al.*, *Nature* **498**, 521–525 (2013).
23. For structure determination, we proceeded with the clade D construct because its expression level was the highest. The approach involves determination of local structures of the monomers and assembly of the trimer with intermonomer distance restraints derived from NOEs between structurally equivalent but isotopically differently labeled subunits. We could identify eight intermonomer NOEs using the isotopically mixed labeled sample to calculate a unique assembly solution, which was further validated and refined with other conventional NOE data.
24. Gd(DOTA) is a water-soluble and membrane-inaccessible molecule, so that the paramagnetic relaxation enhancement (PRE) it generates decreases with distance from the bilayer surface.
25. P. Zhu *et al.*, *Nature* **441**, 847–852 (2006).
26. R. W. Sanders *et al.*, *PLOS Pathog.* **9**, e1003618 (2013).
27. J. P. Julien *et al.*, *Proc. Natl. Acad. Sci. U.S.A.* **110**, 4351–4356 (2013).
28. J. T. West, P. B. Johnston, S. R. Dubay, E. Hunter, *J. Virol.* **75**, 9601–9612 (2001).
29. J. Chen *et al.*, *J. Virol.* **88**, 1249–1258 (2014).
30. C. Berlioz-Torrent *et al.*, *J. Virol.* **73**, 1350–1361 (1999).
31. S. A. Jeffs *et al.*, *Vaccine* **22**, 1032–1046 (2004).
32. J. M. Kovacs *et al.*, *Proc. Natl. Acad. Sci. U.S.A.* **111**, 18542–18547 (2014).
33. J. Guenaga *et al.*, *J. Virol.* **90**, 2806–2817 (2015).
34. Y. Do Kwon *et al.*, *Nat. Struct. Mol. Biol.* **22**, 522–531 (2015).
35. M. C. Wiener, S. H. White, *Biophys. J.* **61**, 434–447 (1992).

ACKNOWLEDGMENTS

We thank S. Harrison and S. Rits-Volloch for generous advice and assistance; D. Barouch, B. Haynes, and A. Carfi for critical reading of the manuscript; and the NIH AIDS Reagent Program, Division of AIDS, National Institute of Allergy and Infectious Diseases, NIH, for reagents. The data presented in this manuscript are tabulated in the main paper and in the supplementary materials. The atomic structure coordinate and structural constraints are deposited in the Protein Data Bank under the accession number 5JYN. The chemical-shift values are deposited in the Biological Magnetic Resonance Data Bank under the accession number 30090. This work was supported by NIH grants AI084794 (to B.C. and Dan H. Barouch), GM083680 (to B.C.), AI106488 (to B.C.), HL103526 (to J.J.C.), and AI127193 (to B.C. and J.J.C.), Collaboration for AIDS Vaccine Discovery (CAVD) grant OPP1040741 (to Dan H. Barouch from the Bill and Melinda Gates Foundation), and the Center for HIV/AIDS Vaccine Immunology–Immunogen Design AI-100645 (to Barton F. Haynes). The NMR data were collected at the NMR facility of National Center for Protein Science Shanghai (supported by Chinese Academy of Sciences grant XDB08030301) and Massachusetts Institute of Technology–Harvard Center for Magnetic Resonance (supported by NIH grant P41 EB-002026).

SUPPLEMENTARY MATERIALS

www.sciencemag.org/content/353/6295/172/suppl/DC1
Materials and Methods
Figs. S1 to S20
Tables S1 to S4
References (*36*–*52*)

17 March 2016; accepted 13 June 2016
Published online 23 June 2016
10.1126/science.aaf7066

NEUROPHYSIOLOGY

Cilia-based flow network in the brain ventricles

Regina Faubel,[1] Christian Westendorf,[2] Eberhard Bodenschatz,[2] Gregor Eichele[1]*

Cerebrospinal fluid conveys many physiologically important signaling factors through the ventricular cavities of the brain. We investigated the transport of cerebrospinal fluid in the third ventricle of the mouse brain and discovered a highly organized pattern of cilia modules, which collectively give rise to a network of fluid flows that allows for precise transport within this ventricle. We also discovered a cilia-based switch that reliably and periodically alters the flow pattern so as to create a dynamic subdivision that may control substance distribution in the third ventricle. Complex flow patterns were also present in the third ventricles of rats and pigs. Our work suggests that ciliated epithelia can generate and maintain complex, spatiotemporally regulated flow networks.

The ventricular system of the brain consists of four interconnected, cerebrospinal fluid (CSF)–filled cavities, lined with ependyma whose apical surface bears bundles of motile cilia (*1*). CSF directional flow through the ventricles is driven by continuous CSF secretion into the ventricles and by orchestrated beating of the cilia. Motile cilia are eyelash-shaped cellular protrusions containing a microtubule-based axoneme that, by bending, confers motility. The direction of cilia beating depends on coupling of planar cell polarity signaling with hydrodynamic forces (*2*, *3*). CSF flow toward the exit of each ventricle affords an efficient washout of waste (*4*) such as neurotoxins and protein aggregates. Additionally, CSF flow delivers nutrients, signaling molecules, microRNAs, and exosomes (*5*–*12*). How these CSF components reach their target sites is an important question that prompted us to investigate the CSF flow dynamics along the ventricular walls. We conducted this analysis in mice in the ventral part of the third ventricle (v3V; Fig. 1A) because of its simple geometry and close juxtaposition to potential targets, including the physiologically important periventricular hypothalamic nuclei that control circadian rhythms, hormone release, thermoregulation, blood pressure, satiety, and feeding (Fig. 1B).

Organotypic v3V wall explant cultures were established, and cilia-generated flow was visualized by adding 1-μm fluorescent beads. Global flow was determined by particle tracking, and near-wall flows were extracted, yielding a highly complex flow map (Fig. 1C) that was consistent among animals (the number of animals used is given in table S1). Flow from the inflow duct fanned out after passing by the anterior commissure. A first flow was directed anteriorly toward the optic recess (Fig. 1C, flow 1). A second stream of the fan moved ventrally (flow 2). A third stream advanced posterodorsally (flow 3) and confronted, at Bregma level –0.9, an opposing flow (flow 4). When 70-kDa fluorescein isothiocyanate (FITC)–dextran was applied locally to the head of flow 6, it propagated as prescribed by streamlines of the flow map (Fig. 1D). Movie S1 shows the flow of FITC-dextran when applied to the heads of flows 1, 2, or 3. Injections to flows 1 and 2 resulted in an initially coherent flow that then fanned out, thereby dispersing the tracer over a sizable territory. Local application to the head of flow 3 revealed the ability of ciliated ependyma to produce a winding flow that replicates the shape of the streamlines seen in the flow map. Thus, the flow map may reflect the propagation of macromolecules in CSF.

To explore how the confrontation of flows 3 and 4 affects transport along the wall, beads were applied to v3V whole mounts (movie S2). Flow 4 carried beads anteriorly; near the site of confrontation with flow 3, beads moved into two mirror-symmetrical streams that intimately followed the ventricular wall and transported the beads down into the v3V. This flow dynamic created a separatrix that, together with flow 5, divided the v3V into two volumes. This flow-induced boundary hindered the passage of tracer. Flow 6 formed another intraventricular boundary that hindered flow 7 from drawing tracer away from flow 4. The flow pattern remained unchanged up to a distance of ~120 μm above the ependyma (fig. S1), and flows along the two walls were related by mirror symmetry (fig. S2). The velocity map showed that flow velocity at 21°C varied across the v3V wall within the range of 150 to 500 μm/s (fig. S3, A and B). Thus, it takes only a few seconds to move substances from the entrance of the v3V to its floor. These velocities are typical for cilia-driven flows (*13*).

We next analyzed cilia movement in the v3V and found that the flow map matched the cilia beating pattern. To show this, we captured movies

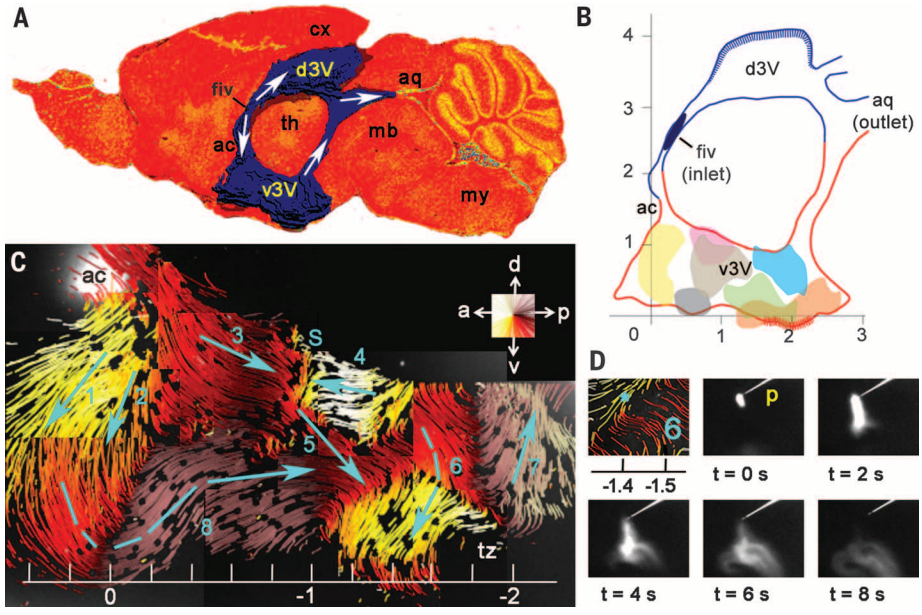

Fig. 1. Anatomy of the third ventricle in the mouse and flow map of the v3V. (**A**) Sagittal section through the third ventricle (blue), consisting of a dorsal (d3V) and a ventral (v3V) part connected by two ducts. As indicated by white arrows, CSF enters the v3V through the foramen interventriculare and exits through the aqueduct. (**B**) The position of periventricular hypothalamic nuclei [reconstructed from (*22*)]. Blue and red outlines differentiate the d3V and v3V, and hatching indicates the choroid plexus (blue) and median eminence (red). Medial preoptic nucleus, yellow; suprachiasmatic nucleus, gray; anterior hypothalamic area, brown; paraventricular nucleus, pink; ventromedial nucleus, green; arcuate nucleus, orange; dorsomedial nucleus, blue. (**C**) The flow map of the v3V, generated by particle tracking, shows that near-wall flow is subdivided into multiple flow domains. The associated eight major flow directions are indicated with turquoise arrows. (**D**) FITC-dextran, applied at the head of flow 6 (asterisk) from a femtopipette (p), follows the streamlines of the flow map shown in the first panel (*t*, time). Scales in (B) to (D) are Bregma levels in millimeters. a, anterior; ac, anterior commissure; aq, aqueduct; cx, cortex; d, dorsal; fiv, foramen interventriculare; mb, midbrain; my, myelencephalon; p, posterior; S, separatrix; th, thalamus; tz, tanycyte zone; v, ventral.

[1]Max Planck Institute for Biophysical Chemistry, Am Fassberg 11, 37077 Göttingen, Germany. [2]Max Planck Institute for Dynamics and Self-Organization, Am Fassberg 17, 37077 Göttingen, Germany.
*Corresponding author. Email: gregor.eichele@mpibpc.mpg.de

of rectangular fields of beating cilia bundles across the entire v3V in a mosaic-like fashion. Using custom-made software, the cilia movement was extracted from each movie; results were then stitched together to generate a v3V-wide map of the time-averaged cilia beating pattern. At the separatrix, the flow pattern (Fig. 2A) corresponded to the beating orientation of underlying cilia (Fig. 2B and movie S4). At the entrance of the v3V, the tripartite flow also corresponded to the cilia beating orientation (fig. S4 and movie S5). Thus, cilia form distinct modules in which they beat coherently and, in this way, locally control the flow of the overlying fluid. As these two examples illustrate, the arrangement of cilia modules accounts for the complex flow map with its distinct flow domains.

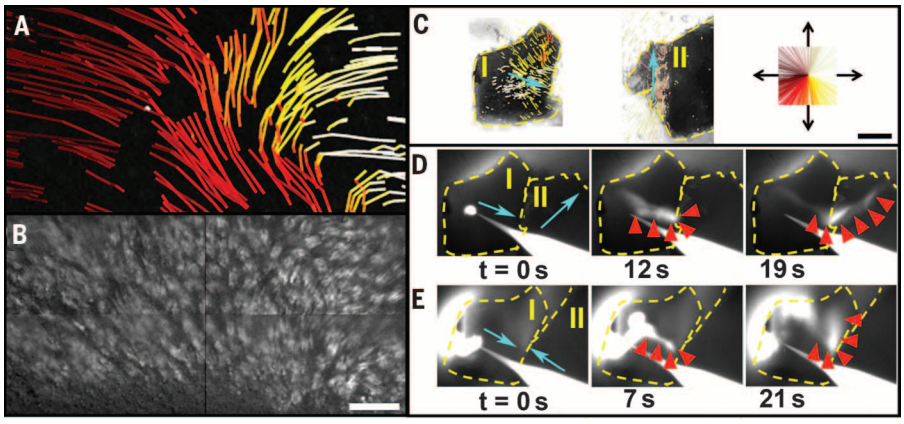

Fig. 2. Cilia beating and fluid flow directions match. (**A**) Flow map of and (**B**) time-averaged cilia beating orientation in the separatrix region [the flow map is color-coded as in Fig. 1C]. Computational analysis of cilia movement reveals obliquely opposing cilia orientation (movie S4) that corresponds to the pattern of the tracks shown in (A). (**C**) Flow map of two isolated fragments (I and II) of ependyma. (**D** and **E**) Time series show the flow of locally applied FITC-dextran across fragments I and II, which were recombined in vitro head to tail (D) or head to head (E). Red arrowheads flank the flow of FITC-dextran, turquoise arrows indicate cilia beating direction, and yellow dashes denote fragment borders. Scale bars, 30 μm [(A) and (B)] and 100 μm [(C) to (E)].

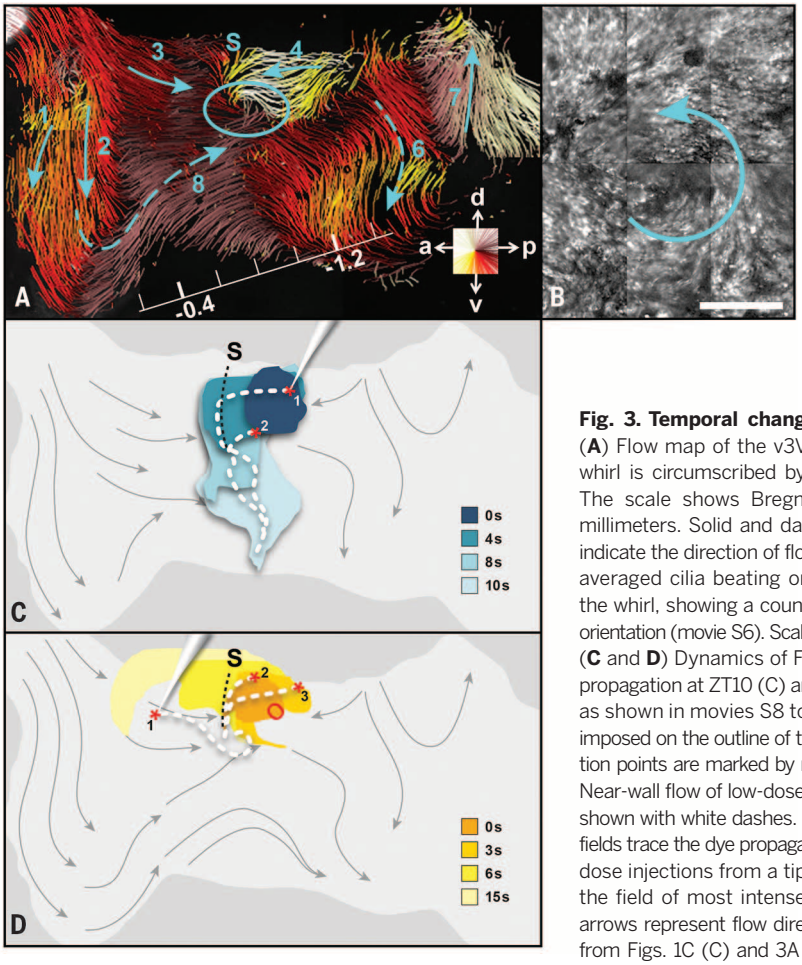

Fig. 3. Temporal changes in flow. (**A**) Flow map of the v3V at ZT23. A whirl is circumscribed by the ellipse. The scale shows Bregma levels in millimeters. Solid and dashed arrows indicate the direction of flow. (**B**) Time-averaged cilia beating orientation in the whirl, showing a counterclockwise orientation (movie S6). Scale bar, 50 μm. (**C** and **D**) Dynamics of FITC-dextran propagation at ZT10 (C) and ZT23 (D), as shown in movies S8 to S11, superimposed on the outline of the v3V. Injection points are marked by red asterisks. Near-wall flow of low-dose injections is shown with white dashes. Nested color fields trace the dye propagation for high-dose injections from a tip placed into the field of most intense color. Gray arrows represent flow directions taken from Figs. 1C (C) and 3A (D). A black dashed line represents the separatrix. The red circle in (D) represents a reference mark from movie S10.

When the v3V wall was cut into pieces, the flow pattern in each fragment was virtually identical to that observed at the intact wall before cutting (fig. S5). Thus, cilia modules may determine flow independently of context. In keeping with this idea, we isolated two fragments (I and II) from the v3V wall (Fig. 2C) and recombined them at different angles. When the two fragments were combined head to tail, focally applied FITC-dextran translocated from one piece to the next (Fig. 2D). When the same two fragments were oriented with cilia beating in opposite directions, tracer applied to fragment I progressed toward the interfragment boundary, at which the flow was diverted upward by the counterflow originating from fragment II (Fig. 2E). Thus, transport along bent flows and formation of boundaries can be achieved by appropriate arrangement of cilia modules. Furthermore, cilia beating direction in each module is necessary and sufficient to sculpt the associated flow domains.

There are major physiological differences between an animal at rest (Zeitgeber time, ZT0 to ZT12) and an awake animal (ZT12 to ZT24) (*14*). The flow maps at ZT10 (Fig. 1C) and ZT23 (Fig. 3A) showed differences. At ZT23, we observed a prominent whirl ventrally of the separatrix. This whirl resulted from a circular arrangement of cilia beating (Fig. 3B). Movie S6 shows how this counterclockwise whirl relates to the separatrix. Recording the same region at ZT10 revealed a substantially different pattern devoid of a whirl (movie S7). At ZT10, separatrix and flow 5 formed a vertical intraventricular boundary. When a low dose of FITC-dextran was injected into flow 4, the tracer flowed ventrally, along the boundary, to reach the floor (white dashes in Fig. 3C, movie S8). This boundary withstood a high FITC-dextran dose (blue fields in Fig. 3C, movie S9). When low or high doses of FITC-dextran were injected into flows 3 or 4 at ZT23, tracer remained in the dorsal part of the v3V (Fig. 3D and movies S10 and S11), indicating the presence of a dorsoventral boundary in this region.

The appearance of a whirl at ZT23 leads to a major change in the global flow pattern: The vertical intraventricular boundary that was present at the end of the resting phase was absent at the end of the awake phase. This raises the possibility that the distribution of CSF varies with the time of the day. Our FITC-dextran tracer experiments show that mixing of the flow is very weak. This is also supported by comparing the time scale of mixing, estimated from the flow gradient, with the time that it takes the flow to transverse the ventricle.

Mammalian third ventricles differ in size and morphology (*15*), yet both the modular organization and the flow domains are largely conserved

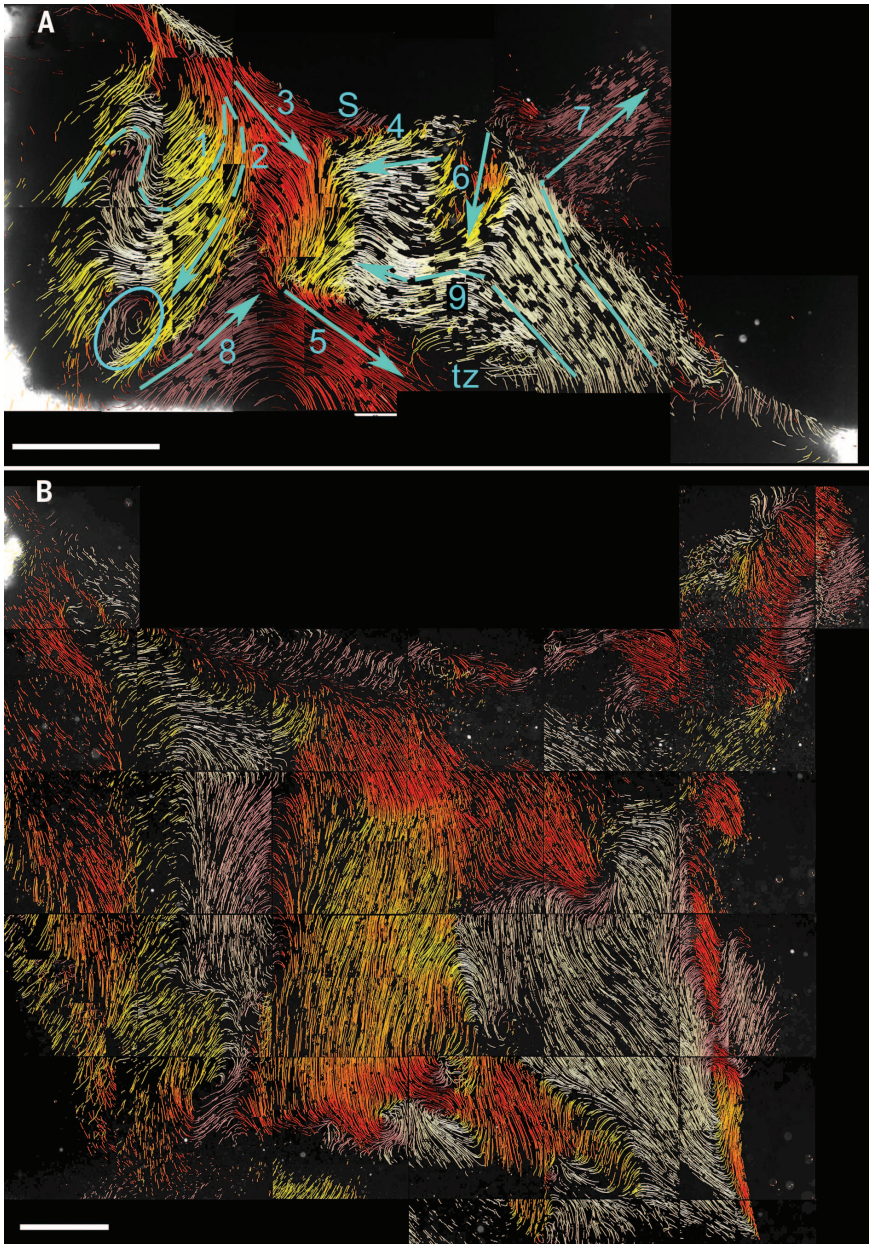

Fig. 4. Flow maps of rat and pig v3Vs. (**A**) The flow map of the rat v3V strongly resembles that of the mouse v3V, except for an anteroventral whirl (ellipse), an S-shaped flow (1), and a posterior flow (9) that emerges from the floor of the posterior part of the v3V. (**B**) The flow map of the pig v3V shows that it is highly organized and has cilia modules, separatrices, and whirls. Scale bars, 1 mm. Color coding is as in the previous figures.

between mice and rats (compare Fig. 1C with Fig. 4A). The ventricular recesses in the rat are more prominent than in the mouse. Accordingly, when we examined cilia-generated flow in the v3V of rats, flow 1, directed at the supraoptic recess, was S-shaped, and a new flow (flow 9) emerged from the posterior floor of the v3V, to which the infundibular and inframammillary recesses are connected. The v3V of pigs differs in size and architecture from those of rodents (*16*), yet we also observed flow domains in pig v3V (Fig. 4B).

A combination of straight and bent flows guides molecules across several hundred microns. For example, flow initiating at the entrance of the v3V extends as far as the arcuate nucleus. This flow may play a role in delivery or uptake of substances in this region, which is characterized by an abundance of chemosensory tanycytes (*17*). Tanycyte cell bodies are in contact with CSF, and their processes extend several hundred micrometers deep into the brain parenchyma, thus acting as bridges between the ventricle and neurons (*18*).

The similarity in design of the transport networks across species suggests a genetic regulation of network development. Hypothalamic nuclei arise from radial glia cells (*19*) that acquire their fate by coexpressing a combination of transcription factors (*20*). The later descendants of these radial glia cells also form the ependymal cell sheet (*21*), and thus cilia modules therein might also be specified by a particular combination of regionally expressed transcription factors. Such orchestrated development would establish a direct relationship between potential targets, the hypothalamic nuclei, and the structure of the transport network.

Fluid dynamics has long described complex types of movement in other systems. Now we show that complex fluid movements are also present in the brain in the form of a transport network driven by coordinated cilia beating patterns. In addition to targeted substance delivery, cilia generate separating flows and whirls that may establish and modulate intraventricular boundaries capable of concentrating locally released compounds and preventing their entry into off-target regions. Transient local changes in the beating pattern evoked a major change in ventricular subdivision. The cellular and structural bases that underly such changes in beating direction are unknown but may be driven by transient changes in cell-cell interactions and in planar cell polarity.

REFERENCES AND NOTES

1. M. R. Del Bigio, *Acta Neuropathol.* **119**, 55–73 (2010).
2. B. Guirao *et al.*, *Nat. Cell Biol.* **12**, 341–350 (2010).
3. E. R. Brooks, J. B. Wallingford, *Curr. Biol.* **24**, R973–R982 (2014).
4. W. C. Worthington Jr., R. S. Cathcart 3rd, *Ann. N. Y. Acad. Sci.* **130**, 944–950 (1966).
5. A. Kramer *et al.*, *Science* **294**, 2511–2515 (2001).
6. M. Y. Cheng *et al.*, *Nature* **417**, 405–410 (2002).
7. S. Kraves, C. J. Weitz, *Nat. Neurosci.* **9**, 212–219 (2006).
8. S. C. Robins *et al.*, *Nat. Commun.* **4**, 2049 (2013).
9. A. Guldbrandsen *et al.*, *Mol. Cell. Proteomics* **13**, 3152–3163 (2014).
10. Y. Zhang *et al.*, *J. Proteomics* **119**, 90–99 (2015).
11. D. Chiasserini *et al.*, *J. Proteomics* **106**, 191–204 (2014).
12. K. Sawamoto *et al.*, *Science* **311**, 629–632 (2006).
13. J. B. Freund, J. G. Goetz, K. L. Hill, J. Vermot, *Development* **139**, 1229–1245 (2012).
14. C. Richter, I. G. Woods, A. F. Schier, *Annu. Rev. Neurosci.* **37**, 503–531 (2014).
15. R. Nieuwenhuys, H. J. ten Donkelaar, C. Nicholson, *The Central Nervous System of Vertebrates* (Springer-Verlag, 1998).
16. B. Félix *et al.*, *Brain Res. Bull.* **49**, 1–137 (1999).
17. T. C. Mathew, *Anat. Histol. Embryol.* **37**, 9–18 (2008).
18. M. Bolborea, N. Dale, *Trends Neurosci.* **36**, 91–100 (2013).
19. M. Shimada, T. Nakamura, *Exp. Neurol.* **41**, 163–173 (1973).
20. J. L. Ferran, L. Puelles, J. L. Rubenstein, *Front. Neuroanat.* **9**, 46 (2015).
21. N. Spassky *et al.*, *J. Neurosci.* **25**, 10–18 (2005).
22. K. B. J. Franklin, G. Paxinos, *The Mouse Brain in Stereotaxic Coordinates* (Academic Press, 1997).

ACKNOWLEDGMENTS

We thank A. Bae, A. Pumir, and C. Lo for valuable comments and suggestions; C. Thaller for technical assistance; J. Schröder-Schetelig for providing multirecorder software; and D. Hornung and T. Baig for providing euthanized minipigs. This work was supported by the Max Planck Society.

SUPPLEMENTARY MATERIALS

www.sciencemag.org/content/353/6295/176/suppl/DC1
Materials and Methods
Figs. S1 to S6
Table S1
References (*23*–*25*)
Movies S1 to S11

9 December 2015; accepted 10 June 2016
10.1126/science.aae0450

IMMUNOTHERAPY

Reengineering chimeric antigen receptor T cells for targeted therapy of autoimmune disease

Christoph T. Ellebrecht,[1] Vijay G. Bhoj,[2] Arben Nace,[1] Eun Jung Choi,[1] Xuming Mao,[1] Michael Jeffrey Cho,[1] Giovanni Di Zenzo,[3] Antonio Lanzavecchia,[4] John T. Seykora,[1] George Cotsarelis,[1] Michael C. Milone,[2]*† Aimee S. Payne[1]*†

Ideally, therapy for autoimmune diseases should eliminate pathogenic autoimmune cells while sparing protective immunity, but feasible strategies for such an approach have been elusive. Here, we show that in the antibody-mediated autoimmune disease pemphigus vulgaris (PV), autoantigen-based chimeric immunoreceptors can direct T cells to kill autoreactive B lymphocytes through the specificity of the B cell receptor (BCR). We engineered human T cells to express a chimeric autoantibody receptor (CAAR), consisting of the PV autoantigen, desmoglein (Dsg) 3, fused to CD137-CD3ζ signaling domains. Dsg3 CAAR-T cells exhibit specific cytotoxicity against cells expressing anti-Dsg3 BCRs in vitro and expand, persist, and specifically eliminate Dsg3-specific B cells in vivo. CAAR-T cells may provide an effective and universal strategy for specific targeting of autoreactive B cells in antibody-mediated autoimmune disease.

Pemphigus vulgaris (PV) is a life-threatening autoimmune blistering disease caused by autoantibodies to the keratinocyte adhesion protein Dsg3 (*1*). CD20-targeted B cell depletion results in short-term disease remission in 95% of pemphigus patients, but 81% relapse and fatal infection may occur (*2*). After CD20-targeted depletion, serum autoantibody titers drop, indicating that short-lived plasmablasts are the source of autoantibodies in PV and targeting of $CD20^+$ memory B cell precursors indirectly depletes autoantibody-secreting $CD20^-$ plasmablasts (*3*, *4*). Relapsing pemphigus demonstrates the same anti-Dsg3 B cell clones observed during active disease, whereas disease remission is associated with disappearance of circulating anti-Dsg3 B cells (*5*). Thus, targeted elimination of anti-Dsg3 memory B cells should cure PV without the risks of general immunosuppression.

Recently, chimeric antigen receptor (CAR) technology has revolutionized cancer therapy. A CD19-specific CAR, consisting of an extracellular single-chain variable fragment (scFv) antibody to CD19 fused to T cell cytoplasmic signaling domains, activates T cell cytotoxicity upon contact with $CD19^+$ B cells, causing specific and permanent elimination of B cells and durable remission of leukemia (*6*–*14*). In PV, pathogenic memory B cells express anti-Dsg3 B cell receptors (BCRs). We reasoned that by expressing Dsg3 as the extracellular domain of a chimeric immunoreceptor, cytotoxicity would become specific for only those B cells bearing anti-Dsg3 BCRs, providing targeted therapy for PV without general immunosuppression. Such a strategy would directly eliminate surface immunoglobulin $(sIg)^+$ anti-Dsg3 memory B cells and indirectly eliminate sIg^- Dsg3-specific short-lived plasma cells that produce the disease-causing antibodies. We thus created a chimeric autoantibody receptor (CAAR) (fig. S1A), with the autoantigen Dsg3 as the CAAR extracellular domain, in order to engineer T cells to kill autoimmune B cells in PV.

Dsg3 consists of five extracellular cadherin (EC) domains, with residues important for cell adhesion residing in EC1 and EC2 (*15*). Autoantibodies to EC1, EC2, EC3, EC4, and EC5 occur in 91, 71, 51, 19, and 12% of PV sera; no PV sera target only the EC4 and/or EC5 domains (*16*). Since T cell activation depends on the intermembrane distance of the immunologic synapse (*17*), we reasoned that shorter conformational fragments of Dsg3 should enhance CAAR efficacy. We therefore designed a panel of Dsg3 CAARs for expression in primary human T cells (Fig. 1A), using Dsg3 EC1-3/EC1-4/EC1-5 as the extracellular domain, fused to a dimerization-competent CD8α transmembrane (*18*) and CD137-CD3ζ cytoplasmic signaling domains, which were used successfully in CD19 CAR clinical trials (*6*, *7*). EC1-3/EC1-4 CAARs demonstrate robust surface expression of mature, conformational Dsg3 in primary human T cells, whereas EC1-5 CAAR expression is more variable (fig. S1, B to D).

We first evaluated the ability of Dsg3 CAAR-T cells (CAAR-Ts) to kill anti-Dsg3 B cells in vitro, using antibody-secreting hybridomas that target EC1 (AK23), EC2 (AK19), and EC3-4 (AK18) (*19*), or K562/Nalm-6 cells expressing pathogenic F779/anti-EC1 or PVB28/anti-EC2 IgG cloned from PV patients (*20*, *21*) (fig. S2). All BCRs were expressed at a density comparable to human B cells (fig. S3). Dsg3EC1-3/EC1-4 CAAR-Ts demonstrate interferon-γ (IFN-γ) secretion and specific cytolysis against anti-EC1/EC2 but not control targets (Fig. 1, B and C, and fig. S4). Dsg3EC1-5 CAAR-Ts exhibit minimal cytolysis, and Dsg3EC1-3 CAAR-Ts do not lyse anti-EC3/4 targets. Thus, the Dsg3EC1-4 CAAR demonstrates the best combination of potency and breadth, with specific cytolysis of cells expressing anti-Dsg3 BCRs.

To investigate the mechanism of CAAR-T activation, we examined the molecular organization within CAAR-Ts upon binding sIg target by total internal reflection fluorescence microscopy. CAAR-Ts form immunologic synapses analogous to T cell receptor (TCR)–peptide/major histocompatibility complex (MHC) interaction (*22*, *23*), with actin reorganization and centripetal movement of CAAR-IgG clusters resulting in a central supramolecular activation complex (SMAC)–like structure (fig. S5A and movie S1). The protein tyrosine phosphatase CD45 is excluded from early CAAR-IgG microclusters (fig. S5B and movie S2), similar to findings with the anti-CD19 CAR (*24*) and the native TCR-MHC synapse (*25*), suggestive of a kinetic segregation model for CAAR activation (*26*).

PV patients have serum anti-Dsg3 IgG that might neutralize, or alternatively could help stimulate, Dsg3 CAAR-Ts. We therefore evaluated Dsg3 CAAR-T cytotoxicity in the presence of soluble monoclonal IgG matching the targeted BCR to maximize the neutralization capacity of the soluble IgG. Soluble anti-Dsg3 IgG decreases but still preserves compelling CAAR-T cytotoxicity against AK19/PVB28, minimally affects AK23/AK18, and potentiates cytotoxicity against F779 targets (Fig. 2, A and B). Because CAAR-Ts will encounter polyclonal anti-Dsg3 IgG in PV patients, we next tested Dsg3 CAAR-T cytotoxicity against polyclonal targets in the presence of polyclonal PV serum IgG. Dsg3EC1-3, and to a lesser extent Dsg3EC1-4, CAAR-Ts retained efficient levels of cytolysis against AK hybridomas (Fig. 2C), despite the presence of PV serum IgG as well as secreted anti-Dsg3 IgG by these hybridomas. Both Dsg3EC1-3 and EC1-4 CAAR-Ts effectively killed Nalm6 cells expressing human anti-Dsg3 IgG in the presence of PV serum IgG (Fig. 2D). Surface binding competition assays indicate that antibodies that inhibit cytotoxicity (AK19/PVB28) persist on the CAAR-T surface, which reduces the number of accessible CAAR molecules to bind target cells, while noninhibitory F779/AK23/AK18 are more rapidly replaced by competing antibodies, with AK18 replacement occurring even at 4°C, suggesting low affinity (Fig. 2, E and F). Indeed, surface plasmon resonance analysis indicates that noninhibitory antibodies tend to have faster off-rates and lower affinity (Fig. 2, G and H, and fig. S6A). Furthermore, F779 and PV serum IgG stimulate Dsg3EC1-4 CAAR-Ts, more so than the Dsg3EC1-3 CAAR-Ts, to secrete low levels of IFN-γ and proliferate (fig. S6, B and C). Thus, the effect of soluble antibodies to Dsg3 on CAAR-T function and activation is a complex process that is affected by affinity and binding kinetics of the

[1]Department of Dermatology, University of Pennsylvania, Philadelphia, PA 19104, USA. [2]Department of Pathology and Laboratory Medicine, University of Pennsylvania, Philadelphia, PA 19104, USA. [3]Laboratory of Molecular and Cellular Biology, Istituto Dermopatico dell'Immacolata (IDI-IRCCS), 00167 Rome, Italy. [4]Institute for Research in Biomedicine, 6500 Bellinzona, Switzerland.
*Corresponding author. Email: aimee.payne@uphs.upenn.edu (A.S.P.); milone@mail.med.upenn.edu (M.C.M.) †These authors contributed equally to this work.

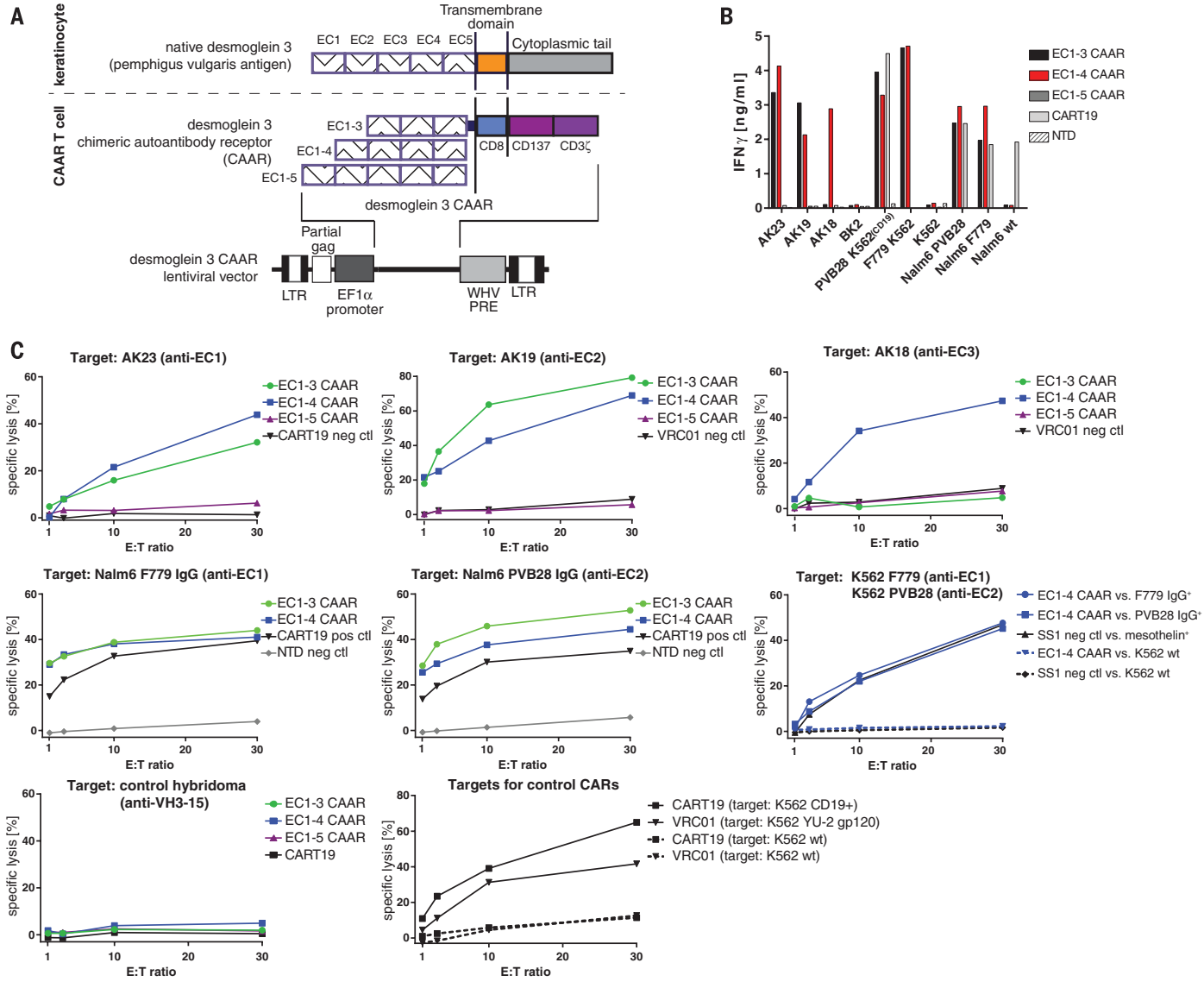

Fig. 1. Dsg3 CAAR-T cells demonstrate specific and potent cytotoxicity. (**A**) Schematic of native Dsg3, Dsg3 CAAR, and lentiviral vector for stable CAAR expression. (**B**) Specific IFN-γ production by CAAR-Ts as measured by ELISA from coculture supernatant after 24 hours. Cultures were set up in duplicate; mean values are shown. Similar results were obtained in independent experiments from at least five different healthy T cell donors. (**C**) ^{51}Cr release after 4 hours of T cell–target cell coculture at indicated effector to target (E:T) ratios to measure specific cytotoxicity by Dsg3 CAAR-Ts against distinct anti-Dsg3 target cells. Mean values of triplicate cultures are shown. Similar results were obtained in independent experiments from at least five different healthy T cell donors.

antibody, as well as the relative position of the epitope in the CAAR molecule, highlighted by the different susceptibility of the EC1-3 and EC1-4 CAARs to blockade and activation. Collectively, these data suggest that soluble anti-Dsg3 IgG will not prevent and may in fact promote CAAR-T efficacy and persistence due to CD137-mediated costimulatory signals that have been shown to enhance CAR-T activity (*27*–*30*) and ameliorate T cell exhaustion (*31*).

We tested the in vivo efficacy of Dsg3 CAAR-Ts against AK23/AK19/AK18 target cells in a PV mouse model (*19*). We selected the PV hybridoma model for in vivo proof of concept, because this model allows preclinical testing of human Dsg3 CAAR-T efficacy against B cells targeting distinct and defined Dsg3 epitopes. Furthermore, the mice have polyclonal serum anti-Dsg3 IgG (like PV patients) that might neutralize or eliminate CAAR-Ts, and disease burden can be serially and objectively quantitated by bioluminescence imaging. NSG (NOD-scid-gamma) mice were injected with a polyclonal mixture of bioluminescent AK18/AK19/AK23 hybridomas, followed by injection with either Dsg3 CAAR-Ts or control CAR-Ts at day 5 (fig. S7A), at which time serum antibody titers to Dsg3 were detectable by enzyme-linked immunosorbent assay (ELISA) (Fig. 3A). Dsg3 CAAR-Ts robustly control all PV hybridomas, resulting in decreased Dsg3 serum autoantibody titers (Fig. 3A), absence of autoantibody binding (Fig. 3B) and blistering in oral mucosa (Fig. 3C), and significantly delayed or no hybridoma outgrowth (Fig. 3D). Dsg3EC1-4 CAAR-Ts showed equal efficacy when tested against each individual hybridoma in vivo (fig. S8, A to G). We further analyzed a subset of Dsg3EC1-4 CAAR-T–treated mice with increasing bioluminescence at day 18. Increasing flux was due to outgrowth of sIg^- hybridomas that comprised ~1% of injected cells (fig. S8, H to J). This mechanism of CAAR-T escape observed in mice is irrelevant in patients because sIg^- long-lived plasma cells do not significantly contribute to PV autoantibody production. Dsg3 CAAR-T frequencies in both "escape" and "cured" mice were comparable, indicating that lack of CAAR-T cell persistence or loss of Dsg3 CAAR expression is not responsible for CAAR escape in vivo (fig. S8K).

We further tested the in vivo efficacy of Dsg3EC1-4 CAAR-Ts against human $CD19^+$ Nalm-6

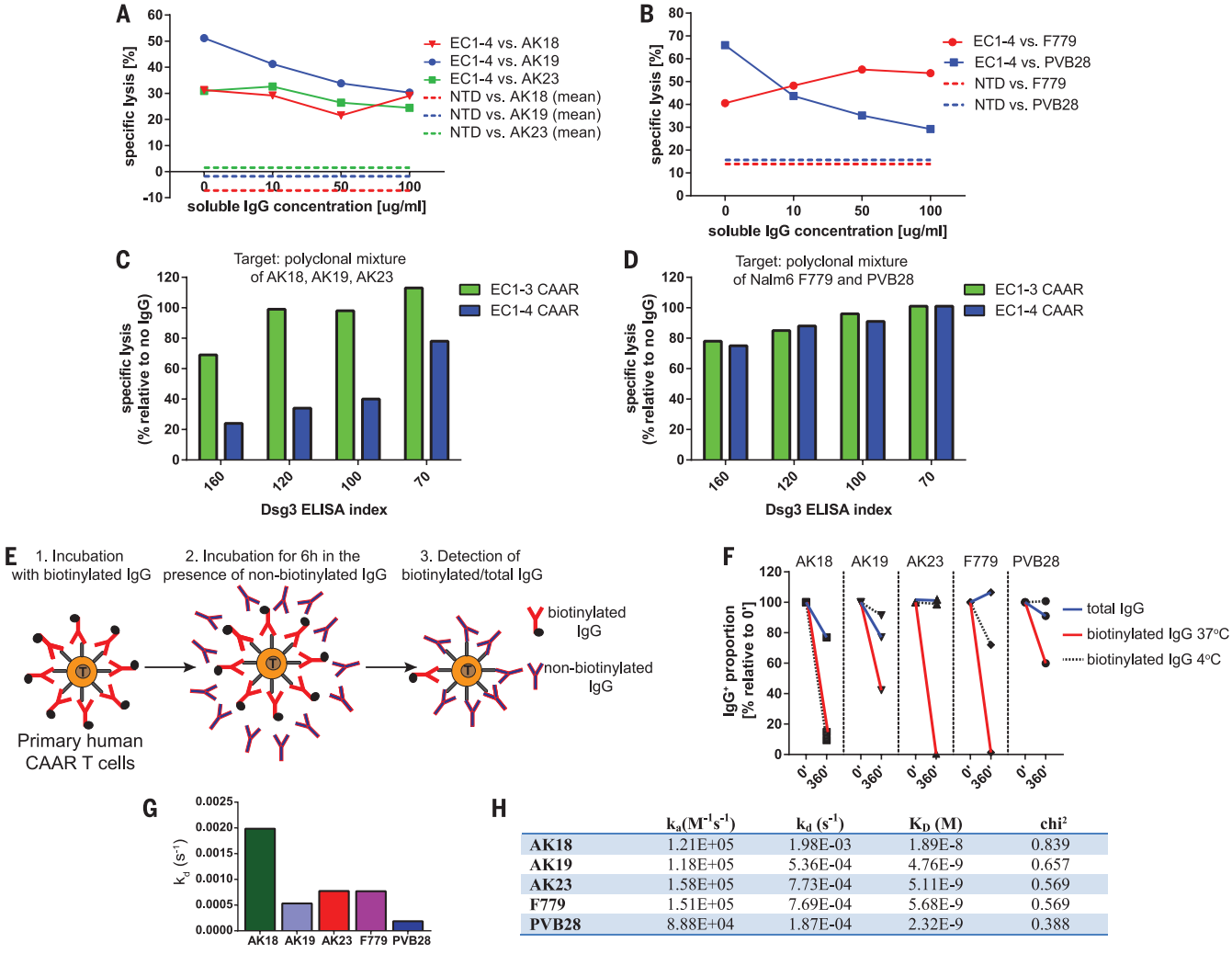

	$k_a(M^{-1}s^{-1})$	k_d (s^{-1})	K_D (M)	chi²
AK18	1.21E+05	1.98E-03	1.89E-8	0.839
AK19	1.18E+05	5.36E-04	4.76E-9	0.657
AK23	1.58E+05	7.73E-04	5.11E-9	0.569
F779	1.51E+05	7.69E-04	5.68E-9	0.569
PVB28	8.88E+04	1.87E-04	2.32E-9	0.388

Fig. 2. Dsg3 CAAR-T cells maintain cytotoxicity in the presence of soluble antibodies to Dsg3. (**A** to **D**) ^{51}Cr release after 4 hours of T cell–target cell coculture at an E:T ratio of 30:1 to measure specific cytotoxicity by Dsg3 CAAR-Ts in the presence of [(A) and (B)] soluble, monoclonal antibodies to Dsg3 at indicated concentrations or [(C) and (D)] soluble, polyclonal antibodies to Dsg3 at indicated Dsg3 ELISA indices. Mean values from triplicate cultures are shown. Results are representative of two independent experiments with CAAR-T cells from two different donors. (**E**) Experimental setup for pulse-chase antibody cell-surface binding assay. (**F**) Total surface IgG and retained biotinylated IgG were detected by flow cytometry after 6 hours of culture with excess nonbiotinylated IgG at 4°C and 37°C to assess the blocking property of soluble IgG toward each B cell clone. Similar results were replicated in three independent experiments with Dsg3EC1-4 CAAR-T cells from three different T cell donors. (**G** and **H**) Surface plasmon resonance demonstrating higher off-rates (k_d) and lower affinity (higher K_D) of nonblocking antibodies AK18, AK23, and F779. Values were calculated from four different concentrations, as indicated in fig. S6A.

B cells expressing anti-Dsg3 BCRs (F779/PVB28) cloned from PV patients. This model additionally allows comparison with anti-CD19 CAR-Ts (CART19) that have proven clinical efficacy (*6*, *7*). Although CAAR-T treatment is delayed until the exponential growth phase of the target cells, Dsg3 CAAR-Ts effectively eliminate anti-Dsg3 Nalm-6 B cells with efficacy comparable to CART19, measured by bioluminescence and flow cytometric analysis of bone marrow/spleen (Fig. 3, E to G, and fig. S7, B and C). Collectively, these models show that Dsg3 CAAR-Ts eliminate anti-Dsg3 BCR^+ but not BCR^- cells in vivo, indicating specific cytolysis, as opposed to bystander activation and off-target cytolysis, even in the presence of soluble anti-Dsg3 IgG. Notably, CAAR-Ts persist in the presence of soluble autoantibodies to Dsg3 in vivo (fig. S8K), indicating that circulating autoantibodies do not cause Fc-mediated clearance of CAAR-Ts. Furthermore, CAAR-Ts showed engraftment and persistence in the spleen 3 weeks after CAAR-T transfer, even in the absence of target cells (fig. S8L), suggesting that persistence of CAAR-Ts does not depend on target cell encounter.

We next addressed CAAR-T safety by evaluating off-target effects against keratinocytes, which express desmocollins and desmogleins, the physiologic binding partners of Dsg3. The Dsg3CAAR does not exhibit CD3ζ-mediated signaling in reporter cells after incubation with keratinocytes (Fig. 4, A and B), in contrast to positive control anti-Dsg3/1 (Px44) CAR. Correspondingly, Dsg3EC1-4 CAAR-Ts do not lyse human keratinocytes in vitro, whereas Px44 CAR-Ts show potent lysis (Fig. 4C). To evaluate toxicity in vivo, we tested CAAR-Ts in human skin-xenografted mice (Fig. 4D). Px44 CAR-Ts exhibit exuberant epidermal infiltration by day 3 (Fig. 4, D and E). Despite similar T cell density in the graft dermis, Dsg3EC1-4 CAAR-Ts do not demonstrate enhanced skin toxicity compared with CART19, which has shown no skin side effects in humans. Additionally, no off-target toxicity against other tissues was observed in Dsg3EC1-4 CAAR-T–treated mice (fig. S9). Because human Dsg3 rescues the loss of mouse Dsg3, indicating functional interaction between human Dsg3 and mouse desmosomal components (*32*), these experiments indicate that Dsg3EC1-4 CAAR-Ts cause no toxicity to desmosome-bearing tissues in vivo. The absence of off-target toxicity to desmosome-bearing tissues might be explained by several factors. The intermembrane distance in desmosomes is 35 nm (*15*), greater than the 15-nm optimum

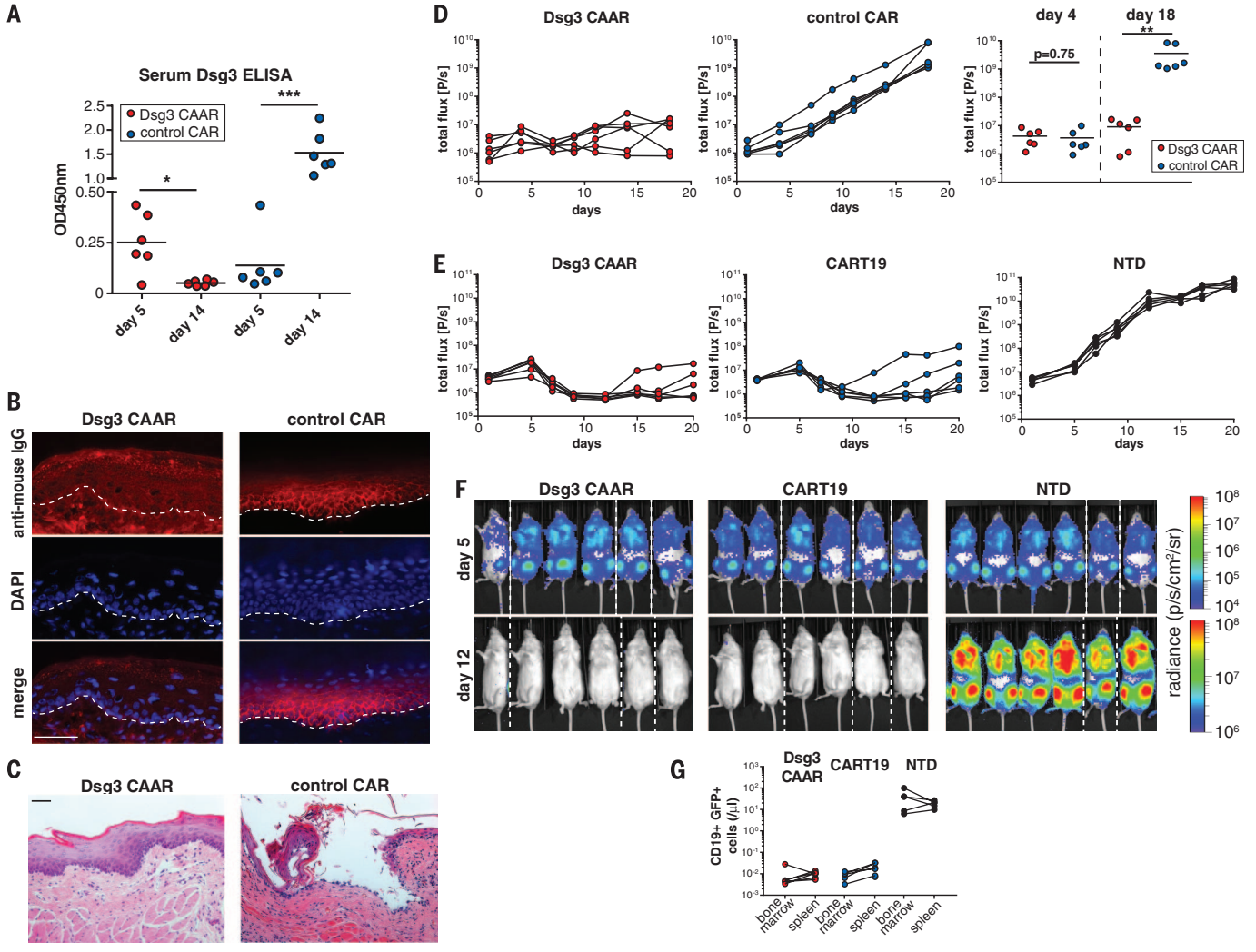

Fig. 3. Dsg3 CAAR-T cells eliminate anti-Dsg3 target cells in vivo. (**A**) Serum anti-Dsg3 ELISA was performed on days 5 and 14 to quantify IgG production by hybridoma cells before and after CAAR-T treatment. Paired *t* test, two-tailed; $*P < 0.05$; $***P < 0.001$. (**B**) Direct immunofluorescence of mucosa samples to detect IgG deposition after CAAR-T or control T cell treatment. Absence of IgG deposition was seen in all CAAR-T–treated mice. (**C**) Histologic mucosal blister formation (i.e., acantholysis) was assessed after CAAR-T treatment. None of six CAAR-T–treated mice, versus five of six control T cell–treated mice, demonstrated acantholysis; $P = 0.015$, Fisher's exact test. Scale bars in (B) and (C), 50 μm. (**D**) Serial quantification of hybridoma burden by bioluminescence imaging. Unpaired Mann-Whitney test, two-tailed, $**P < 0.01$; results were replicated in an independent experiment with T cells from a different donor. Symbols represent one mouse each; horizontal black lines represent the mean of each group. (**E**) Bioluminescence imaging quantification of Nalm6 CD19$^+$ B cells expressing PVB28/F779 IgG after Dsg3 CAAR-T, anti-CD19 CAR-T (CART19), or nontransduced T cell (NTD) treatment. (**F**) Bioluminescence on days 5 and 12 after Nalm6 injection. Dashed lines separate images from different cages. (**G**) Flow cytometric quantification of Nalm6 cells in bone marrow and spleen in the three treatment groups 22 days after Nalm6 injection.

distance for T cell activation. Additionally, cadherin-cadherin affinity is in the micromolar range (*33*), whereas CAR-T function typically requires nanomolar affinity (*34*–*36*). Finally, Dsg3 truncation (EC1-3/EC1-4) potentially compromises CAAR interaction with desmosomal ligands while preserving epitopes required for autoantibody binding, thus preventing off-target toxicity.

We also considered that FcγR-expressing cells bind serum antibodies to Dsg3 and might become targets for Dsg3 CAAR-Ts, although significant toxicity is unlikely because anti-Dsg3 IgG comprises only a small fraction of total serum IgG. In the presence of PV serum, cytotoxicity against CD64$^+$ (FcγR$^+$) K562 cells was undetectable (fig. S10, A and B). Additionally, Dsg3EC1-4 CAAR-T treatment in the setting of circulating anti-Dsg3 IgG does not reduce FcγR-expressing cells such as neutrophils and monocytes in vivo (fig. S10C), indicating that redirected killing via CAAR-antibody-FcγR interaction does not occur. Furthermore, CAAR-T reporter cells do not activate when exposed to bone marrow B cells that harbor a polyreactive and/or autoreactive repertoire (*37*), in contrast to CART19, which reacts with bone marrow B cells (fig. S11). Thus, toxicity by Dsg3EC1-4 CAAR-Ts is undetectable, underscoring the specificity of the CAAR concept.

In summary, CAAR-Ts represent a targeted approach to therapy of antibody-mediated autoimmune diseases, with the potential for generation of long-term memory CAAR-Ts that can potentially cure disease. CAAR-Ts expressing the PV autoantigen Dsg3 specifically kill anti-Dsg3 target cells, even in the presence of circulating autoantibodies, and without off-target toxicity. We acknowledge that short-term observations of CAAR-T safety and efficacy in preclinical models are inherently limited. Nevertheless, several of the limitations of CAR-T therapy for cancer likely will not apply to CAAR-T therapy of autoimmunity. Target cell escape due to epitope spreading or somatic mutation is impossible, because B cells that no longer bind Dsg3 will become irrelevant to disease. Additionally, memory B cells depend on

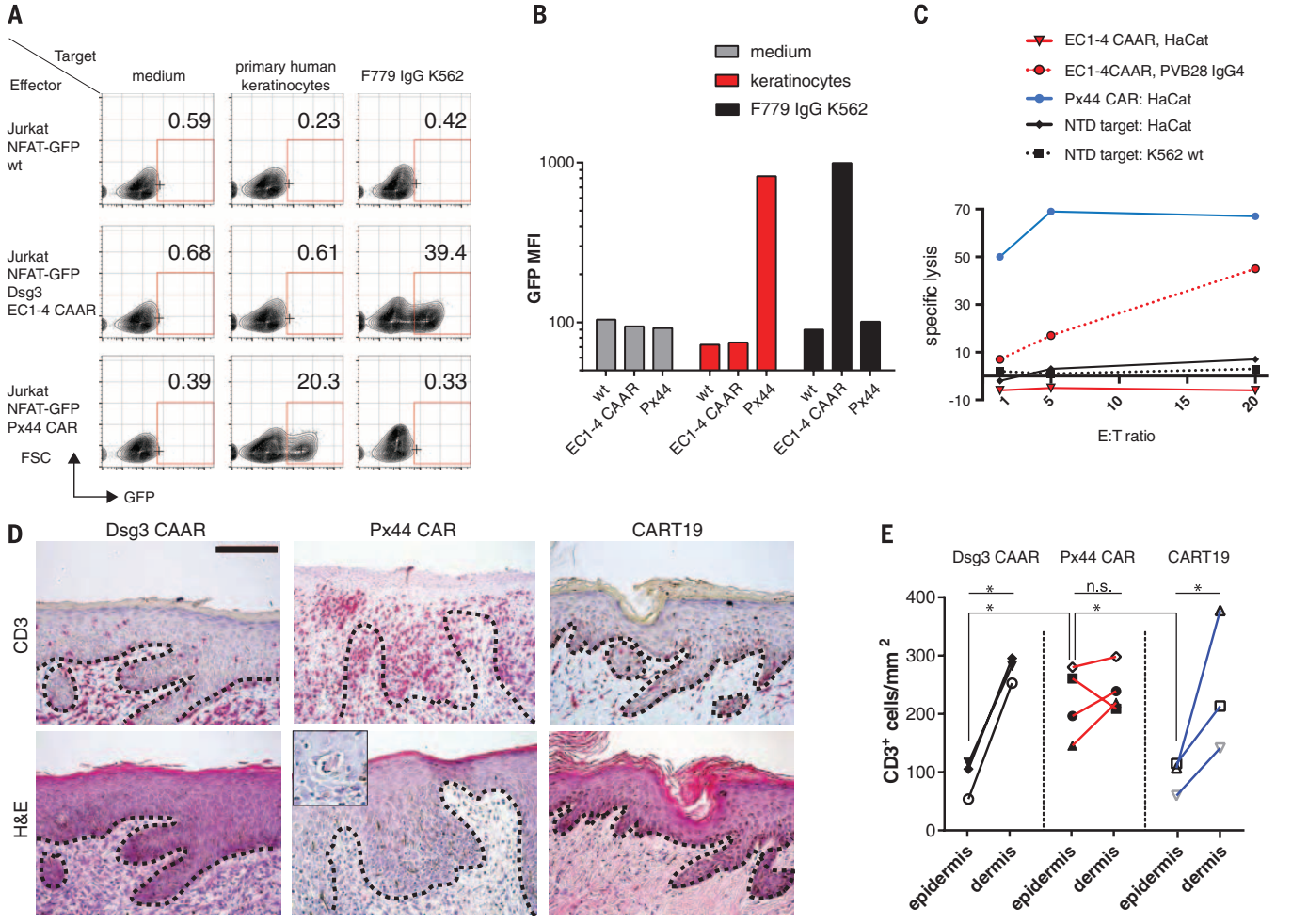

Fig. 4. Dsg3 CAAR-T cells do not show off-target toxicity. (**A**) Flow-cytometric quantification of CAAR-mediated signal transduction, as indicated by nuclear factor of activated T cells (NFAT)–driven green fluorescent protein (GFP) expression in Jurkat reporter cells, using anti-Dsg3/1 Px44 CAR as a positive control for keratinocyte expression of Dsg3. Numbers indicate percentage of live, single cells in the GFP-positive gate. (**B**) Mean fluorescence intensity of GFP expression from (A). Representative data were replicated in at least five independent experiments with keratinocytes from different human donors. (**C**) ^{51}Cr release after T cell–target cell coculture at indicated E:T ratios to measure cytotoxicity by Dsg3 CAAR-Ts and controls against human HaCat keratinocytes. Mean values of triplicate cultures are shown; similar results were obtained in two independent experiments. (**D**) Microscopic analysis of human skin xenografts to evaluate epidermal infiltration by Dsg3CAAR-Ts, positive control Px44 CAR-Ts, and negative control CART19. (Inset) Dyskeratotic keratinocytes surrounded by T cells. Dashed line shows dermal-epidermal junction. Scale bar, 125 μm. (**E**) Quantification of T cell infiltration into epidermis and dermis of human skin xenografts. Each symbol represents one mouse; ratio-paired *t* test, two-tailed, *$P < 0.05$; n.s. nonsignificant; data are pooled from two independent experiments.

survival and activation signals through the BCR; thus, anti-Dsg3 B cells that down-regulate sIg are unlikely to persist or mature into antibody-secreting cells. Tumor lysis and cytokine release syndrome are also unlikely since Dsg3-reactive B cells are predicted to comprise only a small fraction of the total B cell population. Ultimately, various combinations of CAARs could be combined to maximize efficacy in diseases in which autoantibodies targeting multiple autoantigens are pathogenic. Thus, CAAR-T cells represent an innovative therapeutic strategy that avoids the risks of general immunosuppression and can likely be applied to other autoantibody-mediated diseases.

REFERENCES AND NOTES

1. A. S. Payne, J. R. Stanley, in *Dermatology in General Medicine*, K. Wolff *et al.*, Eds. (McGraw Hill, New York, 2012), chap. 53.
2. N. Colliou *et al.*, *Sci. Transl. Med.* **5**, 175ra30 (2013).
3. R. Eming *et al.*, *J. Invest. Dermatol.* **128**, 2850–2858 (2008).
4. L. Lunardon *et al.*, *Arch. Dermatol.* **148**, 1031–1036 (2012).
5. C. M. Hammers *et al.*, *J. Invest. Dermatol.* **135**, 742–749 (2015).
6. D. L. Porter, B. L. Levine, M. Kalos, A. Bagg, C. H. June, *N. Engl. J. Med.* **365**, 725–733 (2011).
7. S. L. Maude *et al.*, *N. Engl. J. Med.* **371**, 1507–1517 (2014).
8. M. L. Davila *et al.*, *Sci. Transl. Med.* **6**, 224ra25 (2014).
9. D. W. Lee *et al.*, *Lancet* **385**, 517–528 (2015).
10. J. N. Kochenderfer *et al.*, *J. Clin. Oncol.* **33**, 540–549 (2015).
11. R. J. Brentjens *et al.*, *Blood* **118**, 4817–4828 (2011).
12. C. R. Cruz *et al.*, *Blood* **122**, 2965–2973 (2013).
13. B. Savoldo *et al.*, *J. Clin. Invest.* **121**, 1822–1826 (2011).
14. C. J. Turtle *et al.*, *J. Clin. Invest.* **126**, 2123–2138 (2016).
15. A. Al-Amoudi, D. C. Díez, M. J. Betts, A. S. Frangakis, *Nature* **450**, 832–837 (2007).
16. B. Ohyama *et al.*, *J. Invest. Dermatol.* **132**, 1158–1168 (2012).
17. K. Choudhuri, D. Wiseman, M. H. Brown, K. Gould, P. A. van der Merwe, *Nature* **436**, 578–582 (2005).
18. S. Hennecke, P. Cosson, *J. Biol. Chem.* **268**, 26607–26612 (1993).
19. K. Tsunoda *et al.*, *J. Immunol.* **170**, 2170–2178 (2003).
20. G. Di Zenzo *et al.*, *J. Clin. Invest.* **122**, 3781–3790 (2012).
21. M. J. Cho *et al.*, *Nat. Commun.* **5**, 4167 (2014).
22. C. R. F. Monks, B. A. Freiberg, H. Kupfer, N. Sciaky, A. Kupfer, *Nature* **395**, 82–86 (1998).
23. A. Grakoui *et al.*, *Science* **285**, 221–227 (1999).
24. J. R. James, R. D. Vale, *Nature* **487**, 64–69 (2012).
25. R. Varma, G. Campi, T. Yokosuka, T. Saito, M. L. Dustin, *Immunity* **25**, 117–127 (2006).
26. S. J. Davis, P. A. van der Merwe, *Nat. Immunol.* **7**, 803–809 (2006).
27. I. Melero *et al.*, *Nat. Med.* **3**, 682–685 (1997).
28. Z. Ye *et al.*, *Nat. Med.* **8**, 343–348 (2002).
29. S. Yang *et al.*, *Proc. Natl. Acad. Sci. U.S.A.* **101**, 4990–4995 (2004).
30. Z. Zhao *et al.*, *Cancer Cell* **28**, 415–428 (2015).
31. A. H. Long *et al.*, *Nat. Med.* **21**, 581–590 (2015).

32. D. A. Culton *et al*., *J. Invest. Dermatol.* **135**, 1590–1597 (2015).
33. P. Katsamba *et al*., *Proc. Natl. Acad. Sci. U.S.A.* **106**, 11594–11599 (2009).
34. M. Hudecek *et al*., *Clin. Cancer Res.* **19**, 3153–3164 (2013).
35. K. Watanabe *et al*., *Blood* **124**, 4799 (2014).
36. S. Srivastava, S. R. Riddell, *Trends Immunol.* **36**, 494–502 (2015).
37. H. Wardemann *et al*., *Science* **301**, 1374–1377 (2003).

ACKNOWLEDGMENTS

We thank D. Margolis, S. Prouty, T. Dentchev, C.-Y. Tsai, and S. Nunez-Cruz for technical assistance and consultation on the studies and J. R. Stanley for helpful discussions. The data reported in this manuscript are tabulated in the main paper and in the supplementary materials. Constructs and cell lines are available from the corresponding authors under a Material Transfer Agreement with the University of Pennsylvania. C.T.E., V.G.B., M.C.M, and A.S.P. have filed patent PCT/US15/28872, 2015, which relates to compositions and methods of chimeric autoantibody receptor T cells. C.T.E. and A.S.P. have filed Provisional Patent Application 62/222,132, 2015, which relates to the VRC01 chimeric antigen receptor. Research reported in this publication was supported in part by the Penn Institute for Immunology (A.S.P. and M.C.M.); the Dermatology Foundation Charles and Daneen Stiefel Scholar Award (A.S.P.); the National Institute of Arthritis and Musculoskeletal and Skin Diseases of NIH (A.S.P., R01-AR057001 and R01-AR068288; M.J.C., T32-AR007465 and F31-AR066456; G.C., R01-AR055309; and Skin Diseases Research Core grant P30-AR057217); Deutsche Forschungsgemeinschaft (C.T.E., EL711/1-1); the National Cancer Institute of NIH (V.G.B., T32-CA009140); the National Heart, Lung, and Blood Institute of NIH (V.G.B., K12-HL087064); and the Italian Ministry of Health (G.D.Z., Ricerca Finalizzata RF10-2309790). The content is solely the responsibility of the authors and does not necessarily represent the official views of the National Institutes of Health.

SUPPLEMENTARY MATERIALS

www.sciencemag.org/content/353/6295/179/suppl/DC1
Materials and Methods
Figs. S1 to S11
Table S1
Movies S1 and S2
References (*38*–*55*)

17 March 2016; accepted 9 June 2016
Published online 30 June 2016
10.1126/science.aaf6756

Electronic Pipettes

Gilson has redesigned and expanded the range of its easy-to-use, PIPETMAN M line of single and multichannel electronic pipettes. The pipettes now include guaranteed performance in repetitive pipetting mode and a programmable custom mode, enhancing results reliability. For sensitive biological assays like qPCR, repeatable results depend on accurate, precise pipetting, but until now most pipettes have promised performance in only one standard pipetting mode for both standard and repetitive tasks. Gilson now guarantees reliable performance from the first to the last aliquot. Five pipetting mode options enable researchers to perform a large number of applications: pipet (standard), repetitive, mix, reverse, and custom (personalized), with a fast access menu to all the modes plus intuitive navigation. The new personalized pipetting mode lets researchers create their own multistep pipetting protocols, which can be executed automatically using the simple PIPETMAN M software interface.

Gilson
For info: 800-445-7661
www.gilson.com/pipetmanm

Coulometer

The new Metrohm 917 Karl Fischer Coulometer is a compact, stand-alone coulometer offering several unique features that make it ideal for fast, precise determination of low-level water content. A vivid touchscreen display, simple method recall, and an integrated pump combined with reagent and sample handling make the 917 compact coulometer the fastest, most convenient solution for routine moisture analysis. The 917 is intelligent, automatically recognizing when a sample has been injected and starting the titration without a prompt. The 917's operation is further simplified with automatic sample-weight transfer from a laboratory balance, and laboratory information management system compatibility. Quick access to frequently used methods allows titration to begin with a single touch on the high-resolution color touchscreen. Furthermore, the 917 is compact, requiring only 8 in. of linear bench space. The coulometer can be connected to an oven for thermal sample preparation, enabling it to support the broadest range of sample types.

Metrohm
For info: +41-(0)-71-353-85-85
www.metrohm.com

Gel Scanning System

The Bio-1000F is an innovative, user-friendly, and cost-effective scanning device that integrates image capture, gel preview, and gel extraction essential for routine nucleic acid gel electrophoresis. Using a combination of high-sensitivity, 300-dpi sensors and blue LED illuminators, the Bio-1000F is compatible with all ethidium bromide-alternative fluorescent stains and provides publication-quality images. With a sensitivity of up to 0.04 ng per band, the Bio-1000F gives significantly enhanced results over the more traditional CCD-based gel documentation systems. Users simply place their gel onto the scanning area, close the lid, and wait for the image to be captured. A convenient orange screen shields the user from excessive exposure to the blue light. Users can visualize band patterns and conduct gel extraction directly on the Bio-1000F. Less than 30 cm wide, the Bio-1000F has a compact design that enables it to fit easily into any small space in a crowded laboratory.

Eikonix
For info: +44-(0)-1223-515440
www.eikonix.com

Liquid Nitrogen Generator

The Asynt CryoSyn is a unique, on-demand liquid nitrogen (LN_2) and nitrogen gas generator (available in 10-L, 20-L, 40-L, 60-L, and 120-L capacity models) for industrial, medical, food and agricultural, biological, and general laboratory applications. CryoSyn eliminates the need for storage and transportation of LN_2, thereby making its use more convenient, reducing running costs, and eliminating traditional evaporation/contamination problems. The CryoSyn control system gives operators all the information necessary to ensure an efficient and consistent supply of LN_2 and nitrogen gas. Designed to ensure high operational safety, the CryoSyn operates automatically and provides information on nitrogen flow, trend graphs, service alarms, and records. Operating off a single-phase electrical supply, the 10-L, 20-L, and 40-L CryoSyn units are fully mobile and fit through a standard doorway, enabling easy transport between locations. CryoSyn offers a typical return of investment in less than two years.

Asynt
For info: +44-(0)-1638-781709
www.asynt.com

Refractometers

The RFM-T Series of high-precision Peltier temperature-controlled benchtop refractometers features a wide measuring range of up to 1.70 RI (refractive index), precision to six decimal places RI (three decimal places °Brix), and an all-new, 7-in. touchscreen user interface. The RFM-Ts are ideally suited for quality control applications within the food and beverage, chemical, petrochemical, pharmaceutical, flavor, and fragrance industries as well as in academic research. There are currently five models, each addressing a particular application. RFM900-T models cover the widest of measurement ranges and incorporate a Kalrez prism gasket to protect the instruments from the harsh chemicals at the upper end of their refractive index range. RFM300-T models are specifically designed for the food and beverage sector and feature a very flat prism dish for easy cleaning between viscous samples. The touchscreen and graphic user interface help the operator quickly navigate through the menus. On-screen graphical prompts support method loading, calibration, and routine maintenance.

Xylem
For info: 978-778-1010
www.xylem.com

Electronically submit your new product description or product literature information! Go to www.sciencemag.org/about/new-products-section for more information.

Newly offered instrumentation, apparatus, and laboratory materials of interest to researchers in all disciplines in academic, industrial, and governmental organizations are featured in this space. Emphasis is given to purpose, chief characteristics, and availability of products and materials. Endorsement by *Science* or AAAS of any products or materials mentioned is not implied. Additional information may be obtained from the manufacturer or supplier.

want new technologies?

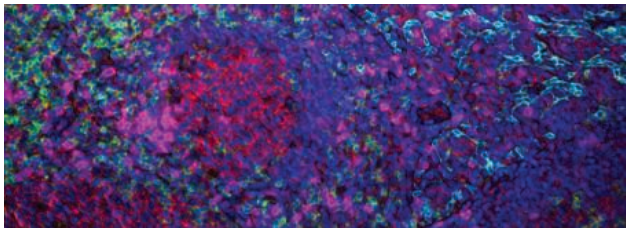

antibodies
apoptosis
biomarkers
cancer
cytometry
data
diseases
DNA
epigenetics
genomics
immunotherapies
medicine
microbiomics
microfluidics
microscopy
neuroscience
proteomics
sequencing
toxicology
transcriptomics

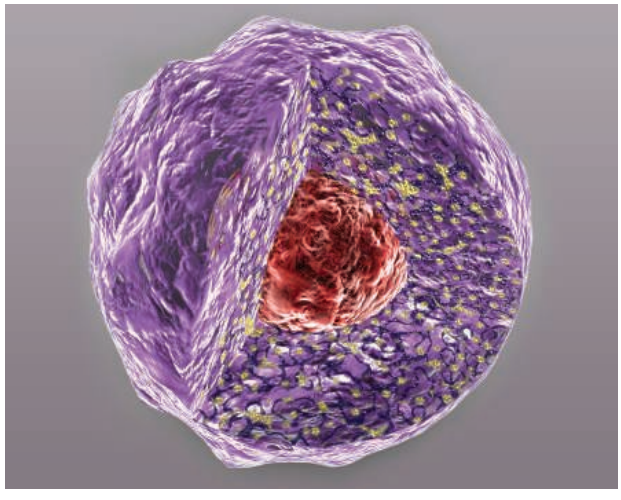

watch our webinars

Learn about the latest break-throughs, new technologies, and ground-breaking research in a variety of fields. Our expert speakers explain their quality research to you and answer questions submitted by live viewers.

VIEW NOW!
webinar.sciencemag.org

Science
AAAS

Brought to you by the *Science*/AAAS Custom Publishing Office

@SciMagWebinars

R&D Systems is Your New Trusted Source for Luminex® Instrumentation!

Direct access to Luminex staff for world-class on-site and 24x7x365 remote support

Unlimited emergency equipment repair

Discounts and special acquisition programs tailored to any lab's budget

Learn more about Luminex® instruments | rndystems.com/luminexinstruments

bio-techne®

Global info@bio-techne.com bio-techne.com/find-us/distributors TEL +1 612 379 2956
North America TEL 800 343 7475 **Europe | Middle East | Africa** TEL +44 (0)1235 529449
China info.cn@bio-techne.com TEL +86 (21) 52380373

bio-techne.com

Science Careers Advertising

For full advertising details, go to ScienceCareers.org and click For Employers, or call one of our representatives.

Tracy Holmes
Worldwide Associate Director
Science Careers
Phone: +44 (0) 1223 326525

THE AMERICAS

E-mail: advertise@sciencecareers.org
Fax: +1 (202) 289 6742

Tina Burks
Phone: +1 (202) 326 6577

Nancy Toema
Phone: +1 (202) 326 6578

Online Job Posting Questions
Phone: +1 (202) 312 6375

EUROPE / INDIA / AUSTRALIA / NEW ZEALAND / REST OF WORLD

E-mail: ads@science-int.co.uk
Fax: +44 (0) 1223 326532

Sarah Lelarge
Phone: +44 (0) 1223 326527

Kelly Grace
Phone: +44 (0) 1223 326528

Online Job Posting Questions
Phone: +44 (0) 1223 326528

JAPAN

Katsuyoshi Fukamizu (Tokyo)
E-mail: kfukamizu@aaas.org
Phone: +81 3 3219 5777

Hiroyuki Mashiki (Kyoto)
E-mail: hmashiki@aaas.org
Phone: +81 75 823 1109

CHINA / KOREA / SINGAPORE / TAIWAN / THAILAND

Ruolei Wu
E-mail: rwu@aaas.org
Phone: +86 186 0082 9345

Danny Zhao
E-mail: dzhao@aaas.org
Phone: +86 131 4114 0012

ScienceCareers
FROM THE JOURNAL SCIENCE AAAS

ScienceCareers.org

10 ways that *Science* Careers can help advance your career

1. Register for a free online account on **ScienceCareers.org**.
2. Search thousands of job postings and find your perfect job.
3. Sign up to receive e-mail alerts about job postings that match your criteria.
4. Upload your resume into our database and connect with employers.
5. Watch one of our many webinars on different career topics such as job searching, networking, and more.
6. Download our career booklets, including Career Basics, Careers Beyond the Bench, and Developing Your Skills.
7. Complete an interactive, personalized career plan at "my IDP."
8. Visit our Career Forum and get advice from career experts and your peers.
9. Research graduate program information and find a program right for you.
10. Read relevant career advice articles from our library of thousands.

Visit **ScienceCareers.org** today — all resources are free

ScienceCareers

FROM THE JOURNAL SCIENCE AAAS

SCIENCECAREERS.ORG

THE UNIVERSITY OF TENNESSEE HEALTH SCIENCE CENTER

The College of Dentistry at the University of Tennessee Health Science Center-Memphis invites applications for the position **Assistant Professor** (PIN #22932) that is a 12-month tenure eligible appointment in the Department of Bioscience Research. The ideal candidate for the position will be an investigator with an innovative and actively funded research program that is related to omics research (e.g., proteomics, metabolomics, genomics, transcriptomics, etc).

Review of applications will begin immediately and will continue until the position is filled.

For complete qualification/application information, see **http://uthsc.edu/hr/employment/job-list-faculty.php or http://uthsc.edu/hr/employment/job-desc.php?pin=22932**.

The University of Tennessee is an EEO/AA/Title VI/Title IX/Section 504/ADA/ADEA/V institution in the provision of its education and employment programs and services.

FRED HUTCH
CURES START HERE™

Senior Faculty Leadership Position in Immunology at Fred Hutchinson Cancer Research Center

The Vaccine and Infectious Disease Division (VIDD) of the Fred Hutchinson Cancer Research Center seeks exceptional applicants for a full-time senior faculty leadership position in immunology at the Full Member rank (comparable to Professor). The primary responsibility of this position will be to develop and lead a comprehensive, cross-disciplinary integrated research center (IRC) involving multiple investigators that will focus on pathogen-induced cancers. The candidate will be expected to conduct laboratory-based translational immunology research as part of this IRC and within VIDD, and an emphasis on mechanisms of memory/effector cell induction and immune dysfunction in the context of cancer or cancer-associated infections is highly desirable.

Candidates for this position must have a well established, robust, funded program that is nationally and internationally recognized for excellence in immunology, immunotherapeutic design, or viral oncogenesis.

Applicants must have an MD (or foreign equivalent) or PhD (or foreign equivalent). Selection criteria include excellence in scholarship, creativity in research, and demonstrated leadership in the profession.

VIDD scientists integrate clinical care, computational methods, and basic science research in immunology, virology, and vaccine design to reduce the global burden of infectious disease.

The Fred Hutchinson offers a vibrant intellectual environment within a beautiful, lakeside campus in Seattle's South Lake Union biotech hub. VIDD occupies a new building that is connected by walking trails to Seattle Cancer Care Alliance and the other four Divisions of the Fred Hutch and by trolley to major research partners such as the University of Washington School of Medicine, Seattle Children's Research Institute, Center for Infectious Disease Research (formerly Seattle Biomedical Research Institute), and the Infectious Disease Research Institute.

Interested candidates should submit a CV, a concise research plan statement, and the names and contact information for three (3) references to: **fredhutch.org/job/6653**. Specific inquiries can be directed to **Julie McElrath** at **206-667-1858**. Applications should be received by **August 15, 2016** to assure consideration and will be evaluated as received.

The Fred Hutchinson Cancer Research Center is an Affirmative Action, Equal Opportunity Employer. All qualified applicants will receive consideration for employment without regard to, among other things, race, religion, color, national origin, sex, age, status as protected veterans, or status as qualified individuals with disabilities. We strongly encourage applications from women, minorities, individuals with disabilities and covered veterans.

By **Carlos A. Aguilar-Trigueros**

The questions that opened doors

A couple years ago, I asked my Ph.D. adviser why he decided to give me a position in his lab. His answer was simple. "Because you were so focused on finding good questions," he told me. I found this answer amusing, because my early scientific training hadn't fostered this skill at all. In my undergraduate years at the University of El Salvador, the biological world had been presented as a series of known facts, and students were not trained to question them. There is little research tradition in El Salvador, and my professors didn't provide examples of what scientific inquiry is really about. I had entered university wanting to become a scientist, but my commitment was fading; my studies began to seem pointless. Then, late in my undergraduate studies, my path to a research career opened when I met a scientist who taught me about asking questions and showed me the human side of science.

I got her name from the German Embassy—one of many embassies some friends and I visited to inquire about scholarship opportunities for conducting research abroad. She had just finished her Ph.D. in Europe and moved to El Salvador with her husband, a physics professor at our university. I was excited to talk to someone who had done research abroad, so I visited her at her office.

After a few discussions, she came up with the idea of starting a journal club for students looking for topics for their bachelor's theses. The plan was to meet every Friday afternoon to discuss papers on plant-fungal interactions—her field of study, which I soon decided to pursue because her enthusiasm was so contagious. The journal club was a transformational experience. I had been trained to understand that what I read in a paper should be taken as truth, but now, for the first time during my academic career, my classmates and I were deconstructing papers and identifying their strengths and flaws. This was definitely not the approach to science that my professors had taught.

Reading papers that my new mentor had written during her graduate studies and those of people she knew also gave the science a human side. Before, scientific articles were just sheets of paper bearing cryptic messages, written in a foreign language by people I didn't know who worked at distant universities. Now, I could imagine the people behind them—and even imagine being one of those people myself. Her stories about her experiences as a graduate student were also enlightening. In El Salvador, there are no doctoral programs in the natural sciences or mathematics, so I was fascinated to learn that one could dedicate a lifetime to generating questions and collecting data to answer them.

"I was fascinated ... that one could dedicate a lifetime to generating questions."

The journal club and my other discussions with this scientist made the possibility of becoming a researcher feel more tangible and helped give me the courage to continue with biology. Instead of abandoning my interest in the natural world and changing my major, I sent emails to professors and programs overseas, seeking a chance to pursue graduate studies. Those emails contained the "good enough" questions that helped me secure an amazing internship at the Smithsonian Tropical Research Institute in Panama, where I had more time and training to refine my questions. From there, I moved on to my challenging but rewarding doctoral studies at the Free University of Berlin.

Now, as a postdoctoral fellow, I am working to solidify my science career. It is too soon to know where it will take me, but I hope to somehow help improve the research and training environment in El Salvador. In the meantime, I'd like to offer some encouragement to potential scientists in countries like mine, and pass on thanks to the mentors who help our research dreams become reality. Everybody can do science, but in countries like ours it requires a little extra creativity, perseverance, and patience to find the proper environment to develop your skills. Keep questioning. ■

Carlos A. Aguilar-Trigueros is a postdoctoral fellow at the Free University of Berlin. Send your science career story to SciCareerEditor@aaas.org.

ILLUSTRATION: ROBERT NEUBECKER